
A novel polymeric prosthetic heart valve: design, manufacture, and testing



Jacob Brubert

Department of Chemical Engineering and Biotechnology
and

Queens' College,
University of Cambridge,
UK

September 2015

This dissertation is presented for the degree of
Doctor of Philosophy

In memory of my grandparents.

Declaration

This dissertation is the result of my own work and includes nothing which is the outcome of work done in collaboration except as declared in the Preface and specified in the text.

It is not substantially the same as any that I have submitted, or, is being concurrently submitted for a degree or diploma or other qualification at the University of Cambridge or any other University or similar institution except as declared in the Preface and specified in the text. I further state that no substantial part of my dissertation has already been submitted, or, is being concurrently submitted for any such degree, diploma or other qualification at the University of Cambridge or any other University of similar institution except as declared in the Preface and specified in the text.

This dissertation contains fewer than 65,000 words including appendices, bibliography, footnotes, tables and equations and has fewer than 150 figures.

Jacob Brubert

Abstract

In this thesis a flexible leaflet polymeric prosthetic aortic heart valve was designed, manufactured, and tested. The prosthesis was designed with the aim of overcoming the need for anticoagulant therapy, which is required for current mechanical prostheses; while also having lifelong durability, which current bioprosthetic heart valves are not able to achieve.

Inspired by the anisotropic architecture of collagen in the natural valve, a shortlist of polystyrene based block copolymers (BCPs), which can be processed to yield mechanically anisotropic materials, was proposed. The shortlist was evaluated based upon processability, biostability, *ex vivo* haemocompatibility, and a novel material performance index comprising the flexural modulus and the cyclic fatigue stress predicted by fracture mechanics methods. Polystyrene-*block*-polyethylene-polypropylene-*block*-polystyrene with 22 mol% polystyrene (SEPS22) was selected for further testing and use in the design.

Haemocompatibility and calcification of the BCPs was assessed against reference materials. In measures of coagulation and thrombogenicity the BCPs were better than polyester, but worse than expanded polytetrafluoroethylene and pericardium graft materials. In measures of inflammation, the BCPs and polytetrafluoroethylene were better than polyester and pericardium. A durable heparin coating gave SEPS22 superior haemocompatibility compared to all the reference materials. The BCPs calcified less than pericardium, but calcification still accelerated failure.

The technique of injection moulding discs of the BCP from a point was used to create a novel biaxial structure of cylindrical polystyrene domains. A combination of modelling and bench-scale injection moulding was used to select a point from which the prosthetic heart valve injection tool cavity should be filled. By simultaneously injecting at a point at the centre of the free edge of each leaflet, a bioinspired orientation was produced.

Based upon hydrodynamic testing, a spherical form leaflet design was selected. The hydrodynamic performance of the complied with the ISO 5840 standard for cardiac valve prostheses, but the fatigue performance was inadequate due to the leaflets being thinner than specified due to manufacturer error. Fatigue prediction and finite element analysis were used to conjecture that correctly manufactured polymeric valves could theoretically reach the ISO limit, indicating that there is potential for polymeric prostheses to overcome the issues of durability and need for anticoagulation.

Summary

In this thesis I designed, manufactured, and tested a flexible leaflet polymeric prosthetic heart valve. The prosthesis was designed with the aim of overcoming the need for anti-coagulant therapy, which is required for current mechanical prostheses; while also having lifelong durability, which bioprosthetic heart valves are not able to achieve. No flexible leaflet polymeric heart valve has yet reached the clinic successfully.

Inspired by the anisotropic architecture of collagen in the natural valve, I proposed a shortlist of polystyrene based block copolymers (BCPs) which can be processed to yield mechanically anisotropic materials. The BCPs self-assemble at the nano-scale to form stiff polystyrene cylinders in a rubbery bulk. I formed a shortlist of cylinder-forming BCPs which I evaluated based upon processability, biostability, and *ex vivo* haemocompatibility.

To select optimal polymeric materials for a prosthetic heart valve I proposed a material performance index, in which leaflet thickness was the design variable, and flexural modulus and fatigue stress were combined in the ratio $\frac{E_{flex}}{\sigma_f^3}$, such that superior materials had a lower performance index. To rapidly evaluate the durability new materials I used fracture mechanics methods for the prediction of the cyclic fatigue stress, σ_f . I selected polystyrene-*block*-polyethylene-polypropylene-*block*-polystyrene with 22 mol% polystyrene (SEPS22) for further testing and use in the design.

Two potential leaflet designs were proposed. One was based on *cylindrical* surfaces (Burriesci et al., 2010), the other on *spherical* surfaces (Zaffora, 2011). Prototype valves were injection moulded from SEPS22 and their hydrodynamic performance tested *in vitro*. The spherical form valve had a smaller effective orifice area, but lower regurgitation, than the cylindrical form valve. Only the spherical form valve complied with the ISO 5840 standard, and so this design was selected. The spherical form valve design was subsequently improved by increasing the thickness of the stent posts which reduced their deflection during diastole.

I proposed injection moulding as a means to orient the stiff polystyrene domains and thus manufacture prostheses with a bioinspired orientation. When the polymer melt was isothermally injected from a point, into a thin disc, the (Giesekus and 3rd order fluid) viscoelastic constitutive models provided the best description of the velocity and pressure field. The (generalised Newtonian) Carreau-Bird model also provided an acceptable description of the velocity field. The ratio of shear to extensional deformations was used to predict the layered biaxial orientation of polystyrene cylinders which was found in the point injected samples. To determine the optimal point at which to inject the valve,

I used a combination of modelling (using the Carreau-Bird model and shear-extension ratio) and bench-scale injection moulding. By simultaneously injecting at a point at the centre of the free edge of each leaflet, a bioinspired orientation was produced.

The haemocompatibility of the shortlisted BCPs was tested with reference to expanded polytetrafluoroethylene (ePTFE), polyester (PES), and glutaraldehyde-fixed bovine pericardium (BP) graft materials using fresh human blood in modified Chandler loops. In measures of coagulation and thrombogenicity the BCPs were better than PES, but worse than ePTFE and BP. In measures of inflammation, the BCPs and ePTFE were better than PES and BP. A heparin coating was applied to SEPS22 which made the BCP superior to all the other materials, in both categories. There was minimal loss of the coating from the surface of SEPS22 after three weeks of dynamic straining in buffered solution. Hence, heparin coated and uncoated SEPS22 would be suitable for use in cardiovascular devices.

Degenerative aortic stenosis is caused by calcification. Calcification also threatens polymeric prostheses. The candidate BCPs were tested using a device which flexed the materials whilst they were immersed in calcifying solution. The BCP materials calcified less than the glutaraldehyde-fixed pericardium reference, but calcification was shown to increase the flexural stiffness and accelerate failure of the BCPs. Heparin coating of SEPS22 improved its durability in both calcifying and non-calcifying solutions.

I tested the hydrodynamic performance and durability of the bioinspired spherical leaflet form prostheses; the effective orifice area of the valve was $1.59 \pm 0.02 \text{ cm}^2$ (ISO 5840: $> 1 \text{ cm}^2$); and regurgitation was $5.06 \pm 0.61 \text{ ml/stroke}$ (ISO 5840: $< 10\%$). In terms of hydrodynamics the polymeric prostheses were inferior to a reference bioprosthetic valve. The polymeric prostheses survived 4×10^6 cycles at 100 mmHg and 200 BPM (ISO 5840: $> 2 \times 10^8$ cycles). The leaflets of the valve were thinner than specified (due to inaccurate tooling), reaching 150 μm instead of 300 μm at crucial points. This was a major contributor to the premature fatigue failure of the valve.

By extrapolating the fatigue prediction and using the results of finite element analysis, I predicted that correctly manufactured polymeric valves could theoretically reach the minimum ISO fatigue limit, indicating that there is potential for polymeric prostheses to overcome the issues of durability and need for anticoagulation.

Acknowledgements

I owe a great many thanks to a multitude of people. First and foremost, my supervisor Dr Geoff Moggridge who has provided guidance and support throughout. I received funding from the WD Armstrong fund, a travel grant from Queens' College, and lab funding from the British Heart Foundation (New Horizons grant NH/11/4/29059), without which this project would not have been possible.

My thanks go to Drs Marta Serrani and Joanna Stasiak who have been invaluable colleagues, particularly with respect to their experience of finite element analysis and small angle X-ray scattering. I am grateful to have had the polymer processing expertise of my advisor, Dr Bart Hallmark.

I was fortunate to spend time at the laboratories of Prof. Maria Laura Costantino at Politecnico di Milano, and Prof. Hans Pieter Wendel at Universität Tübingen, who were generous with both their time and resources in support of my project.

In the lab, Francesco de Gaetano (Milano), Michaela Braun (Tübingen), and Sergio Mercado (Cambridge) all taught me a great deal and were unsparing with their time. I constructed several items of equipment in this project which would not have been possible without the patient help of the electrical and mechanical workshops, particularly Gary Chapman.

I have had three fantastic years of research, which was very much aided by some great colleagues and friends within the Department of Chemical Engineering and Biotechnology, particularly those of the "M1 office". The Sparrows, 308ers, sardines, Queensmen and women, boys of Mussell Fort, and especially Cassi, you've made these years an awful lot of fun.

I am indebted to my family for so much. Within the scope of this thesis, Simon's scrupulous proof reading, and Sarah and Zach's delicious distractions.

Thank you everyone,

Jacob

Preface

The results of Chapter 2 were presented at the Design of Medical Devices (DMD) conference in Minneapolis, MN, April 2015, and subsequently published in the Journal of Medical Devices, 2015; 9(2):020912-020912-2.

The results of Chapter 3 were presented at the European Society of Biomaterials (ESB) conference in Liverpool, UK, September 2014; and published in the Journal of Materials Science: Materials in Medicine, 27(2), 1-12: 10.1007/s10856-015-5628-7.

The results of Chapter 4 were presented, as a poster, at the Materials in Medicine Conference, in Faenza, Italy, October 2013.

The results of Chapter 6 were published in Soft Matter journal, 2014, 10, 6077-6086. A patent was also filed as a result of this work: Heart Valve, British Patent Application 1403454.0, filed February 2013.

Material from throughout this thesis was presented at PCR London Valves, London, UK, October, 2014.

In this thesis I used, among many other techniques, small angle X-ray scattering (SAXS) and finite element (FE) modelling. When explicitly noted, the SAXS measurements were performed by Dr Joanna Stasiak, and the FE models were built and run by Dr Marta Serrani, who both worked on the British Heart Foundation grant at the Department of Chemical Engineering and Biotechnology, University of Cambridge, UK.

Contents

Declaration	iii
Summary	v
Acknowledgements	vii
Preface	viii
Nomenclature	xix
1 Background	1
1.1 Introduction	1
1.2 Anatomical and physiological introduction	2
1.3 Heart valve disease	8
1.4 Heart valve replacement	13
1.5 Cells, structure and function	14
1.6 From the inception of prosthetic heart valves to their current state	19
1.7 Design, development and testing methods	28
1.8 Flexible leaflet polymer prosthetic heart valves	29
1.9 Possible failure routes	37
1.10 Bioinspiration	39
1.11 Polymers	43
2 Polymer selection	47
2.1 Introduction	47
2.2 Materials and methods	68
2.3 Results	72
2.4 Discussion	81
2.5 Conclusion	84
3 Biocompatibility	87
3.1 Introduction	87
3.2 Materials and methods	93
3.3 Results	98

3.4	Discussion	107
3.5	Conclusion	112
4	Calcification	115
4.1	Introduction	115
4.2	Materials and methods	122
4.3	Results	125
4.4	Discussion	129
4.5	Conclusion	132
5	Valve design	133
5.1	Introduction	133
5.2	Materials and methods	147
5.3	Results	152
5.4	Discussion	162
5.5	Conclusion	166
6	Valve fabrication	167
6.1	Introduction	167
6.2	Point injection	171
6.3	Flow characterisation	178
6.4	Orientation modelling	197
6.5	Controlling orientation in the injection moulded valve	206
6.6	Final valve injection	217
6.7	Conclusion	219
7	Valve testing	221
7.1	Introduction	221
7.2	Hydrodynamics	222
7.3	Valve fatigue testing	223
7.4	Failure analysis	225
7.5	Conclusion	237
8	Concluding remarks	241
8.1	Conclusions	241
8.2	Further work	245
A	Valve development flow chart	251
B	Derivation of performance indices for material selection	255

C	Construction of the final valve	257
D	Cross model	259
E	Mooney-Rivlin model	261

List of Figures

1.1	Functional anatomy of the heart.	2
1.2	Cross sectional schematic of the aortic root.	3
1.3	Valve nomenclature.	4
1.4	Typical pressure and flow curves at the valves.	6
1.5	Leonardo da Vinci's sketches of flow in the sinuses of valsalva	8
1.6	Leaflet cross section.	15
1.7	Porcine valve stained for collagen.	17
1.8	Valve tissue mechanical properties.	19
1.9	Bileaflet mechanical valve.	21
1.10	Bioprosthetic valve.	22
1.11	Medtronic CoreValve transcatheter aortic valve implant.	26
1.12	FE modelling of orientation in an anisotropic valve.	41
1.13	Change in strain energy density after the optimisation of orientation. . .	42
1.14	Chemical structures of common polymer groups.	44
2.1	Block copolymer phase diagram.	49
2.2	Reversing the curvature of a leaflet.	56
2.3	Dynamic mechanical analysis of SIBS30-L.	59
2.4	Schematic and actual Ashby maps.	60
2.5	Elastomer Ashby map.	61
2.6	Typical σ -N curve.	62
2.7	Tensile testing samples.	65
2.8	Crack growth rate as a function of tearing energy (Lake, 1983).	68
2.9	Compression moulding schematic.	70
2.10	Dimensions of samples used for mechanical testing.	70
2.11	Shrink-induced cracking in SIBS30.	73
2.12	FTIR spectra of fresh and aged polymer samples.	74
2.13	Mass loss after accelerated ageing.	74
2.14	Stress-strain plots of polymers in tension.	75

2.15	Strain energy density of polymers in tension.	76
2.16	Crack tip position for SEBS20.	78
2.17	Crack growth rate against strain energy density.	78
3.1	Schematic of the Chandler Loop.	92
3.2	SEM micrographs of block copolymers contacted with blood.	100
3.3	Photograph and SEM micrograph of pericardium contacted with blood. .	101
3.4	Haemolysis and thrombin generation in blood.	101
3.5	Platelet count, activation, and adsorption.	103
3.6	Inflammatory markers.	105
3.7	Viability of L929 cells directly contacted with materials.	106
3.8	Analysis of heparin coating before and after ageing.	108
4.1	Cross sectional detail of calcification device.	123
4.2	Surface calcium concentrations.	126
4.3	SEM micographs of calcified samples.	127
4.4	Days to failure for samples in calcifying and non-calcifying solutions. . .	128
4.5	Change in flexural modulus after calcification.	129
5.1	Axial view of leaflet edges of a tricuspid valve.	137
5.2	Valve dimensions depend on positioning.	139
5.3	Open form of the valve of Thubrikar and Klemchuk (1990).	144
5.4	Cylindrical leaflet form valve.	146
5.5	Original and updated spherical form valves.	147
5.6	Cylindrical form valve surface construction dimensions.	148
5.7	Spherical form valve surface construction dimensions	149
5.8	Schematic of pulse duplicator.	151
5.9	EOA_G of prototype valves.	152
5.10	Regurgitation of prototype valves.	153
5.11	Energy loss over prototype valves.	154
5.12	Components of energy loss over prototype valves.	154
5.13	Images during systole for cylindrical form valve.	155
5.14	Images during systole for spherical form valve.	156
5.15	Images during diastole for spherical form valve.	157
5.16	Effect of leaflet thickness on opening of the spherical form valve.	158
5.17	Spatial variation in leaflet thickness.	159
5.18	Photographs during diastole of spherical form valve with fixed posts. . .	160
5.19	EOA_G when stent posts are fixed radially.	160

5.20	Regurgitation when stent posts are fixed radially.	161
5.21	Updated spherical form valve CAD.	165
5.22	FE modelling of spherical form valve with two stent post designs.	165
6.1	Schematic of injection moulder.	172
6.2	Schematic of SAXS setup.	174
6.3	SAXS pattern from a Z-axis beam and azimuthal integration for a point injection moulded sample.	175
6.4	SAXS maps of three point injected discs.	175
6.5	SAXS pattern for an in-plane beam and schematic.	177
6.6	Schematic of radial flow problem.	178
6.7	BOY 22D injection moulder.	181
6.8	Steady shear rate sweeps for SEPS22.	182
6.9	Steady shear sweeps at various temperatures.	183
6.10	Pressure and screw position during injection moulding.	184
6.11	Experimental pressure vs. generalised Newtonian pressure predictions. . .	185
6.12	Oscillating rheometry sweep of SEPS22 melt.	186
6.13	Normal stresses during pulse shear.	189
6.14	Normal stresses and viscosity during shear rate sweep.	190
6.15	Experimental vs. Newtonian and 3 rd order viscoelastic model pressures. .	191
6.16	Shear rate sweep data and results of the Giesekus model.	193
6.17	Disc segment mesh.	194
6.18	Velocity profiles for analytical and FE models.	196
6.19	Shear and extensions rates in Giesekus and Carreau-Bird models.	202
6.20	Vectorial shear and extension predicted by the Giesekus and Carreau-Bird models.	203
6.21	SAXS scan of PS cylinder orientation in a segment of a disc.	204
6.22	Correctly predicted orientation.	205
6.23	Schematic of stretch and shear at the critical value.	205
6.24	Correct prediction of orientation as a function of C_{sC} , and the flow-thickness- orientation space.	206
6.25	Inflows and outflows for valve injection.	208
6.26	FE valve mesh.	208
6.27	Predicted and measured orientation at various depths in valves injected from commissures.	210
6.28	Predicted and measured orientation at various depths in valves injected from the free edge.	211

6.29	Predicted and measured orientation at various depths in valves injected from the centre of the free edge.	213
6.30	Modelling of final cavity filling.	218
6.31	Final injection moulded valve.	219
6.32	SAXS mapping of leaflets of final valve.	220
7.1	Images of failed valves.	224
7.2	Mooney-Rivlin model and actual strain energy density.	227
7.3	von Mises stresses predicted by FE analysis during diastole.	228
7.4	Maximum strain energy density in the valves as a function of applied pressure.	229
7.5	Fracture mechanics and crack nucleation fatigue models.	232
7.6	Crack growth rates for SEPS22 in solution.	233
7.7	Predicted and measured valve fatigue life.	234
7.8	Birefringence and SAXS of tensile bar samples.	237
7.9	Light microscopy of the surface of SEPS22 samples.	238
8.1	Bridging and looping in triblock copolymers.	249
A.1	Flow chart for the selection of a polymeric material for use in a prosthetic heart valve.	252
A.2	Flow chart for the design of a polymeric prosthetic heart valve.	253
B.1	Uniformly loaded beam schematic.	255
D.1	Comparison of the Carreau-Bird and Cross model viscosities.	260

List of Tables

1.1	Pressures upon and deformations of native and diseased valves.	9
1.2	Echocardiographic parameters for stenosis and regurgitation.	10
1.3	Bioprosthetic heart valve deformations.	23
1.4	Early attempts at flexible leaflet polymeric prostheses.	30
1.5	Later reports of polymeric prostheses.	33
1.6	Failure routes for prosthetic heart valves.	37
2.1	Cylinder forming triblock copolymers.	50
2.2	Shortlist of block copolymers and reference polyurethane.	69
2.3	Tensile moduli of polymers.	76
2.4	Summary of durability and flexural stiffness properties which yield the performance indices.	80
3.1	Haemocompatibility ranking of materials.	112
4.1	Ion concentrations in calcifying solution.	124
4.2	Survival of samples during immersed durability tests.	129
5.1	Typical aortic root dimensions.	138
5.3	Surfaces used to described trileaflet aortic valves and prostheses.	141
5.4	Design features for heart valve leaflets.	145
5.5	Mooney-Rivlin parameters for strain energy density of SEPS22.	152
5.6	Summary of hydrodynamic data for the prototype valves.	161
6.1	Injection rates and sample thickness for point injected specimens of SIS30.	172
6.2	Giesekus model parameters.	193
6.3	Bird-Carreau model parameters.	194
6.4	Comparison of pressure drops recorded and predicted using analytical and FE models.	195
6.5	Processing conditions for injection of valves.	207

7.1	Hydrodynamic valve performance and ISO standards.	223
7.2	Results of quasi-real time durability testing of valves.	225
7.3	Mooney-Rivlin parameters for anisotropic SEPS22.	226
7.4	Fracture mechanics growth parameters and effective flaw sizes.	231
C.1	Steps in the construction of the final spherical valve geometry	257
D.1	Cross model fitting parameters for SEPS22 at 150 °C	259
E.1	Mooney-Rivlin parameters optimised for the tensile strain energy density of SEPS22	262

Nomenclature

Acronyms and abbreviations

<i>Symbol</i>	<i>Description</i>	<i>Units</i>
$(TPG_d)_{10}$	Transvalvular pressure supported for 10% or more of the cycle	mmHg
$(TPG_d)_{MAX}$	Maximum diastolic transvalvular pressure difference	mmHg
β -TG	β -thromboglobulin	
BSA	Body surface area	m ²
FWHM	Full width half maximum (of azimuthal integration of SAXS data)	°
TPG_d	Transvalvular pressure gradient during diastole	mmHg
b	Block (as found in a block copolymer)	
AAS	Atomic Absorption Spectrometer	
ADP	Adenosine diphosphate	
AFM	Atomic force microscopy	
ATR	Attenuated Total Reflectance	
BCP	Block copolymer	
BSA	Body surface area	m ²
CH	Corline Heparin	
CNC	Computerised numerical control	
CTAD	Citrate-Theophylline-Adenosine-Dipyridamole anticoagulant	
ECM	Extracellular Matrix	
EDX	Energy dispersive X-ray	
EOA	Effective Orifice Area	cm ²
EPDM	Ethylene propylene diene terpolymer	
ePTFE	Expanded polytetrafluoroethylene	
ESC	Environmental stress cracking	

<i>Symbol</i>	<i>Description</i>	<i>Units</i>
ESRD	External sewing ring diameter	mm
EWf	Essential work of fracture	J m ⁻²
FDA	Food and Drug Administration	
FE	Finite Element	
FSI	Fluid structure interaction	
FTIR-ATR	Fourier Transform Infra-red spectroscopy with attenuated total reflectance mount	
GAG	Glycosaminoglycan molecules	
GOA	Geometric orifice area	cm ²
HAp	Hydroxyapatite	
IC	Interstitial cells	
IOD	Internal orifice diameter	mm
ISO	International standards organisation	
LCA	Left coronary artery	
LLDPE	Linear low density polyethylene	
LVOT	Left ventricular outflow tract	
MRI	Magnetic resonance imaging	
PDMS	Polydimethylsiloxane	
PES	Polyester	
PET	Polyethylene terephthalate	
PMN-Elastase	Polymorphonuclear lastase	
PS	Polystyrene	
PU	Polyurethane	
PVC	Polyvinylchloride	
QALY	Quality Adjusted Life Year	years
RCA	Right coronary artery	
SAXS	Small angle x-ray scattering	
SBS	Polystyrene- <i>block</i> -polybutadiene- <i>block</i> -polystyrene	
SC	Solvent cast	
SC5b-9	Serum complement 5b-9	
SE	Stent-leaflet boundary	
SEBS	Polystyrene- <i>block</i> -polyethylene/polybutylene- <i>block</i> -polysyrene	
SEM	Scanning electron microscopy	
SEPS	(Poly)styrene- <i>b</i> -ethylene-propylene- <i>b</i> -styrene	

<i>Symbol</i>	<i>Description</i>	<i>Units</i>
SI/BS	(Poly)styrene- <i>b</i> -ethylene-butadiene- <i>b</i> -styrene	
SIBS	(Poly)styrene- <i>b</i> -isobutylene- <i>b</i> -styrene	
SIS	(Poly)styrene- <i>b</i> -isoprene- <i>b</i> -styrene	
TA	Texture analyser	
TAD	Tissue annulus diameter	mm
TAT	Thrombin-antithrombin complex	
TAVI	Transcatheter aortic valve implants	
TE	Tissue engineered	
vWF	von Willebrand Factor	
XPS	X-ray Photoelectron Spectroscopy	
XRD	X-ray powder diffraction	
xSIBS	crosslinked polystyrene- <i>block</i> -polyisobutylene- <i>block</i> -polystyrene	.

Dimensionless groups

<i>Symbol</i>	<i>Description</i>	<i>Units</i>
C_s	Ratio of shear rate to stretch rate	
C_v	Ratio of vector shear rate to vector stretch rate	
C_{sC}	Critical ratio of shear rate to stretch rate	
C_{vC}	Critical ratio of vectorial stretch rate to shear rate	
De	Deborah number	
R	Dimensionless radius	
Re	Reynolds number	

Symbols - Greek

<i>Symbol</i>	<i>Description</i>	<i>Units</i>
σ	Total stress tensor	Pa
τ	Shear stress tensor	Pa
τ_E	Viscoelastic component of stress tensor	Pa
τ_V	Purely viscous component of stress tensor	Pa
χ	Polymer-solvent interaction, or Flory-Huggins parameter	

<i>Symbol</i>	<i>Description</i>	<i>Units</i>
$\dot{\epsilon}$	Extension rate	s^{-1}
ϵ	Engineering strain	
ϵ_{flex}	Flexural strain	
η	Viscosity	Pa s
η_{∞}	Infinite shear rate viscosity (Bird-Carreau model)	Pa s
η_v	White-Metzner viscosity	Pa s
η_{0W}	Zero shear rate viscosity in Cross model	
η_{b0}	Zero shear rate viscosity (Bird-Carreau model)	Pa s
λ	Wavelength	m
λ_b	Natural time (Bird-Carreau model)	s
λ_r	White-Metzner relaxation modulus	s
λ_s	Stretch ratio, where s corresponds to a vector direction	
μ	Dynamic viscosity	Pa s
∇	Tensor gradient	
$\nabla \cdot$	Tensor divergence	
ρ	Density	$kg\ m^{-3}$
σ	Engineering stress	Pa
σ^*	Tear rupture stress	Pa
σ_c	Commissural stress, per unit length	$Pa\ m^{-1}$
σ_{cov}	Covariance	
$\sigma_{f\parallel}$	Fatigue stress with principal stress parallel to the fibre direction	Pa
σ_{flex}	Flexural stress	Pa
τ_W	Critical stress level for transition to shear thinning in Cross model	Pa
θ	Angle in radial coordinate system	
θ_c	Half angle between the leaflets at the commissure	$^{\circ}$
$\vec{\gamma}_v$	Shear vector	
$\vec{\epsilon}_v$	Stretch vector	

Symbols - Latin

<i>Symbol</i>	<i>Description</i>	<i>Units</i>
\mathbf{I}	Identity matrix	
ΔP_m	Mean pressure gradient	mmHg

<i>Symbol</i>	<i>Description</i>	<i>Units</i>
ΔP_{max}	Peak pressure gradient	mmHg
\vec{n}	Surface normal	
\vec{v}	Velocity vector	m s^{-1}
A	Crack area	m^2
a	Mobility parameter in Giesekus equation	
a_0	Initial flaw size	m
A_e	Pre-exponential factor in Arrhenius rate equation	mol s^{-1}
a_f	Critical flaw size for failure	m
a_m	Length of monomer unit	m
B	Power-law crack growth model coefficient	
b	Half-thickness of the disc	m
b_f	Flexural sample width	m
c	Crack length	m
d_{com}	Commissural spacing, normal to reflection lines	mm
E_a	Activation energy	J mol^{-1}
$E_{flex\parallel}$	Modulus when the contours of constant displacement are parallel to the stiff cylinders	Pa
$E_{flex\perp}$	Modulus when the contours of constant displacement are perpendicular to the stiff cylinders	Pa
F	Power-law crack growth model exponent	
f	Fraction of monomers A in a block copolymer chain	
F_{rev}	Maximum force for curvature reversal	N
h	Unstrained length of crack growth sample	m
I_{\parallel}	Material performance index when leaflet opening is improved by anisotropy	$\text{m}^4 \text{N}^{-2}$
I_P	Material performance index for polymers in prosthetic heart valves	$\text{m}^4 \text{N}^{-2}$
I_W	Material performance index parameter for the design of a uniform cross-section beam or wing	
I_{\perp}	Material performance index when leaflet opening is not improved by anisotropy	$\text{m}^4 \text{N}^{-2}$
k	Reaction rate constant	$\text{mol}^n \text{s}^{-1}$
k_g	Geometry related constant for tearing energy in a tensile bar	
L	Strained length	m

<i>Symbol</i>	<i>Description</i>	<i>Units</i>
L_0	Unstrained length	m
l_c	Characteristic length	m
L_s	Length of s , where s is defined in the subscripts section	mm
m	Power law fluid consistency index	
m_λ	Viscoelastic relaxation modulus power law consistency factor	
m_v	Viscoelastic power law consistency factor	
N	Polymerisation index	
n	Power law fluid power index	
n_λ	Viscoelastic relaxation modulus power law index	
n_b	Power law index (Bird-Carreau model)	
n_v	Viscoelastic viscosity power law index	
n_W	Cross model power law index	
P	Pressure	Pa
P_H	Hydrostatic pressure	Pa
Q	Flow rate	$\text{m}^3 \text{s}^{-1}$
R	Gas Constant	$\text{J K}^{-1} \text{mol}^{-1}$
r	Radius	m
R_f	Regurgitant fraction	
r_p	Pressure measurement radius	Pa
T	Absolute temperature	K
t	(Leaflet) thickness	m
T_e	Energy release rate or tearing energy	N m^{-1}
T_m	Melting temperature	K
T_{ODT}	Order-disorder transition temperature	K
U	Total internal energy	J m^{-3}
V	Volume	m^3
V_c	Closing volume	ml
V_l	Leakage volume	ml
v_m	Mean velocity	m s^{-1}
V_{rev}	Retrograde flow in one cycle	ml
V_{sv}	Stroke volume	ml
W	Strain energy density in test piece	Pa
z	Axial position in radial coordinate system	

<i>Symbol</i>	<i>Description</i>	<i>Units</i>
L	Denotes stretching parallel to the PS domain orientation	
R	Denotes stretching perpendicular to the PS domain orientation	

Subscripts and superscripts

<i>Symbol</i>	<i>Description</i>	<i>Units</i>
A	Aortic/distal side of the valve	
c	At the commissure	
f	At edge of disc	
v	Ventricular/proximal side of the valve	
$cc-aa$	From the coronary arteries to the aortic annulus	
max	Maximum	
min	Minimum	
stj	Sino-tubular junction	
TAD	(At the) tissue annulus (diameter)	

Chapter 1

Background

1.1 Introduction

The first heart valve prostheses were developed and implanted in humans during the 1950s (Bodnar and Frater, 1992): since then ten of millions of lives have been transformed worldwide. Nonetheless, research and development of heart valve prostheses remains an important public health endeavour. The current gold standards for heart valve replacement are not a complete solution to heart valve disease: they leave patients with a reduced lifespan or quality of life compared to healthy patients of the same age (D’Arcy et al., 2011). There are two main types of prosthesis - biological and mechanical valves. Those from biological materials allow patients to lead a relatively normal life, not requiring anticoagulant therapy, but have a limited durability of up to approximately 15 years. Mechanical valves rarely fail in a human lifetime, however they require lifelong anticoagulant therapy which increases the risk of fatal bleeds. This thesis examines whether it may be possible to overcome these 2 issues.

This introduction will first provide a general description of heart valve anatomy and physiology before reviewing the pathologies which lead to native heart valve failure. I will consider the extent of heart valve disease and replacement before turning to the prosthetic implants which have been developed to date. I will perform a critical review of the prosthetic valves that have achieved clinical success, as well as those that have fallen by the wayside, setting a context for the research that is presented in this thesis.

1.2 Anatomical and physiological introduction

Valves are abundant throughout the cardiovascular system, and lead to unidirectional flow (an observation that led William Harvey to propose the theory of circulation in 1617). All valves in the circulation are passive; they do not require any muscular activation to function. The four cardiac valves are located at the entry and exit of the cardiac chambers, as illustrated in Figure 1.1.

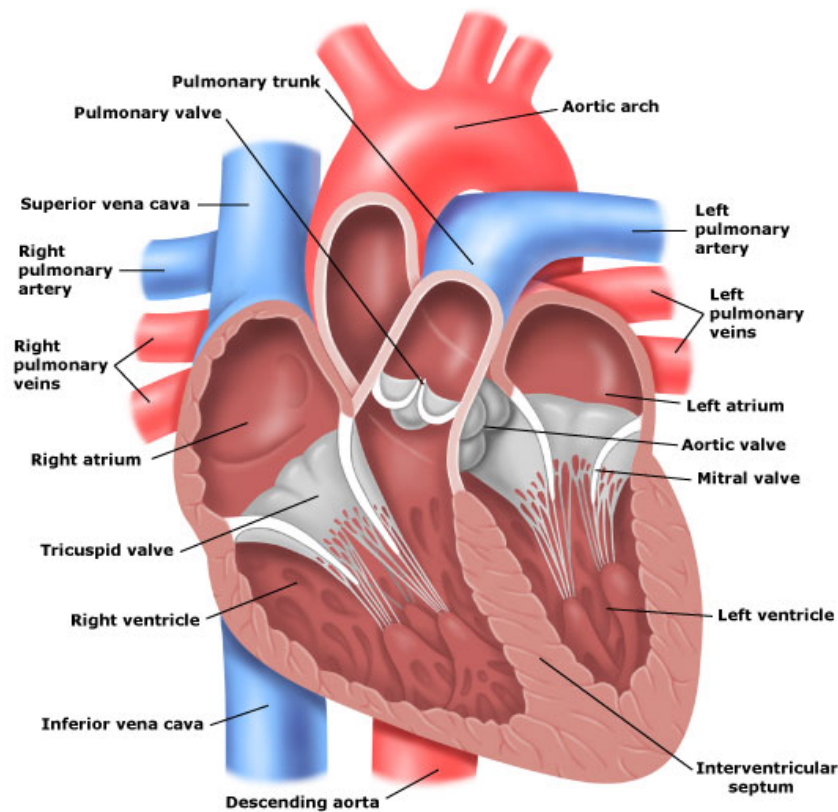


Figure 1.1: Functional anatomy of the heart showing the four cardiac valves. Taken from Medcore (2012).

The heart provides the pressure head to circulate blood throughout the body. The left side of the heart receives oxygenated blood which is pumped to the body, while the right side pumps the returning deoxygenated blood to the lungs. A cardiac cycle commences with atrial contraction, forcing blood through the mitral and tricuspid valves, and contributing around 10% to the final ventricular volume at resting heart rates, and up to 40% at high heart rates. Blood is then forced from the ventricles when they contract during systole, opening the aortic and pulmonary valves, and closing the mitral and tricuspid valves. The ventricles passively dilate during diastole causing the aortic and pulmonary valves to close, while the mitral and tricuspid valves open to allow the ventricles to refill. To

recommence the systolic phase, the atria contract.

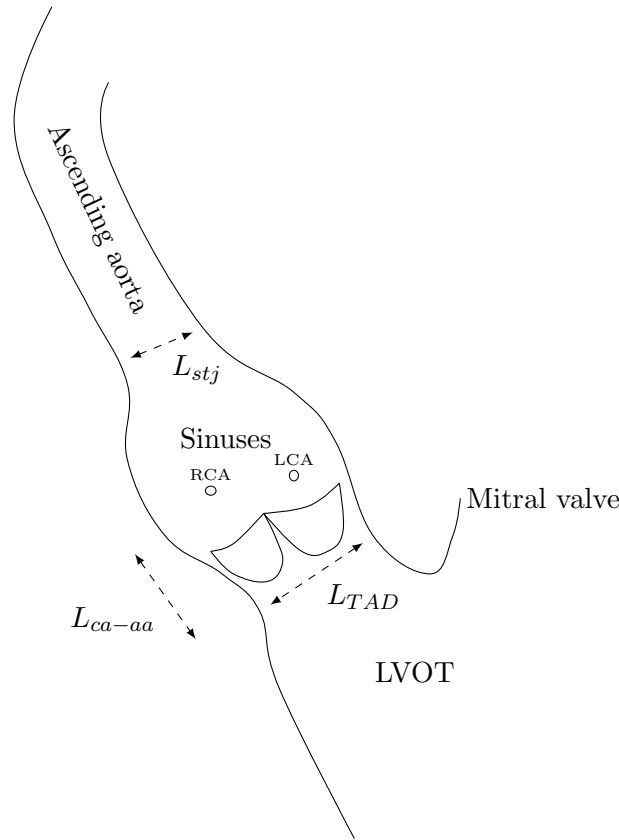


Figure 1.2: Cross sectional schematic of the aortic root. RCA and LCA indicate the right and left coronary arteries respectively, the non coronary leaflet is not shown. L_{TAD} indicates the diameter of the aortic annulus (TAD), which occurs at the narrowest point in the root, near to the nadirs of the leaflets. L_{stj} is the diameter at the sino-tubular junction, L_{ca-aa} is the distance between the aortic annulus and the coronary arteries. LVOT refers to the left ventricular outflow tract.

The work presented in this thesis concentrates on the development of aortic prostheses and as such the discussion of anatomy and physiology is focussed on this valve. The reasons behind this choice are expanded upon in Section 1.3 and 1.4. As depicted in Figure 1.2, the aortic valve is located in the aortic root where the aorta joins the left ventricle. The proximal end (nearest to the heart) of the root is the transition from muscular cardiac tissue to fibrous arterial tissue. This join is termed the annulus, and occurs near to the narrowest point in the root which is termed the *true* annulus. This annulus has a diameter from 18 to 30 mm, which roughly scales with body size. The aortic root then expands into 3 *sinuses*, before contracting to the *sino-tubular* junction where it joins the aorta.

The nomenclature used to refer to locations on both the native and prosthetic valves is displayed in Figure 1.3a. The aortic valve contains 3 crescent shaped *leaflets*, or *cusps*,

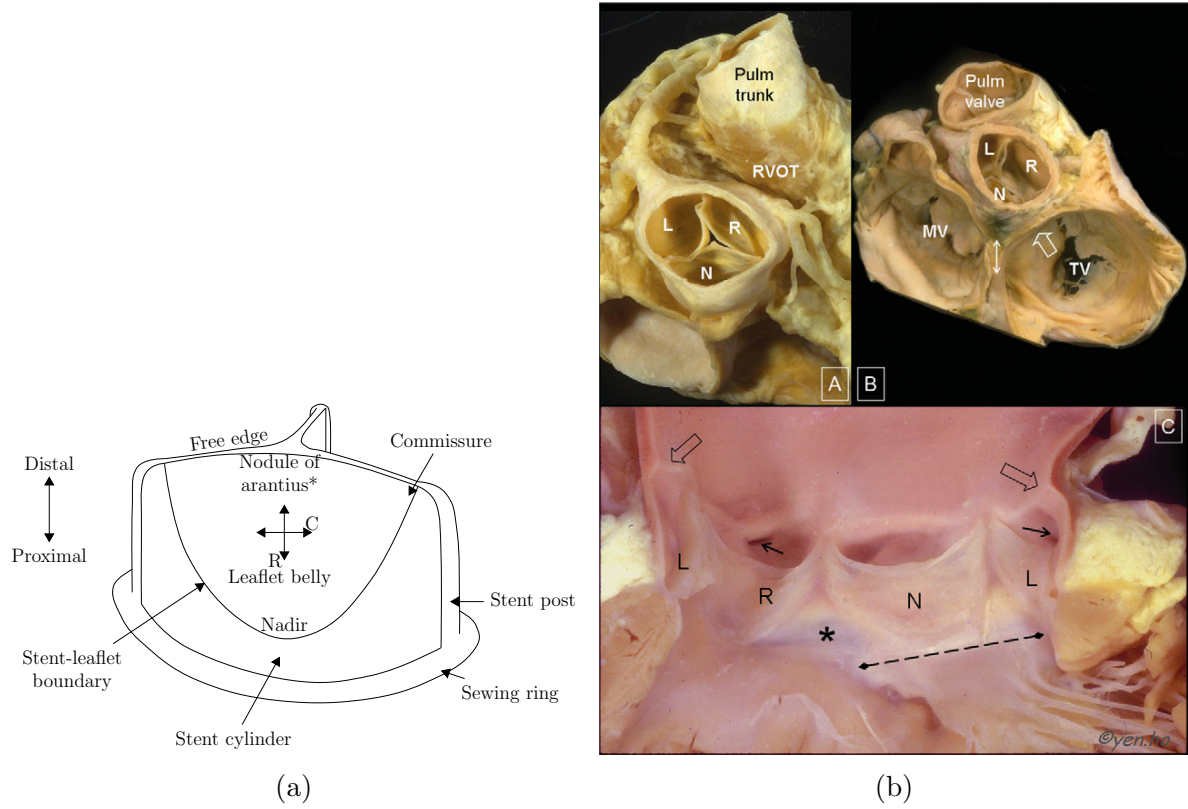


Figure 1.3: (a) shows the nomenclature used to describe the parts of a prosthetic valve. The nodule of Arantius (where the collagen bundles meet) is only found on the native leaflet, not on a prosthetic valve. All positions on this prosthetic *leaflet* are also found on the native leaflet. C and R refer to the circumferential and radial directions on the leaflet. (b) is from (Ho, 2009), images A and B show a dissected human heart with the left (L), right (R), and non-coronary (N) cusps of the aortic valve marked. In image C, the aortic valve has been opened longitudinally. The open arrows indicate the location of the sino-tubular junction, the small arrows indicate the coronary artery orifices and the dotted line marks the fibrous tissue separating the mitral and aortic valve. With permission from Oxford University Press.

which are joined to the sinuses along their proximal sides, and have a distal free edge. The most proximal point on the leaflet-sinus boundary is the leaflet's nadir, while the central point of the free edge is the nodule of Arantius¹. The vertices where the free edge meets the aorta are called commissures.

The cusps are referred to as the right coronary, left coronary and non-coronary cusps; named according to the artery to which they are nearest. The nadir of each leaflet of the valve is at the level of the annulus, while the commissures of each leaflet are approximately 15 mm distally. The coronary arteries are found in the sinuses and are the first blood

¹Name after the prominent 16th century anatomist Giulio Cesare Aranzi, from the University of Padua.

vessels to depart from the artery. The position of the aortic valve leaflets within the aortic sinus relative to the intricacies of the anatomy is shown in Figure 1.3b. In particular, note the proximity of the left ventricular outflow tract (LVOT) to the coronary ostia in Figure 1.2, a prosthetic valve must not obstruct either structure.

A typical resting heart rate is 70 bpm, with a cardiac output of 5 l min^{-1} . This equates to approximately, 40 million cycles each year, or 3 billion cycles in a lifetime: hence any implant which dares to imitate the native organ must have remarkable resilience. At rest, in general, the systolic phase lasts $\frac{1}{3}$ of the cycle period and the diastolic phase for the remaining $\frac{2}{3}$. Roughly 70 ml are ejected from both sides of the heart during each stroke (the stroke volume). The pressure in the aorta oscillates between 120 and 80 mmHg in a normal, healthy heart. Typical pressure and flow rate profiles are presented in Figure 1.4. Qualitatively, the cardiac cycle consists of the following phases:

1. *Atrial contraction*: completes the filling of the ventricles, up to ~ 120 ml each. The mitral and tricuspid valves close.
2. *Isovolumic contraction*: the start of ventricular contraction causes the ventricular pressure to increase. The phase finishes once the aortic and pulmonary valves are opened, and blood starts to flow.
3. *Systole*: the ventricles continue to contract causing rapid ejection of blood into the aorta and pulmonary artery. The maximum flow rate ($\sim 20\text{ l min}^{-1}$) is rapidly reached, and the diminishing flow continues until the minimum ventricular volume (~ 50 ml each) is reached, and the aortic and pulmonary valves close.
4. *Isovolumic relaxation*: All 4 valves are closed. The ventricles relax, and the ventricular pressure falls.
5. *Diastole*: The mitral and tricuspid valves open, and the relaxed ventricles are filled with blood. Ventricular filling is completed by the contraction of the atria as step 1 resumes.

1.2.1 Valvular biomechanics and haemodynamics

The Reynolds number, Re , is used to describe fluid flow around an object or through a vessel. Re is the dimensionless ratio of inertial to viscous forces in a flow:

$$Re = \frac{\rho v_m l_c}{\mu} \quad (1.1)$$

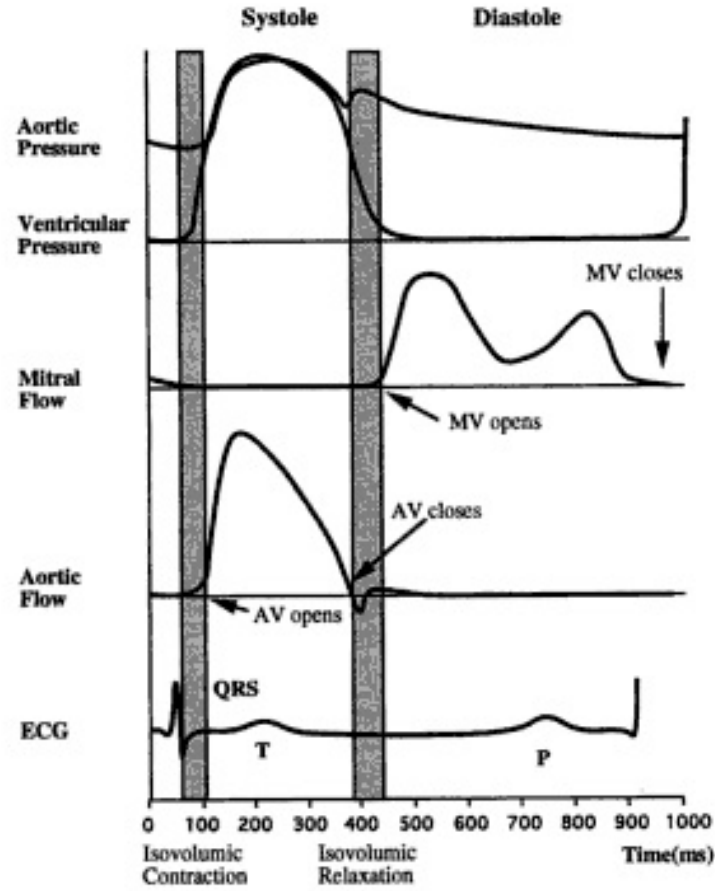


Figure 1.4: Typical pressure and flow curves for aortic (AV) and mitral (MV) valves. ECG is the trace from the electrocardiogram, upon which the QRS complex, T, and P waves are indicated. Taken from Bronzino (2000).

where ρ is the density, v_m is the mean velocity, μ is the dynamic viscosity of the fluid, and l_c is the characteristics length within the flow, which, in this case may refer to the aortic diameter. The systolic flow through the open aortic valve has a Reynolds number between 1500 and 5000. A Reynolds number up to 2100 describes laminar flow, while above 4000 the flow is turbulent. Turbulent flow is characterised by small random variations in velocity and pressure, rapid mixing, and the presence of vortices and high shear forces. In the transition region, for flow in a smooth pipe, elements of both flow types may be present.

High shear forces in blood lead to the release of adenosine diphosphate (ADP) from platelets, causing them to aggregate and blood clots to form; a process which receives further attention in Chapter 3. Importantly, as the flow through the valve may be turbulent, small changes to the flow field and geometry can trigger clot-forming turbulence (Yoganathan et al., 2005).

The time averaged 5 l min^{-1} blood flow through the aortic root is far from having a steady laminar profile. The fluid is initially stationary in the ventricle, so flow is far from developed. Also, blood does not behave as a Newtonian fluid, so a parabolic flow profile is unlikely. Considering the anatomy, ventricular contraction extends to the aortic annulus, while the sinuses dilate under pressure, even before reaching the arch of the aorta. The geometry is not a uniform cylinder and is highly dynamic. Overall, these factors result in a relatively flat flow profile upstream of the valve (observed *in vivo* using 3D magnetic resonance imaging (MRI)), which is slightly skewed (10%) towards the septal side (Balachandran et al., 2011). In healthy individuals the maximum velocity through the aortic valve at rest is approximately 1 m s^{-1} , as measured by pulsed Doppler during cardiac surgery (Mathison et al., 1988).

The opening of the heart valve is driven by the pressure difference between the ventricle and aorta. The curvature of each leaflet must reverse in order to open. This reversal starts at the central ‘belly’ of each leaflet, and all 3 leaflets generally open simultaneously (Thubrikar and Klemchuk, 1990). Closure of the heart valve is more complex. The valve sits at the base of the aortic sinuses, the expansion in diameter at the sinuses leads to interesting haemodynamics. Investigation into flow in the aortic sinuses has a long history; between 1508 and 1513 Leonardo da Vinci completed accurate drawings of a pig’s aortic root, recorded in *Quadratica Anatomica*, an example of which is shown in Figure 1.5. Noticing the peculiar form of the sinuses, da Vinci experimented further by constructing a glass model of the root using a plaster cast. Then, he “let the water that strikes there have millet or fragments of papyrus mixed with it so that one can see the course of the water better from their movements”. da Vinci observed that the swirling vortices that are generated in the sinuses behind the valve’s open leaflets contribute to the closing of the valve. This observation - which is probably the first recorded example of particle image velocimetry - has been corroborated using modern *in vitro* and *in silico* methods (Gharib et al., 2002; Robicsek, 1991).

When the valve leaflets are closed they support a large pressure differential. This causes stresses and strains within the leaflets, which are supported by the aortic wall. All living cells respond to mechanical stimuli in some way, and those cells that make up cardiac valves are no different. Cell deformation - and any changes which result - may be causative of, or associated with, disease. Thubrikar et al. (1980) made *in vivo* measurements of leaflet strain (mostly on dogs using fluoroscopic markers). Based upon excised valves, they assumed that the leaflets were cylindrical, with a thickness of 0.4 to 0.5 mm, from which they estimated the tissue modulus *in vivo*. The results were verified with measurements of the moduli on the excised valves. These results are shown in Table 1.1. It should be

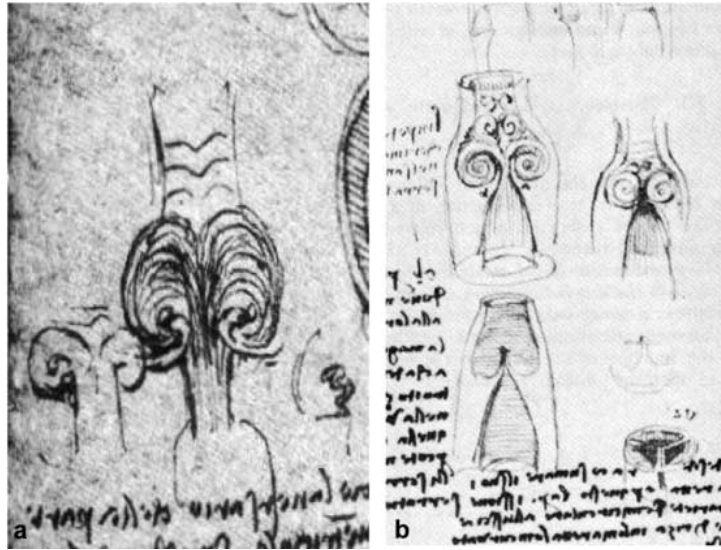


Figure 1.5: Detail of Leonardo da Vinci's sketches of flow in the sinuses of valsalva. From RL19117 verso, with permission from Royal Collection Trust / ©Her Majesty Queen Elizabeth II 2016.(Gharib et al., 2002).

noted that the valve leaflet is a composite structure (discussed further in Section 1.5) and so the listed stress is *not* homogeneous throughout the leaflet.

1.3 Heart valve disease

Valves are responsible for the unidirectional flow of blood and so there are two ways in which this can be compromised. If a valve is unsuccessful at restricting reverse flow, it is described as regurgitant. This may be caused by failure to maintain a tight seal when closed during diastole, or by being too slow to close. Alternatively, the valve may become stenotic, meaning the open orifice area has decreased which disrupts forward flow. This disruption is generally caused by stiffening or thickening, referred to as sclerosis, of the valve's leaflets which stop it from opening fully. Heart valve disease is defined as the presence of either regurgitation or stenosis in any of the valves which compromises the cardiovascular system.

It is quite possible to live a perfectly normal life and be totally unaware of the first signs of heart valve disease. In fact, the prevalence of valve disease based upon clinical suspicion is considerably lower than the prevalence based upon echocardiographic measurements (Iung and Vahanian, 2011). Normally, the first signs that a valve is defective will be a heart murmur, which can be diagnosed via auscultation. However, a heart murmur may be present in the absence of any other symptoms, and may not always indicate heart

Table 1.1: Summary of the pressures exerted on, and the deformations found in native and diseased heart valves, adapted from Balachandran et al. (2011) and ISO 5840. The radial and circumferential directions are declared in Figure 1.3a.

Mechanical parameter	Normal	Diseased (very severe)	Notes
Resting aortic pressure during diastole (max.)	65 to 85 mmHg	≥ 120	
Resting aortic pressure during systole (max.)	100 to 130 mmHg	≥ 210	
Differential pressure across closed valve (max. during diastole)	95 mmHg	185	
Geometric area	3 to 4 cm	≤ 2	(Garcia and Kadem, 2006)
Diastolic tensile strain (circumferential)	9-11%	$\geq 15\%$	Measured in Porcine aortic valve (Yap et al., 2010)
Diastolic tensile strain (radial)	13-25%	15-31%	Measured in Porcine aortic valve (Yap et al., 2010)
Diastolic membrane stress	2.4 kPa		Measured in dogs (Thubrikar et al., 1980)
Systolic membrane stress	0.167 kPa		Measured in dogs (Thubrikar et al., 1980)

valve disease.

Unfortunately, many effects of heart valve disease are not as benign as a heart murmur. Heart valve disease can lead to heart failure, where death is normally a result of stroke, blood clots, or sudden cardiac arrest. A typical heart failure patient will present with shortness of breath, unusual fatigue, and swelling of the ankles, feet, legs, abdomen, and veins in the neck. Heart valve disease may also lead to chest pain upon exertion, irregular heart beats, or dizziness and fainting. Surgical intervention is the only therapy which can restore a normal way of life. No other medical treatments currently exist which prevent or reverse the physical reality of heart valve disease, however the effects and symptoms can often be mediated by lowering the load on the heart, preventing arrhythmias, and taking anti-clotting therapies (National Heart Lung and Blood Institute, 2011). A definitive diagnosis of heart valve disease is normally based upon an echocardiogram which indicates

the incomplete opening or closing of the valve. Table 1.2 shows the clinical definition of severe aortic valve stenosis and aortic regurgitation based upon this data. If left untreated, aortic stenosis has a 5 year mortality of 88.4% with a mean survival of 1.8 years (Clark et al., 2012).

Table 1.2: European Society of Cardiology (ESC) and the European Association for Cardio-Thoracic Surgery (EACTS) guidelines for echocardiographic evaluation of severe aortic stenosis and aortic regurgitation (Vahanian et al., 2012)

	Severe aortic stenosis
Valve area (cm^2)	≤ 1.0
Indexed valve area ($\text{cm}^2 \text{ m}^{-2}$ body surface area (BSA))	≤ 0.6
Mean gradient (mmHg)	≥ 40
Maximum jet velocity (m s^{-1})	≥ 4.0
Velocity ratio ($= \frac{V_{LVOT}}{V_{AV}}$)	≤ 0.25
	Aortic regurgitation
Effective regurgitant orifice area (mm^2)	≥ 30
Regurgitant volume (ml/beat)	≥ 60
<i>Vena contracta</i> width (mm)	≤ 6

1.3.1 Aetiology and epidemiology

Heart valve disease can manifest itself from birth through to old age, though it has differing aetiologies depending on age. Congenital deformities associated with heart valves typically present with bicuspid aortic valves (just 2 leaflets), which occurs in 0.6-0.8% of males and 0.2% of females. While a bicuspid valve will function with little cause for alarm, the deformity results in a highly elevated risk of aortic stenosis, which manifests itself with age (Iung and Vahanian, 2011). More rarely there are cases of unicuspid valves, which also result in stenosis. Quadricuspid valves are found even more infrequently, and result in aortic insufficiency (Thubrikar and Klemchuk, 1990). Occasionally, heart valve disease may be caused by infective endocarditis (inflammation of inner lining of the heart), generally from *Staphylococcus*, or other inflammatory causes. This accounts for 0.9% of aortic stenoses and 11.6% of aortic regurgitation cases, corresponding to 31 cases per million population (Iung and Vahanian, 2011).

For most of the 20th century rheumatic fever was the principle cause of heart valve failure. Rheumatic fever is caused by a group A streptococcal infection which results in a chronic and degenerative disease whose greatest effect is the growth of excess connective tissue

on the heart valves (fibrosis). Currently, over 15 million people are estimated to be affected by rheumatic heart disease, the vast majority in developing countries. A large proportion will require heart valve surgery which is unlikely to be available to them. The near eradication of rheumatic fever in developed countries can be attributed to improvements in hygiene and availability of antibiotics (World Heart Federation, 2012), and hence strategies for eradication of this form of heart valve disease in developing countries are predominantly political and economic issues. For those who have suffered from rheumatic fever, and will develop heart valve disease, heart valve replacement is the only solution. Although the opportunities for cardiac surgery are limited, it is not impossible to have a heart valve replaced in developing countries. Cardiac centres can be found in 18 African countries, and in 2005, over 16,000 cardiac operations took place in Africa. As cardiac surgery is so closely tied to economic growth, the number of operations is expected to increase (Edwin et al., 2011; Pezzella, 2005). Currently, mechanical valves are more commonly implanted due to their durability and affordability. However, the lack of availability of anticoagulants and poor patient compliance means that the implantation of mechanical valves carries a significant risk of a thrombotic event occurring. As such there exists a need for heart valve prostheses which do not require anticoagulation, while being more durable and more affordable than bioprotheses (Zilla et al., 2008).

Despite the decrease in heart valve disease resulting from rheumatic fever, the overall incidence of heart valve disease continues to rise. This rise can be attributed to the *degenerative* form of heart valve disease, which is now the most prevalent type. The incidence of valvular disease is $\leq 2\%$ before the age of 65, but rapidly rises to 8.5% between 65 and 75, and further increases to 13.2% above the age of 75. There is an age adjusted prevalence of 2.5%, corresponding to approximately 1.6 million people suffering from valvular heart disease in the UK (Iung and Vahanian, 2011). In the United States, of the 2.4 million deaths in 2006, 20,260 were attributed to valvular diseases, with aortic disease accounting for 62.5%, and mitral valve disorders 12.6% (Heron et al., 2009; Rosamond et al., 2008). The burden of valvular disease is projected to grow. In the UK for example, the number of people older than 75 years is projected to increase by 50% by 2025 (Malhotra, 2012), leading to the pronouncement by D’Arcy et al. (2011) that “valvular disease is the next cardiac epidemic”.

Aortic stenosis is often referred to as a “degenerative” pathology as it shows a strong correlation with age, however the mechanism associated with valvular diseases is poorly understood. It is clear that smoking, hypertension, hyperlipidaemia, hypercholestraemia and diabetes are the greatest risk factors (D’Arcy et al., 2011).

The distribution of valvular disease type is dominated by pathologies of valves of the

left side, which could be attributed to the higher pressures found on this side. The Euro Heart Survey - which is dominated by degenerative cases - reported that 44.3% of valvular disease was aortic, 34.3% mitral and 20.2% mixed. And within this breakdown, three quarters of disease, for both valves, is associated with the systolic phase - aortic stenosis and mitral regurgitation (Iung, 2003).

1.3.2 Pathological mechanisms and biomechanics

Biomechanics is a major player in the initiation and progression of aortic valve pathologies. Aortic stenosis results from the incomplete opening of the heart valve leaflets which is caused by a mechanical stiffening of the leaflets. Most typically, this stiffness is caused by the deposition of calcium phosphate crystals in a process termed calcification. Specifically, this pathology is termed calcific aortic valve disease. It is tempting to draw parallels between stiffening and blocking of arteries in atherosclerosis, and valve calcification; both display similar inflammation and lead to the release of cytokines which trigger bone morphogenic proteins and cause osteogenic cell phenotypes to develop. However, statin therapy does not halt calcification of the valves and may in fact accelerate it; the evidence is unclear as to whether it is at all preventative (Goldbarg et al., 2007).

Aortic stenosis leads to a significant change in haemodynamics, which is manifested in 2 ways; firstly, an increased resistance to flow, and secondly a change in flow profile. While a healthy valve may have a peak axial velocity of 1.20 m s^{-1} , a severely diseased valve may reach 7 m s^{-1} . This elevation is sufficient to raise shear stresses, causing rupture of blood cells and damage to the endothelial cell layer which coats the aorta (Balachandran et al., 2011).

The mechanisms that lead to aortic regurgitation are less clear. While the majority of cases are due to rheumatic fever, a study of 756 patients in the developed world found that 40% of cases had a mixed or unclear cause, 29% were degenerative, 10% occurred in patients with a bicuspid valve, 11% in patients with an aortic root pathology and 10% due to endocarditis (Varadarajan et al., 2013). Inflammation and scarring is present in all these pathologies, which lead to abnormal valve mechanics. For example, dilation of the aortic root may reduce the contact area between the leaflets during diastole (*coaption*), or scar tissue may lead to stress concentrations and subsequent tears in the valve.

Degeneration and ageing are a common *cause* of both stenosis and regurgitation, but what does ageing do to heart valve leaflets? Christie and Barratt-Boyes (1995) reported that the strain, at fixed stress, in leaflets collected from allograft donors decreased approximately 4%/year from age 15 to 25, and at 1%/year until the age of 58 - and presumably thereafter.

The authors concluded that stiffening of the tissue reduced the performance, due to a reduced coaption area, however they were unable to say whether the change was due to calcification, or if other physiological factors were at play.

1.4 Heart valve replacement

In any patient receiving a diagnosis of severe aortic stenosis (likely via echocardiogram) and who is also symptomatic, aortic valve replacement is indicated. In asymptomatic cases, aortic valve replacement may be indicated by the presence of a low systolic ejection fraction, abnormal exercise test, or when undergoing a coronary artery bypass graft (Vahanian et al., 2012).

Worldwide, between 275,000 and 370,000 valve replacements take place annually (Zilla et al., 2008). In the UK in 2010 there was an incidence of 240 valvular procedures per million population (Society for Cardiothoracic Surgery in GB and Ireland, 2011). Considering the observed prevalence of heart valve disease, it is estimated that roughly 1% of those who suffer from valvular heart disease actually receive a replacement valve. This low fraction is supported by results from the Helsinki ageing study (Lindroos et al., 1993), 476 were aged 75 to 85 years, 14 of whom were diagnosed with severe aortic valve disease (3%). Although 8 of these were symptomatic and eligible for valve replacement, just 2 opted for valve surgery. This opt-for fraction seem to be relatively constant in studies worldwide, and is likely to be because many patients are otherwise healthy and surgery is traumatic.

Although the worldwide number of heart valve procedures has remained relatively stagnant for the past decade, the number of procedures is expected to increase dramatically in the coming decades; this rise will be predominantly driven by an increase in access to cardiac surgery. Cardiac surgery is available to the majority of European and North American patients, but just 10% of the Indian and Chinese populations have had access over the past decade. Africa is still poorly served: there are 112 times as many cardiothoracic surgeons per capita in Europe as Africa (Zilla et al., 2008). Considering the overall picture, Yacoub and Takkenberg (2005) predicted that worldwide, valve replacements would triple from 290,000 in 2003 to over 850,000 by 2050.

Over 85% of valve replacements are performed using open heart surgery. First time surgery for an aortic valve replacement carries a mortality risk of 2% (Society for Cardiothoracic Surgery in GB and Ireland, 2011). First reoperation increases that risk to 10% (Jones et al., 2001), and further reoperations carry even higher risks. This is a highly

traumatic surgery. Under general anaesthesia, an incision is made down the chest, the sternum is sawn open, the pericardium opened and the patient is placed upon a heart-lung bypass machine. The heart is stopped, the aorta opened, the native valve excised, and the prosthetic valve implanted. The incisions through the aorta and pericardium must be closed, the patient brought off the bypass and the heart restarted. In an octogenarian population heart valve replacement may require approximately 5 days in the intensive care unit, and a 2 week hospital stay (Kolh et al., 2007). However, we should recall the benefits: once a patient presents with angina, syncope or dyspnea, only 50% survive to 2 years. Without valve replacement, 75% of patients will be killed by aortic valve disease. Survival after replacement is nearly equal to average survival rates when adjusted for age, until valve degradation becomes an issue after 10 years (Carabello, 2002).

1.4.1 Selection of valve

For several reasons, the focus of this thesis is on the aortic valve. Firstly, it is the valvular disorder with the highest mortality risk. Furthermore, age-related valvular disease is often caused by calcification which leads to stenosis, while the lingering effects of rheumatic fever (which causes regurgitation) become rare; the ratio of aortic stenosis to mitral regurgitation is expected to increase in an ageing population. Secondly, aortic prostheses are occasionally used as mitral valve replacements, however the converse does not occur. Finally, mitral disease is dominated by regurgitation, for which some interventions do not use complete prosthetic valves. Instead, a surgical or transcatheter repair is performed in which the native leaflets are tightened.

1.5 Cells, structure and function

The aortic valve is passive - opening and closing is driven purely by fluid forces - and hence it contains no muscular tissue. The principal structures of the valve are the fibrosa and ventricularis, which are separated by the spongiosa layer, as shown in Figure 1.6. These three layers have five principle constituents: collagen, elastin, glycosaminoglycans (GAGs), endothelial cells and interstitial cells. All structural and constituent types play a specific role and can shed light on ways in which synthetic implants might cope with the biological, chemical, and mechanical environment.

Proceeding from the ventricular side of the leaflet, the first structure is appropriately named ventricularis. This layer contains both elastin fibres and collagen bundles, however

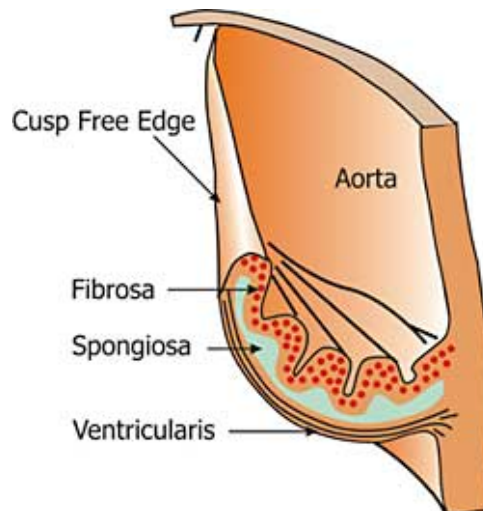


Figure 1.6: Cross section through a leaflet of the aortic valve. From USC Cardiovascular Thoracic Institute.

this surface of the leaflet is smooth, unlike the fibrosa, which promotes laminar flow over the open valve.

The central layer is the spongiosa. This consists primarily of glycosaminoglycan molecules (GAG). Various functions have been proposed for this layer. It is widely accepted that it provides a form of lubrication between the ventricularis and the fibrosa allowing them to move past each other with ease. The spongiosa contains many, well ordered fibroblastic cells which produce collagen for the valve. The fibrosa is found on the aortic side, which is the thickest layer in the valve. This layer is predominantly composed of collagen bundles. The fibrils of collagen are neatly arranged, and are lubricated by proteoglycans which contain one of more covalently bonded GAG chains.

The blood contacting surfaces of the valve and blood vessel are coated with endothelial cells. These cells line the cardiovascular system and are the barrier between blood and the extracellular matrix (ECM). The endothelial cell has multiple roles; as the barrier between the blood and the rest of the body it holds the keys to permeation, while taking part in the immune response, coagulation, growth regulation, production of ECM (Sumpio et al., 2002), and the modulation of blood flow and blood vessel tone. In fact, no other material or tissue is known to interact with blood in the same way as endothelial cells do. Other cell types, tissues, natural and synthetic materials, including of course polymers, will lead to a changes in the blood, generally for the worse.

Cardiac valves contain cells which are phenotypically unique and with a structure not found elsewhere in the body (Butcher et al., 2007). Interstitial cells (IC) are the most abundant cell type present in heart valves. IC are a type of myofibroblast which are

concentrated in the spongiosa but may be found throughout the valve. The ICs also tend to be oriented circumferentially across the leaflet. ICs in the spongiosa are anchored to collagen fibres in the ventricularis and fibrosa layers of the valve. This anchoring is likely to act as a “strain sensor” which can sense when the valve is straining more than usual, so signalling that more collagen should be synthesized. As well as producing collagen, the fibroblasts also break down collagen. Compared to other tissues, the valve has a particularly high tissue turnover which may contribute to the durability of the healthy valve (Thubrikar and Klemchuk, 1990), and so one cannot compare the durability of polymers with that of regenerative tissues.

It is no surprise that valve disease is often associated with IC dysfunction. In calcific valve disease, IC differentiate to become osteoblast valvular interstitial cells which can lead to the formation of calcific nodules. However the picture is not entirely clear: IC seem to have a complex and symbiotic relationship with EC, making it hard to develop targeted therapies (Liu et al., 2007a).

1.5.1 Collagen

The fibrous protein, collagen is found throughout the body. In some tissues, such as tendons, it is the primary component. Collagen forms most of the organic matrix in bone and is the predominant component of the ECM throughout the body. Amino acids are arranged in a triple helices (~ 300 nm), which are crosslinked to form collagen fibrils (~ 1 μ m), that bundle to form collagen fascicles. The collagen fibrils found in soft tissues (such as tendons) have a modulus of approximately 1.2 GPa (Fratzl, 2008), which is similar to many common thermoplastics such as acrylonitrile butadiene styrene (ABS) and thermoplastic polyurethanes (Granta Design Ltd., 2003). Collagen also has an ultimate tensile stress of 120 MPa, which is double that of the equivalent synthetic plastics. These mechanical properties go some way to explaining the ubiquity of collagen throughout the body.

The mechanical properties of collagen are non-linear and dependent upon environment. Alongside the anisotropy of the fibres; water content, crosslink density, mineralization, strain, and strain rate must be considered. Single collagen fibres have a non-linear stress-strain response - initially they are soft, but stiffen significantly once they reach about 10% strain (Shen et al., 2008). This quirk might be important in the cusps of the heart valve as it allows the valve to be opened easily, while having strength when stresses are high.

In the aortic valve, bundles of collagen are located in the fibrosa. These bundles commence

at the commissures of the valve and run roughly parallel to the free edge of each cusp in the circumferential direction. At the centre of each cusp the bundles become connected resulting in a dense reinforcement which runs radially from the centre of the free edge to the nadir. This thickening is referred to as Arantius' Nodule (Sauren, 1981).

To investigate the orientation of collagen across the valve, I explanted and dissected a healthy porcine valve which I stained for collagen with Van Gieson's Picrofuschin solution (VWR International Ltd). I mounted one cusp on a metal frame to simulate a loaded conformation. Figure 1.7 shows the prepared cusp. The circumferential collagen structure is visible, with radial collagen interconnections between the large bundles. The thickening at the centre of the leaflet is also clear.

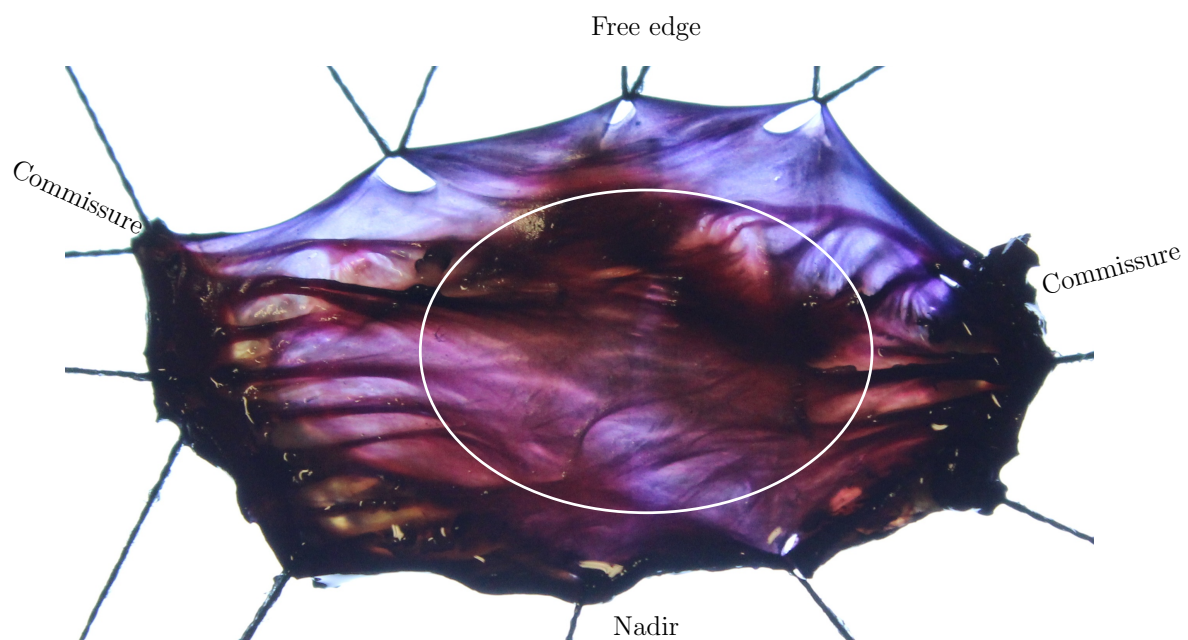


Figure 1.7: Leaflet from a porcine valve suspended between stretched threads and stained for collagen using Van Gieson's Picrofuschin. The fibres of collagen clearly extend from the commissures and aortic wall circumferentially across the cusp. The white ellipse marks the central area where the bundles branch and combine. The leaflet is 20 mm wide.

I observed that the main collagen fibres were oriented circumferentially (Figure 1.7), but it is established that older, more developed leaflets have greater bundle branching and connectivity (Sauren, 1981). In a study, using high resolution digital imaging with transmitted elliptically polarized light, Doebling et al. (2005) reported that collagen structure is more complex than previously thought. The fibres show significant branching and are also arranged in multiple layers which is thought to aid the sliding of fibres over one another. Furthermore, there is significant variation between leaflets with the right coronary cusp being self symmetric while the remaining cusps are mirror images of each

other. The branched collagen structure in an unpressurised leaflet becomes deformed as the valve is pressurised. Once the transvalvular pressure reaches 20 mmHg (approximately 20% of the resting maximum) the collagen bundles reach their maximum alignment.

1.5.2 Elastin

Tropoelastin protein molecules associate and crosslink to form insoluble elastin fibres. The production of elastin diminishes rapidly with age. However, as elastin has a half life of 74 years we rely upon the fibres that were produced during the first years of life (Weiss, 2010). Although the valve contains a relatively low proportion of elastin (13%, compared to 50% collagen (Vesely, 1998)), it has specific structural roles. Compared to collagen, elastin is soft and much less abundant, indicating that it has a small role in directly supporting large loads. However, the ventricularis can undergo strains of 60% during opening (in the radial direction), and elastin is the only natural material capable of withstanding such strains. Any collagen which is radially oriented in the ventricularis is wavy when unloaded, and so only becomes loaded at high strains. Thus, during small strains the mechanical properties are dominated by elastin.

Valvular elastin is found in sheet structures which are mechanically isotropic and so do not directly contribute to the anisotropic properties of the leaflets. The leaflets undergo large deformations, and yet they are capable of returning to their unloaded starting position. Elastin is also responsible for this property as its preloaded fibres can return collagen fibres to their original positions (Vesely, 1998).

1.5.3 Resultant mechanical properties

The combination of the fibrosa, spongiosa and ventricularis layers result in a heart valve leaflet with a stiffness between 4 and 8 MPa (Weinberg and King, 2004), however, the two most prominent properties of the combined heart valve tissue are the highly non-linear and anisotropic response.

The non-linear mechanical properties of the valve can be attributed to the collagen arrangement. At rest the collagen is crimped such that the fibres are wavy. In this state only a small amount of force is required to stretch the composite material. As the strain increases, the fibres begin to uncrimp and align, resulting in a stiffer material. Finally, once all of the fibres are straightened the maximum stiffness is exhibited (Holzapfel et al., 2000).

The stress-strain properties of frozen and fresh human aortic valve leaflet tissue are shown in Figure 1.8. The data shown here illustrates the non-linear anisotropic response of the tissue. In particular, leaflets can be strained up to 7% in the circumferential direction with a modulus of 0.02 MPa, which then rapidly increases to 6 MPa. In the radial direction, fresh leaflets stiffen at approximately 15% strain with a post-transition modulus of 1.7 MPa.

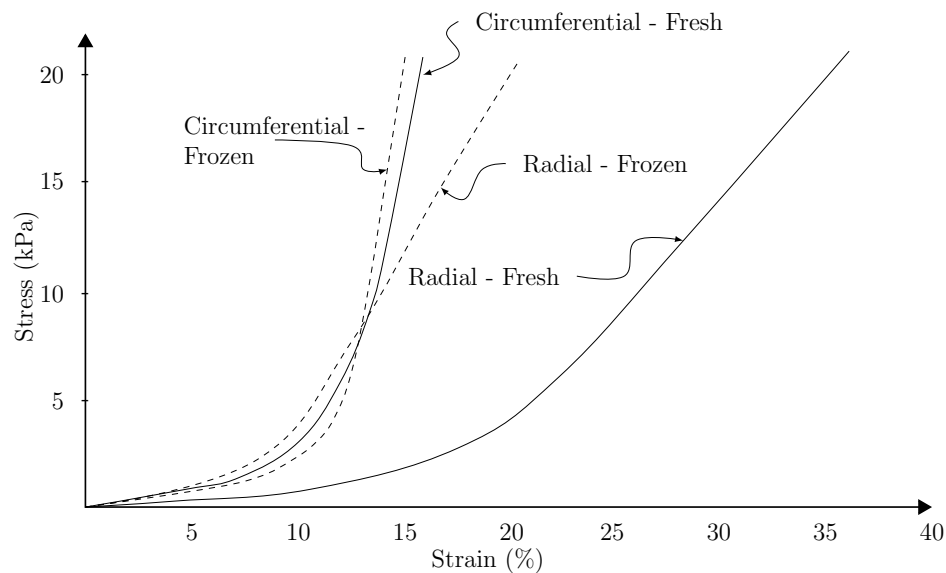


Figure 1.8: Plot of the unaxial stress strain relationship for fresh and frozen aortic valve leaflets in the circumferential and radial directions measured *in vitro*. Adapted from Thubrikar and Klemchuk (1990).

1.6 From the inception of prosthetic heart valves to their current state

Since the first valve replacement, in 1952, a wide variety of prostheses have had some success in humans. The range of prosthetic valves may be described as: autographic, homographic, mechanical, or xenographic. Autographic prostheses involve the transplantation of a valve from elsewhere in a patient's body, typically the pulmonary valve. Homographic replacements involve the use of tissue from the same species, generally cadaveric valves which are often cryogenically preserved before use in a patient (Goffin et al., 2000). Xenographic, hereafter referred to as bioprosthetic, valves utilise the tissue of another species. Mechanical prostheses consist of non-biological materials.

1.6.1 Autographic prostheses

Autographic replacement refers to the use of an existing valve in the patient's body to replace a diseased valve. Most often, a pulmonary autograph is used to replace the aortic valve and an alternate prosthesis is implanted in place of the pulmonary valve. This is termed the Ross procedure. A high quality of life, and good survival rates make the Ross procedure attractive, but the high surgical complexity makes the procedure only sensible in centres of excellence for aortic root surgery (El-Hamamsy and Poirier, 2013).

1.6.2 Homographic prostheses

Prostheses from matched donors perform very well, with excellent haemodynamics and good durability. As donation from a living donor is not possible, only cadaveric valves can be used. This operation was first performed in 1962, however the use of cadaveric implants has now waned due to the difficulty of supply (Dasi et al., 2009).

1.6.3 Mechanical valves

Mechanical heart valves were the first type of prosthesis to be developed and implanted. There is an extensive variety of designs of which the most notable valves are described here in chronological order.

The first valve type to be developed and implanted was the caged ball valve, the Starr-Edwards valve being the most successful in this category. The caged ball design functioned adequately, though improvements that provided a larger effective orifice area, reduced shear, and required less anticoagulant therapy were in quick succession. The monoleaflet valves, for example Bjork-Shiley, Medtronic-Hall and Omnicarbon valves, improved the effective orifice area of the valve, though suffered from reduced durability to such an extent that some models were recalled. The occasional catastrophic failure of monoleaflet valves has been attributed to fluid cavitation as the valve closes, which can lead to surface pitting (Kini et al., 2000). Bileaflet valves, such as the example shown in Figure 1.9, produced by St. Jude Medical, Carbomedics or Edwards-Duromedics, are now seen as the gold standard in mechanical heart valve design (Vongapatansin et al., 1996).

Nowadays mechanical valves possess excellent durability properties. They are capable of withstanding well over 20 years of operation and possess a desirable effective orifice area ($\geq 2 \text{ cm}^2$ for a 23 mm valve) and minimal regurgitation. However, despite their admirable haemodynamic parameters they suffer from serious flow field problems which necessitate

the use of anticoagulant therapy. For example, the bileaflet heart valve possesses several flow channels whose jets have peak velocities of at least 2 m s^{-1} during systole (Pibarot and Dumesnil, 2009) which lead to thrombus forming vortices. In the turbulent vortices encountered downstream from a mechanical valve, shear stresses between 120 and 200 N m^{-2} have been measured using Laser Doppler Velocimetry, which are significantly greater than the threshold shear stress at which thrombus generation occurs. A critical parameter in the design of the bileaflet valve is the angle between the open leaflet and the flow axis; too great and the systolic flow field is severely disrupted, too low and closing of the valve becomes difficult (Yoganathan et al., 2005).

The use of rigid materials in mechanical heart valves requires hinges to achieve rotation. However, over time, they have a tendency to be fouled and clog up. To counter this, a small gap is left between leaflets and the supporting structure that allows a small amount of retrograde flow which helps to keep the hinge clean. Unfortunately this reverse flow can also generate very high, thrombogenic shear stresses (Yoganathan et al., 2005).

The most promising next improvement in mechanical valves is the Lapeyre-Triflo FURTIVA valve. This has three rigid polyether ether ketone leaflets which open to produce a central flow orifice, like the native anatomy. The valve has been tested in a sheep for regulatory approval and performed safely, in line with the reference St. Jude bileaflet mechanical valve (Gallegos et al., 2006). However at the time of writing the valve has not reached clinical trials.



Figure 1.9: Sorin Carbomedics bileaflet mechanical valve with a pyrolytic carbon coating, titanium stiffening ring. The external diameter is approximately 30 mm.

1.6.4 Bioprostheses

In 1969 Alain Carpentier developed a method of fixing biological tissues using glutaraldehyde that improved their *in vivo* stability and reduced degradation (Dasi et al., 2009). Using his technique bioprosthetic valves were first made commercially available in 1972



Figure 1.10: Edwards PERIMOUNT aortic valve prosthesis. The external diameter is approximately 30 mm.

and marketed as the Hancock valve (Cohn et al., 1989). Their implantation is a phenomenal success story: implanted valves rarely require severe anticoagulant therapy and allow patients to rapidly return to their quality of life pre-disease.

Among bioprosthetic valves, a wide variety of designs have evolved in response to failures and shortcomings in design. Practically all bioprosthetic valves are made from either bovine pericardium or porcine aortic root tissue that is fixed with glutaraldehyde. The valves must first be decellularised to reduce immunogenicity. Glutaraldehyde is used to crosslink the proteins in the tissue, which improves durability (Ma et al., 2014).

There are a multitude of bioprosthetic heart valve manufacturers and designs. All aortic prostheses have 3 leaflets which open to form a central orifice, giving them flow dynamics similar to the native valve. Although there are notable differences between fundamentally different designs, there is little to choose between manufacturers (Dasi et al., 2009). There is also a wide variation in patient anatomy, meaning that no single valve is optimal for all patients. It should also be noted that haemodynamic improvements may be counteracted by reduced durability, and improvements in opening can come at the expense of greater regurgitation.

Valves can be classified as either stented or stentless bioprosthesis. A stent refers to any rigid structure placed inside a blood vessel. In a stented bioprosthesis, biological tissue is mounted upon a rigid metallic or polymeric stent. The tissue may be inside or outside of the stent and the leaflets mimic the native cuspal form. The most common stented prostheses are the Carpentier Edwards PERIMOUNT and PERIMOUNT MAGNA, and the Sorin Mitroflow which are composed of bovine pericardial tissue, while the Medtronic Mosaic and Hancock valves use porcine leaflets. Stented valves may be placed intra- or supra-annularly. Supra-annular placement allows valves with a larger diameter to be used, that have a lower resistance to flow. The valves are sutured within the sinuses, however this carries a small risk of occluding the coronary arteries (Ruzicka et al., 2009).

Table 1.3: Typical deformations found in bioprosthetic heart valves, adapted from Balachandran et al. (2011)

Parameter	Normal	Notes
Aortic pressure during diastole (max. at rest)	65 to 85 mmHg	
Aortic pressure during systole (max. at rest)	100 to 130 mmHg	
Differential pressure across closed valve (max. at rest)	95 mmHg	
Peak flow velocities	3.7 m s^{-1}	(Dasi et al., 2009)
Turbulent shear stresses	Mean 200, max 450 N m^{-2}	(Dasi et al., 2009)
Systolic bending strain	14.5%	(Corden et al., 1995)
Diastolic bending strain	8.3%	(Corden et al., 1995)

Stentless bioprosthetic valves do not have a rigid frame upon which the leaflets are mounted. In a stentless valve, the valve suture line may follow the edge of the leaflet, or they may be fabricated from a complete porcine aortic root, and use the natural attachment between leaflets and the aorta (Pibarot and Dumesnil, 2009). Stentless valves are either implanted in place of the resected aortic root or as a tube within the aortic root. They initially fell out of fashion as they were trickier to implant. However, their popularity resurged in the 1990s as they can have better haemodynamics and reduced leaflet stresses. Among stentless valves, the most common is the St. Jude Medical Quattro Valve. Also available are the Edwards Lifesciences Prima Valve, Biocor Valve and the Medtronic Freestyle Valve, and the third generation of valves include the Sorin Pericarbon Freedom and the 3F valve. Although stentless valves may be superior in some patients, there is little conclusive evidence that they should be used in preference to stented valves (Kobayashi, 2011; Siddiqui et al., 2009).

The deformations found in bioprosthetic heart valves are similar to those of native valves. Table 1.3 shows the deformations and haemodynamics of bioprostheses. This can be compared with Tables 1.1 and 1.2, which present structural and haemodynamic data for the native valve. Further to the data listed, Subhani et al. (2013) observed that stented porcine prostheses have inferior valve dynamics relative to the native valve, as they may stay open for 25% less time during a full cardiac cycle.

1.6.5 Failure of bioprostheses

In the first years after implantation, bioprostheses are reliable: <1% of valves suffer structural dysfunction within 5 years. Among valves implanted in the general elderly popu-

lation in the 1980s and 1990s, 20-30% become dysfunctional within 10 years and $\geq 50\%$ failed via structural dysfunction within 12-15 years of implantation (Siddiqui et al., 2009). Newer valve designs, such as the Hancock II valve, reduced structural valve deterioration to approximately 20% over 15 years of implantation (Rizzoli et al., 2003).

In contrast, the failure rate has always been much higher in younger patients: nearly all valves fail in less than 5 years in patients under 35 years old. The higher failure rate in younger people may be attributed to their more active immune system which promotes a greater inflammatory reaction, and higher circulating calcium concentration (Siddiqui et al., 2009).

Structural valve deterioration was tackled by reducing stresses, using anticalcification treatments, and alternative tissue cross-linking methods (Park et al., 1997; Tam et al., 2015; Vyavahare et al., 1997b). The prospect of mitigating the immune response to xenographic tissues through the use of genetically modified pigs is on the horizon, though social and ethical barriers to acceptance do exist (Manji et al., 2012).

A large number of bioprosthetic explants are recovered after premature failure or at patient post-mortem, providing a significant body of evidence for the mechanisms of failure. This knowledge helps to inform the design of polymeric valves. The most likely reason for rapid valve failure (within 2 years) is due to infective endocarditis. This has an incidence of 1-6%, and is most likely to occur in patients with a previous history of endocarditis; poor valve sterilisation is rarely an issue. Thrombosis as a cause of bioprosthetic valve failure is relatively rare, occurring in just 0.1 to 5.7% of cases (Siddiqui et al., 2009).

Calcification and mechanical damage are the two main mechanisms of valve failure. Initially it was thought that calcification led to mechanical damage, but this was unfounded and the two processes can initiate separately (Vesely, 2003). There is a synergy between the two processes - calcification leads to the stiffening of cusps, rupture of tissue and subsequent valve failure. Calcification also occurs at a higher rate in regions of highly localized mechanical forces, be they tensile or compressive (Vesely et al., 1998). The extent of knowledge surrounding calcification mechanisms is described further in Chapter 4.

When calcification is not present in failed bioprostheses, cuspal tearing is most common, particularly in porcine prostheses. These tears are typically located either at the commissures or at the free edge where stresses are highest (Vesely, 2003). The use of flexible stents to reduce mechanical pressures during diastole is presumed to reduce the likelihood of tearing, but has not been proven (Siddiqui et al., 2009). Vesely et al. (1998) proposed

that fixed biological material does not fail due to tensile stresses; instead it is buckling of tissue in compression which leads to valve failure. Compressed tissue can be found at the centre of the free edge of each leaflet on the aortic side. Pannus overgrowth is also recorded as a pathway to failure. The physiological wound healing process can sometimes overshoot, resulting in the growth of collagen rich tissue onto the cusps or into the flow which then leads to valve dysfunction (Siddiqui et al., 2009).

1.6.6 Valve selection

Given the duopoly of bio- and mechanical prostheses, it is appropriate to consider the factors which determine the use of either valve when a patient requires a replacement. The selection of a prosthesis type is made using a multitude of factors: their indication or contra-indication for anticoagulant therapy, their age and life expectancy, and the desires of the patient. A patient fulfilling any of the following criteria will generally receive a bioprosthetic valve: age ≥ 65 , limited life expectancy, contra-indication for warfarin therapy or female of child-bearing age (Pibarot and Dumesnil, 2009).

1.6.7 Transcatheter valve replacement

In 2002, Alain Cribier implanted a prosthetic heart valve via a catheter with an antegrade transeptal approach on a 57-year-old patient who had been deemed inoperable and on whom balloon valvuloplasty had been previously unsuccessful (Cribier et al., 2002). Cribier triggered a disruptive change which has revolutionised the treatment of valvular diseases (Berlin et al., 2014). The Edwards Sapien valve was first to reach the European market, receiving a CE mark in 2007. By 2013, an estimated 90,000 transcatheter aortic valve implants (TAVI) had been implanted worldwide (Bourantas et al., 2013). In the USA, the Food and Drug Administration (FDA) approved the Sapien valve in November 2011, initially restricting implantation to inoperable patients and only using the transfemoral route.

The implantation of prosthetic heart valves using a catheter avoids the need for heart-lung bypass and open heart surgery, thus opening up valve replacement to the cohort of patients whose co-morbidities left them at an unacceptably high risk of death with traditional procedures. The proportion of elderly patients who are refused surgical valve replacement was recorded as 33% by Iung et al. (2005) in the European population; this cohort can now be treated, thus increasing the total number of heart valve implantations (Rodés-Cabau, 2012).

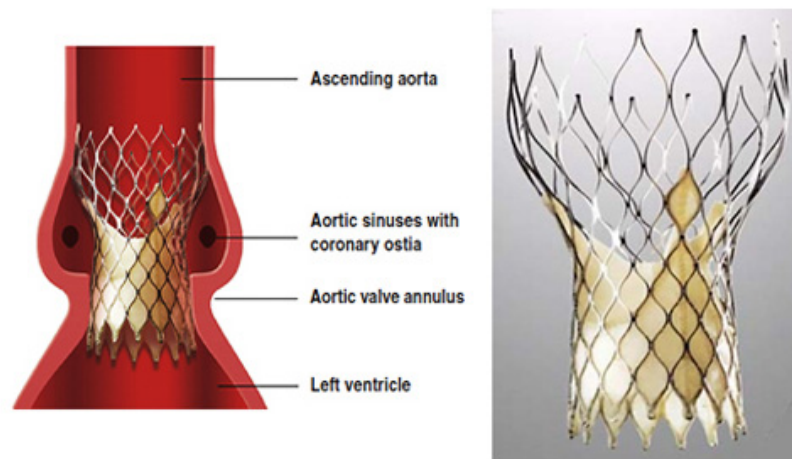


Figure 1.11: The Medtronic Corevalve transcatheter aortic valve implant consists of 3 porcine pericardial leaflets sutured onto a self expanding Nitinol stent. The valve sits in the supra annular position and can be delivered using an 18Fr catheter. Image from of USC Clinical Trials.

In the early 2000s clinicians and valve companies were slow to adopt TAVIs. A decade later they have become ubiquitous in developed countries and it seems that their use is set to increase further. Although TAVI may be clinically justified for inoperable and high risk patients, it still comes under intense scrutiny when cost implications are considered. A typical valve may cost \$40,000, compared to \$5000 for a surgically implanted valve (Neyt and Van Brabandt, 2013). A significantly reduced fee has led to a small number of implantations in developing countries. The standard pricing of TAVI is yet to decrease, although it has been forecast to do so as competition increases.

While there is a large difference in price between surgical and transcatheter valves, it is the overall cost of each procedure that appears to be driving the disparity. The transcatheter procedure - which permits a shorter hospital stay than the surgical procedure - enables the transcatheter valves to have a price premium. In the PARTNER trial there was a cost saving of \$1250 and a modest increase in Quality Adjusted Life Year (QALY) when TAVI was used, where one QALY indicates one year of perfect health, and years spent at below perfect health correspond to values between zero and one. TAVI was economically attractive in 70% of procedures at an incremental cost effectiveness ratio of \$50,000/QALY, compared to surgical heart valve replacement. This was not the case for the transapical approach where surgical valve replacement was more attractive.

1.6.8 Tissue engineering

Tissue engineering refers to the artificially induced growth of a natural biological structure. Tissue engineering (TE) can be autographic if the body's own cells are grown to replace a tissue, or it can use non-autographic stem cells which do not elicit an immune response.

TE heart valves are still under development. One method involves the seeding of a scaffold (mimicking the extracellular components of the heart valve) in an *in vitro* bioreactor before implantation. The scaffold is degraded within the bioreactor and the living valve would be implanted. Alternatively, autologous cells may be recruited to an implanted device - *in situ* TE. This concept is supported by the observation that endothelial progenitor cells are able to adsorb to the surface of certain ventricular assist devices. Furthermore, the coating of stents with CD34 (an antibody found on the surface of endothelial progenitor cells) further encourages adhesion and proliferation (Mendelson and Schoen, 2006).

Researchers pursuing both methods continue to record promising results and there is little doubt that, given time, the successes already seen in other organs (kidney and bone regeneration, for example) can be repeated for heart valves.

Optimism was high in 2000 when autologous heart valves were grown on a polyglycolic-acid mesh in an *in vitro* pulse duplicator before implantation and 8 months of successful function in sheep. *In vitro* and *in vivo*, the tissues remodelled to form a trilaminar distribution of cells and ECM, much like the native valve. Unfortunately, the challenges to translate this to human patients have proven to be insurmountable thus far, due to poor reproducibility (Hoerstrup et al., 2000a,b). More recently, with a focus on replicating the functional anatomic structure of the native heart valve, Masoumi et al. (2014) developed a tri-layered elastomer scaffold for TE heart valves. This biologically inspired structure consists of poly(caprolactone) microfibres separated by a poly(glycerol sebacate) sheet whose microstructure is engineered to have anisotropic mechanical properties. The scaffold was seeded with valvular interstitial cells and mesenchymal stem cells, and cultivated for 4 weeks. The valve tissue matched a variety of mechanical and biological parameters and performed adequately in an isolated ovine heart model (Masoumi et al., 2014).

Despite the promise of developing a TE valve, continued development may not be fully justified given the relatively reliable current solutions for adults. From a regulatory perspective, TE implants may be classified as a drug as opposed to a device, consequently requiring a tougher, longer, period of certification. The *in vitro* culture of valves is unattractive from a scale-up perspective, while the *in situ* recruitment of stem cells must be able to cope with patient variability. As such, TE valves are probably best

suited to paediatric patients who, currently, must have frequent surgeries, with increasing mortality, to replace prostheses which do not grow, and have poor durability. As such, a TE valve - possibly grown from prenatal foetal cells harvested during pregnancy - could be of tremendous benefit for children born with congenital defects (Yacoub and Takkenberg, 2005).

An innovative halfway house between the classical bioprosthesis and a TE valve was proposed by Syedain et al. (2012). Species specific fibroblasts are seeded upon a cylindrical fibrin gel. A pulsatile flow of culture medium is flowed through the gel, leading to the circumferential alignment of the collagen which is synthesised by the fibroblasts. The scaffold is then decellularised, using 1% sodium dodecyl sulfate instead of glutaraldehyde, and the tube is manipulated to form 3 leaflets which are mounted upon a custom frame. The decellularised valves are shelf stable and have good hydrodynamic properties, though no long term fatigue tests have been performed yet. The valves can then be implanted in the same species that the fibroblasts came from, making them allografts. Early studies with an ovine model (cells and valve recipient) have shown promising clinical and recellularisation results.

1.7 Design, development and testing methods

In this thesis, I will describe the design of a novel polymeric heart valve with the aim of overcoming the limited durability of bioprostheses without the requirements for anticoagulant medication that are associated with mechanical valves. The medical device design process starts with the statement of a set of requirements; these may be driven by both regulation and functional analysis (Alexander et al., 2001). The fundamental functional objective of the device is to only permit flow in one direction, and the design outcomes for heart valve prostheses are well defined by the ISO 5840 standard which must be satisfied in order for a valve to gain a CE mark.

This project aims to achieve the following goals:

1. Determination of parameters for the selection of a polymer,
2. Selection of a polymer,
3. Design of the prototype valve,
4. Fabrication of the prototype valve,
5. Evaluation of the biocompatibility of the selected polymer,

6. Evaluation of the *in vitro* performance of the prototype valve,
7. Prediction of the lifetime of the valve,
8. Investigation into the likelihood of calcification, possible effects and causes,

The following sections of this introductory chapter first review the attempts by other researchers to make polymeric prosthetic heart valves, which are used to inform a set of criteria for the design and testing of the valve. I will then introduce the basis from which the novel polymeric prosthetic heart valve will be designed, and review the range of polymeric materials that may be considered.

1.8 Flexible leaflet polymer prosthetic heart valves

1.8.1 Early attempts

The mechanical properties of polymers have long placed polymer prostheses as prime candidates to overcome the failings of mechanical and biological prostheses, but none have yet succeeded. A collection of early polymer prostheses attempts is shown in Table 1.4. The first polymer prostheses were proposed independently by Berge and Lillehei, who fabricated polyurethane and single cusp silicone (Silastic) valves, respectively. A flurry of designs emerged in the following years. The surgeon Hufnagel produced well over 10 different designs of polymer valve with flexible leaflets, but it was his caged-ball mechanical valve was most successful clinically. Polyurethane prostheses were first implanted into dogs in 1959 by Nina Starr Braunwald. The following year she implanted the valve into a 44-year-old women in the mitral position, citing the operation as successful as the patient survived 4 months before death due to arrhythmia (Roe, 1992; Ten Berge, 1958). The valve, however, was not adopted by other surgeons, nor was the procedure repeated.

Further designs were tested throughout the 1960s. From Table 1.4 it seems that polymer heart valve development has taken a path of trial, error, and little improvement. Indeed, Roe (1992) describes the first attempts at valve replacement in the 1960s as operating “in a sea of ignorance”. Designs lacked a scientific basis, and valid testing outside of humans was notably absent. Regardless, the Roe-Moore valve (1960) functioned for 13 years in a single patient without complications, and is a fine example of the potential of polymer prosthetic valves. Despite the early promise of flexible leaflet polymer valves, Roe attributed their demise to marketing factors and fear of manufacturer liability. In the early days of valve development, both flexible leaflet and rigid valves were under consideration,

the Starr Caged Ball Valve (1960) gained commercial backing, mass production, quality control, and significant marketing at the time, and subsequently became the dominant valve (Roe, 1992).

Table 1.4: Early attempts (until 1965) at flexible leaflet polymeric prosthetic heart valves. Polytetrafluoroethylene is abbreviated to PTFE.

Year	Human / animal (# implantations)	Material	Failure mode	Valve name / source
1958	Animal	Polyurethane	Unknown	(Ten Berge, 1958)
1958	Human (50)	Single flap of silicone elastomer (Silastic)	Material fatigue	Lillehei Valve (Roe, 1992)
1959	Human (47)	Dacron mesh impregnated with Silastic monomer	Successful when one cusp was replaced; poor results when 2 or 3 cusps were replaced.	Bahnson cusp (Roe, 1992)
1959	Human (350)	Teflon cloth coated with polyurethane foam	Limited information, but no anticoagulation used with disappointing long term results	Earle B Kay (Roe, 1992)
1960	Human (76)	Dacron	Variable results - poor durability	Muller (Roe, 1992)
1960	Human (minimal)	Polyurethane foam with thin knit Dacron	Attributed to complex implantation technique	Braunwald-Morrow (Roe, 1992)
1960	Human (98)	200 denier PTFE, impregnated with polyurethane and knitted into a round tube	Stiffening and fracture of Teflon cloth	McGoon (Roe, 1992)
1960	Human (8)	Elastomer on PTFE mesh	Longest survival of flexible leaflet valve (one patient for 13 years). Unknown failure.	Roe-Moore (Roe, 1992)

Table 1.4 continued.

Year	Human / animal (# implanta- tions)	Material	Failure mode	Valve name / source
1965	Human	Multiple flexible leaflet models, generally based on Silastic	Unknown	Hufnagel (Roe, 1992)

1.8.2 Modern polymer prostheses development

The dominance of mechanical valves in the 1960s drew attention away from polymer valves. But the arrival of bioprotheses in the 1970s led to a resurgence in interest for polymeric prosthetic heart valves with the aim of achieving durability without the need for anticoagulant therapy. Recently, two further applications of polymer heart valves have become established. The first is the use of polymer valves in artificial hearts and ventricular assist devices. Such devices have gained prominence in surgical applications for their palliative and bridge-to-transplant roles. In these instances the required duration of implantation is limited and polymer heart valves are favoured for their reproducibility and affordability.

The second instance where polymeric valves might have an opportunity to succeed is in the new breed of transcatheter devices. In a TAVI, the biological tissue is mounted on an expandable stent, which must be compressed to one third its diameter to pass through the blood vessels and reach the aortic valve. This crimping may lead to damage of the fixed tissue, reducing the durability of the valve (Zegdi et al., 2011). As of September 2015, very little data has been collected on TAVI durability due to the low life expectancy of those patients who have thus far received them. Nevertheless, it is expected that polymeric materials will cope with the crimping process better than fixed, biological materials. The Triskele valve is the most developed TAVI with polymeric leaflets, though a first-in-man implantation has not yet been performed (Mullen et al., 2013).

Modern polymer prostheses attempts are shown in Table 1.5. The 1990s saw most efforts channelled towards polyurethane based valves, with various combinations of soft and hard

segments used to overcome issues of stability, mechanical durability and calcification. The Aortech valve, fabricated from Elasteon, seemed to be the most promising product of this era with the granting of several patents, though legal and business difficulties seems to have occurred *en route* to market (though not covered in the academic literature).

A particularly promising attempt at a prosthetic valve was published by Kiraly and Hillegass (1980) who identified ethylene propylene diene terpolymer (EPDM)-type polymer, Hexsyn (fabricated by the Goodyear Tyre Company), as holding potential for a polymer prosthesis. Its biocompatibility was reported to be adequate, and Hexsyn displayed remarkable flex life of over 400 million cycles to failure, as compared to 18 million for Biomer and 4 million for both natural rubber and styrene-butadiene rubber. However, in an accelerated tester the valves only survived the equivalent of 2 years - approximately 70 million cycles - which highlights the shortcomings of their fatigue prediction. As such, the valve was only suitable for application in temporary blood pumps, where it performed satisfactorily at a fraction of the cost of bioprostheses.

Supplementary to the attempts tabulated in Table 1.5, a multitude of alternative polymers have been proposed for prosthetic heart valves, though few have followed the route to complete valve fabrication. The majority are commercial polymers based on polyurethane structures, for example, Bionate (biostable polycarbonate urethane), Elasteon (polyurethane with poly(dimethylsiloxane) soft segment), Pellethane (polytetramethylene glycol based PU elastomer), Carbothane, Biomer, Corethane and Chronoflex (Parfeev et al., 1983; Pinchuk, 1994; Pinchuk et al., 2008; Tanzi et al., 1997).

Table 1.5: Later reports (1960 to 2013) of design and testing of flexible leaflet polymeric prosthetic heart valves.

Year	Trial stage	Material	Failure Mode	Location / Name	Source	Notes
1974	Unknown	Unknown	Unknown	University of Notre Dame, USA	Chetta et al 1974 in (Kütting et al., 2011)	
1978				University of Bern, Switzerland	Vucic et al 1978 in (Kütting et al., 2011)	
1982	<i>In vivo</i>	Unknown	Unknown	Pennsylvania State University, USA	Wisman et al, 1982 in (Kütting et al., 2011)	
1982	<i>Ex vivo</i> and <i>in vivo</i> temporary blood pumps	Hexsyn, an EPDM-type polymer	Commissural tears after 107 million cycles in accelerated tester. 3 weeks success in vivo.	Cleveland Clinic Foundation, Ohio, USA	(Kiraly and Hillegass, 1980)	Only financially viable when used in temporary blood pumps
1988	Single animal study (goat)	Polyurethane copolymer (KIII from Nippon Zeon Co. Ltd) polyether-polyurethane with polydimethylsiloxane under silane coupling agent. Similar composition to Cardiothane	Calcification of valve and heart pump.	University of Tokyo, Japan	(Imachi et al., 2001, 1989)	
1990	<i>In vivo</i>	Polyurethane	Repeatedly reached 550 million cycles	Helmholtz Institute, Aachen, Germany / HIA	(Kütting et al., 2011)	Matured into ADIAM valve.
1991	<i>In vivo</i> (sheep)	Polyurethane (Pellethane 75A 2363)	Animals survived. Gross calcification of valves.	University of Utah, USA	(Hoffman et al., 1991)	

Table 1.5 continued.

Year	Trial stage	Material	Failure Mode	Location / Name	Source	Notes
1995	<i>In vivo</i> (Calf)	ADIAMat (proprietary polyurethane)	Superior to bioprosthesis with respect to calcification and durability.	Adiam	(Daebritz et al., 2004b)	Valve never certified.
1996	<i>In vitro</i>	Polyurethane (Estane 58201)	6/6 survived 10 years-equivalent accelerated fatigue test	Glasgow, UK	(Mackay et al., 1996)	
2002	<i>In vitro</i>	Polyurethane	Calcification	Glasgow	(Bernacca et al., 2002)	Last published result. Precursor to proprietary “Elasteon” and the Aortech valve. Patents (US 6171335 and 20060241744) filed in 2006.
2004	<i>In vivo</i> (growing calf)	Polycarbonate Urethane	Superior to bioprostheses. Death due to pannus overgrowth. Moderate calcification of aortic valves.	Aachen / ADIAM	(Daebritz et al., 2004a,b)	Valve deemed superior to bioprostheses
2010	<i>In vivo</i> (Calf)	SIBS with embedded PET fabric and dimyristoyl phosphatidylcholine coating	Material failure and calcification	University of Texas, USA	(Wang et al., 2010)	
2012	<i>In vitro</i>	POSS-PCU	Improved performance currently predicted	UCL, UK	(Rahmani et al., 2012)	Now incorporated into the <i>Triskele</i> TAVI valve

Table 1.5 continued.

Year	Trial stage	Material	Failure Mode	Location / Name	Source	Notes
2013	<i>In vitro</i>	xSIBS	Improved performance currently predicted	Stony Brook University, USA	(Claiborne et al., 2013b)	Successor to Wang et al. (2010). Stresses reduced (in silico) and platelet activation rate not significantly different from Magna tissue valve.

1.8.3 Current polymer prostheses development

Current research into flexible leaflet polymeric heart valves is concentrated in four groups: Stony Brook (NY, USA); Institute of Biomedical Engineering, University College London (UK); Cardiovascular and Biofluid Mechanics Laboratory, Colorado State University (CO, USA); and the Department of Chemical Engineering and Biotechnology, University of Cambridge (UK) in collaboration with Politecnico di Milano (Italy).

The Stony Brook valve is fabricated from a crosslinked block copolymer polystyrene-*block*-polyisobutylene-*block*-polystyrene (xSIBS). The major published work from this effort involved the optimisation of shape for reduced haemodynamic thrombogenicity (Claiborne et al., 2013a). The University College London valve is fabricated from a polycarbonate urethane with polyhedral oligomeric silsesquioxanes nanoparticles, with shape optimised for minimum energy for opening/closing (Burriesi et al., 2010). No fatigue testing or *in vivo* studies are reported for either valve. The Colorado State group proposed the use of interpenetrating networks of hyaluronan and linear low density polyethylene (LLDPE) for prosthetic heart valve leaflets (Prawel et al., 2014). The hydrophilicity of hyaluronan improves biocompatibility, and the addition of LLDPE allows the mechanical properties to be tuned to be similar to the native heart valve tissue. The prototype valves, whose leaflets are made from the novel material, had adequate hydrodynamic results, though have not yet been tested for calcification, durability, or *in vivo* (Kheradvar et al., 2015).

PECA labs are a small spinout company from Carnegie Mellon University (PA, USA) which is developing the “MASA” valve. The device consists of an ePTFE conduit with an integrated valve for paediatric patients who require right ventricular outflow tract reconstruction. An early design of the valve was implanted in 16 patients, with a median age 1.7 years and with successful 6 month follow up (Yoshida et al., 2011). The group are now working towards FDA approval under a humanitarian device exemption as no other therapies are available for the target patient group (PECA Labs, 2015).

1.8.4 Textile prosthetic heart valves

The use of textiles for the design of leaflets for prosthetic heart valves appears to be an attractive solution. From a mechanical perspective, textiles are fabricated from fibres which are renowned for their tensile strength. When incorporated into a fabric, yarns can move past one another and so flexibility can be achieved with minimal sacrifice of strength.

The porosity of textile valves allows the ingrowth of tissue, but this can lead to stiffening

of the leaflets. The use of textiles for transcatheter valves is particularly interesting as the fabric may be very thin which would allow for even smaller delivery sizes. Heim et al. (2014) describe a textile leaflet valve made from polyester which reached the animal trial stage. Although minimal tissue ingrowth was observed on the valve at autopsy, the leaflets were found to have stiffened which was attributed to calcification, and led to the animal's premature death (Heim et al., 2014).

Durability has been the greatest hurdle for the bioprosthetic and polymeric valves reviewed here and thus it is not unsurprising that textile valves suffer from similar issues. To achieve adequate durability, the yarns which make up the mesh must have tensile durability and also be able to resist frictional degradation as they slide past one another (Vaesken et al., 2014). The action of cycling results in rearrangement of the fibres which further complicates the long term prediction of stress distribution in the valve.

1.9 Possible failure routes

To steer the design of a novel valve, I collated the known failure routes for the valve based upon the criteria of ISO 5480, which regulates the design and manufacture of cardiac valve implants; the failings of the valves cited in Section 1.8.2; the routes to failure for bioprosthetic valves in Section 1.6.5; and the requirements stated by Burriesci et al. (2010); these characteristics are shown in Table 1.6.

Table 1.6: Failure routes for prosthetic heart valves.

Clinical Hazard	Device failure route	Notes
Inability to complete implantation	Improper sizing	Poor labelling for size and location
	Asymmetric valve does not rotate Blocks coronary arteries Valve damaged	During handling Poor transportation / storage
	Valve not compatible with standard surgical tools Sewing ring	Non-compliant Inaccessible
Short term issues: endocarditis	Non sterile device	
	Non-sterile accessories	
	Poor packaging	

Table 1.6 continued.

Clinical Hazard	Device failure route	Notes
Other short term contamination	Materials contaminated	Material synthesis Material processing
<i>In vivo</i> diagnostic incompatibility	Device migrates due to poor anchoring Device heating Image distortion	
Haemodynamic issues	Paravalvular leak Increased ventricular load Aortic wall injury	Poor suturing Inflexible cuff / sewing ring Suture breakout / tearing Separation of cuff from frame Transvalvular energy loss too high Effective orifice area too small (patient prosthesis mismatch) Regurgitation too high Flow jet
Thromboembolic event	Material Valve dynamics Catastrophic valve failure	Thrombogenic Activates coagulation cascade Shear vortices Loss of a leaflet Embolisation of whole vale
Long term haemodynamic issue	Pannus overgrowth Stiff fibrous capsule develops around cusps Calcification of leaflets Deterioration of coating or material results in thrombogenic material	
Long term valve failure (durability)	Cuspal tearing Stent post cracking Cracks in joints Creep of stent post / leaflets Calcification - mechanical strain synergistic failure Chemical degradation - mechanical strain synergistic failure	
Bleeding event	Improper anticoagulation regime	

It is clear from Table 1.6 that there are a wide variety of failure routes. Some, such as hydrodynamic performance and thrombogenicity, may be tested with appropriate *in vitro* models. Others, such as long term haemodynamic issues and fibrous encapsulation, require *in vivo* animal models in order to be tested.

From the significant number of failed polymer prosthetic heart valves noted in Section 1.8, it is appropriate to consider the most prevalent route by which they failed. 23 polymeric valves designs are listed in Section 1.8; of the twelve that reported an outcome, one was reported as successful, seven suffered from fatigue failure, four reported calcification with or without failure, one failed with poor biocompatibility. While the fundamental trileaflet design was used for nearly all of these valves, the material was varied. As such, it is evident that material selection is exceedingly important. In his treatise on design, Ashby et al. (2004) noted that the materials determine both function and form, and as such their selection is absolutely critical to successful design. The first requirement to satisfy in the design of a novel prosthetic heart valve is suitable material selection.

From my analysis of 50 years of polymer prosthetic heart valve failure, I drew the conclusion that the most common modes of failure are through poor durability and calcification. Calcification, which will be explored further in Chapter 4, shows many synergies with mechanical fatigue failure, though it is unclear which is causative. Bernacca et al. (1995) noted that many *in vivo* explants have reported that regions of calcification concentrate at points of high stress in the valve's leaflets. However, calcification-related fatigue failure is likely to occur earlier before the deposition of calcium phosphate leads to stenosis. As such, selection of materials on a mechanical basis becomes my first design requirement.

1.10 Bioinspiration

Research into prosthetic heart valves space has explored an extensive range of avenues. A wide variety of biological tissues have been tested, a multitude of mechanical designs developed, and the application of many polymers has been explored. Given this context, I, in the Cambridge group, sought a new source of inspiration - nature. The art of imitating nature, formalised in 1960 by the US air force with the advent of *bionics*, could be applied to prosthetic heart valve design. This field represents the study and imitation of nature's methods, designs and processes. In the 1960s it became clear that while some designs can be copied from nature, there are many ideas from nature which are best adapted or used to serve as inspiration for human-made capabilities (Bar-Cohen, 2005).

The term *biomimicry* denotes the reproduction of a biological process using synthetic methods. The development of a TE valve (Section 1.6.8) is a form of biomimicry. In this thesis I will look towards reproducing *function* rather than *form*, and so when I draw upon elements of the natural design to produce a better valve - without mimicking them - I am *bioinspired*. Among the classical prosthetic valves, the implementation of three leaflets in aortic prostheses is a fine example of successful bioinspired device design. The Cambridge group has now drawn upon the anisotropy of the native leaflets to further inspire the design.

1.10.1 Leaflet anisotropy

The structure of leaflets in the native heart valve was examined in Section 1.5, with particular focus on the distribution of collagen in the aortic valve. It is generally accepted that the arrangement of collagen in the valve plays a significant role in the durability of the valve. Various approaches have been taken to demonstrate the importance of fibres and the effects of orientation.

Liu et al. (2007b) carried out an *in silico* analysis of the effect of fibres on a polymer prosthetic heart valve under diastolic loading. Using leaflets with a spherical form, Liu *et al* parametrically varied the angular distribution of fibres in a single- and double-ply model. 0.1 and 0.2 vol.% of fibres were tested. In the single-ply model, fibres oriented perpendicular to the stent leaflet boundary resulted in a 63% reduction in stress relative to the no fibre case. The double-ply model was used to mimic the native collagen structure more accurately as a rhombic form of fibres is created, somewhat mimicking the branching of collagen bundles, as seen in Section 1.5.1. Comparing the maximum principal stresses in the designs, the authors determined that the double ply arrangement resulted in a minimum of stress. This model was not tested for its opening so there is no way of determining the overall effectiveness of the design.

An analysis performed by Zaffora (2011) commenced with a random orientation of fibres in the leaflet and evolved the model to optimise orientation. The valve was modeled using the mechanical properties of an anisotropic styrenic block copolymer (polystyrene-*block*-polyisoprene-polybutadiene-*block*-polystyrene, 19wt% polystyrene) and the leaflet form was based upon an unknown bioprosthesis. A selection of leaflet thicknesses were examined: 0.15, 0.3 and 0.45 mm. After three iterations the distribution of fibre orientation became stable, and was broadly horizontal or circumferential, as shown in Figure 1.12a. This orientation was very similar to the native valve's collagen orientation (Marom et al., 2013). As shown in Figure 1.13, the maximum strain energy density was reduced from

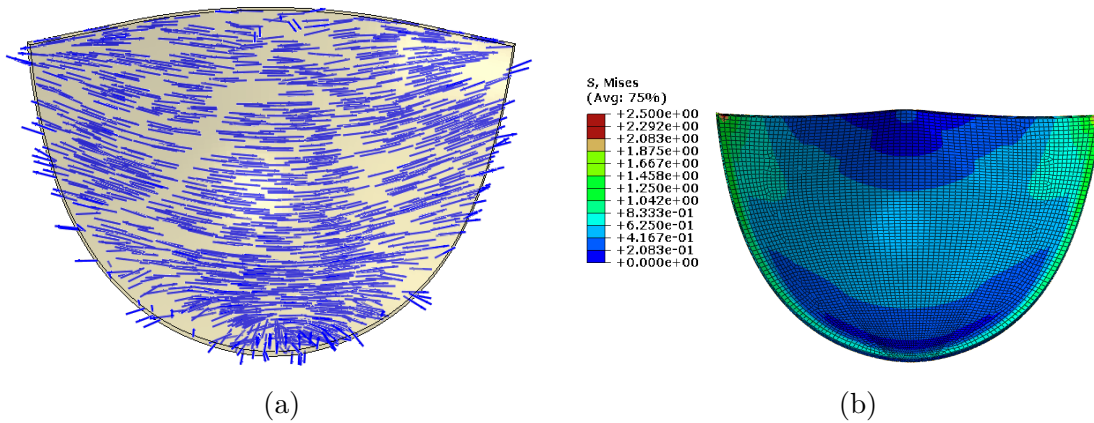


Figure 1.12: Anisotropy was optimised in a polymeric prosthetic heart valve by orienting fibres in the principal strain direction. The leaflet-stent boundary is constrained against translation and a symmetric constraint is applied to the leaflet-leaflet contact. (a) shows the orientation in the undeformed shape. (b) von Mises stresses in the leaflet when loaded to 180 mmHg. The maximum stress is located at the commissure in this instance. Courtesy of M. Serrani and Zaffora (2011).

0.44 MPa to 0.3 MPa. The peak stress locations for these *in silico* valves were found near the commissures. This result is exacerbated by the stent-leaflet edge being fully constrained against translation. The investigators did not model the opening behaviour of the anisotropic valve. Nevertheless, based upon the amount of coaption between leaflets during diastole, a leaflet thickness of 0.3 mm was proposed for manufacture.

It has also been shown that collagen fibres play a role during systole; De Hart et al. (2004) performed *in silico* studies with a bilayered fibrous structure in a 3 dimensional fluid-structure interaction model. In particular, their model showed fluttering of the non-reinforced leaflet during opening which is believed to accelerate fatigue. The fibres seemed to stabilise the leaflet during opening without affecting the transvalvular pressure drop.

Cacciola et al. (2000) created prototype stented and stentless valves with ethylene-propylene-diene-monomer rubber matrix reinforced with high-performance polyethylene. With the leaflets open to form a cylinder, the fibres were either arranged in a unidirectional circumferential manner, or in a periodic sinusoid such that the fibres formed a diamond lattice structure. This structure had a height of 4 diamond units and circumference of 30 diamond units, where each diamond unit had a vertical long axis, with a 60° acute angle. The valves opened and closed with a low transvalvular pressure drop, but had an unacceptable level of regurgitation, which was attributed to the low coaption area. The group at the Eindhoven University of Technology are now pursuing TE alternatives (Kheradvar et al., 2015).

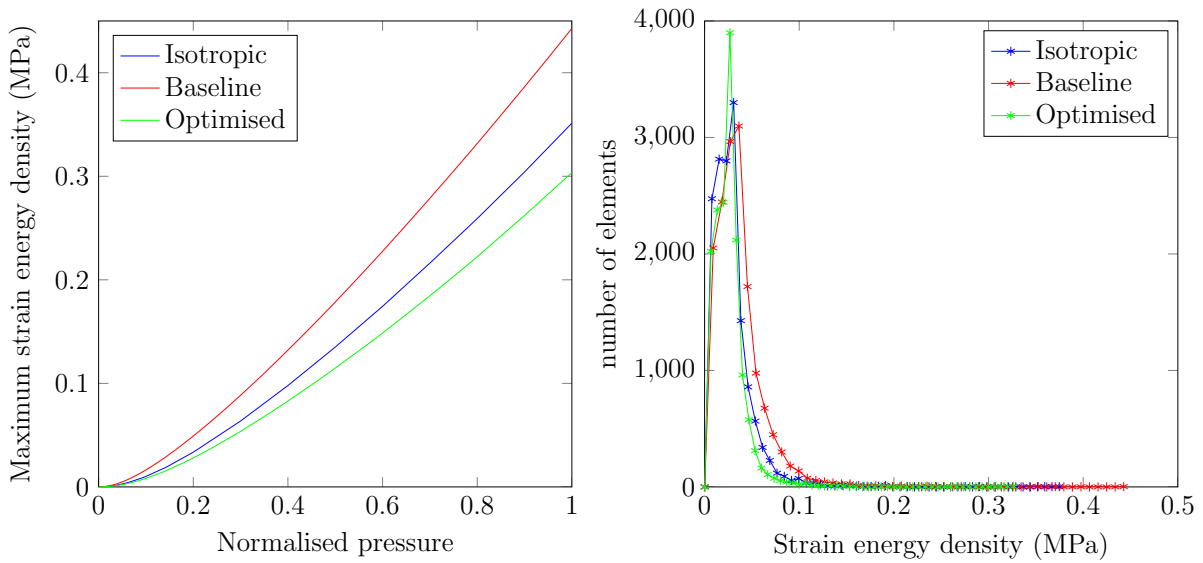


Figure 1.13: Strain energy density in the hyperelastic anisotropic finite element (FE) model of Zaffora (2011) from 0 to 180 mmHg. The data was extracted from the model by Dr Serrani. The isotropic data refers to a random orientation of fibres, baseline data refers to the initial guess in the iteration process where the fibres are all oriented perpendicular to the surface, and the optimised data is obtained after three iterations.

1.10.2 Stent post flexibility

A marked difference between the prosthetic and native heart valves reviewed here is the nature of the mechanical constraint at the commissure. The aortic root, which supports the native leaflets, is relatively compliant as it dilates during systole and contracts during diastole. This movement improves coaption between the leaflets and helps to redistribute stresses. The standard bioprosthetic valve has a relatively stiff stent. The benefit of commissure movement was highlighted by Krucinski et al. (1993) who modelled the cases of rigid, flexible, and flexible and rotatable stents. Flexibility of the stent in the radial direction was noted to reduce shock loading during diastole as the commissure moves inwards. During systole, the sharp bend at the commissure results in compressive and tensile stresses. These can be relieved by allowing the stent post to flex and the leaflet to rotate around the commissure.

In summary, anisotropy and stent flexibility play an important role in the native leaflet. Computational models have indicated that reproducing these characteristics in prosthetic valves would also be beneficial - most significantly by reducing the maximum stress during diastole. One aim of this thesis is to see whether these *in silico* results could be translated to *in vitro* experiments.

1.11 Polymers

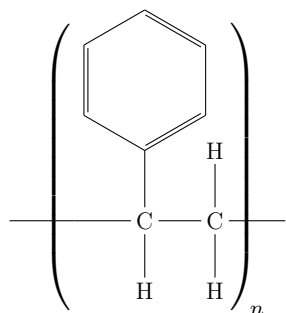
1.11.1 Polymers for medical applications

Since the first man-made plastics were fabricated at the turn of the 20th century, polymers have brought material-based revolutions to many fields. Our understanding of polymer architecture has improved throughout the 20th century, to the extent that during the latter decades the concept of custom polymers - designed from molecular structure to final product - has become a reality (Ebewe, 2000). The use of polymers in the medical industry is driven by several motivations. Polymers can be very cost effective, easily processed in a multitude of ways, fit into quality control systems with ease and can have their properties tuned over a continuous spectrum.

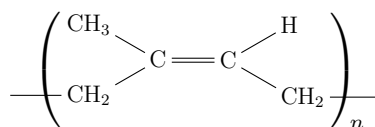
Polymers are generally divided into thermosets and thermoplastic types. The former irreversibly cures under a chemical or thermal stimulus while the latter can transition from solid to liquid multiple times. Polymer behaviour can generally be attributed to chain-chain interactions. Vulcanisation and crosslinking involve the formation of strong intermolecular bonds which prevent polymeric chains from moving independently of one another; this improves the elasticity of the polymer. Vulcanisation generally requires a chemical curative, such as sulfur, peroxide, platinum, a urethane crosslinker, metal oxide or acetoxysilane.

Silicones

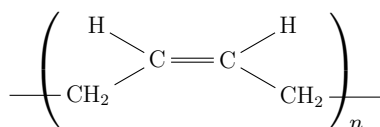
Silicones are the most commonly found polymers among medical devices (Yoda, 1998). They have relatively good biocompatibility, adequate biostability, can be fabricated in a variety of forms and are easily sterilised. Silicones have a polymeric backbone consisting of alternating silicon and oxygen atoms (Figure 1.14), and they can be crosslinked using either peroxide (which leaves a surface bloom) or the preferred platinum systems. Silicones can be moulded using liquid injection moulding, transfer moulding or compression moulding. In liquid injection moulding, the catalyst (typically a platinum curing agent which remains in the finished product) and crosslinker are injected through a mixer before entering the mould at which point the curing process takes place. This is the preferred method for medical devices as the system can be fully contained to reduce contamination, fully automated to reduce the possibility of human error, and cycle times can be faster (LeFan, 2011; MDDI Admin, 1999).



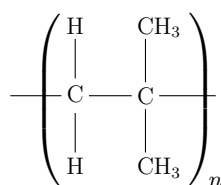
Polystyrene



Polybutadiene



Polyisoprene



Polyisobutylene

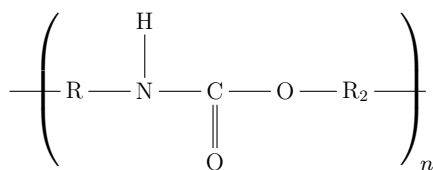
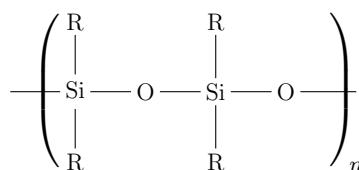
Urethane linkage, where R_1 and R_2 are aliphatic or aromatic sections.Silicone, where R is an organic group, which would be CH_3 in polydimethylsiloxane (PDMS).

Figure 1.14: Chemical structures of common polymer groups used in this thesis.

Polyester

Polyester (PES) is formed by the condensation reaction between a diacid and a dialcohol. Through varying the chemical structure of the reactants, the mechanical properties of the resultant PES can be tuned to be brittle and hard, tough and resilient, or soft and flexible (Nawrat, 2009). The most commonly found PES is polyethylene terephthalate (PET) which was developed independently by Imperial Chemical Industries (ICI) and DuPont in the 1940s. While the most common uses of PES are in clothing and bottles, it can also be found in biostable and biodegradable medical devices. In its flexible state, the polymer can be drawn into yarns, which in turn can be manipulated to form textiles. These textiles have found uses as bandages, sutures, and artificial tendons and ligaments, and have been proposed for artificial heart valves and kidneys. Unfortunately, PES is susceptible to

hydrolytic degradation which can cause fibres to rupture, making it unsuitable for long term *in vivo* implants (Rahman, 2012). Furthermore, PES is quite thrombogenic. This response diminishes over time, and is also mediated by using antithrombotic therapy, but means that PES materials (e.g. Dacron) are rarely used in cardiovascular applications (Kester, 1984). PES meshes do find a use in the sewing rings of prosthetic heart valves as they are rapidly infiltrated by tissue, without a long term inflammatory reaction.

Polyurethanes

Polyurethanes (PU) consist of a chain of organic units joined by urethane links (Figure 1.14). They are formed from a di- or polyisocyanate stream and a polyol stream which are reacted together with chain extenders, catalysts and surfactants. Polyurethane elastomers generally contain “soft” polyether or polyester segments, which phase separate from the harder polyurethane segments. The hard segments form randomly located regions of crystallinity within an amorphous matrix. The phase separation of PU, along with inter- and intra- molecular hydrogen bonding, results in “virtual crosslinking” which results in a high and flat plateau in modulus vs. temperature curves, as also seen for cross-linked rubbers. The size of the phase separated regions, their crystallinity, and the degree of crosslinking in either phase can also be controlled which allows a vast array of properties to be achieved. A variety of processes can be used to manipulate PU into different forms: extrusion, moulding, casting and dip coating, electrostatic and wet spinning of filaments have all been used for medical devices. PU, particularly those with a silicone-containing soft block, have good haemocompatibility. As such they have been used extensively in cardiovascular devices such as blood bags, vascular catheters, vascular grafts, artery bypass, and bladders in left ventricular assist devices, and total artificial hearts (Zdrahala and Zdrahala, 1999).

Early polyurethanes suffered from poor biostability, but they rapidly became the polymer of choice due to their mechanical properties which can mimic native tissues, and their relatively good biocompatibility. Since their inception, polyurethanes have proceeded from hydrolytically unstable polyester types, to hydrolytically stable but oxidatively unstable polyether polyol based PU. Finally, polycarbonate-based PU were developed with adequate hydrolytic and oxidative stability to withstand long term implantation, up to approximately 5 years. Although biostability was a prerequisite of early implants, more modern devices can harness biodegradation and allow native tissues to regenerate in their place (Zdrahala and Zdrahala, 1999).

Thermoplastic elastomers

There are 6 major classes of thermoplastic elastomer: polyamide, copolyester, olefinic, styrenic (Figure 1.14), urethane thermoplastic elastomers, and thermoplastic rubber vulcanizate. Thermoplastic elastomers are attractive from a manufacturing standpoint as they are relatively easy to process (speedy, lower energy requirements and scrap can be recycled). The polymer molecules generally comprise “hard” and “soft” blocks which can be varied in type and length allowing the properties of the polymers to be tuned.

Yoda (1998) claimed that styrenic thermoplastic elastomers would eventually replace silicone in a wide of range of medical applications due to their superior fatigue life and ease of processing. During the 1990s, the use of polystyrene-*block*-polybutadiene-*block*-polystyrene (SBS) and styrene-ethylene/butylene-styrene (SEBS) (see Figure 1.14) became common in catheters, medical tubing, intravenous solution containers, syringe tips, stoppers, dropper bulbs, baby bottle nipples, flexible caps, medical seals, and eye dropper bulbs (Yoda, 1998).

Styrenic block copolymers make up a major class of styrenic thermoplastic elastomers. As they are the focus of this project, I will present a more detailed discussion in Section 2.1.1.

Chapter 2

Polymer selection

2.1 Introduction

A range of polymers have been considered for use in prosthetic heart valves. As seen in Chapter 1, polyurethanes have received the most attention due to their tunable, soft tissue-like mechanical properties, and good biocompatibility. Unfortunately, some valves have failed due to poor biostability, and others due to poor biocompatibility. Silicones, polytetrafluoroethylene, and polyester have also been considered, but failed due to poor durability, calcification, and thrombogenicity, respectively.

As discussed in Section 1.10.1, the collagen of the native heart valve is arranged into bundles which result in an anisotropic material. The fibres extend circumferentially across the leaflet and serve as a means of mechanically supporting the pressure load during diastole, contributing to the durability of healthy heart valves. If this effect can be reproduced in a flexible leaflet prosthetic heart valve it may be possible to overcome the issues of durability that have plagued polymer prostheses thus far. Several researchers have proposed that fibres could be embedded into polymeric matrices to mimic the anisotropic mechanical properties of the native valve, but these attempts failed due to dehiscence of the fibres from the bulk. Another way of achieving anisotropy could be to use a block copolymer.

Block copolymers (BCPs) might be thought of as the “alloys” of the polymer world (Ruzette and Leibler, 2005). While a micro- or nanoblend of a rubbery and glassy polymer may be tuned to like an alloy, these are lost on heating as enthalpic forces cause separation. A BCP containing a rubbery and a glassy polymer can harness the elastomeric properties of polymers at room temperature, combined with the ability to repeatedly mould the

polymer into complex forms at high temperatures, a key characteristic of *thermoplastic elastomers*.

The molecular architecture of BCPs may also be tuned to produce materials which are mechanically anisotropic on the *macroscale*, and could thus mimic the anisotropy of heart valve leaflets (Stasiak et al., 2010). In this thesis I propose the use of a BCP with anisotropic mechanical properties as a material for a prosthetic heart valve.

2.1.1 Block copolymer fundamentals

A BCP molecule consists of 2 or more different polymer chains, or blocks, which can be synthesised using living anionic polymerisation. In the simplest cases BCPs consist of 2 polymer chains joined end-to-end, referred to as a linear BCP and denoted by *A-block-B* or *A-b-B*. More complex molecules can be formed with 3 or more chains which can be arranged linearly, into stars, miktoarm stars, cyclically, or grafted branches (Amado and Kressler, 2011; Hamley, 2004). For these blocks to join, their monomers must be chemically compatible such that they will bond to each other. However, monomeric compatibility does not confer block compatibility, and so the most prominent feature of many BCP at the polymer chain scale is the *strong* repulsion between *unlike* sequences, despite only *weak* repulsion between their *unlike* monomers (Leibler and Leibler, 1980).

If the forces of chain repulsion are strong enough, then microphase separation may occur (at an order-disorder transition) leading to spatial domains into which each polymer block will concentrate. The polymer seeks to minimise the total area of the A-B interface despite this carrying an entropic penalty from the segregation and concentration of the domains. This leads to several order-order transitions as enthalpic and entropic forces are balanced. A full prediction of this transition behaviour for a linear diblock copolymer (*A-b-B*) requires 7 parameters, of varying importance, to describe the blocks and their interactions.

The polymerisation index N , temperature T , and the polymer-solvent interaction, or Flory-Huggins parameter χ , have some importance in determining the structural transitions. However the dominant parameter is the proportion of each block, described by f . Self-consistent mean field theory can then be used to simplify the problem and predict the morphology of the polymer domains based on the aforementioned parameters (Leibler and Leibler, 1980).

For a linear di- or triblock copolymer 4 types of phase separated structure are predicted. When the fraction of block A (f_A) is low, A concentrates into spheres. As f_A increases,

the domains of A form cylinders, double gyroids and then lamellae as f_A approaches 0.5. These structures are illustrated in Figure 2.1. For phase separation to occur χ must be

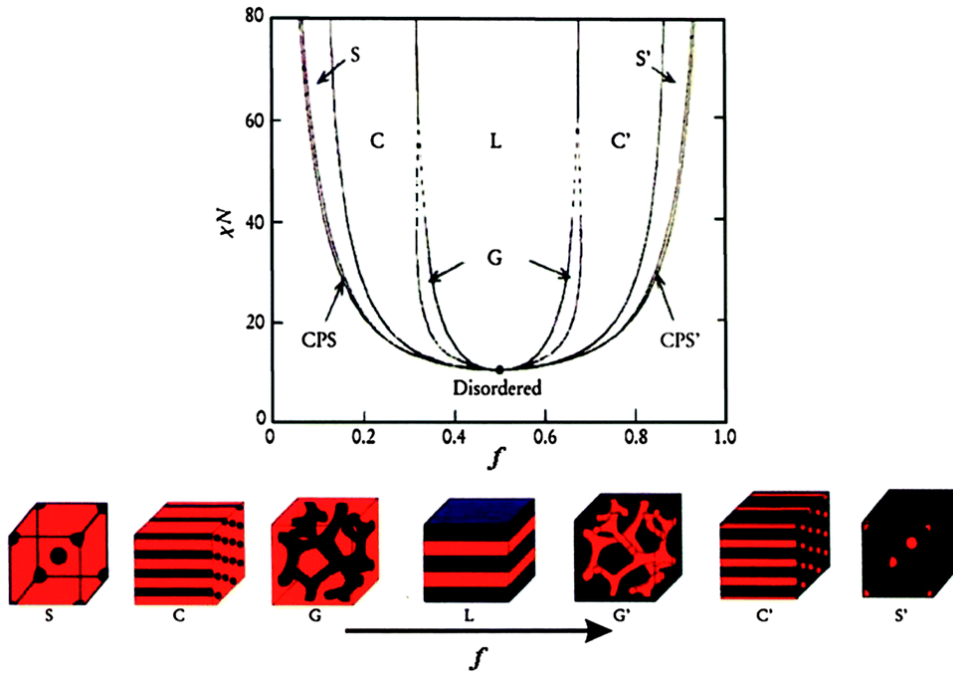


Figure 2.1: Predicted phase diagram for A-B symmetric diblock of Flory-Huggins parameter and polymerisation index, χN , versus the proportion of each block, f . L = lamellae, G and G' = bicontinuous gyroids, C and C' = hexagonally packed cylinders, and S and S' = body-centered-cubic spheres. A narrow region where the spheres take on a closely packed structure (CPS and CPS') is also predicted between the disordered region and S . For $\chi N > 40$ the phase diagram boundary lines tend to be vertical. From Mai and Eisenberg (2012).

positive. χ also influences the sharpness of the transition between domains. However, the order-order transitions have remarkably little dependence on χ , and so there is very little variation in the value of f at which the order-order transitions occur in different phase separating BCPs. The microdomain dimensions do however scale as $D \sim a_m N^{\frac{2}{3}} \chi^{\frac{1}{6}}$, where D is the characteristic length of a repeating structural unit, a_m is the length of a monomer unit, and N is the polymerisation index (Bates and Fredrickson, 1990).

The cylindrical morphology is of most interest because if the cylinders can be aligned, it may be possible to produce mechanically anisotropic materials. Cylinders¹ are formed when the mole fraction of one block is in the region of 18 to 30%. These limits have a small dependence on polymer chain type, but these bounds are relatively unchanged for

¹A note on nomenclature of cylinders: I have introduced the concept of cylindrical domains into which the polystyrene (PS) blocks are concentrated. As well as cylinders, these domains may also be referred to as (PS) nanodomains, (PS) cylinders, or (PS) fibres. Unless otherwise stated, the terms are essentially interchangeable, and are used according to the context.

symmetric, 2-component, triblock architectures (A-*b*-B-*b*-A) (Castelletto and Hamley, 2004).

In order to produce a shortlist of polymers which might be suitable for a prosthetic heart valve, I formed a set of criteria; the BCP must exhibit phase separation at room temperature, the cylindrical morphology must have been reported, the polymer should not contain heavy metal ions, and neither block should be obviously unstable in the presence of water, weak acids, or weak alkalis. Finally, only commercially available BCP were considered at this stage.

I performed a literature search for phase separating BCP, and identified a list of these that exhibit a cylindrical morphology. These are listed in Table 2.1. Among this set of polymers there are a wide variety of architectures - from linear chains, to aromatics, to those containing metal ions. A limited number are stable and commercially available, which are marked in the table.

Table 2.1: List of cylinder forming triblock copolymers using A, B, and C to denote each block (Mark, 2007). Commercial availability of the polymers was determined based upon the Polymer SourceTM catalogue and Google searches.

A	B	C	Archit- ecture	Commer- cially available?
2-exo-3-endo-bis(diphenyl-phosphino)-bicyclo[2,2,1]heptene	Methyltetracyclo-dodecene		A-B	
Butadiene	Dimethylsiloxane		A-B	✓
Ethylene	Ethylenepropylene		A-B	
Ethylene	Ethylethylene		A-B	
Ethylene	Tert-butylmethacrylate		A-B	
Methyltetracyclo-dodecene	Organometallic derivative of norbornene		A-B	
Organometallic derivative of norbornene	Acetylene		A-B	
Lactide	Isoprene		A-B-A	✓
Styrene	2-(3-cholesteryl-oxycarbonyloxy)ethyl-methacrylate		A-B-A	
Styrene	Butadiene		A-B-A	✓

Table 2.1 continued.

A	B	C	Architecture	Commercially available?
Styrene	Ethylene	Butadiene	A-B-C-A	✓
Styrene	Isobutylene		A-B-A	✓
Styrene	Isoprene		A-B-A	✓
Butadiene	Styrene	Isoprene	A-B-C	✓
Ethylenepropylene	Ethylenebutene	Styrene	A-B-C	✓
Styrene	Ethylene	Propylene	A-B-C-A	✓
Styrene	Ethylene	Butene	A-B-C-A	✓
Isoprene	Butadiene	Styrene	A-B-C	✓
Isoprene	Styrene	2-vinylpyridine	A-B-C	✓
Styrene	Butadiene	2-vinylpyridine	A-B-C	✓
Styrene	Butadiene	Methylmethacrylate	A-B-C	✓
Styrene	Ethylenebutene	Methylmethacrylate	A-B-C	✓
Styrene	Isoprene	2-vinylpyridine	A-B-C	
Isoprene	Styrene		Miktoarm star	
Styrene	2-methyl-1,3-pentadiene		Miktoarm star	
Styrene	Isoprene	Butadiene	Miktoarm star	
Styrene	Isoprene	Dimethylsiloxane	Miktoarm star	
Styrene	Isoprene	Methylmethacrylate	Miktoarm star	
Isoprene	Styrene		Super-H star A3-B-A3	

Polymer shortlist

From Table 2.1 I selected the following shortlist of polymers based upon commercial availability and stability. PS refers to polystyrene and *b* represents a polymer block.

- PS-*b*-polyisoprene-*b*-PS (SIS),
- PS-*b*-polyisoprene-polybutadiene-*b*-PS (SI/BS),

- PS-*b*-polyethylene-polypropylene-*b*-PS (SEPS),
- PS-*b*-polyisobutylene-*b*-PS (SIBS),
- PS-*b*-polyethylene-polybutene-*b*-PS (SEBS),

From the table, polyvinylpyridine and polylactide were considered, but not included in the shortlist due to their known toxicity (at all except low concentrations (Allison et al., 2007)) and biodegradability, respectively.

If the PS molar content is between 18 and 30%, PS would be concentrated within the cylinders. PS has a glass transition of $\sim 90^\circ\text{C}$ whereas the rubbery blocks have glass transition $\sim -100^\circ\text{C}$, resulting in cylinders which are stiffer than the bulk. Having generated a shortlist of seven BCP, I sought further criteria to select one polymer for use in a prosthetic heart valve.

2.1.2 Material selection parameters

From the history of polymeric prosthetic heart valve design in Section 1.8, over 30 candidate polymers are found, yet none have succeeded in clinical use. A large proportion of polymer flexible leaflet heart valves failed, typically during *in vitro* fatigue testing, or in a chronic animal model, with poor durability listed as a key cause. There are various causes of inadequate durability. In general terms, the following environmental and use factors can cause the failure of polymers (Hulme and Cooper, 2012):

- Mechanical (creep, fatigue, stress relaxation, impact, environmental stress cracking (ESC) and wear);
- Thermal (degradation and fire);
- Chemical:
 - oxidation (oxygen, ozone, and metal catalysed),
 - biological,
 - other chemicals encountered during use or processing;
- Radiation (sunlight, ultraviolet light and atomic radiation);
- Electrical (arcing and electrostatic build-up).

Within the body the dominant modes of failure are mechanical and chemical. Mechanical forces in the cardiovascular system arise from fluid shear and pressure forces. Chemical forces may arise from hydrolysis or oxidation in aqueous conditions. Or, there may be

chemical species of biological origin; inflammatory cells will secrete enzymes and oxygen radical species with the purpose of breaking down the foreign materials. The proposed implant is passive and permanent, and so must withstand these forces. Each of these forces can cause failure individually, or in combination .

Radiation, extreme temperatures and electrical hazards are unlikely to be encountered in the body to the degree which they would degrade a polymeric material, but resistance to these conditions is still necessary as medical devices must be sterilised prior to implantation.

Combining biological, chemical, and mechanical forces of degradation increases the complexity and expense of testing, and *in vitro* testing systems are unable to simultaneously impart all three forces. The only pre-clinical model which realistically imparts all the forces upon the valve is a chronic, large animal model. In the selection process, the candidate materials were subjected to individual forces *in vitro*.

2.1.3 Stability selection

In the absence of inflammation, the host environment is an aqueous solution containing lipids and proteins, at pH 7.4 and 37°C. Unfortunately for any implantable material, the body is also capable of producing harsher chemical conditions which are intended to break down foreign species. Most typically degradation is achieved through hydrolytic, oxidative or enzymatic conditions (ISO, 2010).

The rate at which biomaterials may degrade is a function of the material, local reactant concentrations, and a set of rate constants (Maxwell et al., 2005). To accelerate ageing of the material, the rate constant or reactant concentration can be increased. The exact mechanisms of degradation are rarely known, so an increase in temperature is used to alter the rate constant. In general, the rate constant of degradation is assumed to be of an Arrhenius form:

$$k_r = A_e e^{E_a/RT} \quad (2.1)$$

where k_r is the reaction rate constant, A_e is the pre-exponential factor, E_a is the activation energy, R is the Gas Constant and T is the temperature. This method clearly relies on the assumption that the same reactions and mechanisms for degradation occur at the reference and accelerated temperatures².

²In the testing of polymeric materials an alternative expression where the rate constant is increased using temperature is commonly used. The accelerated rate at T is related to a reference rate at T_r , by $2^{(T-T_r)/10}$. This relation essentially assumes that the reaction is first order and has a rate constant of $10R \ln 2$, and the same degradation mechanisms occur at the two temperatures (Hukins et al., 2008).

In reality, quantitative lifetime predictions are impossible as chemical degradation cannot be regarded as a linear process, and harsher conditions can promote different degradation mechanisms. The only effective method of assessing chemical durability for material selection is qualitatively and comparatively (Bruck, 1991; Pinchuk, 1994; Vondracek and Dolezel, 1984).

In a simple accelerated degradation test, Pinchuk et al. (2008) demonstrated the stability of SIBS by submerging the materials in boiling concentrated (65%) nitric acid. These conditions resulted in the destruction of silicone and polycarbonate urethane, whereas PTFE and SIBS survived. To test hydrolytic and oxidative stability ISO 10993:13 (for the identification and quantification of degradation products from polymeric medical devices) recommends the use of buffered water and oxidative solutions, respectively, under accelerated conditions of 70 °C. Degradation can then be evaluated by considering any of mass loss, solution viscometry, swellability, rheology, chromatographic methods (e.g. gel permeation chromatography), spectroscopic methods (e.g. Fourier transform infrared spectroscopy) or thermal analysis (e.g. differential scanning calorimetry).

2.1.4 Biocompatibility selection

In this thesis, I propose a *regular* or *classical* implant, as opposed to a TE implant. Classical implants rely upon materials which are chemically and biologically inert, and success is defined by the implant having “no clinically relevant deleterious effect on those tissues or components”. This can be contrasted with TE implants, whose materials are used to deliberately target and activate certain cells in order to create new tissue for the therapeutic reconstruction of the human body (Williams, 2015).

Adequate biocompatibility without the need for anticoagulation is a criteria for the selection of a material for the prosthetic heart valve. Biocompatibility was set as a secondary criteria for selection as large differences in biocompatibility were not anticipated. Previously, the indirect cytotoxicity of SIBS, SIS, SIS, and SI/BS, was assessed by my collaborators in Politecnico di Milano, with no polymers eliciting a positive response. Furthermore, one of the shortlisted BCPs, SIBS, is already in clinical use as a drug eluting coating for the Taxus stent (Boston Scientific), indicating its biocompatibility. Finally, the molecular architecture of the various BCP are not so different, suggesting that they are unlikely to behave markedly differently. An analysis of biocompatibility is presented in Chapter 3.

2.1.5 Material selection function

Once the unstable polymers had been eliminated from the shortlist, another criterion was required to select the most suitable material for my application. In engineering design, selection strategies can be used to choose a material with the most potential for fulfilling a certain purpose. Examples of selection strategies are: *questionnaire based* which requires some expert input and returns “known” solutions, *analogy* based on past cases of material choice, or *free search* with quantitative analysis. The free search method leaves the greatest scope for innovation (Ashby et al., 2004). Elements of this method can be used in the selection of a material for a novel polymeric prosthetic heart valve. In Appendix B I show a detailed example of the derivation of a material selection index. Here, I derive a heart valve performance index.

Material selection should stem from an understanding of the fundamental function of the heart valve; it must open for systole, and resist reverse flow during diastole. Furthermore, a valve should have minimal resistance to flow during systole, while resisting reverse flow indefinitely.

During the opening of a flexible leaflet valve, the curved leaflet must reverse its curvature. The force required to do this, F_{rev} , should be minimised. Once open, the pressure drop over the valve is dominated by the valve’s geometry. In the case of valve closing during diastole the situation is more complex. The forces on the valve leaflet that lead to closure are dominated by dynamic fluid effects; for example, the sinuses of Valsalva promote eddy formation resulting in the initiation of closure. As such, parameters such as valve height and leaflet angle are used to affect the open area and closing dynamics (Burriesci et al., 2010). Neither the open area nor the closing dynamics have a first order dependence on material type, and so I neglected it from the performance index.

Bernacca et al. (2002) performed hydrodynamic studies on valves whose leaflets had various thicknesses. They reported that a reduction in leaflet thickness led to a lower mean pressure gradient over a full cycle. The force which is required to reverse the curvature of a curved surface, F_{rev} , is related to the leaflet’s thickness and the material’s stiffness, and is driven by the transvalvular pressure difference, $P_V - P_A$, as shown in Figure 2.2. Assuming that stress and strain are linearly related, the force required to bend a leaflet of uniform cross section is proportional to the second moment of area of the leaflet, which is proportional to the cube of the leaflet’s thickness, t^3 , (Gupta, 2001; Haworth, 1978). Leaflet opening requires the leaflet to bend, for which the flexural

modulus, E_{flex} , is a good measure of the material's stiffness:

$$F_{rev} \propto E_{flex} t^3 \quad (2.2)$$

Thicker or stiffer leaflets result in valves which perform less well (Bernacca et al., 2002). The pressure required to reverse the curvature of a pure hemisphere is a function of both t^3 and t^4 , and so for a leaflet with spherical and cylindrical structures the power of t should lie between 3 and 4 (Ghista and Reul, 1983). I used t^3 in the following analyses.

To optimise haemodynamics, F_{rev} should be minimised, making Equation (2.2) an objective function which contains one material property E_{flex} , and one design variable t .

The durability of the valve is also a function of material and valve design. The first order determinant of stresses within the leaflet is thickness; thicker leaflets have lower stresses. In a uniformly thick leaflet maximum stresses occur at the leaflet-stent boundary. It

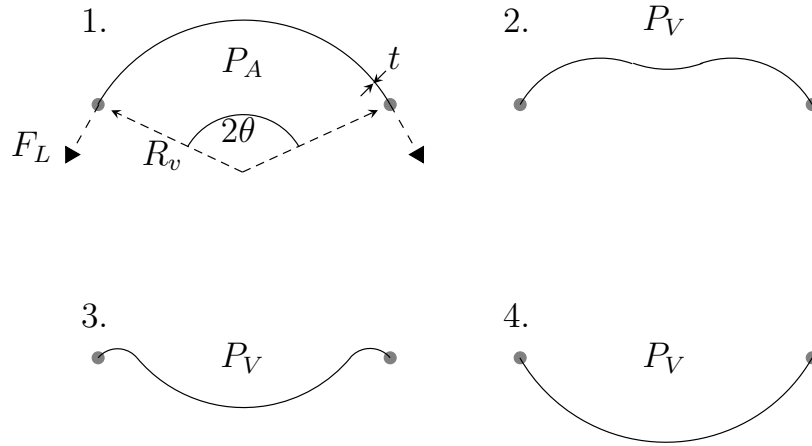


Figure 2.2: 2-dimensional cross-sectional schematics of a leaflet with either a purely cylindrical or spherical form, with characteristic radius, R_v , when closed, and thickness, t . 1 to 4 are forms of the leaflet from closed to open.

1. Aortic pressure, P_A , is greater than ventricular pressure P_V during diastole. The pressure load is supported by the stent. The maximum leaflet stress is found at the centre of the leaflet.

2. Once P_V rises at the start of systole, the curvature of the leaflet can start to reverse. The force required to do this is a function of R , t and the material's modulus.

3. P_V continues to exceed P_A , causing the leaflet to finish opening.

4. The leaflet is fully open during systole. The geometric orifice area is determined by the shape of the leaflet.

The force required to reverse the curvature is the sum of the bending moments along the curved leaflet.

is possible to estimate the stresses within the leaflet if a simple leaflet form is assumed (Figure 2.2 (stage 1)), for a cylinder segment of radius R and arc 2θ , supporting P_A . The stress per unit length, σ_c , at the commissure of the leaflet is:

$$\sigma_c = \frac{\delta P R \tan \theta}{t} \quad (2.3)$$

where δP is the pressure difference ($P_A - P_V$) that must be supported during diastole. The radius of the cylindrical section would be roughly equivalent to the valve annulus radius. For the valve to function properly the stress must be less than some fatigue limit, σ_f :

$$\sigma_f > \frac{\delta P R \tan \theta}{t} \quad (2.4)$$

Thicker or stiffer leaflets lead to lower stresses during diastole making them more durable. Thinner leaflets require a lower pressure to reverse their curvature, leading to better haemodynamics. Given these conflicting criteria, I need to identify the optimal compromise solution.

By combining Equations (2.2) and (2.4), the design variable, leaflet thickness t , can be eliminated, leaving only the material properties and the constants. This quotient becomes a material performance index, I_P , to be minimised:

$$\min(I_P) \propto \underbrace{\left(\frac{E_{flex}}{\sigma_f^3} \right)}_{\text{Material properties}} \underbrace{(\delta P R \tan \theta)^3}_{\text{Constants}} \quad (2.5)$$

The performance index approach to selecting a material for prosthetic heart valve materials was previously considered by Haworth (1978) who used a similar selection function:

$$I_P = \frac{E}{\sigma^{*3}} \quad (2.6)$$

This method was unsuccessful and, crucially, was based upon the tear rupture stress σ^* , which is an unrealistic model for failure in polymer prostheses as it occurs at strains several orders of magnitude greater than those seen in actual prostheses.

Parfeev et al. (1983) took a different approach. They established stress wear limits for various natural, silicone and fluorosilicone rubbers after 10^7 cycles. They also compared the stress wear limits to the materials' moduli to produce a selection index. They went one step further by making estimates of the forces which are generated in heart valve leaflets. Under biaxial tension the maximum stress in a hydrostatically loaded hemi-

spherical membrane is,

$$\sigma = \frac{Pl_s}{2t} \quad (2.7)$$

where P is the pressure, l_s the radius of curvature and t the leaflet thickness, which were taken to be 120 mmHg, 10 to 20 mm, and 0.25 mm respectively. Under these conditions the aortic valve leaflets must be able to withstand 0.32 to 0.64 MPa. Combined with the wear testing they determined that none of the isotropic polymers which were tested would be suitable for an aortic polymer prosthesis, although a reinforced rubber or polyurethane may be suitable. This assertion lends support to my proposal of using an anisotropic material.

Parfeev et al. (1983) performed their durability testing at 22 Hz, which was a higher frequency than normal loading conditions. The properties of polymers are dependent upon frequency and strain rate, and this testing may not have been representative of the actual performance.

In order to check whether it might be possible to accelerate the onset of cyclic failure by increasing the cycle frequency I performed dynamic mechanical analysis of candidate BCP samples (using a TA Instruments Q500). I located the limit of the linear region using a strain sweep before performing a frequency sweep. These results are illustrated in Figure 2.3, as a plot of damping factor, $\delta = \frac{\text{viscous modulus}}{\text{elastic modulus}}$, versus frequency. From these data I observed that, not only is there a large transition in the damping factor at 80 Hz, but also a smaller, β transition at 20 Hz. These transitions arise when deformations occur faster than molecules can rearrange themselves indicating that the material has a different behaviour under these conditions.

The linear region at which these measurements were taken extends up to 0.1% strain. Given the larger strains that occur during leaflet deformations, the transition may occur earlier than 20 Hz, making accelerated testing much trickier. Even at 10 Hz, 10^7 cycles requires one month of testing for just one sample. Thus, a faster method of evaluating fatigue life was sought. This will be discussed in Section 2.1.6.

Material performance indices can also be displayed graphically using Ashby maps, as shown in Figure 2.4a. The material properties are plotted on logarithmic scales, and material performance indices appears as straight lines. Materials lying along the line have an equal performance index, while shifting the line corresponds to different indices. A maximum or minimum leaflet thickness (due to manufacturing constraints, for example) corresponds to a modulus constraint, which is also shown in Figure 2.4a

The world of materials can be plotted on the Ashby map using the CES selector software (CES Selector, Granta Design[®], Cambridge, UK), which can be used to produce results

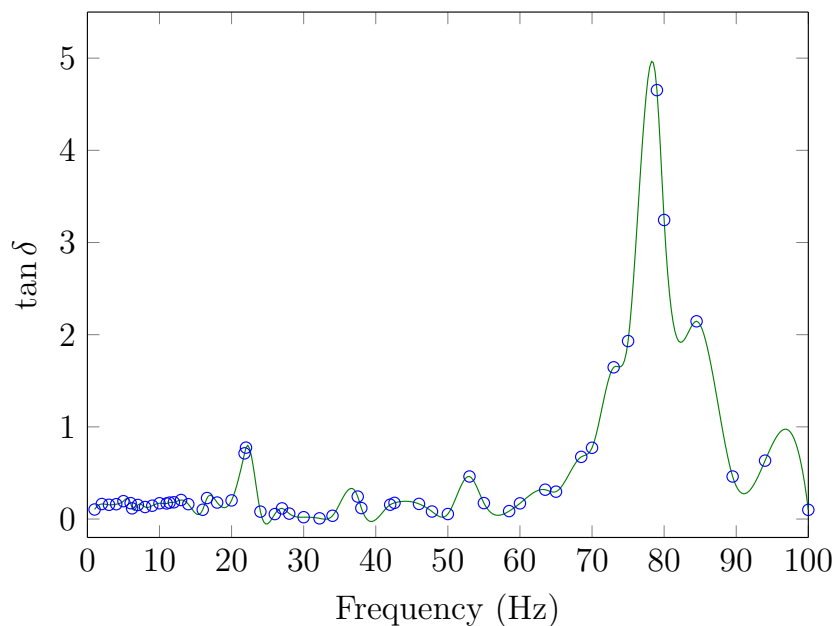


Figure 2.3: Dynamic mechanical frequency sweep of SIBS30 material ($n=3$) at 0.1% strain. A spline is fitted to the data. Note the peak in the damping factor, $\tan \delta$, which is also accompanied by an increase in the elastic modulus which indicates a glass transition occurring at 80 Hz. The peak seen at 20 Hz corresponds to a smaller, β transition.

such as those shown in Figure 2.4b and 2.5. The CES software has the capability to add further selection criteria: in Figure 2.5 a maximum is placed upon the Young's Modulus (0.5 GPa), basic chemical durability criteria are added (*excellent* performance in fresh and salt water, and *excellent* or *acceptable* in weak acids and alkalis), and ISO 10993-1 acceptance, indicating that it would at least be acceptable for use in non-implantable medical devices. The “optimal” materials are marked in this diagram with \blacklozenge (Natural rubber) and \blackstar (polyurethanes - though as some degrade this is marked in grey.). The software contains information on SEBS, a BCP, which is indicated by \clubsuit .

For the purposes of prosthetic heart valve design, the data is somewhat limited as fatigue strength is listed for only 10^6 , and the fatigue data is based on an $R = -1$, where R is the ratio of minimum to maximum stress, indicating equal compression and tension, which does not occur in a valve. Polymers rarely have a linear stress-strain relationship, so Young's Modulus is only a good comparison of stiffness for small deformations. The property bubbles in the plot are also large, and often cover whole orders of magnitude for a single material type - indicating fatigue and modulus vary significantly among types and grade of material and are also dependent on processing.

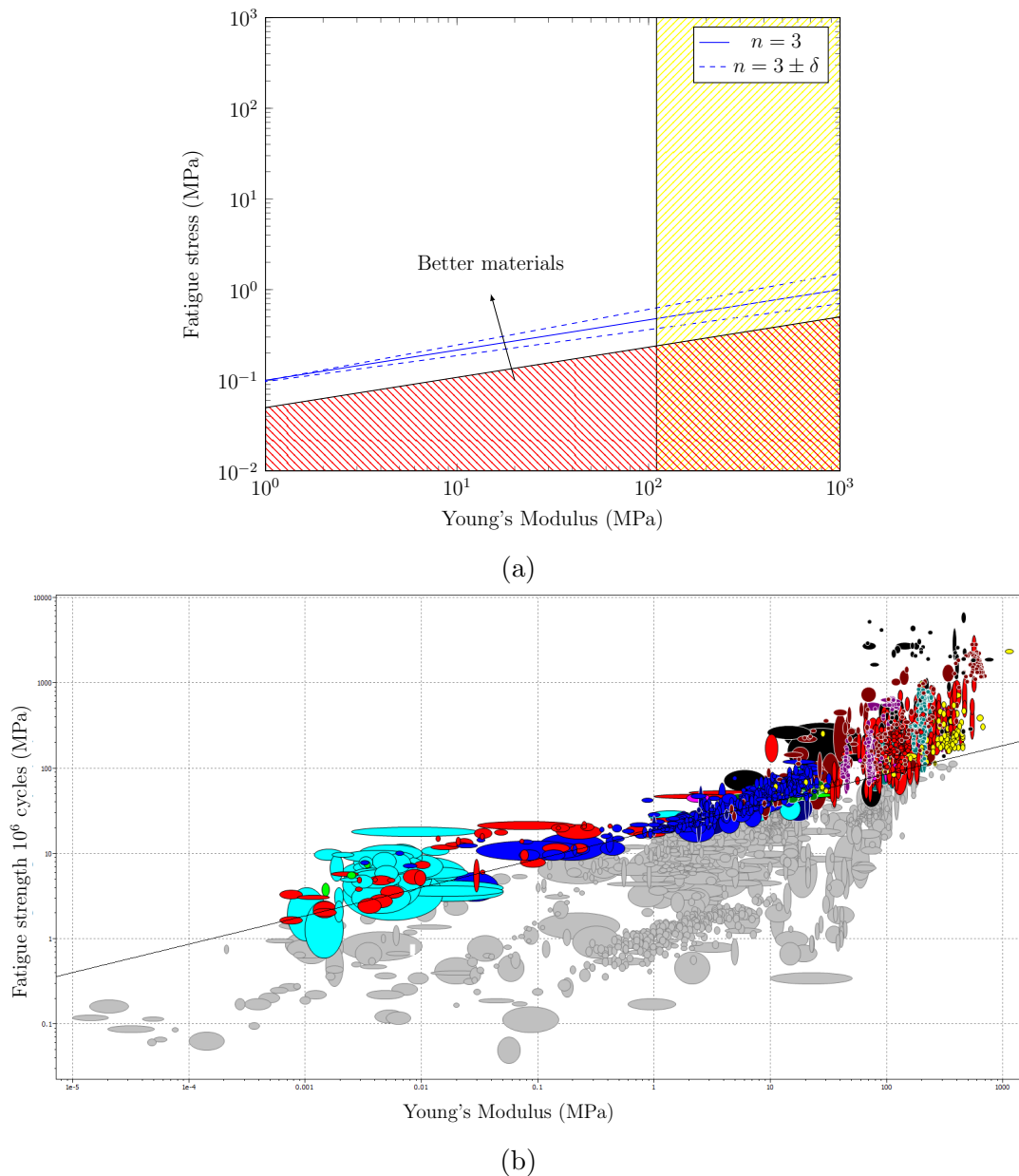


Figure 2.4: Ashby map schematic (a) containing constraints (hashed areas) and material performance index lines (blue). On a log-log plot, the performance index (Equation (2.5)) appears as a straight line, where the gradient corresponds to the index. The heart valve index (with respect to fatigue stress) was assumed to be 3, but it may deviate, altering the optimal material. Superior materials have a lower performance index and are found in the upper left region of the diagram. The red hashed area indicates a theoretical maximum value for the performance index, above which a valve would not open, or would not be sufficiently durable. The hashed yellow area corresponds to maximum modulus constraint. In (b), the “complete material world” is plotted. An inset of the map is shown in Figure 2.5.

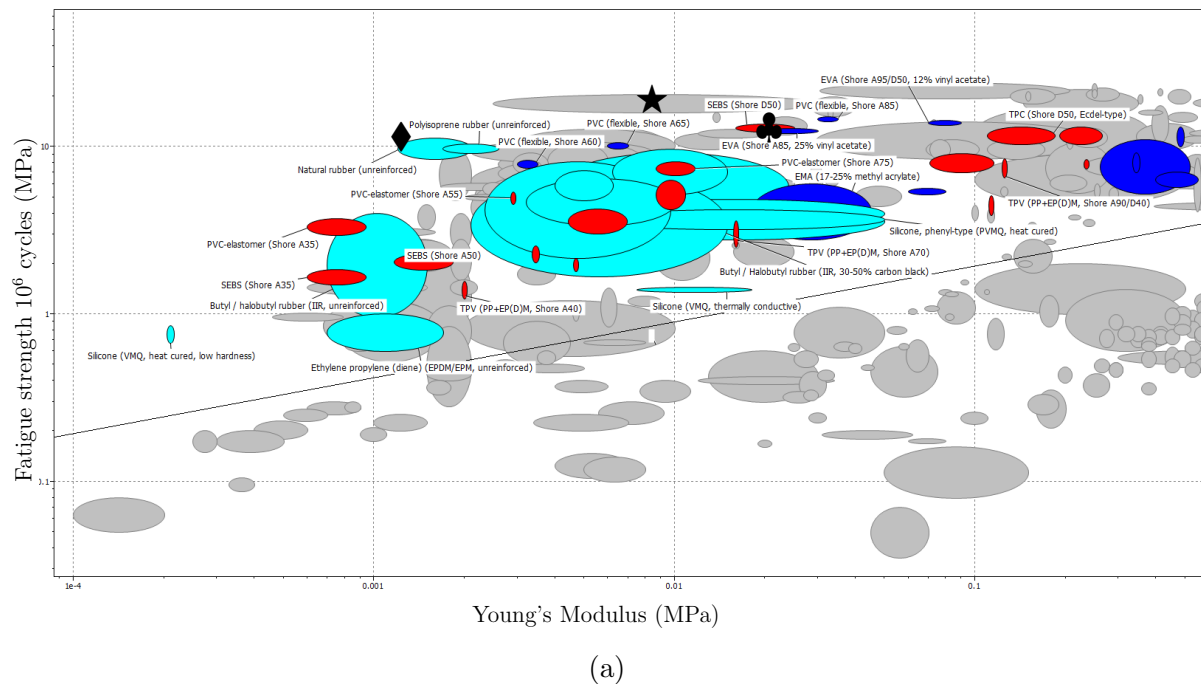


Figure 2.5: Ashby map with Young's Modulus and fatigue stress plotted on logarithmic axes, showing the elastomeric materials. Chemical durability and medical grade criteria were applied (grey indicates that the material failed). Natural rubber (◆) and polyurethanes (★) are the optimal materials, nearest to the top left. A block copolymer, SEBS, is marked with ♣.

2.1.6 Elastomer failure

To select a polymer using the material performance index, Equation (2.5), the material's stiffness E_{flex} and fatigue stress limit σ_f must be determined. The former is relatively rapid and reliable, while the latter is much trickier. Haworth (1978) used large strains and Parfeev et al. (1983) used high frequency to predict the lifetime of elastomeric materials, but these means of extrapolation are not a representative assessment of long term behaviour of polymers.

Within the engineering design community the method of stress vs number of cycle lifetime is commonly used (σ -N). This method requires a large number of samples to be tested at variety of stresses until they fail. When the failure stress is plotted against the logarithm of number of cycles to failure, as shown in Figure 2.6, the curve features low and high cycle limits, and a transition region.

Curves of σ -N were developed for use with polycrystalline engineering materials in which dislocations and slips between shear planes propagate to form crack many times larger than the grain size. σ -N curves can be used to estimate the lifetime of a whole part, but the curves cannot describe the time to failure for a sample which already contains

a crack (Teoh, 2000), or be readily applied to alternative geometries or stress situations (Papadopoulos, 2005). As such, I needed to identify an alternative method.

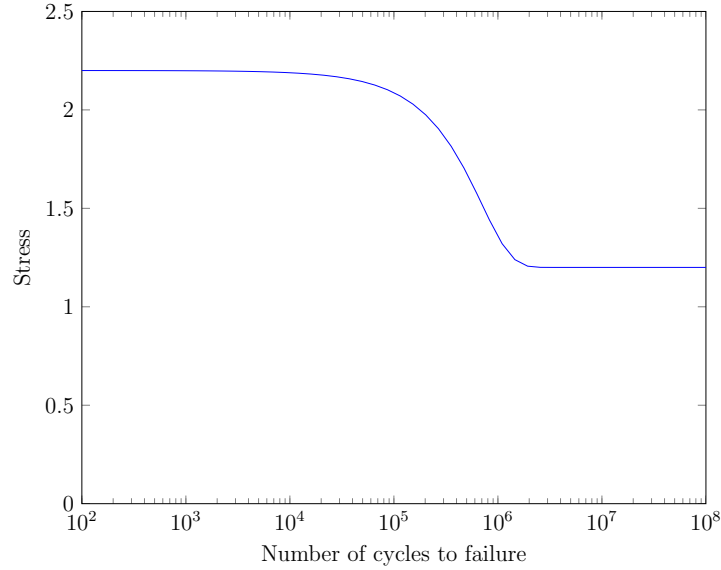


Figure 2.6: Typical σ - N curve for a cyclically loaded sample exemplifying the pertinent features. During experimentation the limiting plateau which is found in high cycle fatigue may occur much later than indicated, and thus not be reached.

When a polymer is cyclically strained the chains will rearrange, a process which is referred to as dynamic stress relaxation. It is reasonable to believe that at low strains these rearrangements are reversible and the polymer behaves elastically, however at high strains these rearrangement can eventually lead to sample failure. El Fray and Altstädt (2003a,b, 2004) made extensive use of a test using stepwise increases in load or strain. Their samples underwent a fixed number of cycles to a particular strain, that was increased stepwise every 10,000 cycles. By analysing the change in elastic and viscous moduli, and the damping factor, it might be possible to spot when a polymer moves from one stretching regime to another, and thus determine a fatigue limit, however no clear changes were observed in their data (Puskas et al., 2009b).

The failure of polymers can also be predicted by examining the nucleation of cracks and then their growth until failure of the material. This method has been used extensively by the automobile industry (Mars and Fatemi, 2002). Fracture mechanics can be used to model the behaviour of the crack. The initial crack may be present due to an inherent flaw in the material, as a result of chemical action, or spontaneous nucleation when the material is strained. If the material is then strained the crack may grow. In this thesis I use the following conventions: extension or stretch ratio, $\lambda_s = \frac{L}{L_0}$, where L is length and L_0 is the unstrained length; and (engineering) strain, $\epsilon = \lambda - 1$. I will also assume incompressibility, $\Delta V = 0$, so $\lambda_x \lambda_y \lambda_z = 1$.

At the tip of a crack the stress becomes concentrated. If the stress exceeds a *critical stress*, the crack will grow. This requires the stress distribution around the every crack tip to be known, as well as the inherent critical stress property for the material. The work carried out by Thomas (1994) indicated that finding a relationship between a “critical stress criterion” and a measurable tearing force would be “impossible”. As a result, subsequent analyses have been based upon an energy criterion, which can be applied over a volume around the tip, rather than a single point maximum.

The use of an energy criterion stems from work by (Griffith, 1921) who applied the concept of a minimum energy criterion to the problem of brittle material fracture. Rivlin and Thomas (1953) then extended this energy criterion method to be used with rubbery materials. This subsequently spawned the development of the J-integral concept which can be used to define the stress and strain fields around the crack tip (Cherepanov, 1967; Rice, 1968). The minimum energy criterion concept assumes that a crack will grow if the elastic stored energy, U , released is greater than the free energy required to create a new surface. For a growing crack, the formation of new area, ∂A , causes the specimen to relax, leading to a decrease in stored elastic energy, ∂U . This decrease in stored energy is referred to as the strain energy release rate or tearing energy, T_e ,

$$T_e = - \left(\frac{\partial U}{\partial A} \right)_l \quad (2.8)$$

where ∂A refers to one face of a crack and l signifies that the change occurs at constant displacement. Whereas a polycrystalline material will fail due to rapid crack growth once the tearing energy rate at the crack tip exceeds a critical value, exceeding this critical value in an elastomer simply leads to slow, incremental crack growth. One reason for this lies in the hysteresis of elastomers. Once a critical stress is exceeded, new surface is formed which dissipates energy and reduces the strain in the surrounding material. In a hysteretic material, a small reduction in strain results in a much greater reduction in stress than for an elastic material, hence reducing the strain energy density available to form new surfaces (Lake and Thomas, 1967).

In the following analyses, the fastest form of crack propagation is considered: mode 1 tensile fracture where the crack grows normal to the principal tensile stress direction. If the crack extends through the thickness of the material then the area, A , of one face of the crack is a product of the crack’s length, c , and the sample’s thickness, t . If, according to Equation (2.8), the static strain is large enough, then it is favourable for a new surface to form and the crack to grow, as opposed to stretch further. A similar relation holds for cyclically strained sample, where the growth of the crack depends on the maximum

value of T_e which is reached during a cycle (Gent et al., 1965). The cyclic crack growth rate can be related to the energy release rate as,

$$\frac{dc}{dN} = f(T_e) \quad (2.9)$$

where c is the length of the crack, N is the number of cycles and T_e is the maximum tearing energy in a cycle. Rivlin and Thomas (1953) demonstrated that the relation between crack growth rate and T_e , as shown in Equation (2.9), is independent of sample geometry, allowing various materials to be compared. Over a large range of strain values, the relationship between energy release rate and crack growth rate can be fitted to a power law model (Mars and Fatemi, 2003):

$$\frac{dc}{dN} = BT_e^F \quad (2.10)$$

where B and F are the coefficient and exponent, respectively, in this power-law model.

T_e itself is a function of the *type* of strain and the strain energy density, W .

The most simple sample geometry in which a crack can be grown is the planar tension crack growth geometry (also known as single edge cut or pure shear geometry) as shown in Figure 2.7a, which produces a plane stress state ($\lambda_x = \frac{1}{\lambda_z}$, $\lambda_y = 1$, where the x-component of λ is λ_x , and so on). The energy release rate is calculated as:

$$T_e = WL_0 \quad (2.11)$$

where W is the strain energy density in the sample and L_0 is the unstrained length of the sample. In this geometry the crack grows at a constant rate independent of the crack length (Papadopoulos, 2005).

By contrast, tensile bar (dogbone or dumbbell) geometries produce an uniaxial strain, where $\lambda_x = \frac{1}{\sqrt{\lambda_y}} = \frac{1}{\sqrt{\lambda_z}}$. This strain state is commonly found in crack nucleation test pieces without a pre-formed crack. This state also has an additional factor in its energy release rate formulation:

$$T_e = 2k_g Wc \quad (2.12)$$

where c is crack length, W is the strain energy density, and k_g is a function of strain and arises due to the change in aspect ratio of cracks when stretched. It can be derived analytically, though an experimental fit is generally used, which has the following

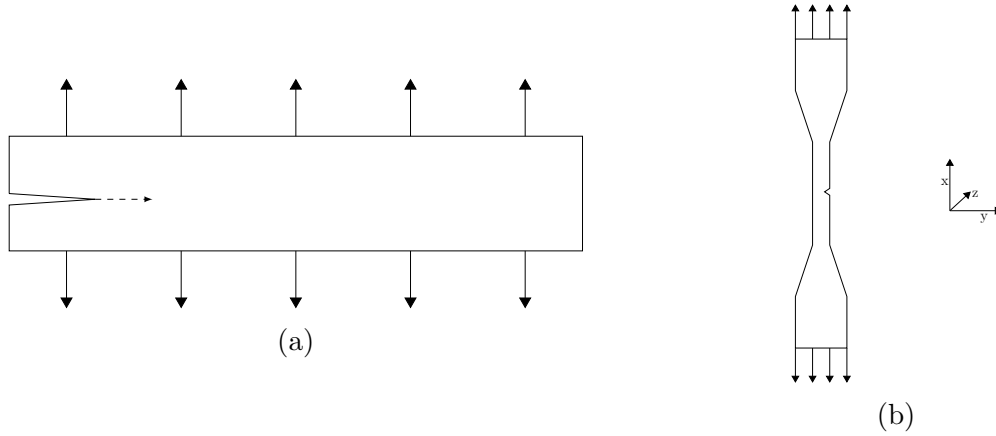


Figure 2.7: Tensile testing samples: (a) planar tension, pre-cracked specimen schematic, and (b) is a uniaxial tension specimen schematic with side crack. The principal strain is in the x-direction for both samples.

dependence on strain, ϵ (Mars and Fatemi, 2002):

$$k_g = \frac{2.95 - 0.08\epsilon}{(1 + \epsilon)^{1/2}} \quad (2.13)$$

Alternatively, trouser, angle or split crack test pieces can be used, though they also have a tearing energy dependent on crack length and strain (Mars and Fatemi, 2002).

2.1.7 Lifetime parameter

Equations (2.10), (2.12), and (2.13), can be combined and integrated to give the number of cycles required to grow a crack from an initial flaw, to the length required for failure during uniaxial cyclic strain:

$$N_f = \frac{1}{F-1} \frac{1}{B(2k_g W)^F} \left[\frac{1}{a_0^{F-1}} - \frac{1}{a_f^{F-1}} \right] \quad (2.14)$$

where k_g is the parameter dependent on strain geometry, W is the strain energy density, a_0 is the initial flaw size, and a_f is the critical flaw size for failure. In general, $a_f \gg a_0$, and so Equation (2.14) can be simplified to:

$$N_f = \frac{1}{F-1} \frac{1}{B(2k_g W)^F} \frac{1}{a_0^{F-1}} \quad (2.15)$$

2.1.8 Other factors

Although once T_e is calculated it is independent of sample geometry, there are several other factors that can play a part in fatigue life. Radir and Thomas (1981) measured crack growth rates for samples with thicknesses between 0.1 and 10 mm. For samples either below 0.5 mm or above 10 mm, crack growth rates were independent of thickness and the crack surface was smooth. Between these bounds, rough or stick-slip crack growth occurred and the rate changed by more than one order of magnitude. They attributed this dependence to the crack tip roughness being of the same order of magnitude as the sample thickness. I tested samples with a thickness of ≤ 0.5 mm, similar to the expected heart valve leaflet thickness, which is in this regime.

Although it is true that the crack growth rate during cyclic loading is a function of the maximum tearing energy, more factors must also be considered. Crack growth rate is also a function of the strain ratio; R is defined as the ratio of the minimum strain in a cycle to the maximum,

$$R = \frac{\epsilon_{min}}{\epsilon_{max}} \quad (2.16)$$

where ϵ is engineering strain. For purely tensile testing R is between 0 and 1. For a sample that is fully relaxed when unloaded, $R = 0$. If $R < 0$ then the sample undergoes compression as well as tension during a cycle. The value of R is particularly important for rubbers (such as natural rubber or polyisoprene) which undergo stress crystallisation. In these materials, for a given T_e , the fatigue life during cyclic straining will be increased when $R > 0$. Heart valve leaflets become fully relaxed and not compressed at their minimum strain so testing should be performed at $R = 0$.

Anisotropy

I propose to take advantage of anisotropy to reduce the strain energy density in the leaflets of the valve. Anisotropic effects were not considered in the theory outlined in Section 2.1.6. To apply the isotropic methods to anisotropic materials requires that the nature of the stress intensification around the crack tip be the same. Sih et al. (1965) demonstrated in both the isotropic and anisotropic cases that stress intensity field which is found around the crack tip diminishes as $\frac{1}{\sqrt{r}}$, where r is the distance from the crack tip. Hence, the assumption that crack growth occurs as a function of T_e is valid (Equations (2.8) and (2.9)) for the anisotropic case.

The phases of failure

I will now explain the risks associated with extrapolating fatigue models. In a polycrystalline σ -N curve shown in Figure 2.8, there are 3 regimes of failure corresponding to low cycle fatigue, a transition regime, and high cycle fatigue. For crack growth rates derived from macro crack growth curves, as described in Section 2.1.6, it is normally possible to fit a power law model to the majority of crack growth rates. In the study by Lake and Thomas (1967) on crack growth rates in rubber, they noticed that the power law relationship between crack growth rate and energy release rate did not hold at low values. They identified four regimes of differing behaviour, as shown in Figure 2.8. Below the threshold tearing energy, T_0 , the crack growth rate was independent of T_e . Immediately above T_0 crack growth had a linear dependence on T_e . In regime 3, at a higher values of T_e , crack growth rate had a power law dependency. Finally, the crack growth rate approached the velocity of elastic waves in rubber, resulting in catastrophic tearing in regime 4. To safely predict lifetime using Equation (2.14), testing and device operation must occur in regimes 2 or 3.

Intrinsic Flaws

It is generally assumed that the failure of a material is dominated by the growth of cracks from some initial size, to a critical size. Even if a sample appears to be macroscopically perfect, with no sharp cracks or flaws there will be intrinsic internal flaws. These could originate from any of the following causes: filler particles, voids in the polymer, imperfect mixing or dispersion of polymer ingredients, imperfections in the mould tool surface, mould lubricants, impurities gained during the moulding process or stress concentrations during cooling (Mars and Fatemi, 2002). It is conventional when predicting elastomer lifetimes to use an effective initial flaw size of 0.02 to 0.06 mm (Lake and Thomas, 1967; Zarrin-Ghalami and Fatemi, 2012).

In the fracture mechanic analyses for lifetime predictions that I have used here, I have assumed continuity and homogeneity of the material. If initial flaws are too small, such as those found in metals, then this may not be true. Fortunately, in polymeric materials the initial flaws are several orders of magnitude greater than polymer chain sizes and filler particles. The domain spacing of cylindrical PS domains in a typical BCP is approximately 30 nm (Stasiak et al., 2010). As flaws are generally much larger, on the order of 40 μm (Choi and Roland, 1996), continuity can be assumed.

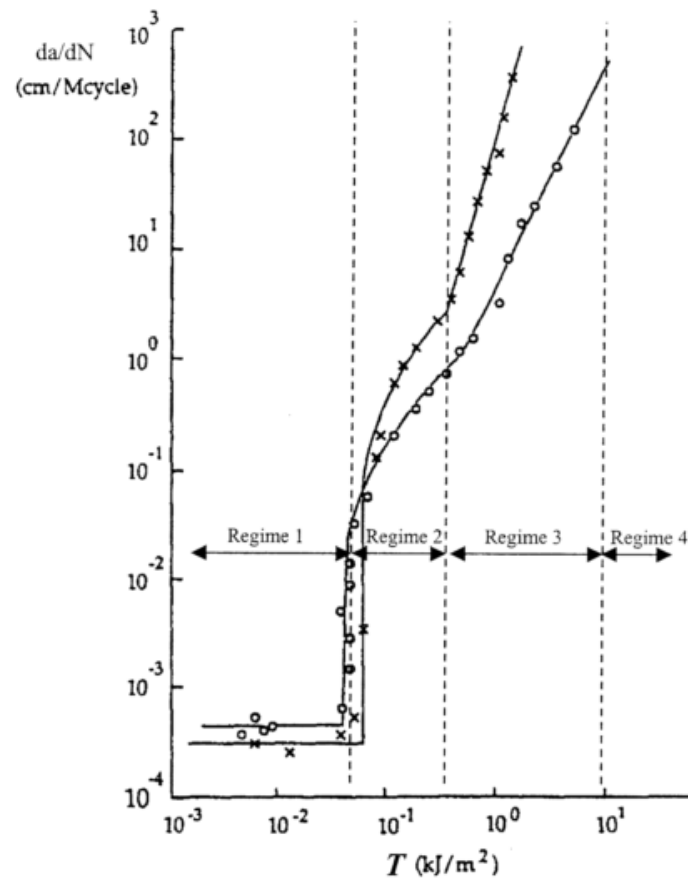


Figure 2.8: Crack growth rate as a function of tearing energy for unfilled natural rubber (NR \circ) and styrene-butadiene rubber (SBR \times). Four regimes are shown: 1 for $T_e < T_0$ in which $\frac{dc}{dN}$ is a constant finite value attributed to environmental conditions (ozone attack); 2 above T_0 where $\frac{dc}{dN}$ is linear; 3 where $\frac{dc}{dN}$ has a power law dependency; and 4 where rapid tearing occurred. From Mars and Fatemi (2002).

2.2 Materials and methods

The shortlist of materials and their specific details is shown in Table 2.2.

PU2363 is a thermoplastic polyurethane based upon methylene diphenyl diisocyanate (Zdrahala and Zdrahala, 1999), which was used as a reference material. Results regarding biostability and mechanical properties of PU2363 are reported in the literature, though when used in pacemaker leads, the combination of adverse chemical conditions and stresses caused failure (known as environmental stress cracking) (Pinchuk et al., 2008; Simmons et al., 2004; Thomas and Jayabalan, 2009). Polyurethanes are the “most optimal” material as shown on the Ashby map in Figure 2.5, and demonstrated by their frequent appearance in polymeric prosthetic heart valves. Sheets of PU2363 were fabricated by solvent casting. The pellets were dissolved in toluene at 10w/v%, then dried on

Table 2.2: Block copolymers and reference polyurethane used in selection procedure.

Polymer	Styrene content (mol%)	Code	Form	Supplier
PS- <i>b</i> -polyisoprene- <i>b</i> -PS	18	D1163P	Pellet	Kraton, Belgium
PS- <i>b</i> -polyisoprene- <i>b</i> -PS	30	D1164P	Pellet	Kraton, Belgium
PS- <i>b</i> -polyisoprene-polybutadiene- <i>b</i> -PS	19	D1170B	Pellet	Kraton, Belgium
PS- <i>b</i> -polyethylene-polypropylene- <i>b</i> -PS	22	G1730M	Pellet	Kraton, Belgium
PS- <i>b</i> -polyisobutylene- <i>b</i> -PS	30	n/a	Pellet	Innovia LLC, FL, USA
PS- <i>b</i> -polyethylene-polybutylene- <i>b</i> -PS	20	G1642H	Fluffy crumb	Kraton, Belgium
PS- <i>b</i> -polyethylene-polybutylene- <i>b</i> -PS	30	G1650E	Fluffy crumb	Kraton, Belgium
Polytetramethylene glycol based PU	n/a	PU2363-80AE	Pellet	Velox, UK

a Teflon coated sheet, in a fume cupboard for a minimum of 24 hours.

Pellets and fluffy crumb BCPs were compacted between aluminium plates at 160 °C using a heated press. Mechanically anisotropic samples with oriented PS domains were fabricated using the method previously described by Stasiak et al. (2009). Silicone mould release was applied before each moulding. A thick strip of polymer is placed in the centre of the aluminium channel mould, as shown in Figure 2.9, and heated to 160°C. The plate is slowly compressed within the channel resulting in planar growth of the sample. The mould is cooled with water for about 2 minutes, to room temperature, before the sample is removed. The sample thickness was controlled using shims placed in the mould. Samples with overall dimensions of $170 \times 170 \times 0.3$ mm were produced. The extension ratio during moulding was ≥ 10 . Small-angle X-ray scattering (further information in Section 6.2.1) was used to confirm that the PS domains were oriented anisotropically.

2.2.1 Biostability

Compression moulded polymer samples, six of each type, were cut into strips which were first dried and weighed 3 times before being placed in polypropylene Fisher centrifuge

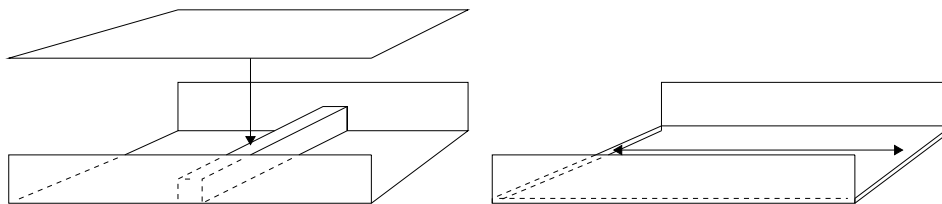


Figure 2.9: Schematic of the moulding process for fabricating oriented samples. A long block of polymer is placed in the centre of the mould. The mould is compressed, squeezing the polymer into a flat sheet. The sides of the mould constrain the growth of the sheet to one direction, leading to uniaxial orientation of the PS cylinders in the sample.

tubes. Distilled water or hydrogen peroxide solution (30%) was added to each tube so each sample was immersed according to ISO 10993:13. The tubes were stored for 3 months at 70 °C. The samples were dried and weighed after the degradation test.

Six samples of each material were also stored at room temperature in oxidising and acidic conditions. These samples were analysed using FTIR with Attenuated Total Reflectance (ATR) using a KBr crystal.

2.2.2 Tensile properties

The uniaxial tensile properties of the polymer samples were measured using tensile dog-bone samples which were cut using a sharp edged stamp. The planar tensile properties of the polymer were measured using a sample with a high aspect ratio. These samples were cut using a sharp scalpel or scissors. The dimensions of both sample types are illustrated in Figure 2.10. Samples were cut such that they are stretched either parallel (L) or perpendicular (R) to the PS domain orientation. Testing was performed using a

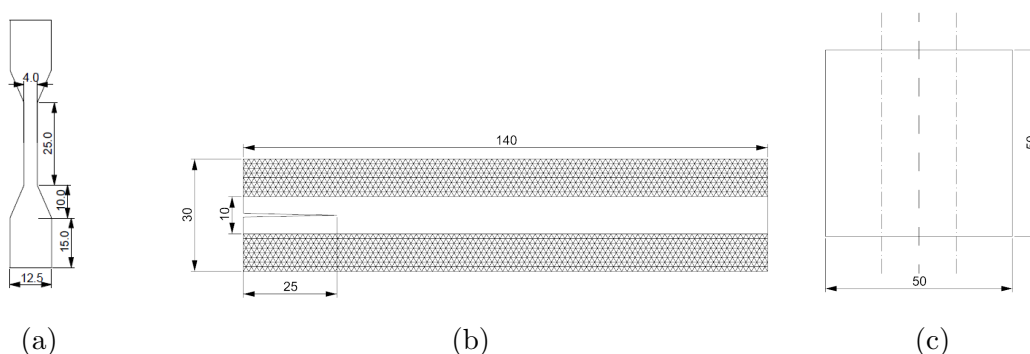


Figure 2.10: Dimensions of samples used for mechanical testing, all with a thickness of 0.3 mm). 2.10a is the tensile bar for uniaxial testing, 2.10b is planar tension and crack growth sample (shown with initial crack), and 2.10c is the flexural sample with the deflecting and support beams indicated by — and --- respectively.

Texture Analyser (TA) (Stable Microsystems, Surrey, UK) using a 30 kg load cell. To test the tensile bar samples, commercially available clamps with rubber coated jaws were used. For the planar tensile samples a set of aluminium clamps with a width of 180 mm were fabricated. Samples were secured using 10 cap head bolts which provided an even gripping force along the sample. The faces of the jaws were coated with neoprene rubber. The TA collected force and displacement data at 200 Hz which were subsequently analysed using MATLAB.

Although it would be preferable to perform this mechanical testing in combination with the chemical environment, this would require a significantly more complex sample mount and could lead to a reduction in sensitivity (Puskas et al., 2009a). Instead, the effects of mechanical and chemical forces were tested separately during selection.

Samples underwent a sinusoidal displacement input with a strain ratio of $R = 0$ (fully relaxed minimum strain). During tensile testing the maximum displacement was incrementally increased, with 120 cycles performed at each strain level. The TA system is displacement controlled, and so strain was determined during a MATLAB post-processing routine.

Strain energy density, W , at strain ϵ , for a fully relaxing stable cycle was calculated using:

$$W = \int_0^\epsilon \sigma d\epsilon \quad (2.17)$$

2.2.3 Flexural properties

Unidirectionally oriented, compression moulded samples (dimensions shown in Figure 2.10c) were tested according to ASTM D790, with bending both perpendicular (R) and parallel (L) to the PS cylindrical domain direction (ASTM International, 2002). Support bars were spaced by 20 mm, the crosshead speed was 5 mm s^{-1} and reached a maximum deflection of 5 mm. 20 cycles were performed on each sample to reduce transient stress relaxation. Flexural strain in the 3 point bend scenario is calculated as follows:

$$\epsilon_{flex} = \frac{6Dt}{L^2} \quad (2.18)$$

where ϵ_{flex} is the strain at the outer surface, D is the central deflection, t is the sample thickness, and L is the support span.

Flexural stress in the outermost fibres for samples with a rectangular cross-section is

calculated using:

$$\sigma_{flex} = \frac{3F_{xH}L}{2b_ft^2} \left[1 + 6 \left(\frac{D}{L} \right)^2 - 4 \frac{tD}{L^2} \right] \quad (2.19)$$

where σ_{flex} is the stress at the outer surface, F_{xH} is the crosshead deflector load, b_f is the sample width, L , t and D are the sample dimensions as before. The flexural modulus is calculated as a ratio of stress to strain:

$$E_{flex} = \frac{\sigma_{flex}}{\epsilon_{flex}} \quad (2.20)$$

For an anisotropic material, the flexural modulus is dependent on the direction of flexure relative to the fibre direction. Parallel modulus, $E_{flex\parallel}$, refers to the stiffness when the contours of constant displacement are parallel to the stiff cylinders, and $E_{flex\perp}$ refers to the perpendicular modulus.

2.2.4 Crack growth

Planar samples were cut from the oriented sheets and a 25 mm crack was created in the sample (Figure 2.10b) using a surgical scalpel. The samples were sinusoidally strained with $R = 0$. The samples were conditioned using 300 to 500 cycles at 110% of the test strain to establish a natural fracture surface and crack tip, and reduce transient stress relaxation. At high crack growth rates, 2000 cycles were performed, at low rate 10,000. Crack length was measured by recording images with a camera every 100 s with subsequent manual analysis in MATLAB. The resolution of the camera was sufficient to allow the crack length to be measured to a precision of 0.05 mm.

2.3 Results

2.3.1 Manufacturing

All the tested polymers were thermoplastic and flowed during compression moulding.

Several important observations were made during polymer processing, I observed that many of the materials displayed significant shrinkage when cooled. This occurred regardless of the rate at which the materials were cooled, though was greatest when cooling was fastest. The shrinkage was greatest for SIBS and led to the shrink-induced cracking as shown in Figure 2.11. This could be mitigated by lining the moulds with non-stick

parchment, although this left the surface with a mottled texture and would be infeasible in a complex injection moulding tool.



Figure 2.11: Sample of SIBS30 (width=17 cm) after compression moulding. The sample was cooled while in the aluminium mould, resulting in rapid shrinkage. The polymer adhered to the mould, and so holes were formed as the sample relaxed.

The difficulty in moulding this polymer is supported by reports from the Stony Brook group, who also compression moulded SIBS materials. They reported oxidation of SIBS during moulding, which may have occurred from their use of high temperatures.

2.3.2 Biostability

I used the relative stability of the polymers in aqueous, acidic, and oxidising conditions as a criteria for selection. At room temperature, I did not record any mass change in the polymers, though FTIR indicated that oxidation may have occurred due to the fall in the C=C peak at 1660 cm^{-1} (Figure 2.12), for the unsaturated polymers (SIS and SI/BS).

Figure 2.13 shows the proportion of mass lost from each sample when incubated at 70°C in air, hydrolysing (H_2O), and oxidising (H_2O_2) conditions. There was a loss in mass over 60 days at temperature regardless of whether the materials were stored in air, hydrolysing, or oxidising conditions. There is a large spread in some results as sample containment was occasionally lost. Most notably, severe ($> 2\%$) mass loss was observed for the unsaturated BCPs, containing an isoprene (SIS18 and SIS30) or butadiene (SI/BS19) soft block, causing the samples to lose their structural integrity. I eliminated SIS18, SIS30 and SI/BS19 from the selection procedure. The saturated BCPs (SE/BS20, SE/BS30, SIBS30 and SEPS22) become the preferred materials for use in a prosthetic heart valve.

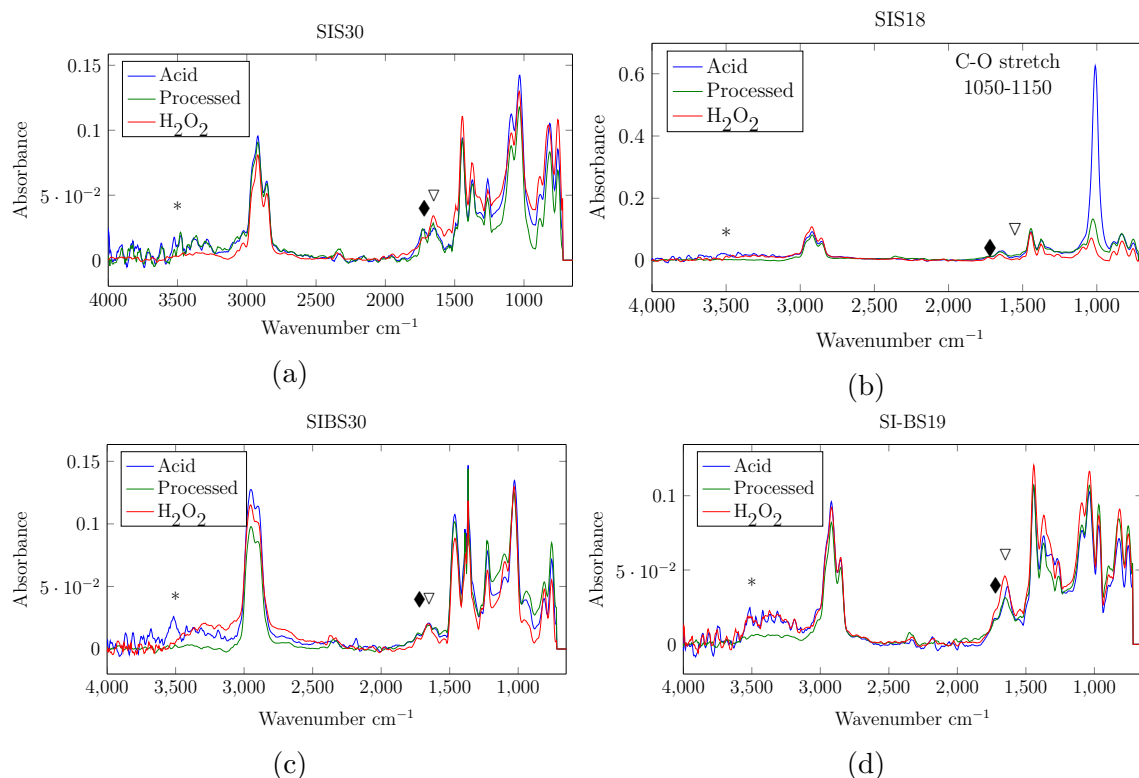


Figure 2.12: (a) to (d) FTIR spectra of polymer samples before (green) and after degradation in oxidising and acidic conditions. *, ∇ , and \blacklozenge indicate the regions of absorbance due to the stretching of O–H, C=C, or C=O bonds which occur at 3700 to 3200, 1680 to 1620, and 1760 to 1665 cm^{-1} respectively. (a) shows SIS30, (b) shows SIS18, (c) shows SIBS30, and (d) shows SI-BS19, refer to Table 2.2 for material details.

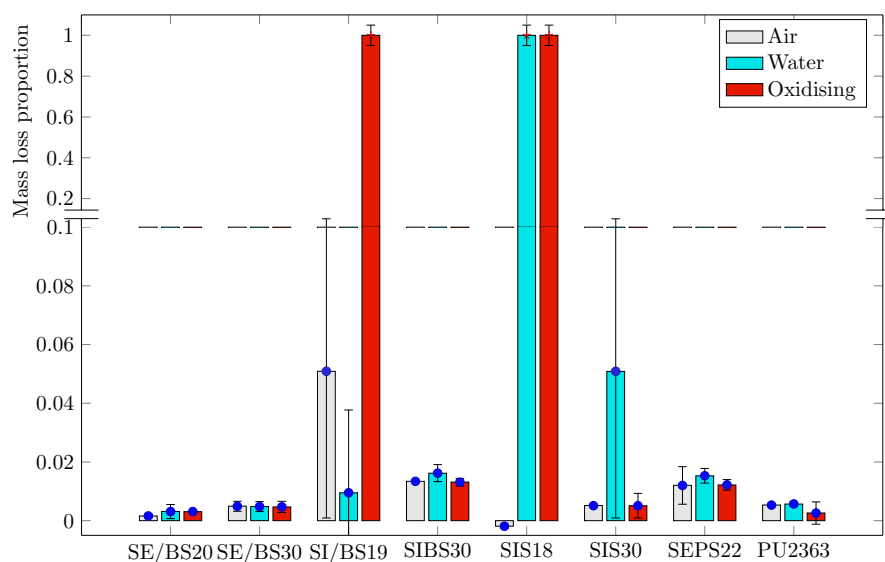


Figure 2.13: Proportion of mass lost during accelerated degradation test for eight samples incubated at 70 °C in air, oxidising, and acidic conditions. Error bars indicate 1 standard deviation from the mean. See Table 2.2 for details of the materials.

2.3.3 Tensile properties

I eliminated SIS and SIBS materials from the selection procedure (on the basis of chemical stability and process-ability), and so the shortlist comprises SEBS29, SEBS20 and SEPS22. I performed tensile tests on the planar and tensile bar geometries for each polymer. A quadratic fit was plotted to the stress-strain data from 0 to 50% strain, as shown in Figures 2.14a and 2.14b. All the polymers have a lower modulus at higher strain, and are thus strain softening. The polyurethane (PU2363) is the least strain softening. This may indicate that the PS cylinders in the styrenic BCPs can be broken when strained.

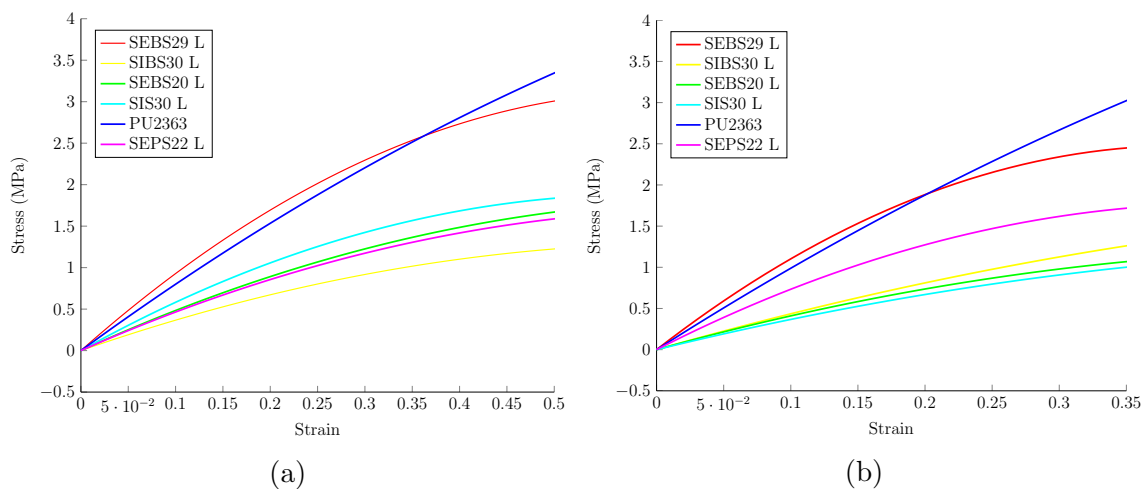


Figure 2.14: Tensile stress strain properties of the shortlisted polymers, from an extending stroke during a sinusoidal oscillation, plotted as a mean quadratic fit from all samples ($n \geq 3$ for each polymer). Errors are indicated by the modulus measurements shown in Table 2.3. (a) are the planar samples and (b) are the uniaxial samples.

For crack propagation and lifetime analyses, the strain energy density relation is more appropriate (Section 2.1.6). These data were collected by performing sinusoidal oscillations at increasing strains, with 30 oscillations at increasing maximum strains. Strain energy density up to the maximum strain was calculated for 5 cycles at each strain level. Up to 10 strain levels were tested, between 0 and 50% strain. A quadratic curve was a good fit to these data, which are shown in Figure 2.15.

The use of a stepwise increasing strain - as opposed to the integration of a single stress-strain curve up to 50% strain - is appropriate for this scenario. The candidate polymers are viscoelastic, and so are sensitive to strain rate and the maximum strain that is reached during an oscillation. The stepwise method avoids the strain response at low strains being masked by artefacts from high strains.

For ease of comparison, the moduli of the polymers is summarised in Table 2.3. The

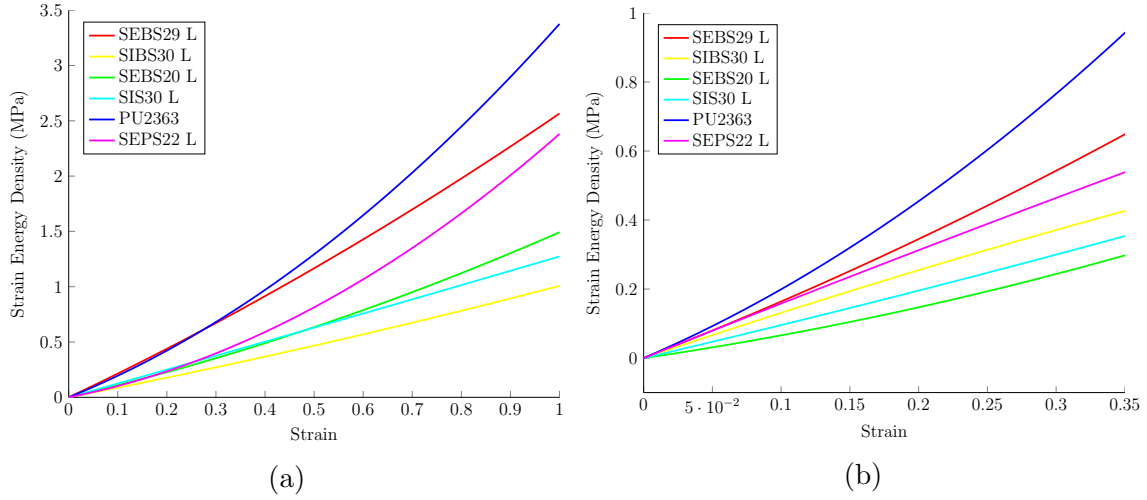


Figure 2.15: Tensile strain energy density properties of the candidate polymers for planar (a) and uniaxial (b) geometries. At least 3 samples were used for each geometry. Each curve is a quadratic fit to the maximum strain energy density from 30 sinusoidal oscillations at stepwise increasing maximum strains. Errors are indicated by the results shown in Table 2.3.

SEBS material was tested with a 20 and 29% PS fraction and, as expected, the higher PS fraction results in a higher modulus.

Table 2.3: Young's moduli (E), secant moduli at 20% strain (E_{sec20}), and strain energy density at 20% strain (W_{20}) (all MPa) for planar ($n \geq 3$) and dumbbell ($n \geq 4$) samples. Candidate BCP materials were measured parallel (L) to the PS cylinder orientation and the reference polyurethane is isotropic. Listed errors are the maximum recorded deviation from the mean value.

Material	Planar						Dumbbell					
	E	\pm	E_{sec20}	\pm	W_{20}	\pm	E	\pm	E_{sec20}	\pm	W_{20}	\pm
SEBS20 L	5.2	1.3	4.8	0.9	0.23	0.10	4.5	0.7	4.2	0.5	0.15	0.03
SEBS29 L	10.1	3.0	9.5	1.9	0.44	0.14	12.6	2.9	10.3	1.9	0.34	0.05
SIBS30 L	4.0	0.5	4.3	0.5	0.18	0.08	4.7	0.3	5.2	0.3	0.25	0.07
SIS30 L	6.4	1.2	5.9	1.1	0.25	0.18	4.0	1.5	4.4	1.3	0.20	0.10
PU2363	8.3	1.1	8.8	1.4	0.42	0.29	10.4	1.1	10.9	0.6	0.45	0.09
SEPS22 L	5.0	0.6	4.1	0.7	0.23	0.05	8.3	0.4	7.6	0.2	0.31	0.04

2.3.4 Flexural properties

I collected data on the flexural properties of the materials when PS domains are oriented both parallel and perpendicular to the bending direction (Table 2.4). The flexural modu-

lus gives an indication of the maximum force and energy required to reverse the curvature of the leaflet.

The flexural properties of the material are a factor (along with the leaflet thickness) in the energy required to open the heart valve leaflets. During bending, a variety of strains are experienced throughout the thickness of the material. As the samples are strained beyond the linear region of stress-strain, it is more appropriate to compare flexural secant moduli which amalgamate the stress response for a material in a variety of strain states. During systole the native valve experiences flexural strains up to 15% (Balachandran et al., 2011).

Using the flexural stiffness data in Table 2.4, the anisotropy ratios, $E_{flex\perp}/E_{flex\parallel}$, were calculated. The anisotropy ratios of the materials vary between 3.15 (SIBS30 and SEBS20) and 9 (SEBS29). In the case of SEBS the ratio increased from 3.15 to 9 as PS content changed from 20% to 29%. For the SIBS and SEPS materials, the manufacturer supplies the materials with differing PS content, however they do not all exhibit a cylindrical (anisotropic) morphology.

2.3.5 Fatigue and performance indices

I recorded crack length against number of cycles. In general, samples showed a consistent crack growth rate with respect to the number of cycles. I halted experiments when at least eight crack lengths could be recorded, or the width to length ratio of the sample became too low. As an example of the data, the crack tip position for SEBS20 under 50% sinusoidal strain is plotted in Figure 2.16.

I frequently observed nucleation of cracks away from the artificial crack tip. These spontaneous cracks were generally adjacent to the clamps. In many cases the cracks that formed were relatively stable and the test crack continued to grow at an unchanged rate. Interestingly, in the case of SIS30 I observed the bridging of the crack tip, a phenomenon that may arise from the strain crystallisation that is observed in natural rubber (polyisoprene) (Zarrin-Ghalami and Fatemi, 2012). Sample to sample variation may have arisen due to the poor control of cooling rate. The plates of the mould were cooled using a slow stream of running water from a tap. An improvement for future work should utilise embedded oil cooling channels, giving better control of cooling rate.

Figure 2.17 shows the crack growth data and tearing energy, with a power-law fit. The coefficient and exponent of the power law models can then be used to determine the fatigue life for the polymer as a function of strain energy density using Equation (2.14).

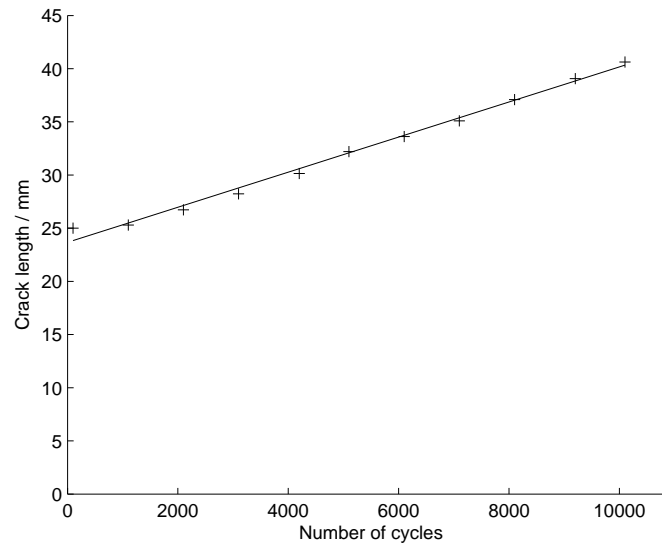


Figure 2.16: Crack tip position for SEBS20 with PS cylinders oriented parallel to the stretching direction with $\varepsilon_{max}=0.21$. Linear fit is $c = 0.00165N + 23.7$.

I determined the maximum allowable strain energy density required to reach 10^7 cycles.

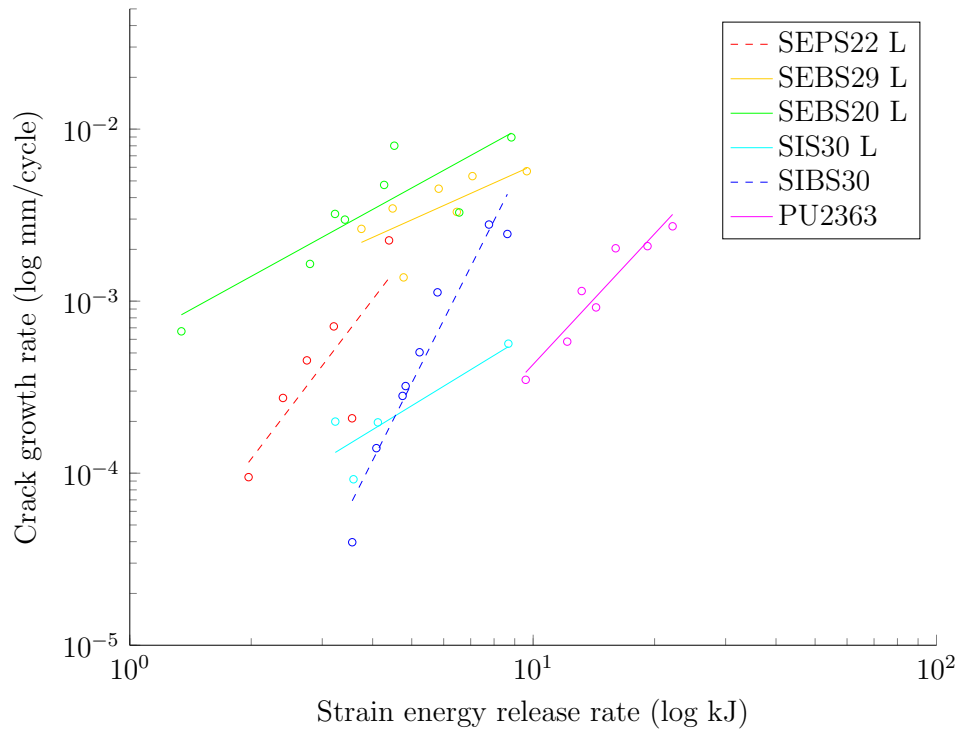


Figure 2.17: Crack growth rate against strain energy density for the shortlisted BCPs with PS cylinders oriented in the direction of strain. A power law model is fitted to each set of points, and the coefficients are reported in Table 2.4.

The macroscopic crack growth experiments allow prediction of lifetime based upon Equa-

tion (2.15). A maximum strain energy density, W_{max} ; and stress, σ_{max} , can be determined based upon a minimum fatigue life of 1×10^7 cycles, corresponding to a valve lifetime of about 100 days at 1 Hz. This lifespan lies within the power-law region (region 3 in Figure 2.8) and could also be compared to industry fatigue data, for example the data which can be obtained from Granta Design's CES Material Selection software, and serves as an absolute minimum for a material to be used in the heart valve.

I combined the leaflet opening (Equation (2.2)) and fatigue (Equation (2.4)) constraints to form the performance index. Eliminating the constants yielded a material performance index, I_P , which is minimised for optimal materials:

$$\min(I_P) \propto \left(\frac{E_{flex}}{\sigma_f^3} \right) \quad (2.21)$$

A crucial tenet of this thesis is that leaflet anisotropy should lead to improved prosthetic heart valves. There are several ways in which anisotropy may improve the valve; first, in Section 1.10.1 the results of Zaffora (2011) were cited. He optimised anisotropy using FE modelling, which led to a reduction in the maximum leaflet stress during diastole. It may be the case that the material's durability is also anisotropic, and so a greater strain energy density and stress can be accommodated in the fibre direction. These advantages may allow the denominator of Equation (2.21) to be increased, reducing I_P , to I_{\parallel} .

Anisotropy may bring further reductions to I_P by reducing the numerator of Equation (2.21). The stresses generated in a leaflet during opening are dominated by flexure. If the stiff fibres are oriented parallel to the contours/flexure direction/fold line, a lower force is required to bend the material than if they are oriented perpendicular. If leaflet opening is limited by bending in the belly of the leaflet (as will be discussed in Chapter 5), then horizontally oriented cylinders in the belly allow the leaflet to open more easily, faster and further.

Prosthetic heart valve leaflets have a Gaussian curvature greater than zero (i.e. they do not have a perfectly cylindrical form). They can be defined by two radii at each point with the tighter of these radii requiring more energy to reverse. By orienting stiff cylinders perpendicular to the tighter radius, the energy required for reversal can be reduced. For a hemispherical surface, where both radii of curvature are equal, anisotropy causes one direction to reverse before the other, along a lower energy path (Lu and Xu, 2003). Practically, this means that anisotropy in the leaflet may allow the curvature to reverse in one direction before the other, requiring less force.

Optimal anisotropy can be included in the material performance index (previously Equa-

tion 2.21), so for the best case material performance index, I_{\parallel} , as:

$$\min(I_{\parallel}) \propto \left(\frac{E_{flex\parallel}}{\sigma_{f\parallel}^3} \right) \quad (2.22)$$

where $E_{flex\parallel}$ is the flexural modulus when bending contours are parallel to the fibre orientation, and $\sigma_{f\parallel}$ is the fatigue stress when the material is stretched parallel to the fibre direction. If the above assumptions regarding leaflet opening are not true, then in the worst case scenario, where bends are perpendicular to the oriented cylinders. An alternative performance index, I_{\perp} can be expressed using $E_{flex\perp}$ in place of $E_{flex\parallel}$ in Equation (2.22).

I analysed the materials using both performance indices, and these results, together with the constituent predicted fatigue stress and flexural moduli are shown in Table 2.4. The strain energy density and crack growth curves (as shown in Figure 2.17) are characterised by power-law model exponents, F , and coefficients, B . As W_{max} is obtained by extrapolating the curves, it is dominated by the value of F .

Table 2.4: Summary of durability and flexural stiffness properties which yield the performance indices for the candidate materials. F and B correspond to the exponent and coefficient in the crack growth model (Equation 2.10). Fatigue lives are estimated using the following parameters (from Equation (2.14)) $N_f = 10^7$, $c_0 = 0.02$ mm, $c_f = 0.3$ mm and $k = 1.2$. W_{max} and σ_{max} are recorded in MPa. I_{\parallel} assumes that the critical bending direction during opening is parallel to the cylinder orientation - and so opening is easier. I_{\perp} assumes perpendicular.

Material	Crack growth		10 ⁷ cycle fatigue limits		E_{flex} (GPa)		Flexural PI	
	B	F	W_{max}	σ_{max}	\perp	\parallel	I_{\parallel}	I_{\perp}
SEBS20 L	5.7×10^{-4}	1.29	0.002	0.09	1.3	4.1	1559.7	4873.8
SEBS29 L	5.5×10^{-4}	1.05	0.0003	0.18	1.7	15.3	312.4	2792.1
SIBS30 L	1.9×10^{-7}	4.63	5.89	1.13	1.1	3.5	0.8	2.4
SIS30 L	2.5×10^{-5}	1.43	0.041	0.22	0.4	2.3	36.6	230.0
PU2363	1.3×10^{-6}	2.52	1.35	0.84	36.1	36.1	61.1	61.1
SEPS22 L	8.3×10^{-6}	3.83	1.81	0.45	0.8	4.1	8.9	43.9

I compared materials using the performance indices I_{\perp} and I_{\parallel} . Having eliminated SIS and SIBS materials from the selection procedure (on the basis of chemical stability and process-ability) the shortlist comprises SEBS29, SEBS20 and SEPS22. SEPS22 has the lowest I_{\perp} and I_{\parallel} , suggesting that it is the best material to select. SEPS22 is also predicted to perform better than PU2363, the reference polyurethane (Thomas and Jayabalan,

2009). To put the differences in performance index in a physical perspective, if SEPS22 and PU2363 valves were designed with optimal thicknesses such that they can reach an equal predicted lifetime, the PU2363 valve would require an opening force at least 50% greater than the SEPS22 valve (in the most “poorly” oriented scenario).

2.4 Discussion

BCPs can be engineered to have anisotropic properties amenable to producing a bioinspired polymeric heart valve. It is relatively easy to envisage how stiff PS cylinders may appear like a short-fibre reinforced polymer. The proposal to embed fibres in a prosthetic valve is not novel. Cacciola et al. (2000) embedded high performance polyethylene fibres in an EPDM matrix (using a dip coating process). The valve was tested *in vitro* but suffered from excess regurgitation. Durability testing of these prototype valves was not reported in the literature. An alternative fibrous polymeric prosthetic heart valves was proposed and tested by Gallocher et al. (2006) who observed catastrophic *in vivo* fatigue failure of SIBS coated polyester leaflets, which was attributed to fibre-bulk dehiscence. The need to consider all means of degradation and durability from the outset of design is imperative. The novelty of using BCPs to provide fibre reinforcement comes from their self-assembly during processing and the intimate chemical linkage between the matrix and fibres.

There is reason to be optimistic that BCP fibres are less susceptible to delamination than conventional fibres. BCP fibres are fundamentally different from short-fibre filled composite polymer as continuous polymeric chains pass between the fibres and the bulk, covalently bonding the fibres to the bulk and reducing the chance of delamination.

In this chapter my aim was to select a suitable polymer. The first criterion that materials must pass was adequate biostability. No absolute biostability test exists, and so a standard, relative, accelerated testing method was employed. Stasiak et al. (2011) proposed that unsaturated polymers - which are generally disregarded due to their vulnerable C=C bonds - might be suitable if they are used at body temperatures in the absence of UV radiation. Although they may be stable under physiological conditions, the accelerated testing definitively demonstrated that the unsaturated materials are less stable than saturated ones. Thus, unless the fatigue or biocompatibility performance of the unsaturated polymers is significantly superior, they should not be considered as potential materials for a prosthetic heart valve.

During compression moulding, I was surprised to observe serious crack-inducing shrinkage

of the polymers, particularly of SIBS30. Temperature dependent shrinkage generally results in $\leq 1\%$ polymer shrinkage (Brydson, 1995). Shrinkage is of most relevance in the polymer rolling industry, where mill rollers are used to produce sheets of polymer. Upon exiting the rollers the sheets shrink in width and length, while growing in thickness, giving rise to the term “mill shrinkage”. Four processing regions have been identified in the rolling industry; in the first three regions shrinkage leads to failure (splitting, crumbling, roughening), and only in the fourth region can a part be properly formed (Tokita and White, 1966). Shrinkage after moulding can be attributed to the relaxation of the strained polymer chains over various time scales. The viscoelastic features of polymers are ever-present. At higher temperatures they continue to exhibit solid-like yielding and tearing, which can occur as a polymer shrinks (White and Tokita, 1968).

To remedy shrinkage one can reduce the strain and strain rate, or increase the temperature. Variation in the polymer molecular weight distribution alters shrinkage, but does not eliminate it (White and Tokita, 1968). In the plate compression moulding system, I was not able to eliminate shrink-induced cracking despite reducing the strain rate to 0.02 s^{-1} and raising the temperature to 200°C - above which oxidation occurred. However I did find that it was possible to alleviate the cracking associated with shrinkage by lining the plates with baking parchment, relieving the pressure from the plates after moulding, and cooling slowly. The baking parchment reduced the “pinning” of the polymer which leads to tears during shrinkage. Pressure relief allowed the polymer to contract and relieve internal stress by increasing its thickness. The use of silicone grease to reduce pinning is plausible, but leaves residues which are undesirable for fatigue and biocompatibility considerations. As the above techniques would not be suitable for use in a prosthetic heart valve tool, I eliminated SIBS30 from the selection process.

The polymeric materials I tested are comparable in stiffness to loaded, native aortic valve tissue. Thubrikar et al. (1980) measured the native leaflet modulus *in vivo*, in dogs using fluoroscopic markers in conjunction with pressure measurements. They reported the leaflets to have a modulus of 5.4 MPa during diastole, which is similar to the BCPs with a PS content of $\sim 20\%$. The biological tissues are of course non-linear in their stress-strain relationship, meaning that the first few % of strain occur when the tissue’s stiffness is 0.5 to 0.003 times lower than the stiffness when loaded (and strain reaches 10%) (Thubrikar et al., 1980). The polymeric materials that I tested do not possess such a useful property and thus this feature of the native tissues cannot be mimicked.

In the prediction of fatigue, I observed significant variations in the maximum strain energy density and stress that each material could withstand. SIBS30 was able to withstand the greatest stress, though it did suffer from spontaneous crack nucleation which might have

arisen from moulded-in stresses, poor orientation, large flaws, or contaminants during moulding. Pinchuk et al. (2008) also claimed that SIBS had a high fatigue life but suffered from creep. The durability of the elastomers containing polyisobutylene may be due to its stereoregularity which increases strain crystallisation (Gonzalez-Alvarez et al., 2004). SEPS22 was the next best material. The SEBS materials displayed the worst fatigue parameters. It is not advisable to directly compare these fatigue predictions with those values issued by ASM via the CES EduPack (Granta Design, Cambridge, UK) as they use $R = -1$, indicating compression and their values are estimates.

El Fray et al. (2006) also performed a fatigue study on SIBS30 using their stepwise increasing strain/stress test (SIST). The material was isotropic (due to uncontrolled compression moulding), and was compared to medical polyester, polyurethane and silicone materials. The SIST method was not able to provide a stress or strain limit for samples, making it hard to make quantitative comparisons. However, the authors did note that SIBS30 crept significantly, which could be attributed to the rearrangement of PS domains in their isotropic samples. The method I have utilised in this study required all materials to be pre-conditioned to remove the significant primary creep which occurs in the first 100 cycles.

Prediction of fatigue requires the extrapolation of crack growth parameters to low strain energy densities. The results of Lake and Thomas (1967) covered a vast range of crack growth rates, as is shown in Figure 2.8. I compared the crack growth rates recorded for BCPs in these experiments (Figure 2.17) with the results of Lake and Thomas (1967) (note the differing units for crack growth rate). The critical strain energy density for survival, W_{max} , can be converted to a tearing energy, T_e . The results I report were within the bounds of regime 3 which fit to the power-law model observed by Lake and Thomas (1967). Regime 2 may also be approximated by a continuous power law, though their experimental results start to deviate, suggesting that a linear model may become more appropriate. At T_0 there is a step decrease in crack growth rate, leading to a regime of no crack growth where the power law model would be inappropriate, in the absence of chemical factors (regime 1).

With reference to the results in Figure 2.17, the minimum permissible tearing energy to reach 10^7 cycles is $\sim 1 \times 10^{-1} \text{ kJ m}^{-2}$, which is greater than the lower limit of regime 2 reported by Lake and Thomas (1967), indicating that these results can be extrapolated to this number of cycles. Below $1 \times 10^{-1} \text{ kJ m}^{-2}$, crack growth rate will continue to decrease up to the threshold tearing energy T_0 at which point the crack growth rate will drop to zero.

While extrapolation may be safe in this range, the role that environmental factors in

fatigue, such as swelling, has not been accounted for (Cho et al., 2000). Furthermore, this method is unlikely to hold up during multiaxial loading scenarios as not all the strain energy is available for the growth of the crack (Mars and Fatemi, 2002).

The differing performance of materials may be attributed to differences in molecular architecture, processing and conditioning. Roche and Perier (2013) investigated the influence of elastomer formulation on cyclic crack growth. Their study was focussed on filled styrene-butadiene rubbers. They observed few differences between growth rates regardless of whether filler particles were evenly or poorly dispersed. The most significant differences that were observed in crack growth rates was between polymers which were aged for different times, suggesting that specific aspects of processing may in fact be dominant in the determination of elastomer lifetime. The growth of cracks in BCP may be significantly influenced by the molecular architecture (Lach et al., 2005; Staudinger et al., 2008). Using the Essential Work of Fracture (EWF) concept to compare various blends of symmetric and asymmetric styrene-*b*-(styrene-*random*-butadiene)-*b*-styrene triblock copolymers, Staudinger et al. (2008) reported that crack blunting was controlled by the dimensions of the soft block phase, whereas the rate of stable crack propagation was controlled by the styrene phases.

The rate of crack growth can be influenced by polymer hysteresis (Mars and Fatemi, 2002). Polymers dissipate energy when stretched, which is reflected by hysteresis in a stress-strain curve. Hysteresis reduces the rate at which cracks grow in elastomers (see Section 2.1.6). Polymers with more hysteresis have a lower power law exponent, F , in crack growth models of dc/dN vs. T_e (Equation (2.10)) (Lake and Thomas, 1967). Further work, outside the scope of this thesis, is needed to determine whether the observed differences in crack growth rate can be attributed to one of the above factors.

2.5 Conclusion

For the design of a prosthetic heart valve, the conflicting goals of improving durability while minimising resistance to blood flow must be reconciled. Myself, working in the Cambridge Group, have been inspired by the anisotropic structure of the native heart valve leaflets, and so have proposed a set of BCPs which can be processed to display anisotropic mechanical properties. I tested the stability of the candidate materials under accelerated degradation conditions (ISO 10993:13), which indicated that the unsaturated BCPs were more susceptible to degradation. The saturated BCPs met the *in vitro*, qualitative requirements of ISO 10993:13 for long term implantable materials.

I have proposed a novel method for selecting materials for polymer prosthetic heart valves based upon their mechanical properties. Principally, this relies upon making predictions of the materials' cyclic mechanical fatigue life. I combined the experience from the testing of rubbers for the automotive industry, with techniques from design engineering to produce a method allowing polymeric candidate materials to be compared. The method which I have developed is a general, quantitative, and robust means of rapidly assessing materials for use in a polymeric prosthetic heart valve, and could also be used for other applications requiring both flexibility and durability. Valve design is driven by the choice of material, but this method allows design and material to be de-coupled, making screening quicker and more efficient.

I collected the tensile and fatigue properties of the short-listed materials to generate a material performance index. SIBS30 had the most favourable index, although it was not possible to satisfactorily compression mould the material without lining the mould, which would not be possible in a complex geometry. SEPS22 had the second most favourable index among the saturated BCP, and could be moulded. Furthermore, well oriented, saturated BCP have a superior performance index to a reference polyurethane material.

SEPS22 was selected as the most suitable material for use in a flexible leaflet polymeric prosthetic heart valve, based upon chemical stability, process-ability, flexibility, and durability, and will thus be taken forward for a more detailed analysis in the rest of this thesis. Another criterion for suitability is biocompatibility, which I will consider in the next chapter.

Chapter 3

Biocompatibility

3.1 Introduction

This chapter discusses the issues concerned with the biocompatibility of materials that could be used in a polymeric prosthetic heart valve. Biocompatibility testing is performed on the BCP, SEPS22, which was selected in Chapter 2, and the other shortlisted BCPs.

Before the biocompatibility of a material is assessed, *biocompatibility* must be defined. Biocompatibility is the biological response when a foreign material, as part of an *in* or *ex vivo* device, comes into contact with a host. The response will develop over time, becoming either clinically acceptable and tolerable to the patient, making it *biocompatible*, or having some clinical effect making it intolerable (Williams, 2014).

Upon closer examination of this definition, several issues require clarification. First, the property of *biocompatibility* is only applicable to a material-host system. For example, PTFE is in widespread clinical use in a multitude of devices and has excellent biocompatibility under international (ISO and FDA) standards. However, when used in metal-on-plastic hip implants, small fragments of PTFE can be abraded and lead to a massive local inflammatory reaction (Charnley, 1963). The hydrophobic surface of PTFE makes cell adhesion particularly difficult, rendering it useless in tissue engineering scaffolds and bioreactors. As such, it is only appropriate to say that “PTFE within a cardiac delivery catheter, for example, is a biocompatible system”.

Second, there is no linear spectrum of biocompatibility. The response of a biomaterial-host system is a complex combination of many entangled pathways with positive and negative feedback loops; there is no single measure which confers biocompatibility and each response is transient (Williams, 2014). For example, PTFE grafts are used to

bypass stenosed blood vessels. Upon implantation they display a minimal host response, but over longer durations the grafts consistently become stenotic as a result of neointimal hyperplasia (Kelly et al., 2002). As I seek to minimise clinically observable effects, I may have to resort to the “least worst option”, for there is no known perfectly biocompatible material (Williams, 2014).

In this chapter I will cover whether the “styrenic BCP-major artery system” may result in clinically acceptable effects.

3.1.1 Host response pathways

The body’s response to any implanted material is rapid. Upon contact with blood, proteins are immediately (≤ 1 s) adsorbed to the implanted material’s surface. The composition of this adsorbed layer will change over time as proteins may rearrange or detach, whilst other proteins may competitively bind. This protein pseudo-surface is of paramount importance as it interacts with cells and thus determines the long term response to the implanted material (Anderson et al., 2004).

The host response to implanted materials is spatially and temporally specific. For example, the surgical implantation of a prosthetic heart valve leaves a wound in the aortic root. In order for this to heal there is a carefully mediated cascade of biological responses. To stem the flow of blood from a wound and provide a scaffold on which healing can take place, a thrombus, or clot, must be formed rapidly. This is initiated either by the activation of factor VII which is triggered by tissue damage (producing tissue factor), or contact with foreign (non-endothelial) surfaces, activating factor VIII. Both of these processes result in an amplifying cascade of protein changes, converging at the activation of factor X. Factor Xa (activated factor X) converts prothrombin to thrombin, triggering fibrinogen to polymerise into fibrin strands, this becoming associated to form a fibrin gel, creating a surface upon which healing can take place. Although this process is entirely physiological in the wound healing response, a foreign material can lead to catastrophic perturbations, such as a stroke-causing embolus of a clot.

While the coagulation cascade is protein-based, whole cells are also rapidly activated. Platelets follow an adsorption, activation, and aggregation cascade. The most abundant platelet surface receptor is glycoprotein IIb/IIIa, which binds to von Willebrand Factor (vWF), fibrinogen, fibronectin, vitronectin or thrombospondin, allowing adsorption to a protein coated surface and platelet aggregation.

When platelets encounter collagen or vWF, or an absence of nitric oxide, endothelial-

ADPase or prostacyclin, they are activated. This results in a shape change and the formation of pseudopodia from their surface. They secrete granules and initiate the arachidonic cycle which leads to the production of thromboxane A₂, initiating a positive feedback loop, causing a platelet plug to form (Napier, 2012).

Platelets' response to shear stresses is dependent on both the magnitude of shear and duration (Ramstack et al., 1979; Sheriff et al., 2010). While red blood cells are lysed at about 600 Pa, platelets are activated by shear stresses as low as 10 Pa, which may be found in pathological regions of the vasculature (Anderson et al., 1978). Short, intense bursts of shear stress, of 255 Pa for as little as 7 ms, are sufficient to liberate β -thromboglobulin (β -TG) as part of the clotting cascade (Wurzinger et al., 1985). The shear activation of platelets occurs through the binding of glycoprotein Ib-IX-V complex on the surface of the platelets to vWF, activating fibrinogen receptors and leading to platelet aggregation (Andrews et al., 1997).

The formation of a platelet-fibrin mesh at a lesion or foreign body becomes a scaffold upon which the acute inflammation process takes place. Damage to the vasculature results in the release of cytokines causing the emigration of leukocytes to the implant and perivascular. In the minutes and days following injury, neutrophils (polymorphonuclear leukocytes) are the most abundant cell type present at the wound. Neutrophils are shortlived at the implant site, apoptosing after 24 to 48 h, to be replaced by monocytes. These inflammatory cells are able to differentiate into macrophages, which aim to engulf the material so that it can be excreted. However, when foreign objects are greater than 1 μ m in size this becomes "frustrated phagocytosis". Initially the cell will attempt to degrade the material surface, producing a hydrolytic and oxidative environment. If this does not successfully break down the material, a continuous fibrotic capsule will be formed which shields the host from the implant. To form this capsule, phagocytic cells fuse into multinucleated giant cells which combine with extracellular matrix (ECM) components and fibroblasts to surround the foreign body. This capsule may range in thickness from tens to hundreds of microns, and generally reaches a quiescent phase within a month (Ainslie et al., 2009; Anderson et al., 2004).

The innate immune system also responds by recruiting phagocytic cells to the wound and activating the complement system. The complement cascade consists of three activation routes: classical, lectin, and alternative, which converge with the formation of complement protein C3 convertase. The alternative route commences with C3 and C3b adsorbing to a material, which lead to the production of C3 convertase. C3 convertase triggers the terminal pathway, leading to the production of serum complement 5b-9 (SC5b-9), the membrane attack complex, which forms pores in target cells, causing them

to lyse (Andersson and Andersson, 2003). A biocompatible material-host system will result in minimal activation of the complement cascade.

3.1.2 Host response to prosthetic heart valves

Prosthetic heart valve implants in current clinical use are passive, and the prostheses are recognised as foreign and can disrupt the normal physiology. Upon implantation, the leaflets of the valve are exposed to blood, causing proteins to be adsorbed, and contributing to the activation of the coagulation cascade. Combined with the effects of fluid shear stresses, the coagulation cascade may be activated and thrombi generated.

The only surface which is truly compatible with blood is a layer of endothelial cells. In a classical implant which is implanted without endothelial cells, spontaneous, natural endothelialisation of the implant must be relied upon to achieve this level compatibility. Unfortunately, trananastomotic growth is self limiting, and it is rare for endothelial cell layers to extend more than 1 to 2 cm from an anastomosis on a static graft. Glutaraldehyde-fixed biological tissues can have some residual cytotoxicity, reducing the likelihood of endothelial cell proliferation. New methods of detoxification are able to reduce inflammation and calcification, though have a minimal effect on thrombogenicity (Remi et al., 2011). Micro thrombi are rapidly and persistently formed on the leaflet before endothelialisation can take place. *In vitro* endothelialisation prior to implantation can allow a confluent layer of endothelial cells to form, which can lead to a reduction in thrombogenicity. However, the method is complex, and results in a minimal change in calcification and inflammation relative to detoxification (Trantina-Yates et al., 2001).

Although there is an ongoing search for materials which promote complete endothelialisation, the prospects for successfully forming an endothelial shell on a prosthetic heart valve are slim. The most likely candidates for endothelialisation should be autographic transplants, which are performed in the Ross procedure (by grafting the pulmonary valve to the aortic position). Unfortunately, explanted transplants had a thin fibrous sheath formed around the transplanted valve, indicative of minor inflammation without endothelialisation. The very act of implantation or transplantation seems to be enough to trigger non-immune-related cell death (Hopkins, 2006)

Acute inflammation is inevitable in the minutes and days after implantation, and this may be followed by a chronic inflammatory response. For a classical implant, it seems that the best possible trajectory is the formation of a stable fibrous capsule which signifies the end-stage of healing. Wound healing then requires the production of granulation tissue in which fibroblasts proliferate, allowing the formation of a fibrous capsule. Alternatively,

chronic inflammation can lead to the fusion of macrophages to form foreign body giant cells which may prevail for the lifetime of the implant, though it is unknown whether they remain activated (Anderson, 2001).

The growth of fibrotic tissue onto the leaflets of a bileaflet mechanical heart valve can severely interfere with their function, and provides material for embolisation. Pyrolytic carbon is used to coat the surface of mechanical heart valve leaflets due to its lack of thrombogenicity and durability, but the material's surface does not resist fibrous encapsulation. Mechanical heart valve designers have instead placed a small ridge on the leaflet housing which halts tissue growth¹.

On the one hand, fibrotic growth on the leaflets of a prosthesis may be beneficial as it shields the cells from the foreign material. On the other hand, ingrowth of fibrous tissue into the sewing ring is absolutely necessary. The prosthetic valve must form a tight seal with the aortic root to avoid paravalvular leak and to secure the valve. Polyester knits are the materials most commonly used for the sewing ring. Polyester is commonly used for long term implantable materials; it can be found in septal occluders, hernia repair meshes, wound dressings, breast supports and left ventricular assist devices (Weinberg and King, 2004). The high surface area and porosity of fabrics generally promotes a high ratio of macrophages and foreign body giant cells to fibrotic cells, and polyester does invoke a mild, long-term inflammatory reaction (Anderson, 2001; Sigler and Jux, 2007). Nevertheless its widespread use can be explained by its integration with scar tissue, relatively low inflammatory response and lack of biodegradation.

The chronic inflammation of permanent foreign bodies is highly dependent on anatomical location, animal host for testing, and the time period of observation. So the results of certain materials and designs cannot easily be translated. As such, *in vitro* and generic *in vivo* testing systems for chronic inflammation are not often suitable, and chronic inflammation will not be tested in this chapter.

3.1.3 Haemocompatibility testing systems

The results of haemocompatibility testing can be strongly influenced by the choice of testing procedure. The test should simulate the conditions experienced by blood and cells around prosthetic heart valves, with particular attention to shear stresses imparted on the blood.

Static tests are generally unacceptable for the assessment of haemocompatibility. To

¹Personal communication with Professor Richard Bianco, 2015.

simulate realistic blood flow situations, systems use either centrifugation, planar flow chambers, loop systems, circulation models or agitators to generate realistic shear stresses (Braune et al., 2013). The system should be selected for reproducibility, sensitivity, practicality, and flexibility, whilst demonstrating accurate representation of the environment in which blood flows.

I used the Chandler loop system which consists of loops that are $\frac{2}{3}$ filled with mildly anticoagulated blood, with the remaining $\frac{1}{3}$ filled with air, as show in Figure 3.1. A strip of test material is tightly placed in the loop such that it rotates with the tubing without being dislodged by the blood. The loops are then rotated in a water bath, causing physiological shear rates of blood over the material. The Chandler Loop method has a high ratio of sample surface area to blood volume to maximise sensitivity, with the sample surface area similar to that of a prosthetic heart valve, with a minimum amount of blood from a single donor, so enabling repetition and multiple materials to be tested (Seyfert et al., 2002).

The standard Chandler Loop setup has an air-blood interface in the loop which is necessary for inducing flow, but also causes significant blood trauma and thus leads to an increase in leukocyte activation, thrombi and protein denaturation. The Modified Chandler Loop uses polyvinylchloride (PVC) loops with a covalently bonded heparin coating to reduce background activation (Sinn et al., 2011; Streller et al., 2003).

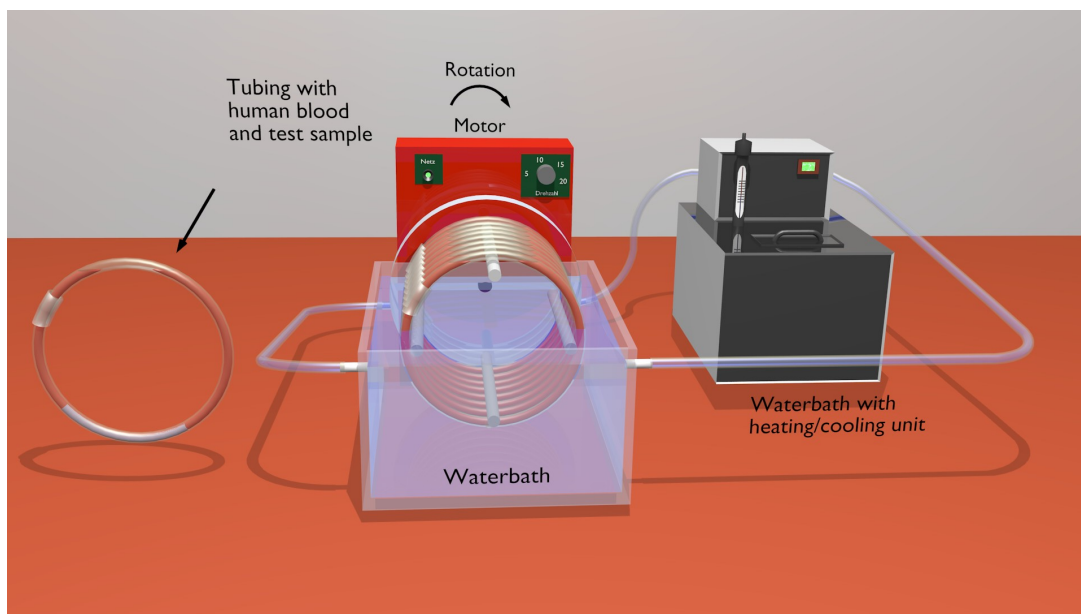


Figure 3.1: Chandler loop set up with six loops rotating in a water bath.

3.1.4 Reference materials

The parameters associated with biocompatibility vary from donor to donor, and from day to day for a single donor (Vienken, 2008). As such, it is impossible to predict the extent of an *in vivo* response, from *ex vivo* data, without the use of reliable reference materials.

Low-Density Polyethylene and Polydimethylsiloxane (PDMS) (both gamma irradiation sterilised) were proposed as *Primary Reference Materials* for biocompatibility testing in 1984 by the National Heart, Lung and Blood Institute (NHLBI). The materials initially served as adequate reference materials for *in vitro*, *ex vivo*, and *in vivo* testing but the gamma sterilisation resulted in some cytotoxicity. However, there was no full evaluation of the materials at the time of implementation, and they have not received widespread use in medical devices, nor as reference materials in testing (Belanger and Marois, 2001).

Without a universal standard, reference materials must have a well characterised *in vivo* response for the appropriate host system. Samples must also be manipulated inside the flexible PVC tube in the Chandler Loop system, so they should be thin and flexible. Expanded polytetrafluoroethylene (ePTFE) and polyester (PES) are commonly used as reference materials. ePTFE has good haemocompatibility so serves as a positive control, with the proviso that it can promote stenosis narrow diameter vascular grafts. PES is mildly thrombogenic and inflammatory, so serves as a negative control.

3.2 Materials and methods

3.2.1 Materials and sample preparation

I tested the proposed BCP, from Chapter 2, SEPS22, for biocompatibility using a Modified Chandler Loop. ePTFE and PES vascular grafts, manufactured by Jostent, were used as reference materials. I also compared the selected polymer to a Bovine Pericardium patch, fixed with glutaraldehyde (trade name Peri-Guard, with Apex Processing, Synovis Life Technologies, Inc. MN, USA). Three other shortlisted BCPs: SIS30 and SI-BS19 (both Kraton), and SIBS30 (Innovia LLC), were previously tested by Prof. Hans Wendel's group (Klinisches Forschungslabor der Klinik für Thorax-, Herz- und Gefäßchirurgie, Universität Tübingen) using the same system.

I compression moulded the BCP samples at 160 °C in an electrically heated hydraulic press to a thickness of 0.3 mm. Melt flow during moulding was minimal, so the samples were not mechanically anisotropic. Strips of 9 × 150 mm were cut from the polymer sheets

and reference materials for tests in the Modified Chandler Loop. Samples were sterilized using 70% ethanol before testing.

3.2.2 Coating of materials

In the event that a material does not appear to be sufficiently biocompatible it may be possible to coat the material, or modify the surface, to mediate the host response. Certain synthetic coatings seem to be able to reduce fibrinogen adsorption and thus cellular adsorption significantly, such as polyethylene glycol, zwitterionic groups including phosphorylcholine, sulfobetaine, carboxybetaine, and polycarboxybetaine (Vladkova, 2013). Alternatively, biological molecules may be grafted to the surface to have an active influence. Surface heparinisation is one of the most promising methods for improving the blood compatibility of polymeric materials. Heparin is a highly sulfated, anionic blood polysaccharide (5–25kDa) that naturally occurs on the intravascular endothelium. Heparin binds to anti-thrombin anionically, accelerating the rate at which anti-thrombin inactivates thrombin.

I coated one set of SEPS22 samples with the Corline Heparin (CH) Surface. The CH coating consists of the covalent binding of macromolecular heparin which conjugates to an inert polyamine chain. End-on attachment of heparin, with a spacer arm, is the most effective way to retain the activity of heparin when surface bound (Golander and Larsson, 1986). The substrate polymer was primed for coating by forming a cationic surface on the uncharged synthetic material. This was then heparin coated by exposing to a dilute water solution containing CH conjugate, manufactured by Corline® (Uppsala, Sweden). CH conjugate binds to any cationic surface with very a strong affinity due to the high concentration of anionic groups (Kidane et al., 2004; Wendel and Ziemer, 1999). 70 moles heparin are irreversibly bound to each mole of the surface-bound carrier chain. The coated surface has a concentration of heparin of 0.5 to 1 $\mu\text{g cm}^{-2}$, which has the capacity to bind 2 to 4 pmol cm^{-2} of antithrombin (Christensen et al., 2001).

3.2.3 Donors

Blood was drawn from healthy volunteers aged between 20 to 50 years. Donors were chosen with exclusion criteria eliminating smokers, drug-taking in the last 2 weeks, especially aspirin, oral contraceptives, and non-steroidal antiinflammatories. Blood was carefully drawn without stasis by venipuncture with butterflies (1.4 mm) directly into sterile pre-anticoagulated containers (1.5 IU/ml Heparin-Natrium 25000, Rathipharm

GmbH, Ulm, Germany). Unless otherwise stated, six, screened, consenting donors were used for each of these tests.

3.2.4 Chandler Loop method

Samples of material measuring 9×150 mm were inserted into heparin coated PVC tubes (50 cm length) (Carmeda coating, Medtronic), and the ends of the tubes were joined with silicone tubing to form continuous loops. 20 ml of blood was added to each tube. The loops were rotated vertically at 30 rpm in the water bath maintained at 37°C . After 90 min of circulation the blood was collected in appropriate syringes for analysis as follows: 2.7 ml with 1.6 mg ml^{-1} potassium-EDTA added for complement and blood cells analysis; 10 ml citrated blood (0.14 ml of $0.106\text{ M C}_6\text{H}_5\text{Na}_3\text{O}_7 \cdot 2\text{H}_2\text{O}$ citrate) for acute inflammation, coagulation cascade activation and haemolysis analysis; 4.5 ml anticoagulated blood (450 μl of 0.109 M ; citrate-theophylline-adenosine-dipyridamole (CTAD), Becton Dickinson GmbH, Heidelberg, Germany) for β -TG analysis. The samples were centrifuged immediately at 2000 G for 20 min with a cryofuge (Model 8000, Heraeus, Osterode, Germany) to separate plasma samples. These were then aliquoted into 400 μl samples, shock-frozen in liquid nitrogen and stored at -70°C .

3.2.5 Parameters for analysis

According to ISO 10993:4, blood-contacting materials should be evaluated for thrombogenicity, platelet activation, coagulation, protein adsorption and inflammatory markers.

Thrombogenicity

Scanning electron microscopy (SEM) was used to observe platelet adhesion and aggregation, leukocyte adhesion, and fibrinogen adsorption on the surface of the material. After circulation in the Chandler loop, the polymer samples were incubated overnight in 2% glutaraldehyde (Serva, Heidelberg, Germany) containing PBS (phosphate buffered saline, Invitrogen Gibco, Karlsruhe, Germany) solution and subsequently rinsed in pure PBS. The remaining water was removed from the samples using 40 to 100% of ethanol (Merck, Darmstadt, Germany) in ascending concentrations. Finally all samples were critical point dried and sputtered with gold palladium before analysis with SEM (Cambridge Instruments, Cambridge, UK, type 250 MK2).

Platelet activation

The activation of platelets leads to the release of β -TG. β -TG concentration was measured using an ELISA (Diagnostica Stago Asnieres, France).

Coagulation cascade

The formation of thrombin causes fibrinogen to cleave into fibrin monomers. The concentration of thrombin-antithrombin complex was measured by ELISA (Siemens Healthcare Diagnostics Products GmbH, Marburg, Germany).

The adsorption of factor XII and fibrinogen to a surface leads to their conformational change and the activation of platelets. Platelets adsorb via their GPIIb/IIIa receptor, leading to their activation. The concentration of GPIIb/IIIa (also known as CD41 antigen) was measured using an in house ELISA method, as devised by Paul et al. (2009).

Inflammation

Local inflammation is characterised by the activation of neutrophils and phagocytes seeking to expel a pathogen from the body. Neutrophils release the proteinase PMN-elastase (Erlenkötter et al., 2008). The concentration of PMN-Elastase was measured by ELISA (Milenia Biotec GmbH, Giessen, Germany).

Protein adsorption

The adsorption of proteins to the material surface determines the host response. The blood contacted materials are placed in EDTA to preserve the state of the adsorbed plasma proteins (Engberg et al., 2011). The concentration of fibrinogen and CD41 were measured using in-house methods

Blood cell count

Red and white blood cell and platelet counts were performed on EDTA-blood (potassium-EDTA, 1.6 mg ml^{-1}) immediately after sampling using a fully automated cell counter system (micros 60 ABX Hematology, Montpellier, France). Haemolysis was detected using a colorimetric assay for free plasma haemoglobin (Cyan haemoglobin test, UKT, Germany).

Complement system

The activation of the complement cascade leads to the release of serum complement protein 5b-9 (SC5b-9), whose concentration was measured with an ELISA (Quidel, San Diego, CA, USA).

3.2.6 Coating durability

To assess the durability of the heparin coating I aged heparin coated samples *in vitro* in three ways: static in PBS solution, dynamically strained in PBS solution, and in a 3% hydrogen peroxide solution which simulates the oxidising conditions which may be experienced during an inflammatory reaction. Coated and uncoated control samples were also used. All samples were kept at 37 °C for 3 weeks.

Heparin is the most negatively charged molecule found in nature, so a heparin coated sample should have a lower surface energy. This change in surface energy might be measured by investigating the water contact angle on the polymer surface. The contact angle which a drop of water makes with the sample is a measure of the hydrophobicity of the material. I performed a preliminary experiment to investigate whether there was a difference in contact angle between coated and uncoated samples. On uncoated samples of SEPS22 I found the contact angle to be 92.0° compared to 78.6° on heparin coated specimens. This difference was significant ($p \leq 0.001$). Water contact angle on the samples was recorded at seven spots.

Although the presence of heparin may be inferred from the water contact angle on the surface, this gives no indication of the presence of a functional group. Kristensen et al. (2006) used X-ray photoelectron spectroscopy (XPS), and Harada et al. (2005) used Fourier Transform Infra Red spectroscopy with an attenuated total reflectance sample mount (FTIR-ATR) to evaluate surface concentrations of heparin.

In XPS, an X-ray is fired at the surface leading to the emission of outer shell photoelectrons from surface molecules. A specific fingerprint of photoelectron energies can be used to identify and measure the concentration of specific groups which are found in the outer 10 nm of the surface. I sent samples for XPS analysis at the Nexus facility at Newcastle University. XPS was performed using Kratos Axis Nova XPS system with an Al K α (1486.6 eV) source. Five spots upon three samples of each material were analysed.

In FTIR, infra red light is shone on to a material at a range of frequencies. Each chemical bond in the material absorbs radiation at a characteristic frequency. The reflected or

transmitted light is detected which is analysed by a fourier transform, to derive the absorption at a range of frequencies. I performed FTIR using an ATR sample mount, unlike Harada et al. (2005), I was not able to consistently detect changes in the relevant absorption peaks on the polymeric substrates as they appeared to be masked by a peak from COH groups, so this method was not used.

The concentration of heparin which leached from the coating into the PBS solution was determined using the toluidine blue method (van Bilsen et al., 2008). Polymer samples (65 cm^2) were stored in glass vials containing 20 ml of PBS, pH 7.4 at room temperature. Periodically, 2 ml of the PBS solution was taken and mixed with a 0.005% toluidine blue solution. Following heparin-dye-precipitation, the absorbance of the dye-depleted solution was measured at 631 nm and the concentration of the released heparin was calculated from the heparin calibration curve, as constructed using sodium heparin salt from intestinal mucosal source (Sigma, UK).

3.2.7 Effect of anticoagulant drugs

The preferable scenario would be for the *in vitro* haemocompatibility study of a material to mimic the expected *in vivo* scenario as closely as possible. This suggests that anticoagulant therapies should be implemented into the testing. However, Braune et al. (2013) noted that no internationally accepted guidelines are defined for the concentrations of anticoagulant to be used *in vitro*. Salicylic acid (Bayer, Germany) was added *in vitro* to yield a concentration of 20 mg l^{-1} .

3.2.8 Analysis

For the post-processing of data I used MATLAB (Mathworks, MA, USA). Results were plotted as histograms with error bars representing the mean \pm standard error. A two tail ANOVA with the Bonferroni correction was used to compare normally distributed samples of equal size., significant comparisons with $p \leq 0.05, 0.01, 0.001$ are indicated by marking with *, **, and ***, respectively.

3.3 Results

In the polymer selection of Chapter 2, a set of BCPs were tested by our collaborators for their haemocompatibility; these materials constituted “run 1”. Having selected a

material, and collected preliminary observations on the relative biocompatibility of the polymers, I then assessed the haemocompatibility (at Prof. Wendel's lab) of the selected polymer, SEPS22. This was compared to fixed bovine pericardium, as an additional reference material due to its extensive use in bioprotheses. I also tested SEPS22 with a heparin coating. These materials are "run 2".

3.3.1 Thrombogenicity

SEM images of the polymeric materials are shown in Figure 3.2. No large thrombi were found on the surface of the polymeric materials. Morphological differences were observed between the proteins adsorbed on the surface of each polymer. Addition of the heparin coating resulted in a very different morphology of the protein layer. A subconfluent protein layer is adsorbed onto the uncoated materials. The protein layer is fibrous with some cellular entrapment and joining of fibres. In contrast, the heparin coated samples resulted in the formation of a weaker fibrous mesh, suggesting a lower level of protein adsorption. Holes in the protein layer were observed on some uncoated samples, which may have arisen due to the detachment of adsorbed cells during the drying process.

SEM images of the ePTFE (not shown) also had a subconfluent protein layer, which did not have the fibrous morphology as seen on the BCP materials. Although ePTFE is porous, no ingress of proteins or cells could be detected by SEM. On the polyester sample (not shown) there was significant adsorption of proteins and red blood cells, though no large thrombus formation. While no blood was adsorbed to the surface of the polymeric samples after rinsing in PBS, the bovine pericardium samples retained significantly more blood, as shown in Figure 3.3. Under SEM, the sample displayed significant protein adsorption and thrombus formation.

3.3.2 Hemolysis and coagulation

I did not find any significant differences between materials for red blood cell counts of blood discharged from the loops after testing. Free haemoglobin concentration is a marker of red blood cell destruction, which may occur if a material is highly incompatible with human blood; all BCPs performed at least as well as the reference materials, with SI-BS19, SIBS30, and uncoated SEPS22 resulting in less haemolysis than the reference materials (Figure 3.4a).

The generation of thrombin occurs in the common pathway of the coagulation cascade. The concentration of thrombin-antithrombin complex (TAT) in blood was measured be-

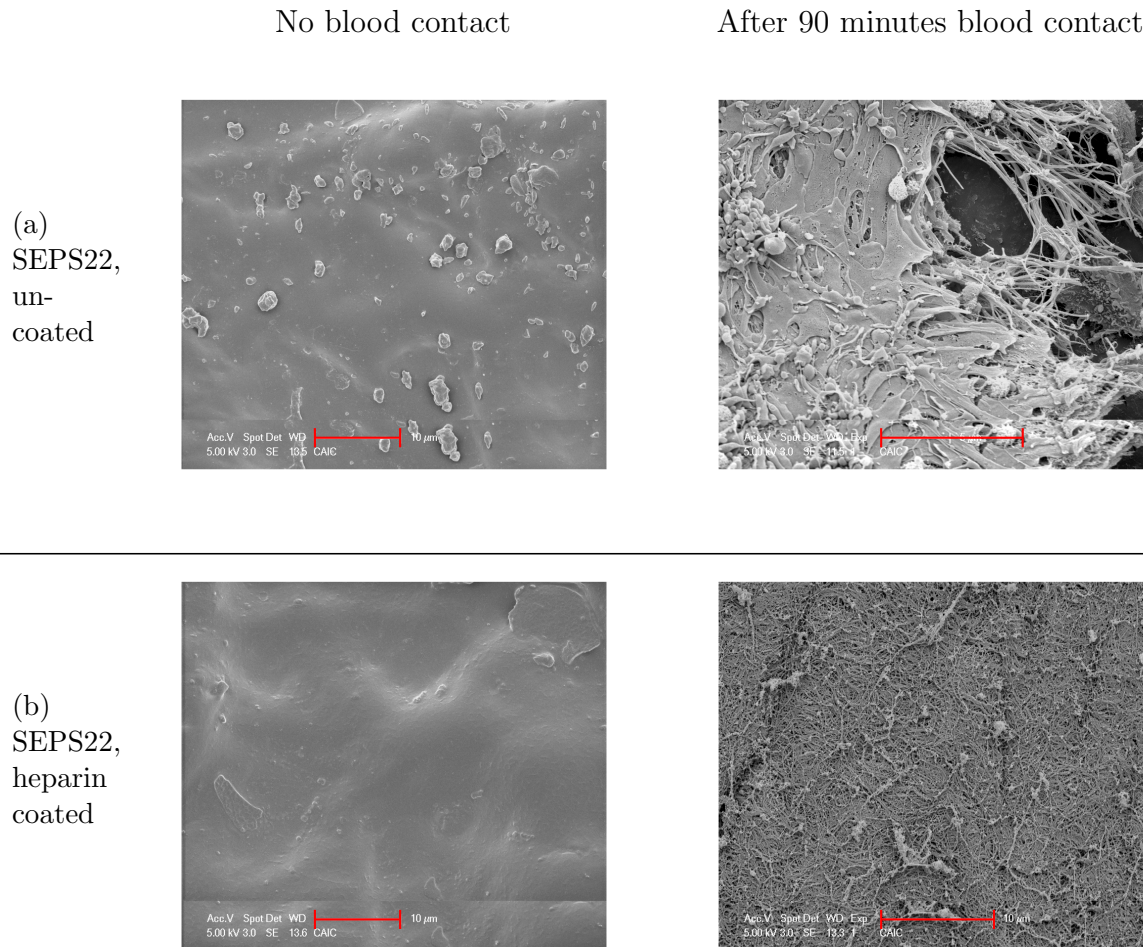
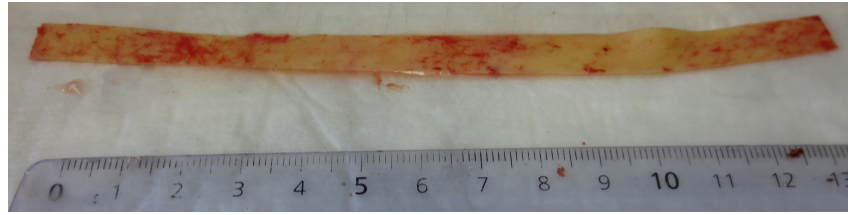


Figure 3.2: SEM images of polymer surfaces before and after contact with blood (scale bar is 10 μm on all images). The coated and uncoated surfaces are macro- and microscopically smooth, but have a protein coating after blood contact. The uncoated sample (a) appears to have activated platelets adsorbed to its surface. The coated surface (b) has a confluent layer of fibrin, but there are no activated platelets on the surface.

fore and after contact with the materials (Figure 3.4b). In both runs the fresh blood and control tube were found to contain an identical level of thrombin, indicating that the heparin coating of the PVC tubing was effective at reducing background activation. All reference materials resulted in activation of the coagulation cascade. The uncoated BCP were more activating than ePTFE, itself more activating than bovine pericardium, but less activating than polyester. In the second run, SEPS22 was also more activating than bovine pericardium. The addition of a heparin coating to SEPS22 resulted in the least activation of the coagulation cascade. However, differences between materials were not statistically significant ($p > 0.05$).

(a) Photograph



(b) SEM

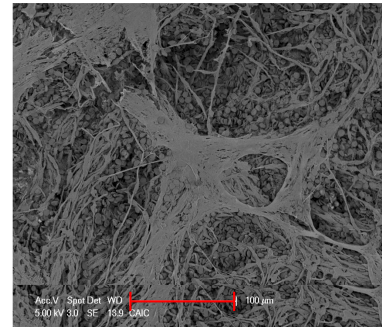


Figure 3.3: (a) Bovine pericardium sample after blood contact showing adherence of blood to the surface of the material. Under SEM (b), where the **scale bar** is 1 mm and 100 μm in the left and right images respectively, there is a mild thrombus with a fibrin mesh with entrapped erythrocytes.

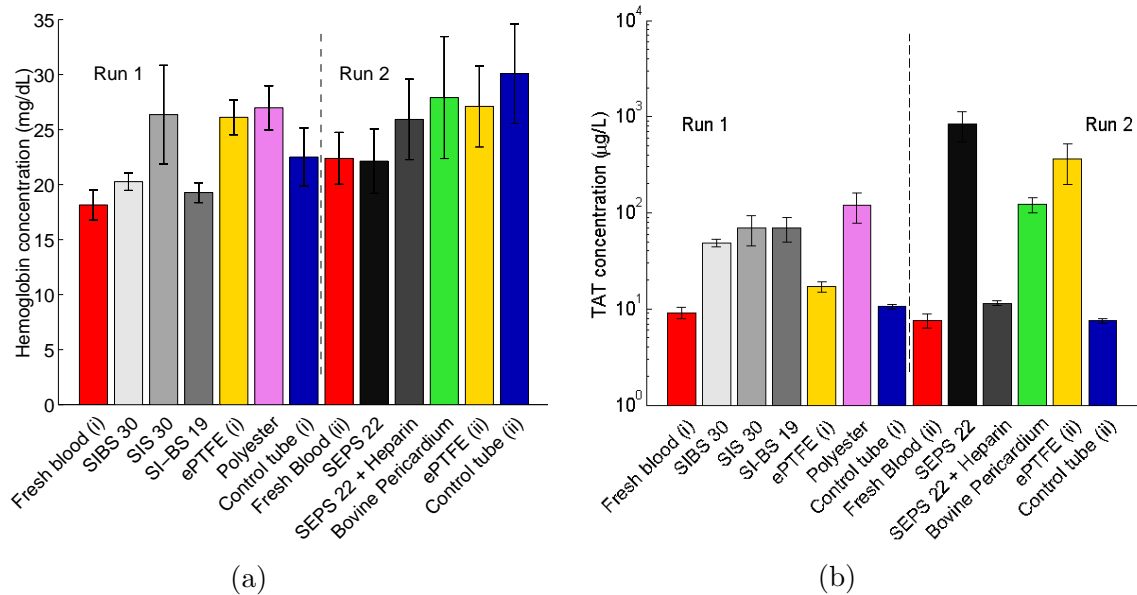


Figure 3.4: Results of measurements on 13 materials as tested in two separate runs. (a) Free haemoglobin is released during haemolysis and was measured using a photometrical test. (b) thrombin is generated in the common pathway of the coagulation cascade as measured by the concentration of thrombin-antithrombin complex.

3.3.3 Platelets

I found that the BCP and reference materials led to activation of platelets. Platelets may be adsorbed to the material surface, aggregate to each other, or become activated, releasing α -granules. The reduction in platelet count (Figure 3.5a) indicates that platelets were adsorbed or activated.

When platelets come into contact with a foreign surface they can be activated. Activation proceeds through the formation of pseudopodia, adhesion, aggregation and release of platelet factors from the granules. All uncoated materials caused a drop in platelet count in the discharged blood (Figure 3.5a) either through activation or adsorption of the platelets to the material. BCPs, ePTFE and bovine pericardium showed similar platelet counts, whereas polyester resulted in a significantly greater reduction in platelet numbers. Activation of platelets leads to the release of β -TG (Figure 3.5b), which was analysed by ELISA. In the first run, β -TG was significantly greater on the BCP than on the haemocompatible control, ePTFE. In run 2, there were no significant differences between the BCPs and reference materials. The addition of a Heparin coating to SEPS22 led to lower β -TG levels (Figure 3.5b).

Adsorption of platelets to the material surface can result in the deposition of CD41 receptor protein on the material surface (Figure 3.5c). I found that the BCP materials had significantly less adsorbed CD41 than the negative control, polyester. Heparin coating of SEPS22 also reduced CD41 adsorption. Platelets and leukocytes can bind to fibrinogen which is adsorbed to the material's surface. High levels of adsorbed fibrinogen lead to thrombus generation and localised inflammation (Hong et al., 2001). I found that fibrinogen adsorption was significantly lower on the BCPs than on the control materials (Figure 3.5d).

3.3.4 Innate immune response

Foreign materials can activate the innate immune system. I measured the white blood cell count, concentration of PMN-Elastase and SC5b-9 before and after circulation in the Chandler loop.

The BCP materials did not have a significant effect on white blood cell count. There was, however, a significant reduction ($p \leq 0.05$) in white blood cell count for samples contacted with polyester and bovine pericardium (Figure 3.6a). The activation of the immune system may be inferred from the release of PMN-Elastase as neutrophils degranulate; bovine pericardium and polyester resulted in greater releases of PMN-Elastase than the

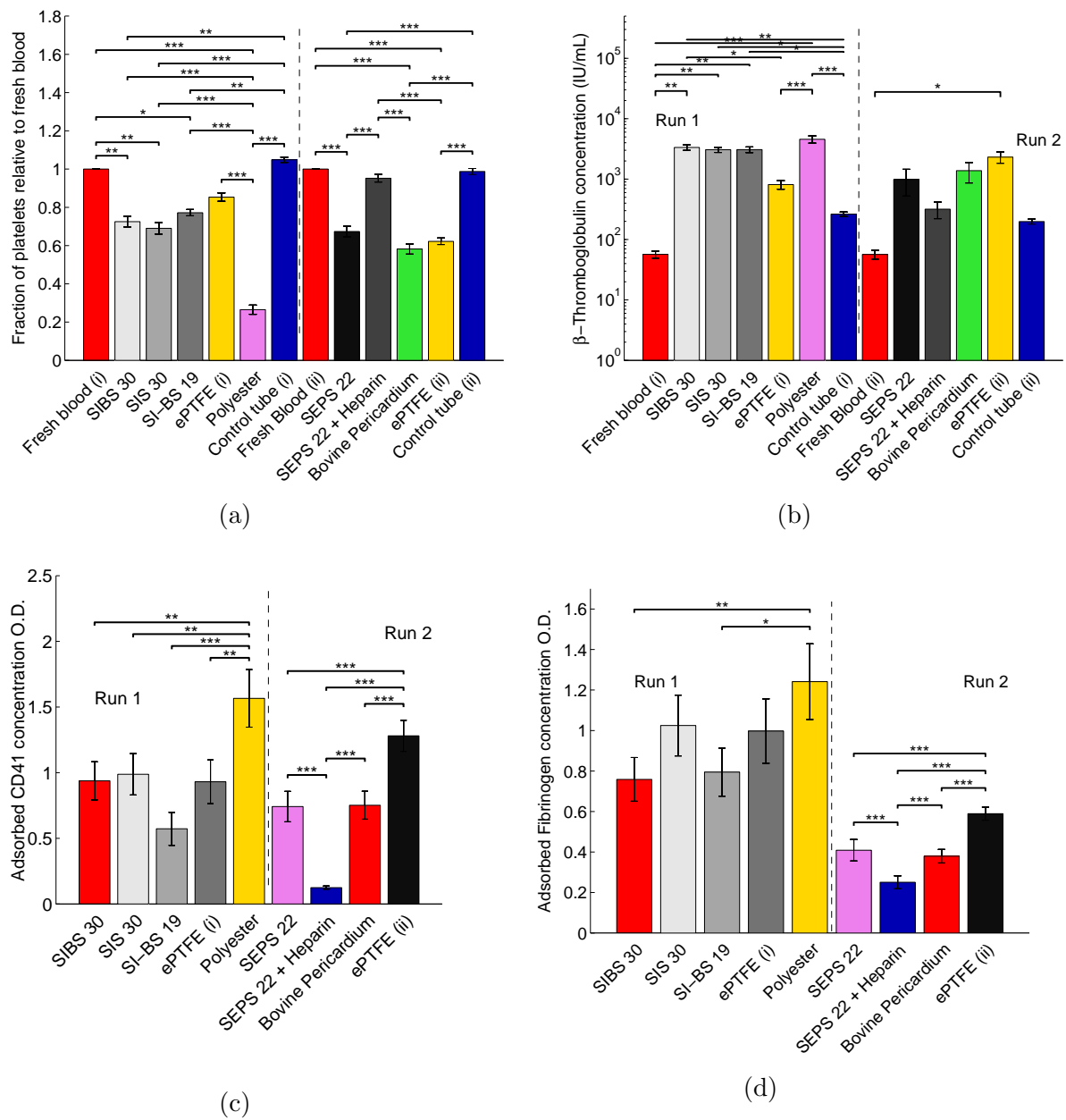


Figure 3.5: Results of measurements on 13 materials as tested in two separate runs. (a) Platelet count before and after contact with each of the materials. (b) shows the concentration of β -TG. The presence of β -TG indicates that platelets have been activated. (c) shows the surface concentration of CD41. The adsorption of platelets to the materials can be quantified by measuring the surface concentration of CD41 receptor. (d) The surface concentration of fibrinogen is shown. Adsorbed fibrinogen is used by platelets and leukocytes to bind to a material surface.

tested BCPs (Figure 3.6b). The coating of SEPS22 with heparin had no effect on either of these inflammatory measures. Plasma protein SC5b-9 is used to lyse pathogenic cells in the final stage of the complement cascade, where the alternative and classical pathways

converge (Hastings, 1992), and is a marker of the degree of inflammatory response which may be caused by a material. All materials led to some activation of the complement cascade, though none as much as bovine pericardium ($p < 0.001$) (Figure 3.6c).

3.3.5 Cell viability

Indirect contact cytotoxicity tests were previously performed on shortlisted materials by our collaborators (Prof. M. Costantino, Politecnico di Milano). They found no significant cytotoxicity associated with leaching from the materials. The proposed use of these BCPs is in a permanent implant with direct contact with fibroblast and smooth muscle cells. In accordance with ISO 10993-1, I tested cell viability in direct contact with these materials. I used the standardised L929 fibroblast strain and measured cell count after 48 hours with an MTS assay. The final cell numbers are shown in Figure 3.7.

The rapid proliferation of murine fibroblasts on the surface of the materials implies that cells are viable on the material. I did not find any significant differences between proliferation on compression moulded (SEPS22), solvent cast (SEPS22 SC), or heparin coated (SEPS22 H) surfaces of SEPS22 ($P \geq 0.15$). Only the uncoated SEPS22 led to significantly more proliferation than the PS control well ($P = 0.034$). Differences in manufacturing which may lead to variations in surface texture did not affect the extent of proliferation of cells upon the surface; furthermore the solvents used during casting were not cytotoxic. All BCP processing resulted in relatively smooth surfaces. In contrast, the results for ePTFE and PES were for venous graft material which had ridges of approximately 1 mm which was likely to have reduced the rate and extent of proliferation. Proliferation was significantly lower on PES than in the PS well ($P = 0.000025$). I did not find cells to be viable on the bovine pericardium surfaces, which is possibly due to residual leaching of the glutaraldehyde used for fixation.

Proliferation of fibroblasts should ensure good colonisation around the sewing ring of a prosthetic heart valve, and possibly aid the fibrous encapsulation of the leaflets which may reduce the rate of calcification. The cell culture used in these experiments was static, which means that predictions for the growth of fibroblasts on a material implanted in the structurally and fluidly dynamic aortic root are uncertain. Furthermore, predictions of chronic inflammation cannot be made without assessing the response of directly contacted macrophages.

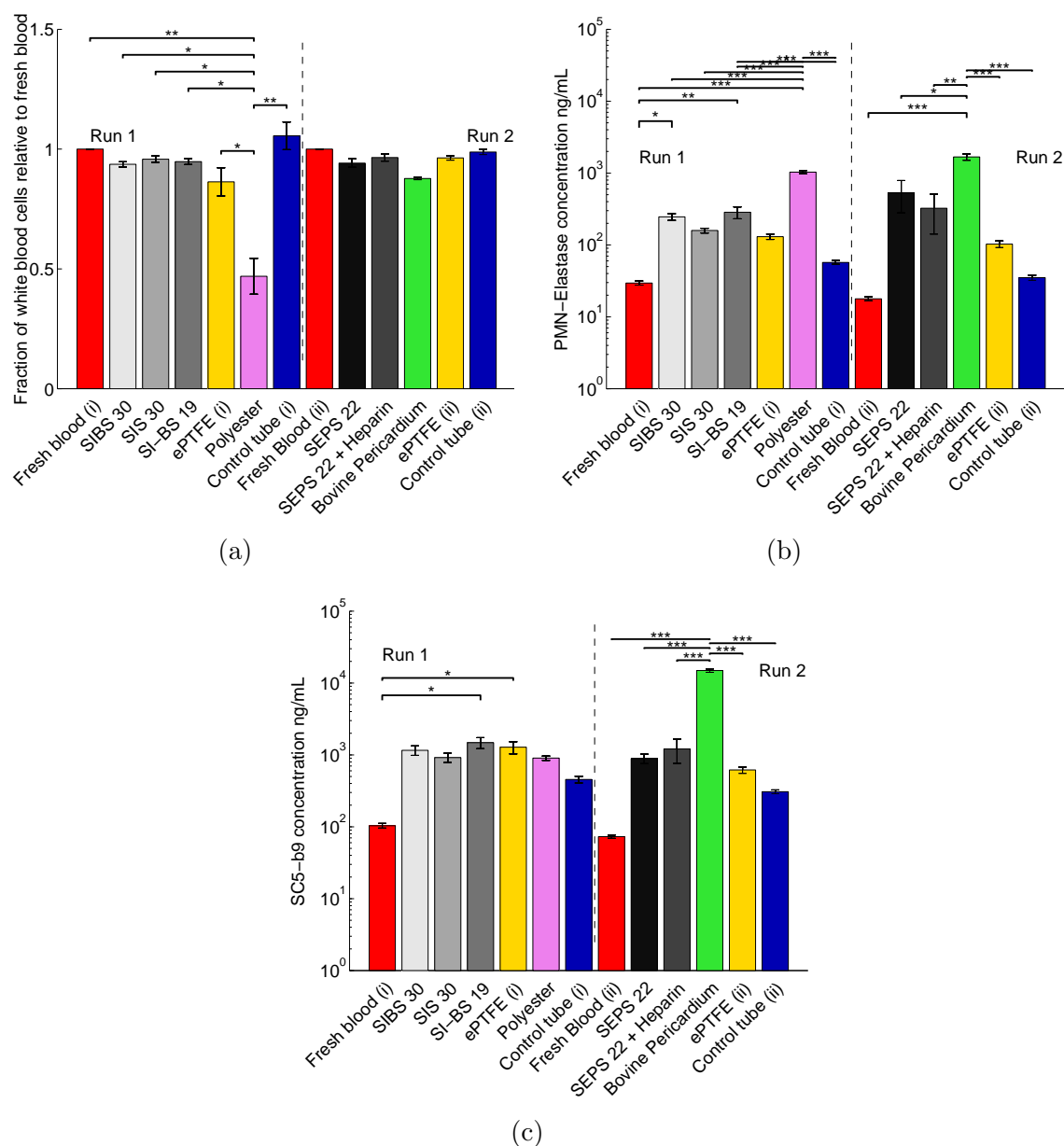


Figure 3.6: Activation of leukocytes occurs during inflammation and results in the release of PMN elastase and loss of white blood cells. Polyester and bovine pericardium both led to a significant reduction in leukocyte counts. (a) None of the BCPs led to a fall in leukocyte numbers. (b) The concentration of PMN elastase was analysed by ELISA, all materials led to release, though all BCP were significantly less inflammatory than both polyester and bovine pericardium. (c) SC5b-9 is associated with the final stage of the complement cascade and leads to the formation of membrane attack complexes that are used to perforate the membrane of a pathogen or cell. All materials led to the activation of the complement cascade, though all polymers were significantly less inflammatory than bovine pericardium.

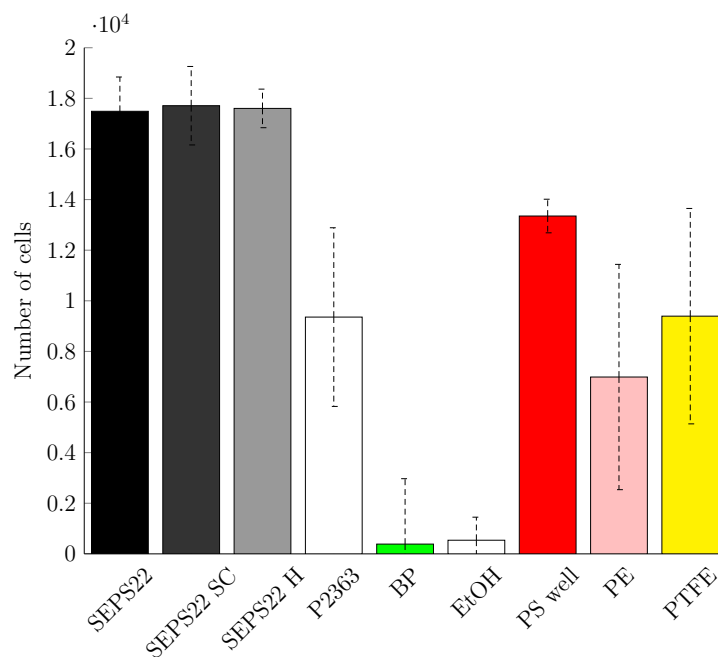


Figure 3.7: Cell numbers on material that were seeded with 5×10^3 cells, and cultured for 48 h. Cell density was measured using an MTS assay. Error bars indicated standard deviation from the mean ($n=7$). PS refers to polystyrene.

3.3.6 Coating durability

I aged the heparin coated samples for 3 weeks in air, PBS, and oxidising solutions. The amount of heparin on the surface can be detected by XPS which quantitatively detects the presence of sulphur in $-\text{OSO}_3$ and $-\text{NSO}_3$ groups of active heparin (Figure 3.8b). The heparin coating also influences the hydrophobicity of the material, which I measured by contact angle. The XPS and water contact angle results are shown in Figure 3.8.

The heparin coated samples which were strained dynamically have a significantly greater contact angle than those that were held statically ($P = 0.0029$) and a lower sulphate group concentration, which suggests that the coating may have been affected by cyclic strain. Alternatively, strain may alter the surface morphology, which then might affect the interaction with the water droplet. The contact angle of samples which were held in oxidising solution was equal to that of the control samples (no coating), and significantly greater than the coated samples which were stored in buffer solution. This indicates that the coating was degraded by oxidising species.

I found a reduction in surface sulphur concentration (Figure 3.8c) for both the dynamically strained and the static samples, though the difference between them was not statistically significant. There was a large reduction in surface concentration of sulphur for the samples which were statically stored in oxidising solution. The least amount of heparin

was present on samples exposed to oxidising solution. Contrary to the difference in contact angle between the statically and dynamically aged samples, the average area of their S 2p spectra were very similar. Concerning the samples from PBS solution, phosphate spectra were also detected, suggesting that the heparin coating became partially covered by a layer of phosphate salts. This could also have contributed to a slight decrease in the sulphur peak from heparin.

Figure 3.8d shows that the percentage of released heparin increased sharply during the first day of the immersion and then the release curve plateaued at around 8% of the adsorbed heparin. The observed heparin release was probably due to physically adsorbed heparin on the polymer surface, which diffused into the PBS solution during the first day of the experiment. As the heparin coated samples were thoroughly washed during sterilisation, and the adsorbed protein profiles are significantly different, it is unlikely that the biocompatibility improvements are a result of heparin leaching.

3.4 Discussion

In this chapter I used the Chandler Loop model to characterise the *ex vivo* response of human blood to implantable materials. The Chandler Loop model is an established means of simulating thrombus generation, as observed *in vivo* (Gardner, 1974). Furthermore, the average shear rates generated in the Chandler Loop can be estimated for comparison to the physiological environment (Touma et al., 2014). The selected loop dimensions and rotation rate create shear rates which are comparable to those found in a major artery, between 50 and 300 s^{-1} (Hathcock, 2006). However, the continuous rotation of the loop does not produce the transient flow seen at the aortic root. The Modified Chandler Loop was successful at eliminating background activation of the coagulation cascade; the control loop (containing no sample) was not significantly different to fresh blood for coagulation parameters.

Day-to-day and donor-to-donor variation is a significant consideration in biocompatibility testing (Seyfert et al., 2002). As such, absolute analyte levels for the test materials should be compared to the reference material results. PTFE, polyester, and bovine pericardium are used extensively in *in vivo* and *ex vivo* vascular implants and are appropriate choices of reference materials as the host response is well characterised. ePTFE is an inert biomaterial with good haemocompatibility (ASTM International 2009). ePTFE is characterised by its highly hydrophobic surface and lack of functional groups, but its major performance draw back as a graft material is its restenosis in small vessels. As

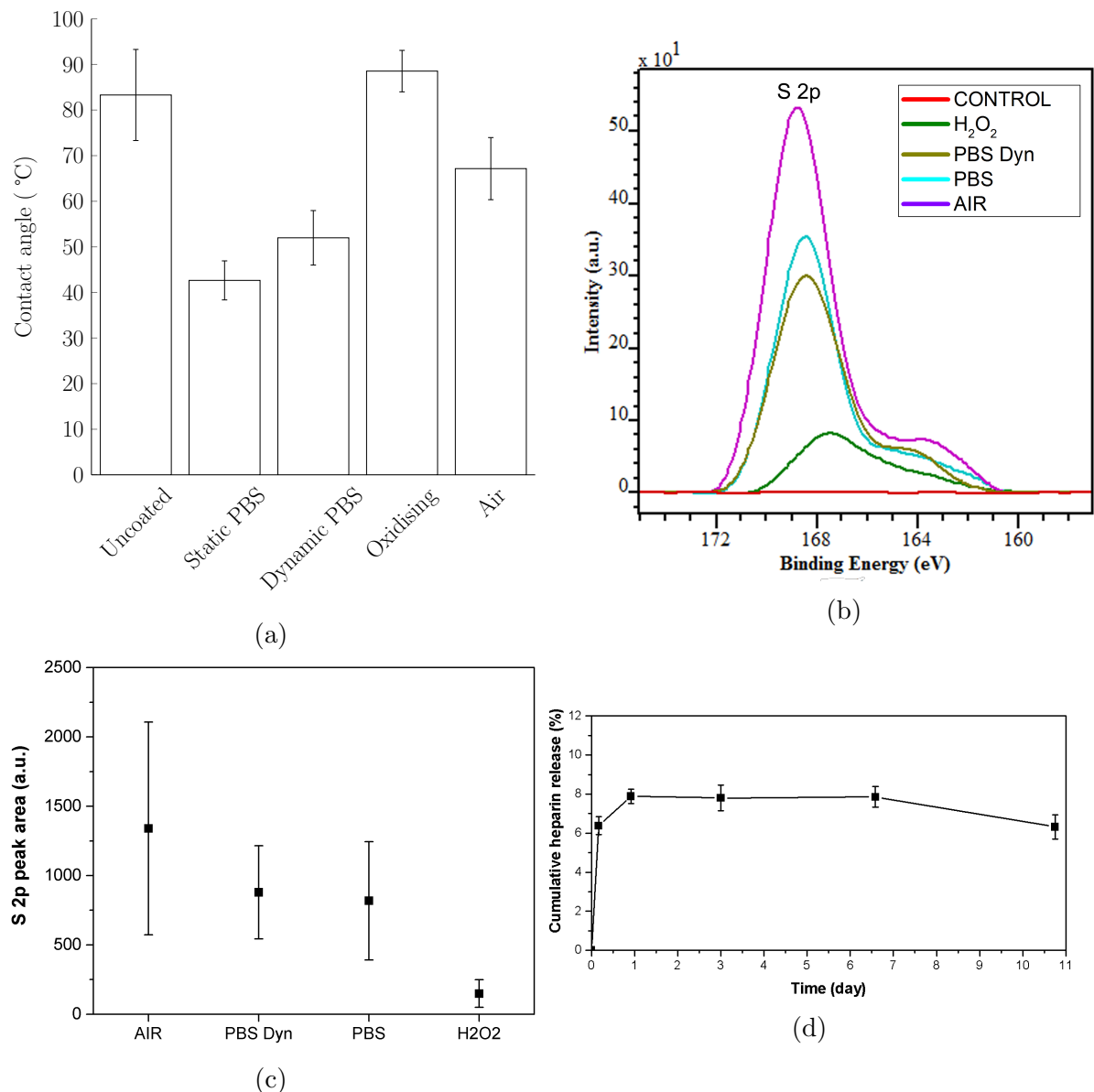


Figure 3.8: Analysis of heparin coating after ageing of samples under various conditions. (a) shows the water contact angle on SEPS22 polymer coated with Corline Heparin Surface after ageing. At least 8 readings were taken for each sample and the error bars represent the standard deviation of samples. (b) shows the XPS measurements of the surface of heparin coated polymers with a peak at 169.5 eV which can be attributed to the $-\text{OSO}_3$ and $-\text{NSO}_3$ groups in heparin. (c) shows the area of the XPS sulfur peaks for the test samples stored in air, PBS, and H_2O_2 , and dynamically strained in PBS. (d) heparin concentration leached from coated samples incubated in PBS for 11 days. The XPS and heparin leaching graphs were prepared by Dr J. Stasiak.

a prosthetic heart valve material it has suffered from excessive calcification and poor durability (Bezuidenhout and Zilla, 2014). The use of polyester (Dacron) in heart valve applications is limited to the sewing ring where it is rapidly encapsulated in fibrous tissue.

In applications of continuous contact with blood the material has resulted in the failure of polymeric prosthetic heart valves tested *in vivo* (Gallocher, 2007).

The experiments performed here on bovine pericardium in the Chandler Loop are the first to be reported in the literature. The pericardium had minimal thrombogenicity and activation of the coagulation cascade, and these are reflective of its *in vivo* performance; pericardial leaflets on prosthetic heart valves do not require major anticoagulation therapies, though patients are generally prescribed aspirin. Among all materials, the inflammatory measurements (leukocyte count, PMN elastase, SC5b-9) were greatest for blood contacted with pericardium, which might be expected from a xenographic transplant. Improved pericardium processing methods, with alternatives to glutaraldehyde and post-fixation washing, could improve cell viability and reduce inflammation (Remi et al., 2011).

The BCP materials did not cause significant haemolysis or activation of the coagulation cascade relative to ePTFE. Activation of platelets can be inferred from a release of β -TG, whilst the adsorption of CD41 to a surface is an artefact of platelet adsorption to the surface. Platelet activation is lowest for ePTFE, but is closely followed by the test BCPs. High levels of adsorbed CD41 might not correlate with SEM images of adsorbed platelets because they could have been washed off due to flow during the test (Weber et al., 2002). Polyester resulted in significantly greater destruction of platelets and adsorption of CD41. The test BCPs were significantly less activating and adsorbing than polyester. Contact with ePTFE resulted in significantly less β -TG release than contact with BCP. However, adsorbed CD41 levels were not significantly different between BCP and ePTFE, possibly due to the hydrophobic surface of both materials. The addition of heparin coating mediated the activation and adsorption response, resulting in the lowest platelet activation amongst test materials.

The absence of hydroxyl and amine groups in the shortlisted biomaterials is a useful property in minimising the activation of the (alternative) complement cascade (Chenoweth, 1987). The protein adsorption profiles for the BCPs are similar to ePTFE and bovine pericardium, so the long term biocompatibility performance of the polymers should also be similar. As these protein adsorption levels are taken at physiologically relevant flow rates, similar levels of cell adhesion may also be possible *in vivo*. The adsorption of proteins is indicative of the long term performance of a biomaterial, in particular, elevated fibrinogen adsorption aids the adhesion of platelets and macrophages which can lead to a chronic, local, inflammatory reaction. SEPS22 and SI-BS19 resulted in significantly lower protein adsorption than occurred on ePTFE. Heparin coated samples resulted in a minimum of CD41 and fibrinogen adsorption suggesting that as long as the coating is

present and active, superior biocompatibility may be achieved.

The strength of adsorption of proteins to the surface may indicate the ease with which inflammatory cells bind to the materials. In run 1 the BCP and ePTFE had lower adsorption of CD41 and fibrinogen than polyester, supporting the claim that these materials are less inflammatory. Interestingly, in run 2, SEPS22, Heparin coated SEPS22, and pericardium were less adsorbent than ePTFE, suggesting that the long term binding of inflammatory cells to ePTFE is greater than to other materials. While ePTFE certainly has acute haemocompatibility, the long term performance of ePTFE grafts in narrow vessels is poor due to neointimal hyperplasia (Kelly et al., 2002). The binding of inflammatory cells can be predictive of the long term performance of implanted materials, but long term predictions of inflammatory behaviour are not advisable from such short term studies.

The surfaces of the BCPs are dominated by $-\text{CH}_3$ groups. Sperling et al. (2005) produced alkanethiols with uniform monolayers containing either $-\text{CH}_3$, $-\text{COOH}$ or $-\text{OH}$. Platelets adhered to the $-\text{CH}_3$ surface, but not to the $-\text{OH}$ surface, whereas leukocytes behaved inversely. The $-\text{OH}$ was the only surface to induce significant complement cascade activation, explaining the minimal complement activation observed on the test BCPs (Chenoweth, 1987; Engberg et al., 2011).

Between the various BCP materials there were few differences in any of the haemocompatibility parameters. This may be attributed to the similarity of the material's surface chemistry. The soft block (polyethylene, polyisoprene, or polyisobutylene) is expected to coat the surface and the minor differences in molecular architecture do not affect the surface properties (surface energy) significantly.

The polymeric materials were not cytotoxic. In the heart valve scenario, the proliferation of fibroblasts should ensure good colonisation around the sewing ring, and possibly aid the fibrous encapsulation of the leaflets which may reduce the rate of calcification. *In situ* endothelialisation from anastomoses over distances greater than 10 mm is unlikely. Further work should evaluate the response of endothelial and monocyte-macrophage cultures to surface contact.

The addition of a heparin coating is well known for improving haemocompatibility by reducing the hydrophobicity of polymer materials (Goosen and Sefton, 1979), as well as having a biological interaction with plasma proteins (Amiji and Park, 1993). The reduction in protein adsorption, as measured by assay and observed under SEM, helps to reduce coagulation and inflammatory activation, resulting in the most haemocompatible material in these tests.

These experiments were limited to 90 minutes of circulation, and so the long term performance of the heparin coating was evaluated separately. The *in vitro* ageing indicated that some heparin may be lost during the washing phase, followed by a slow release of heparin over a period of weeks and months. This is the first reported study on the durability of heparin coating on dynamically strained substrates. Dynamically stretching the polymer did increase the water contact angle, but there was no statistically significant change in S 2P surface concentration, indicating that dynamic strain may not in fact accelerate the loss of heparin. On the other hand, ageing in hydrogen peroxide destroyed the coating, suggesting that macrophages may affect the coating. The durability of the Corline Heparin Surface on pyrolytic carbon was evaluated by Kristensen et al. (2006) using XPS and antithrombin binding capacity. Although they also observed a loss in heparin conjugates from the carrier chain after 3 weeks of continuous high shear flow, there was no reduction in antithrombin binding capacity.

The inactivation of heparin via ion-exchange mechanisms with endogenous cations and proteins has also been reported suggesting that long term performance is unlikely to be satisfactory even if heparin is not leached from the surface (Amiji and Park, 1993). Heparin may mediate the short and medium term response and ideally aid the formation of a stable fibrous capsule, but long term performance requires further investigation, particularly for this polymeric substrate.

3.4.1 To anticoagulate?

I have also to consider whether there was a bias in my selection of healthy donors, who may not be clinically representative of patients receiving a prosthetic heart valve (Vienken, 2008). Furthermore, even when bioprostheses are implanted, patients are typically prescribed a mild anticoagulant, aspirin or clopidogrel for example. To investigate whether this resulted in any significant effects, I added 20 mg l^{-1} aspirin to blood from just one donor. Following the same method as detailed in Section 3.2 the heparin coated BCP was tested for haemocompatibility in blood anticoagulated with salicylic acid.

Anticoagulation of the blood samples led to a reduction in all measures of coagulation activation and inflammation after rotation in the Chandler Loop. Anticoagulation of blood did not affect the haemocompatibility parameters for blood which was contacted with the heparin coated material. Overall, the addition of aspirin makes the testing method less sensitive to differences between materials.

Low-dose aspirin is prescribed for post-operative patients as an antiplatelet drug due to its ability to inhibit the production of thromboxane and prostacyclin. Both are lipids

which can be found in platelets, and are involved in platelet activation. The activated form, thromboxane A₂, has prothrombotic properties; it stimulates the activation of new platelets and increases platelet adhesion. Aspirin inhibits the ability of cyclooxygenase I enzyme to synthesize thromboxane and prostacyclin (Kyrle et al., 1987). The heparin coated material activates antithrombin, leading to an inhibition of thrombin and factor Xa which breaks the coagulation cascade, making the anticoagulating action of aspirin futile.

In summary, anticoagulation is unlikely to mediate impact of implanting a heparin coated BCP, however, the thrombus-inducing shear stresses may still warrant anticoagulation after the implantation of polymer leaflet heart valve.

3.5 Conclusion

I tested a shortlist of nano-cylinder forming BCP with favourable mechanical properties for haemocompatibility and cell viability according to ISO 10993, with a view to their use in polymer-based prosthetic heart valves. None of the BCP test materials elicited an adverse host response in haemocompatibility or direct fibroblast contact results. In conclusion, I am able to rank the materials, as shown in Table 3.1.

Table 3.1: Qualitative ranking of tested materials for activation of the coagulation cascade and inflammatory reaction

Least activation of the coagulation cascade	
Heparin Coated SEPS22	Least acute inflammatory reaction
Bovine Pericardium	Heparin Coated SEPS22
ePTFE	SEPS22, SI/BS19, SIBS30, SIS30, ePTFE
SEPS22, SI/BS19, SIBS30, SIS30	Bovine Pericardium, Polyester
Polyester	Greatest acute inflammatory reaction
Greatest activation of the coagulation cascade	

The uncoated BCPs performed better than polyester reference material in terms of coagulation, platelet activation and inflammation, indicating that their haemocompatibility should be sufficient for use in a prosthetic heart valve. One of the BCPs, SIBS, has received considerable attention as a *haemocompatible* material (Pinchuk et al., 2008): in this

study, I show that this accolade may be extended to several other BCPs. Furthermore, the addition of a heparin coating results in a significant improvement in haemocompatibility parameters. The heparin coating was found to be largely still present after 3 weeks of testing under dynamic stretching in PBS, although it was degraded after contact with oxidants. Based on these results, none of the tested BCP should be eliminated on the grounds of haemocompatibility. Relative to bovine pericardium, the BCP are less inflammatory, and further development of the valve can continue to use SEPS22, as selected in Chapter 2.

Chapter 4

Calcification

4.1 Introduction

The principle cause of aortic stenosis is calcification of the valve. Calcification involves the nucleation and growth of calcium phosphate crystals, necessary for bone, but unwanted elsewhere. Although extracellular calcium concentrations mean that the solubility product is reached for several calcium salts, active cell mechanisms have evolved to limit nucleation and propagation of calcium deposits in healthy, soft tissues. Pathological valves and prostheses lack these processes making them susceptible to calcification (Siddiqui et al., 2009).

In this chapter I first review the calcification of native valves before going on to consider bioprosthetic and polymeric valves. Based upon this review, a novel testing device is designed and built. This is used to determine the propensity of BCPs to calcify and the effect that this has upon the material's function.

4.1.1 Calcification of native valves

Researchers have long sought to determine the aetiology and mechanisms of native valve calcification such that it may be predicted, prevented, and cured. In 1663 Rivière reported “caruncle-like masses obstructing the left ventricular outflow to the aorta”, and in 1846 Hasse suggested that degenerative valve disease was a result of valve ossification. Möenckeberg’s description of valvular calcification in 1904 was the first to identify the deposition of calcium-phosphate on the leaflets, causing sclerosis (Leopold, 2012).

Aortic stenosis caused by calcification is the dominant pathology of the aortic valve:

it outnumbers cases of regurgitation by three to one in developed countries (Iung and Vahanian, 2011). During stenosis, the aortic valve thickens and stiffens, with calcific nodules forming on the aortic side of the leaflets. Brittle crystals are formed on the leaflets by the most thermodynamically stable calcium-phosphate structure, hydroxyapatite, $\text{Ca}_{10}(\text{PO}_4)_6(\text{OH})_2$. Hydroxyapatite (HAp) is the most abundant crystal form in bone, though bone also contains carbonate and magnesium crystals, crystal defects, and other types of crystalline structures making it more of a “bioapatite” (Chakraborty et al., 2006; Demer and Tintut, 2008).

Calcific nodules are certainly associated with the macroscopic stiffening of aortic valves and other tissues, but it appears as though HAp particles are present long before the manifestation of disease. Bertazzo et al. (2013) used nano-analytical electron microscopy to examine calcified and non-calcified human leaflets. They found spherical (500 nm to 5 μm diameter) particles on leaflets before any other symptoms of calcification such as stiffening and fibrosis. These HAp spheres were not seen in bone, and they were in fact more crystalline than bone, suggesting that therapeutic dissolution of these nucleation points would be impossible without also dissolving bone.

HAp particles seem to be present in all valves, but osteogenic cells are certainly involved in the heterotopic ossification of pathological leaflets (Egan et al., 2011). Circulating osteogenic precursor cells can be found at the valve, along with native aortic valve stromal interstitial cells and both morph into an osteoblast bone-like phenotype responsible for the bone-like calcifications (Cho and Kim, 2009; Giachelli et al., 2005; Rajamannan et al., 2011).

Although the stiffening and calcification of valves shares the characteristics of inflammation and the presence of bone morphogenic proteins with atherosclerosis, valvular pathologies are distinct (Akat et al., 2009). Most prominently, statins appear to be a miracle drug with respect to atherosclerosis, but no benefit has been seen in treatment of human valvular disease (Amann, 2008; Ehrenstein et al., 2005; Farzaneh-Far et al., 2001; Helske and Kupari, 2007; Hermans et al., 2010). The finding of cells that cause calcification certainly aids the search for new therapies to prevent or halt the progression of valvular calcification (O’Brien, 2006), but it is impossible to know whether these cells might cause the calcification of a polymeric prostheses.

4.1.2 Calcification of bioprostheses

Calcification is also associated with bioprosthetic valve failure. Pure stenosis as a result of calcification leads to 10-15% of failures in porcine bioprostheses. 75% of failures are

caused by tears, which are accompanied by calcification, and are manifested haemodynamically by regurgitation (Siddiqui et al., 2009). During analysis of explanted bioprostheses from both humans and animals, antibodies and mononuclear inflammation were detected, indicating that inflammatory and immune processes play a role in calcification. However, calcific valve failure does not satisfy Koch's Postulates of disease (Anderson et al., 2004). There was no significant difference in the mineralisation of subcutaneously implanted bioprosthetic valve leaflet material in mice with or without an immune system. This implies that the observed inflammatory response is more likely to be a secondary response to valve damage rather than a cause of failure (Levy et al., 1983; Schoen and Levy, 2005).

In the native healthy valve, active inhibitors and calcium ion pumps reduce the concentration of calcium from approximately 10^{-3} M extracellular to 10^{-7} M intracellular, limiting crystallisation of the ECM. The tissue of a fixed bioprosthetic valve lacks these active cell processes. Furthermore, the fixed tissue abounds with nucleation sites such as phosphate lipids in the dysfunctional cell membranes, alkaline phosphatase, and collagen and elastin fibres (Levy et al., 1983; Schoen and Levy, 1992, 2005; Siddiqui et al., 2009). Indeed, when bioprosthetic valve material is placed subdermally in rats, mineral deposition commences within 24 to 48 h (Schoen et al., 1986).

Full calcification of bioprostheses takes ~ 2 years in children and ~ 13 years in young adults suggesting that bioprosthesis calcification is limited by crystal growth rather than nucleation. Calcification is faster in younger patients due to higher levels of extracellular phosphate (Jono et al., 2000), and their more active immune system which causes more fibrocalcification (in which a combination of inflammatory and osteogenic cells are implicated) (Hopkins, 2006; Weiss et al., 2013).

The dynamic valve environment also plays a role in bioprosthetic valve calcification. Calcified nodules are known to localise to regions of high mechanical stress. Flexure and shear lead to the the disruption of collagen fibres which then serve as foci for calcium-phosphate nucleation (Bernacca et al., 1992a; Thubrikar et al., 1983). As such, stress reductions can lead to significant improvements in bioprosthetic heart valve durability.

Anticalcification treatment of bioprostheses can disrupt calcification by removing dead cell debris, phospholipids, and other lipids; modifying collagen structure or chemistry; or restoring of glycoaminoglycans (Schoen and Levy, 2009). Specifically, tissue treatments have used ethane hydroxybiphosphonate, α -amino-oleic acid, ferric or aluminium chloride exposure, or sodium dodecyl sulphate (Vyavahare et al., 1997a). In my experiments I opted to use an ethanol incubation step after glutaraldehyde fixation to alter the amide groups of collagen and remove cholesterol and phospholipids, which has been shown to

significantly reduce calcification (Vyavahare et al., 1997b).

4.1.3 Polymeric valve calcification

Calcification was reported in 6 of the 27 polymeric prosthetic heart valve trials listed in Section 1.8. Of these, failure as a result of calcification was reported in the valve made from SIBS with embedded PET fabric and dimyristoyl phosphatidylcholine coating (Wang et al., 2010) and a polyurethane valve (Hilbert et al., 1987). Calcification has also been reported as a cause of failure for the polymeric membranes of total artificial hearts (Imachi et al., 2001; Yang et al., 1999).

On the one hand, like bioprostheses, polymers lack the active ion pumps of living tissue. On the other, polymers do not contain the phosphorus rich cell debris and disrupted collagen that encourages nucleation. On blood contacted polymeric surfaces two types of calcification have been identified. First, heterogeneous nucleation of calcium-phosphate crystals can occur on the surface or at the interface between the leaflet surface and microthrombi or fibrous sheaths; this mechanism will be referred to as surface calcification. Second, degenerated cells, which are found in thrombotic material or the fibrous sheath, can become calcified; which will be referred to as calcification of adsorbed (biological) matter (Hilbert et al., 1987).

Pettenazzo et al. (2001) performed a comparison of *in vitro* and *in vivo* calcification of bioprostheses. For the *in vitro* environment the valves underwent accelerated pulsatile testing in a simulated body fluid with no biological material. The *in vivo* valves were identical St. Jude Medical bioprostheses which had failed and been explanted. Using SEM and X-ray powder diffraction (XRD), they showed that very similar hydroxyapatite-octacalcium phosphate deposition occurred in both cases, indicating that biological mechanisms are unlikely to be causal (Pettenazzo et al., 2001). *In vitro* studies by Bernacca et al. (1992b); Boloori Zadeh et al. (2013); Hamon et al. (1982), and the *in vivo* trials of the “jellyfish” valve (Imachi et al., 2001), all considered calcification to be a surface process (as opposed to calcification of adsorbed matter).

Calcification of adsorbed biological matter is unlikely to be a major cause of failure, and so I will not consider the chemical-biological synergies in this chapter. Nevertheless, as BCP materials are less inflammatory and adsorbent than bovine pericardium *in vitro*, as well as being smoother, they should accumulate less cellular debris, making them less vulnerable to adsorbed matter calcification than bioprostheses.

It is a simpler task to isolate the factors which affect the rate of calcification of polymers,

than when biological matter is present. Heterogeneous crystal nucleation is a balance of enthalpy vs. entropy, which is controlled by the local chemical potential (or supersaturation) of the ions, the surface chemistry and morphology. The interfacial free energy at the surface is always a positive term, and destabilises small crystal nuclei. When nuclei above a critical size are formed, they may grow at the surface (DeYoreo and Vekilov, 2003).

With a view towards understanding physiological calcification of hard tissues such as teeth and bones, Liu et al. (2012) performed a fundamental study into the effect of surface functionalisation on calcium-phosphate crystallisation. Gold surfaces were functionalised with equal surface densities of $-\text{COOH}$, $-\text{CH}_3$ and $-\text{NH}_2$, and exposed to calcium-phosphate solutions. SEM, XPS and AFM were used to assess the morphology and rate of calcium phosphate deposition. They found that amine and carboxylic acid surfaces became calcified, whereas the methyl surface inhibited calcification and had a lower nucleation and growth rate than the raw gold control surface.

Two mechanisms were proposed: on negatively charged surfaces (such as the surface coated with carboxylic acid groups) Ca^{2+} were adsorbed and concentrated before PO_4^{3-} ions were adsorbed to form the crystal framework. On the positively charged $-\text{NH}_2$ surface, homogeneous clusters of Ca^{2+} and PO_4^{3-} with a negative charge imbalance were adsorbed to the surface. In both cases, once the first surface layer is formed, the modulating effect of the functional groups becomes weak and crystal growth proceeds as a function of solution concentrations and by the rate of mass transfer to the surface (DeYoreo and Vekilov, 2003).

Despite most polymer prosthetic heart valve surfaces being uncharged, calcification is still observed. Various mechanisms have been proposed to affect surface calcification, these can be divided into the following categories:

- Biological (without surface debris): native calcification inhibitors are removed, whilst proteins with an affinity for calcium transport calcium-phosphate to the valve site (Anderson, 1981; Fisher and Termine, 1985).
- Chemical cation complexation: calcium forms complexes with appropriate functional groups within the biomaterial, polyether soft segments of polyurethanes for example, which then sequester phosphate to maintain charge neutrality, resulting in the deposition of insoluble calcium phosphate within the material (Hamon et al., 1982; Long and Urry, 1981).
- Mechanical: high cyclic stress and strain results in macromolecular breakdown, exposing calcium binding sites (Harasaki et al., 1987; Thubrikar et al., 1983), and microcracks

(Imachi et al., 2001) in which calcium-phosphate nucleates.

- Surface morphology: rough surfaces promote nucleation (Bolori Zadeh et al., 2013).

Regardless of polymer type or valve design the proposed prosthesis will not contain active cells, and thus no native calcification inhibitors will be present. Therefore the biological hypothesis does not need to be tested in the following experiments. The chemical cation complexation mechanism will be considered by testing various types of polymer and coating. Similarly, mechanical mechanisms and surface morphology will be considered, as they can be controlled by valve design and manufacture respectively.

Cyclic strain is necessary in *in vitro* models. Bernacca et al. (1992b) observed negligible calcification in static tests on polyurethane, but the same materials calcified significantly under cyclic strain in a valve, eventually failing. In the absence of mechanical strain, artificial surface defects and roughness on Angioflex (a proprietary polyether based polyurethane) increased the rate of calcification (Bolori Zadeh et al., 2013). Bernacca et al. (1992b) and (Imachi et al., 2001) both observed calcification deposits localising to areas of high strain. Imachi et al. (2001) hypothesised that repetitive strain may create (micron-sized) cracks in the polymer surface exposing previously covered calcium binding sites, allowing calcium or phosphate ions to congregate, precipitate, stiffen the material and lead to further breakdown.

None of the aforementioned studies make a distinction between polymeric prosthesis calcification which leads to stiffening and stenosis, and calcification that is associated with tearing and regurgitation. Presumably stiffening of polymeric materials can lead to tearing during flexure. In the following experiments the effect of calcification on mechanical properties will be considered. Furthermore, I will aim to find out whether polymer mechanical fatigue, or calcification cause failure (Bernacca et al., 1992b).

4.1.4 Polymer anticalcification strategies

In response to the failure of several polymeric heart valves, various anticalcification strategies have been tested. The segmented polyurethane, Biospan[®], received a biphosphonate-diethylamino coating (via bromoalkylation). Biphosphonates are well known to block the growth of hydroxyapatite, whilst the diethylamino groups reduce the water uptake of the polyurethane, improving the elastomer's durability and successfully improving the valve (Alferiev et al., 2003).

The grafting of sulfonated poly(ethylene oxide) to the polyether polyurethane (Pellethane 2363-80AE) reduced calcium deposition on leaflets implanted in a dog by more than 50%

(Han et al., 2006). The sulfonated poly(ethylene oxide) groups are highly dynamic, hydrophilic, and negatively charged, possibly repelling the phosphate groups. Bernacca and Wheatley (1999) applied heparin, taurine, 3-aminopropyltriethoxysilane and polyethylene oxide surface modifications to polyetherurethane (chain extended with either butanediol or ethylene diamine). They reported that polyethylene oxide modification led to a lower durability and greater calcification, whilst the other modifications improved durability.

The UCL group tested the anticalcification potential of polyhedral oligomeric silsesquioxane-poly(carbonate-urea)urethane (POSS-PCU) relative to glutaraldehyde-fixed bovine pericardium and polyurethane, using an in-house accelerated pulsatile pressure device to load membranes of equal thickness of the materials to 120 mmHg. The polyhedral oligomeric silsesquioxane separates into nano-sized particles in the polymer, which increases the tensile and tear strength of the material, as well as reducing hydrophilicity and water absorption. In their study the POSS-PCU material calcified less, and had a smaller change in mechanical properties than the polyurethane reference sample (Ghanbari et al., 2010). As the authors did not run the experiment without the calcium and phosphate ions, it is impossible to ascertain to what extent the acceleration of degradation could be attributed to calcification. Furthermore, polyurethane has a lower modulus than POSS-PCU, meaning that polyurethane strained more than POSS-PCU under equal pressure, indicating that larger or more micro-cracks may be formed in polyurethane.

4.1.5 Calcification testing

It is generally accepted that *in vitro* models of calcification are an acceptable model for *in vivo* studies if ion concentrations are maintained at physiological levels (single batch testing being unacceptable) (Park et al., 2000), and materials are dynamically loaded (Bernacca et al., 1992b; Krings et al., 2006; Mavrilas, 2004; Mavrilas et al., 1999; Pettenazzo et al., 2001). There is no consensus regarding the composition and control of the calcifying solution. Some studies have used physiologically representative buffered solutions which produce realistic bioapatite structures containing other ion defects (such as magnesium and carbonates) (Golomb and Wagner, 1991; Starcher and Urry, 1973), while others have removed the buffers, and used control of pH to maintain appropriate concentrations of calcium and phosphate ions (Kapolos et al., 1997; Krings et al., 2006). In the pH control method, the measurement and control of pH allows the calcification rate to be inferred for single samples.

ISO 5840 now mandates calcification testing of devices prior to accreditation, but given the widespread occurrence of calcification, a rational design methodology for prosthetic

heart valves should evaluate the potential of *materials* to calcify. The screening mechanism should recreate physiological tensile strains (10 – 15% (Balachandran et al., 2011)) and bending ($\sim 10\%$ (Corden et al., 1995)), in a physiologically representative chemical and thermal environment.

4.2 Materials and methods

4.2.1 Calcification

A novel calcification device was fabricated in the Department of Chemical Engineering and Biotechnology, University of Cambridge. The device, shown in Figure 4.1, allows up to 21 samples to be simultaneously flexed and strained whilst immersed in calcifying solution. The device is made from 10 mm PMMA, and the samples are secured using PMMA washers and polystyrene screws (to reduce the dissolution of unwanted ions).

BCP materials (SIBS30, SI/BS19, SIS18, SIS30, and SEPS22) were manufactured by compression moulding as previously described (see Section 2.2). Dynamically strained oriented samples were stretched in the stiff direction. For comparison, SIBS30 was also solvent cast. In a second run, performed under my supervision by Miranda Xu and Andrew Cheung, the calcification of heparin coated SEPS22 was evaluated (Corline Heparin Surface, as previously described in Section 3.2.2). Porcine pericardium tissue was obtained from a local slaughterhouse (Huntingdon Life Sciences). The tissues were washed in phosphate buffered solution before fixation in glutaraldehyde solution: 0.4% for 48 h followed by 0.2% for 1 week. A selection of the pericardium samples underwent anti-calcification treatment using 80% ethanol (Vyavahare et al., 1997b), these being referred to as Pericardium AntiCa. The reference polyurethane, Pellethane 2363-80AE (further details in Section 2.2), was also formed by compression moulding.

Samples measuring $50 \times 8 \times 0.5$ mm were cut using a straight blade and mounted either on a static plate or on the deflection device. The plate and device were placed in a plastic container holding the calcifying solution. The container was placed in a water bath which was held at 37°C . Between experiments the container and stretching device were washed using 0.1 M nitric acid.

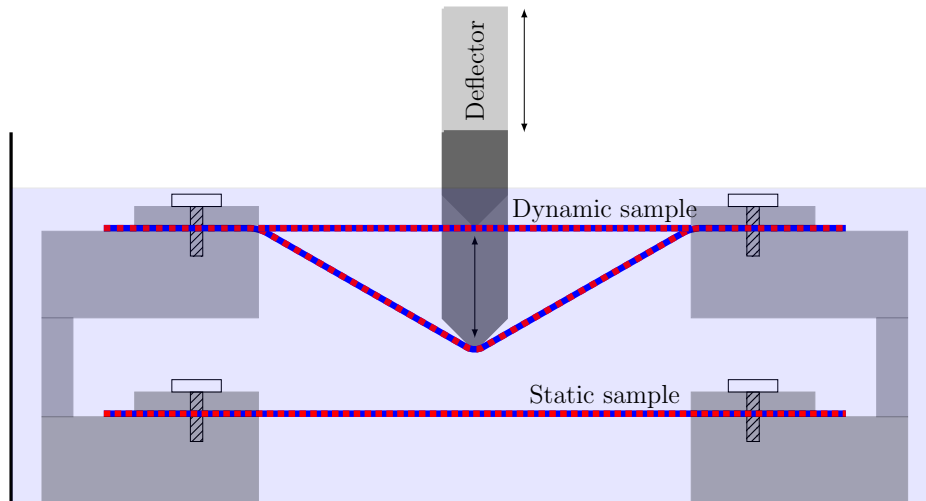


Figure 4.1: Cross section detail of the novel calcification device showing the 3-point bend and static test positions and mounting systems immersed in calcifying solution. The polymeric samples are indicated by the red-blue lines. The deflector for dynamic testing is driven by a rotating cam. The static samples are situated directly below the strained samples.

Calcifying solution

The calcifying solution contained ions at the concentrations listed in Table 4.1. The solution was brought to pH 7.2 using HCl solution. All reagents were purchased from Sigma Aldrich (Gillingham, UK) and solutes were dissolved in reverse osmosis water. The solution was changed every 3 days during the experiment to maintain the electrolyte concentrations and pH. Samples were also tested in a solution that did not contain Ca^{2+} or HPO_4^{2-} ions (“non-calcifying solution”), but was otherwise identical.

4.2.2 Analysis of calcification

After calcification, samples were briefly rinsed in distilled water. The samples were cut from the device and dried before the calcium-phosphate deposits were dissolved by placing the samples in 0.5 M nitric acid solution. Calcium concentration has been evaluated by other authors using inductively coupled plasma (Bolori Zadeh et al., 2013), colorimetric assay (Ghanbari et al., 2010), and atomic absorption spectrometry (AAS) (Brockbank and Song, 2003; Pettenazzo et al., 2001). I selected AAS (using Varian AA 240, now Agilent) for accuracy and speed. In AAS, the atomised solution absorbs at a particular wavelength. While absorption should be linearly related to the ion concentration via the Beer-Lambert law, this is rarely the case. A rational curve (Equation (4.1)) was fitted to

Table 4.1: Ion concentrations in calcifying solution and their plasma equivalents. The solution was brought to pH 7.2 using HCl solution.

Ion	Calcifying ion concentration (corresponding plasma concentration (Kokubo, 1990)) (mM)
Na ⁺	142 (142)
K ⁺	5 (5)
Mg ²⁺	1.5 (1.5)
Ca ²⁺	2.5 (2.5)
Cl ⁻	128 (103)
HCO ₃ ⁻	27 (27)
HPO ₄ ²⁻	1 (1)
MOPS buffer	5

the calibration readings using OriginPro 9 software.

$$\frac{a}{c} = P + Qa + Ra^2, \quad (4.1)$$

where a is the measured absorption, c is the concentration of the solution, and P , Q , and R are curve fitting parameters.

Tensile testing

The flexural stiffness of polymers was tested before and after static calcification using a 3-point bend fixture (Texture Analyser, Stable Microsystems, Surrey, UK).

Scanning electron microscopy

After calcification testing, dried polymeric samples were imaged using scanning electron microscopy (SEM), with elemental ratios assessed using energy dispersive X-ray (EDX).

Atomic force microscopy

Sample roughness was evaluated using atomic force microscopy (AFM) (Veeco Dimension 3100, NY, USA). The root-mean-squared height at four spots on each sample was used to characterise surface roughness. AFM measurements were performed by Miranda Xu and Andrew Cheung, whose masters' research project I supervised.

4.3 Results

4.3.1 Calcium surface concentration

The surface concentration of calcium on samples is shown in Figure 4.2. Dynamic strain resulted in a statistically significant increase in calcification for all polymeric samples (Student's *t* test, $p < 0.05$). Absolute surface concentrations could not be compared between the three runs, I, II, and III, as the mechanical, chemical, and thermal conditions were not identical. In Figure 4.2b the calcium surface concentration after dynamic III on the heparin coated SEPS22 is significantly lower ($p < 0.05$) than upon the uncoated polymer.

4.3.2 SEM and EDX

A selection of SEM images are presented in Figure 4.3. The extent of crystallisation is much greater on the dynamic BCP samples than on the static ones. Surprisingly, on the static BCP sample surfaces (Figures 4.3b and 4.3d) a “mud cracking” pattern is present, but could not be found on the BCP control samples. On the dynamic samples, the surface cracking could only be found where the calcium phosphate layer was thin. Contrary to expectations, such as according to the surface morphology hypothesis, crystalline deposits did not localise to the cracks. The “mud cracking” surface feature could have been caused by chemical or environmental attack (Hayes et al., 2015). This behaviour was also seen on samples tested in the Chandler Loop for their haemocompatibility (Figure 3.2). Surface cracking was observed on both the more durable (saturated and coated) polymers and the unsaturated BCPs, which failed.

Liu et al. (2012) took images of calcification on uniformly functionalised surfaces of $-\text{NH}_2$ and $-\text{CH}_3$. In comparison to their images, those produced here do not resemble the globular deposits caused by homogeneous nucleation as seen on the functionalised surface. Furthermore there was an absence of a uniform HAp layer on the surface which developed on their $-\text{COOH}$ surface. The more dense and uniform distribution of crystals observed on dynamic materials may result from fluid shear forces removing larger particles.

Analysis of the elemental concentrations of the crystals revealed Ca, P, Mg and Na in decreasing concentrations. The atomic ratio of calcium to phosphorus indicates the calcium-phosphate crystalline state. In HAp, $\text{Ca:P}=5:3$. The mean ratio over all samples was 1.96:1, with some points containing Ca-P ratios greater than 3:1, suggesting that fully developed HAp was yet to form. EDX measurements performed by Pettenazzo

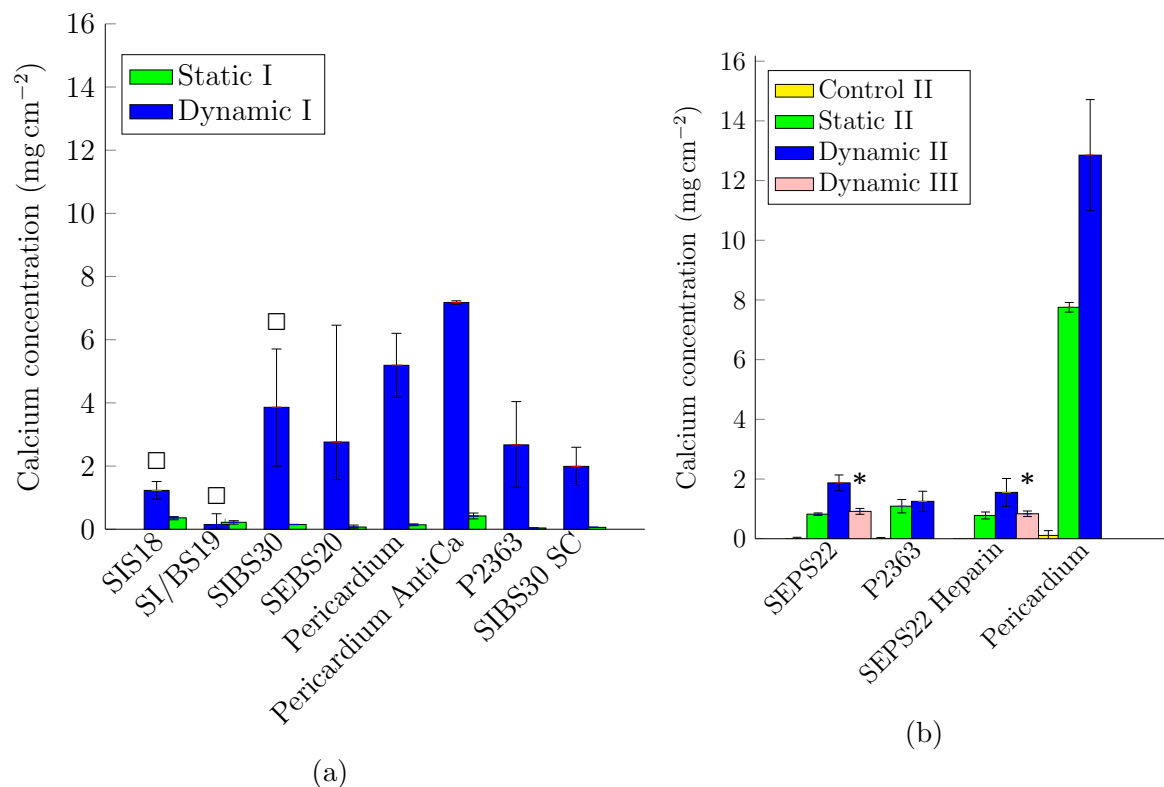


Figure 4.2: Results from the measurements of calcium on the samples. (a) shows the surface concentration of calcium on the test materials after 12 days in solution. The error bars indicate the minimum and maximum recorded values (3 to 5 samples per material). The \square symbol is used to indicate the samples that failed during testing. (b) shows the calcium surface concentrations for a smaller range of materials in experiments performed by Miranda Xu and Andrew Cheung. One experiment (bars marked II) was run with all materials (Control, $n=5$; Static, $n=5$; Dynamic, $n=5$). A second experiment (Dynamic III) concentrated on SEPS22 and heparin coated SEPS22 ($n=10$). In both experiments the materials were calcified for 8 days, but there were fluctuations in temperature. The error bars indicate the standard deviation of readings. The bars marked with * are significantly different from one another (Student's t-test, $p < 0.05$). Full details on the polymers can be found in Table 2.2.

et al. (2001) of calcified bioprostheses indicated that octacalcium phosphate ($\text{Ca:P}=4:3$) was formed before HAp, though their study was considerably longer (44 vs. 8 days). The authors also suggested that amorphous calcium-phosphate was a precursor to octacalcium phosphate and HAp on the valve. Amorphous calcium phosphate is formed with $1:1 < \text{Ca:P} < 11:5$, which could account for the high ratios measured here (Dorozhkin, 2009). The presence of magnesium (with the modal $\text{Ca:Mg}=11:1$) suggests that whitlockite ($\text{Ca:Mg}=9:1$), the second most abundant crystal form in bone, may be present. This mixed elemental composition of the crystalline deposits is indicative of bioapatite.

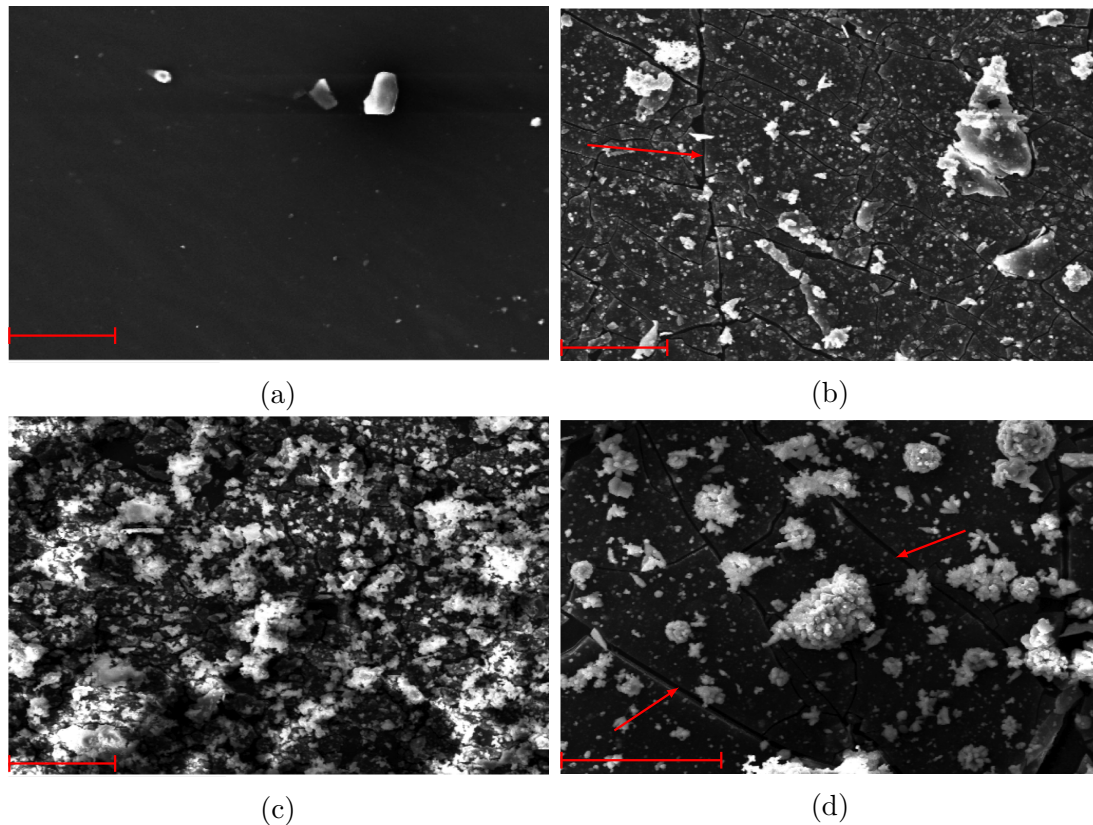


Figure 4.3: SEM micrographs of BCP samples before and after calcification. Image (a) is an uncalcified sample, showing a potential surface defect or contaminant upon which crystals might seed. Image (b) is statically calcified SIBS30, (c) is dynamically calcified SIBS30, and (d) is statically calcified SIS18. Most of the white deposits on the surface show calcification. The scale bar indicates 50 μm . The red arrows in (b) and (d) indicate cracks on the surface of the static samples which, contrary to expectations, the calcium-phosphate crystals did not localise to.

4.3.3 Effect on mechanical properties

Calcification of prosthetic heart valves can lead to sclerosis or tearing. During my first calcification study, the SIS18, SIS30, SEBS20, and SI/BS19 samples failed due to tearing or cracking within 5 days or 9×10^5 cycles (Figure 4.4). Tears occurred near to the deflector. Split samples were sutured together to continue their dynamic movement. All dynamically strained samples crept during the test, which aided the survival of some samples.

In the second set of calcification studies, SEPS22, heparin coated SEPS22, P2363 and pericardium were tested. Some of the coated and uncoated SEPS22 polymer also failed during this test. However, failure rates should not be compared between the runs as strain varied. Table 4.2 shows that the heparin coating brings about a marked improvement

in the polymer's durability. Furthermore, a greater proportion of SEPS22 samples failed in calcifying solution than in the non-calcifying solution, indicating that calcification *accelerated* failure for this uncoated polymer.

The root mean squared roughness of SEPS22 and heparin coated surfaces was measured to be $255 \pm 118\text{nm}$ and $128 \pm 42\text{nm}$, respectively. The uncoated surface was significantly rougher (Student's t-test, $p < 0.95$) than the coated surface, which may contribute to the higher calcium concentration.

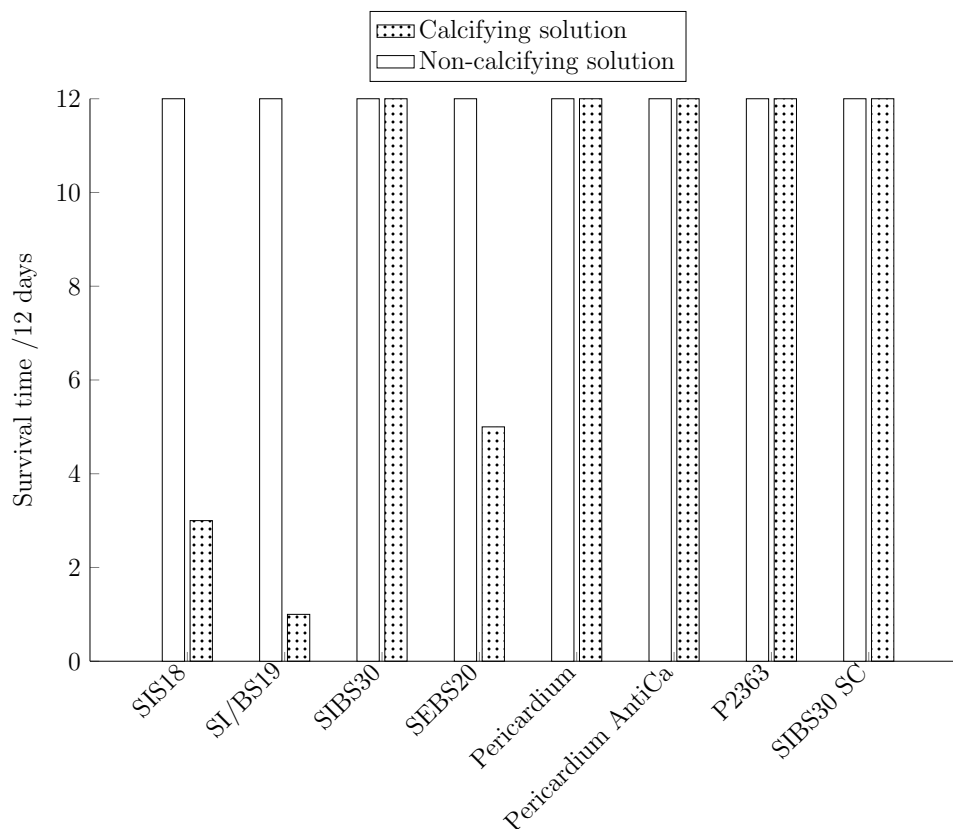


Figure 4.4: Days to failure for samples in calcifying and non-calcifying solution when dynamically strained at 2 Hz. Bars which reach 12 days correspond to samples which did not fail. There were 3 to 5 samples of each material and the bars are shown as an average. AntiCa indicates that the pericardium underwent anticalcification treatment. Full details on the polymers can be found in Table 2.2.

To investigate the stiffening of polymers, secant moduli (at 5, 10, 20% strain) were measured before and after calcification of statically mounted samples. Figure 4.5 shows that despite a large variation in surface calcium concentration, samples stiffened by a uniform amount of 0.1 to 0.2.

Table 4.2: Proportion of samples surviving immersed durability tests in calcifying and non-calcifying tests, as performed by Andrew Cheung and Miranda Xu.

Material	Number of samples failed in test period	
	Calcifying solution	Non-calcifying solution
SEPS22	12/15	4/5
SEPS22 Heparin	5/15	3/10
P2363	0/5	Not tested

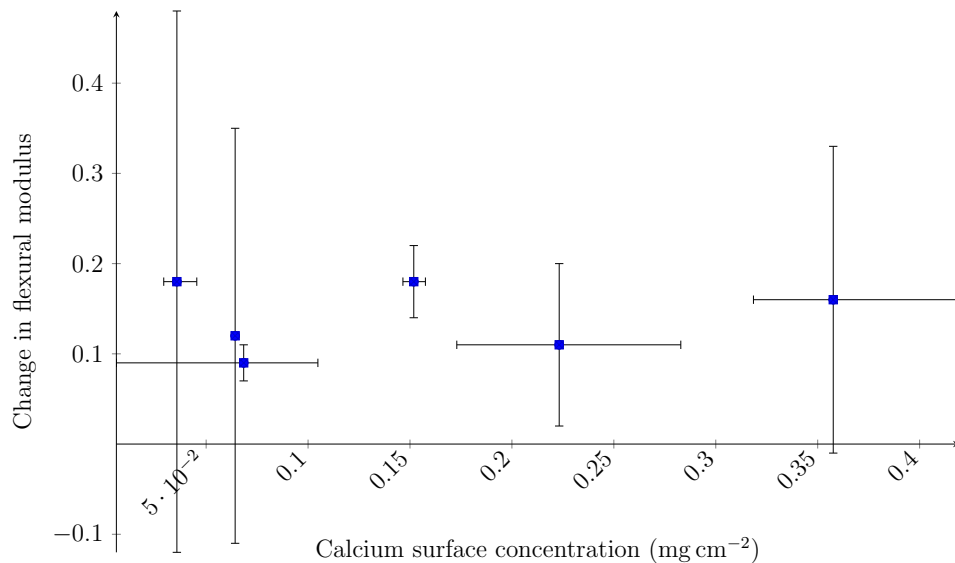


Figure 4.5: Proportional change in secant moduli (5, 10, 20%) of uncoated polymeric materials after static calcification as a function of the calcium surface concentration. Each point represents a polymeric material, and error bars represent the range of values.

4.4 Discussion

The synergy of mechanical stress and calcification is well documented and so the calcification of valves is affected by the stress distribution. As such, calcification studies should isolate material effects from design. The calcification of isolated heart valve materials by Bolori Zadeh et al. (2013), Mavrilas (2004), and Park et al. (2000) used a continuous flow of solution, or calcium and phosphorus levels were topped-up by each of these authors, but none dynamically strained the material. Ghanbari et al. (2010) are the only authors to dynamically strain isolated heart valve materials. Their test system design marks a significant improvement in calcification testing, and demonstrated that the group's material, POSS-PCU, was superior to polyurethane and pericardium. No anticalcification treatment was applied to the pericardium, as is now commonplace among bioprostheses. The samples underwent tensile strain as opposed to flexure - an important deformation in prosthetic heart valve calcification. Also, the softer polyurethane would have been

strained significantly more than POSS-PCU, whereas in an *optimal* heart valve softer materials allow for thicker leaflets, reducing the stress and strain during diastole (refer to Chapter 2 for further information).

In response to these shortcomings I proposed a novel device to improve the simulation of material calcification *in vitro*. In the device, a large number of immersed samples (up to 21) simultaneously undergo a 3-point bend. Deflection was tuned to achieve physiological strains of tensile (10 – 15%) and bending ($\sim 10\%$), in a physiologically representative chemical and thermal environment. The device successfully strained samples and accelerated their calcification. Unfortunately, sample creep resulted in changes in stress and strain over time which the fixed displacement deflector could not adjust for. An improvement would be to retain the 3-point flexure characteristics, but use constant cyclic pressure or stress.

Dynamically straining materials led to a large increase in the rate of calcification on all materials. Pericardium samples calcified significantly more than polymeric samples. Despite the sample size being limited no large differences were observed when treated and untreated pericardium were compared.

Heparin is the most negatively charged biological molecule, implying that it could promote the adsorption of Ca^{2+} ions and accelerate calcification. In fact, the heparin coated surface calcified significantly *less* than the uncoated SEPS22. It was a surprise to observe that the heparin coating led to a significant improvement in the durability of the polymer. When I previously imaged blood contacted heparin coated SEPS22 (Figure 3.2), cracking was visible beneath the confluent protein layer.

Submerged polymers failed during dynamic straining. Using some polymers can lead to environmental stress cracking (ESC) under some conditions. Solvents with a similar solubility parameter to the polymer lead to crack tip softening, causing crazing at the crack tip and ultimately leading to crack growth and failure (Wright, 1996). The mud-cracked surface that I observed in my samples seems to have an environmental cause as it occurs in both blood and water, but is unlikely to be true ESC as no solvents are present. Further experimentation should evaluate whether solvent cast polymers (which have a smoother surface and fewer frozen-in stresses) also exhibit surface mud-cracking upon contact with aqueous solutions.

Bernacca and Wheatley (1999) reported an improvement in polyurethane durability after heparin coating. Among hydrophilic polyurethanes, coatings which reduce water absorption can lead to durability improvements (Alferiev et al., 2003). This mechanism however, is unlikely to be at work in SEPS22 as it has a very low water absorbency and is quite

hydrophobic (water contact angle $\sim 90^\circ$). In my experiments there was contact with a rigid bar, and in the valve there is leaflet-leaflet contact. I suggest that the heparin coating reduces surface wear during contact.

In Figure 4.5 I showed that among the polymeric samples which were statically calcified, the change in stiffness of the sample was not related to the surface concentration of calcium. Over a 7-fold variation in the surface concentration, the stiffness of each material increased by a uniform 10 to 20%. This result suggests that the concentration of calcification is not the only marker of a change in mechanical properties.

Ghanbari et al. (2010) reported that polyurethane samples were *weakened* after calcification testing as they displayed only 25% of their original tensile strength. However this could be attributed to mechanical rather than chemical fatigue in their experiment. POSS-PCU retained its tensile properties (despite also calcifying). In my study, calcification led to stiffening of static samples, and snapping of flexed samples. As such, I propose that calcification fills surface defects: this makes polymers stiffer when flexed and eventually causing their failure, but has little effect their properties in tension. This proposition is well aligned with the observations made of porcine bioprostheses which typically sclerose or tear at regions of flexure (Siddiqui et al., 2009).

Various hypotheses have been proposed to account for the difference in calcification rate between polymers (see Section 4.1.3): mechanical (Harasaki et al., 1987; Imachi et al., 2001; Thubrikar et al., 1983), chemical (Hamon et al., 1982; Long and Urry, 1981), surface morphology (Boloori Zadeh et al., 2013), and biological (Anderson, 1981; Fisher and Termine, 1985). Micron-sized surface cracks were observed upon my materials but calcium-phosphate crystals did not localise to them. Assuming that the cracks were present during calcification, this counters the micro-crack theory of Imachi et al. (2001).

Bernacca et al. (1992b) questioned whether calcification or mechanical fatigue was causal of failure. A higher proportion of coated and uncoated SEPS22 samples failed under calcifying conditions than non-calcifying conditions indicating that calcification can accelerate failure. It is well known that strain reduction certainly improves leaflet durability (see Chapter 2 for further details). Strain reduction also reduces calcification, though it is unclear at what point a reduction in calcification reduces either tearing or stiffening. Further work would need to investigate the quantitative relationship between (cyclic) strain and calcification rate to ascertain whether there is a critical strain level at which calcification becomes accelerated. With regard to informing the design of the prosthetic heart valve, the importance of strain reduction is reiterated by these studies.

4.5 Conclusion

In my investigation of calcification I tested the effect of calcium phosphate crystals upon BCPs. Calcification stiffens the polymers, but also tears them during flex. Material calcification thus has a bearing on heart valve design. The polymers calcified significantly less than the biological materials. However, BCP durability may be compromised by immersion in solution, and further reduced by calcification. The addition of a heparin coating improved durability under both conditions, and could be used in the final valve if durability is poor.

The rate of crystallisation is the sum of nucleation, growth, and removal rates; and each one is controlled by surface chemistry, morphology, and deformations, alongside solution chemistry and dynamics. SEM images indicated that calcium-phosphate crystals did not localise to surface cracks. The rougher surface of uncoated SEPS22 corresponded with its higher calcification rate. The negatively charged heparin coating would be expected to increase calcification, on the contrary the rate was lower on heparin coated SEPS22, suggesting that more complex chemistry would need to be investigated.

Chapter 5

Valve design

5.1 Introduction

For a prosthetic valve to approach the performance of a healthy, native valve, the prosthesis' form, the material selection and the manufacture all must work in perfect harmony. Over 50 different designs of prosthetic heart valve have been implanted, yet none have come close to matching the healthy, native valve for durability and haemodynamics (Dasi et al., 2009).

The effect of the valve design on haemodynamics is the focus of this chapter. First I identify the haemodynamic measures used to assess cardiac valves and prostheses. I go on to consider the local anatomy and design constraints before reviewing previous leaflet designs that have been trialled. This leads into my proposals for valve form and I go on to identify two potential designs, which I prototyped and tested in a pulsatile flow loop. I conclude by selecting a design for full manufacture.

5.1.1 Evaluating valve performance

A pathological valve can lead to an increase in cardiac workload, and an increase in thrombus-inducing shear stresses in blood. A stenotic aortic valve does not fully open during systole, whilst a regurgitant valve leaks during diastole. In order to assess the severity of valvular pathology (which may be asymptomatic), or the function of a prosthesis, valvular performance must be assessed quantitatively. In the clinic, (transthoracic) echocardiography is the standard tool used to assess cardiac valves non-invasively. Cardiac MRI is, however, preferred for measuring the geometric orifice area (GOA) of an

open valve (Garcia and Kadem, 2006). Sonic reflections are used to detect structures in the heart, and the Doppler effect is used to measure blood flow velocities. Echocardiography gives direct measurements of velocities in the left ventricular outflow tract, upstream of the valve (indicated by the suffix $_v$), in the valve orifice (indicated by the suffix $_o$), and on the aortic side (indicated by the suffix $_a$) of the valve.

An estimate of the energy loss over the valve is often taken as a mean (systolic) (ΔP_m), or peak pressure drop across the valve (ΔP_{max}), which are inferred from velocity data (using the Bernoulli equation) (Bach, 2010).

$$\Delta P_m = P_v - P_o = 4(v_o^2 - v_v^2) \quad (5.1)$$

where P are pressures and v are velocities at the positions indicated by the suffixes. The velocities are measured in cm s^{-1} , and pressure in mmHg. The velocities can be integrated over the systolic phase to eliminate the fluid acceleration terms and give the mean gradient. The peak velocities yield the peak gradient.

The pressure gradient is dependent on the flow rate through the valve (i.e. velocity and area), and so the Effective Orifice Area (EOA) is a better measure of valve performance. EOA represents the cross sectional area of the *vena contracta* through the valve orifice and is relatively independent of flow rate (Zoghbi et al., 2009). Inaccurate measurements arise due to the increased opening of bioprosthetic valves at higher flow rates, changes in the distribution of velocities through mechanical valves, and sonographer expertise, but otherwise EOA is a good indicator of valve performance (Otto, 2012). EOA is calculated based upon velocity measurements as:

$$EOA_v = \frac{A_v \bar{v}_v}{\bar{v}_o} \quad (5.2)$$

where \bar{v} are temporal average velocities mid-systole upstream and in the valve orifice, and A_v is the flow area immediately upstream of the valve (at the annulus/leaflet nadirs).

Although EOA gives a good indication of the resistance to flow regardless of flow rate, it is highly dependent on the size of the prosthesis, and gives no information about patients' cardiovascular requirements (Garcia et al., 2004). Losses over the valve as a function of patients' cardiovascular requirements can be accounted for by using an indexed effective orifice area. Body surface area (BSA) is an excellent predictor of a patients' cardiac requirement, and can be estimated based on weight and height using the Du Bois formula (Du Bois and Du Bois, 1916). The indexed effective orifice area ($iEOA$), is calculated by taking the ratio of EOA to BSA . It is a remarkably good measure of whether a

prosthesis is functioning well in a clinical setting. $\leq 0.85 \text{ cm}^2 \text{ m}^{-2}$ is used as a cut off to indicate that a prosthesis is poorly matched for a patient, be that due to undersizing or dysfunction, both of which are termed prosthesis-patient mismatch. By indexing the EOA of a valve prior to implantation, clinicians can select more appropriate prostheses (Bleiziffer et al., 2007; Pibarot and Dumesnil, 2006).

If cardiac catheterisation is performed, or prostheses are assessed *in vitro*, both pressure and velocity measurements can be made. The combination of the Bernoulli and continuity equations forms the Gorlin formula to estimate the EOA_G of the valve:

$$EOA_G = \frac{Q}{51.6 \times \sqrt{\frac{\Delta P_s}{\rho}}} \quad (5.3)$$

Where Q is the temporal average, or root mean square, flow rate in mls^{-1} ; ΔP_s is the mean pressure drop over the valve (which is measured directly at the upstream and downstream positions) in mmHg; and ρ is the density of the fluid in g cm^{-3} . Equation (5.3) is specific to the units mentioned as it is derived from the Bernoulli equation, and the constant 51.6 is not dimensionless (International Standards Organisation, 2005).

The values of EOA which arise from the formulae in Equations 5.2 and 5.3, as used *in vivo* and *in vitro*, respectively, should not be directly compared due to the difference in measurement and flow setup (see Section 5.2.3). There do, however, exist internationally agreed standards for EOA_G measured *in vitro*. For a 23 mm diameter valve, the EOA_G must be at least 1 cm^2 (International Standards Organisation, 2005).

The above parameters are good indicators of aortic stenosis, but are less relevant during regurgitation. Regurgitation is the sum of the retrograde flow during closing (closing volume, V_c), and when closed (leakage volume, V_l). *In vivo* regurgitation is assessed by echocardiographic evaluation of the valve morphology, and the area and velocity of regurgitant jets (see Section 1.3 and Table 1.2) (Vahanian et al., 2012). The test fluid was distilled water, as per the ISO standard, although it is not an exact rheological match for blood.

Regurgitation through an aortic prosthesis is normalised with respect to stroke volume. The regurgitant fraction (R_f) can be measured *in vitro* using an ultrasonic flow meter as:

$$R_f = \frac{V_{rev}}{V_{sv}} \quad (5.4)$$

Where V_{rev} is the total volume of retrograde flow, and V_{sv} is the systolic stroke volume, over one cycle. According to ISO 5840, for a 23 mm valve, R_f must be less than 10%.

As clinicians and engineers have sought to improve the performance of prosthetic heart valves, they have identified more accurate ways of comparing valves to one another. Mean pressure gradients and *EOA* are useful, but they assume steady, lossless flow (as per Bernoulli's assumptions) and are not affected by the regurgitation through a valve. For a more general application than these limited assumptions, Leefe and Gentle (1987) proposed the use of energy loss to evaluate the performance of prosthetic heart valves. The energy loss across a valve is a function of the pressure, velocity, and flow rate, before and after the valve (Akins et al., 2008). It is relatively easy to evaluate pressure and flow *in vitro*, and so energy loss can be calculated over one cycle, assuming that there is no change in height over the valve:

$$E_{loss} = \int_{cycle} Q \left[(P_v - P_a) + \frac{\rho}{2} (v_v^2 - v_a^2) \right] dt \quad (5.5)$$

As it is impossible to measure full pressure and velocity data *in vivo* without very invasive procedures, energy loss has been estimated by various groups using combinations of peak jet velocity, aortic valve area, effective orifice area, mean pressure gradient, left ventricular stroke work loss, and change in flow rate over time. Most of these estimates do indeed correlate well with patients suffering from aortic stenosis (Akins et al., 2008; Otto, 2012).

The parameters above are focussed upon the increase in cardiac workload due to a faulty valve. Although they are correlated with increased shear stresses through the valve, they are not good markers of the shear-induced thrombogenicity of a valve. Particle image velocimetry can be used to evaluate the flow and shear field through a valve during a hydrodynamic test, allowing the platelet shear-activation to be estimated (Leo, 2005).

Recently, Girdhar et al. (2012) and Bluestein et al. (2013b) proposed the *in vitro-in silico* Device Thrombogenicity Emulation method (DTE) to measure platelet activation. The shear histories of platelets passing through a cardiac device are computed, based upon an fluid-structure interaction (FSI) model. The shear histories are replicated on acetylated blood *in vitro*, using either a cone and plate or couette shearing device. In the case of a prosthetic heart valve, a modified LVAD can be used to simulate the flow of blood through the valve (Claiborne et al., 2011). Acetylation removes the thrombin feedback loop in the coagulation cascade and stops the formation of a fibrin network, allowing the shear stress trajectories to be repeated. The platelet activation state is measured using a modified prothrombinase assay (Jesty and Bluestein, 1999; Jesty et al., 2003). The DTE is a valuable and novel method for the evaluation of cardiac devices, but its computational and biological complexity makes it inappropriate at this stage of valve design.

5.1.2 Valve design

The 1950s and 1960s saw the development of a broad variety of mechanical heart valve designs. Whereas, since their inception, bioprosthetic and other flexible leaflet aortic valves have successfully relied upon the tricuspid configuration as found in natural valves. As tricuspid valves are found in nearly all mammals, it would appear that evolution has optimised this design. Congenital bicuspid and unicuspid valves have a much greater propensity for aortic stenosis, whereas quadricuspid valves can lead to aortic regurgitation, reinforcing the idea that the tricuspid valve is the optimal design (also see Section 1.3.1).

Instead of merely observing the dominance of tricuspid valves in nature, there might be a simple geometric argument for the trileaflet's effectiveness; each leaflet must go from a closed to open conformation as depicted in Figure 5.1. In a tricuspid valve the free edge of the leaflet must only strain by 5% in order to open, if it is unstrained when closed. A bicuspid valve, on the other hand, would need to strain by 55% to open. Conversely, the closed free edge length in a quadricuspid valve is 27% longer than the open length. Large strains reduce the durability of synthetic and natural tissues (Thubrikar and Klemchuk, 1990), and so for the aortic and tricuspid valves which are situated in stable annuli, the tricuspid formation is the most effective for regulating one-way pulsatile flow.

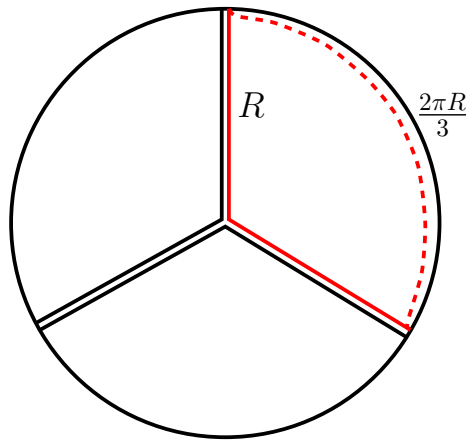


Figure 5.1: A axial view onto the leaflet edges of an example tricuspid valve in a cylinder of radius R . The free edge length of each leaflet in the closed position is equal to $2R$ (solid red). To be fully open, the length of the free edge needs to increase to $\frac{2\pi R}{3}$ (dashed red), requiring the leaflet to strain by 5%. Adapted from Thubrikar and Klemchuk (1990).

5.1.3 Sizing, positioning and sewing ring

Surgical implantation of a prosthetic aortic valve gives the surgeon the freedom to decide precisely how a valve is placed. There are variations in diameter along the axial length of the root from left ventricle to the arch of aorta. Also, the root is not rotationally symmetric, most notably due to the presence of the right and left coronary arteries. A schematic of the aortic root cross section was previously shown in Figure 1.2.

The nadirs of the native aortic valve leaflets are near to the aortic annulus, while the commissures approach the level of the coronary arteries. During surgery, the native leaflets are resected. Early prosthetic valves were positioned intra-annularly, which replicated the positioning of the native valve and ensured that there was no interference between the valve and the coronary arteries. However, aortic valve disease is often associated with patients with small aortic annuli, and so surgeons try to maximise the orifice area of the prosthesis. By positioning the valve supra-annularly, so that the stent and sewing ring are accommodated by the sinus, the orifice area may be equivalent to the native orifice area, improving haemodynamics (Wagner et al., 2007; Zhang and Wu, 2010).

Table 5.1: Aortic root dimensions for a cohort of 80 men and 97 women undergoing TAVR for severe aortic stenosis, based upon CT data reported in Buellesfeld et al. (2013). The annulus was defined as a plane through the nadirs of the 3 leaflets, and the left ventricular outflow tract (LVOT), sinus and ascending aorta were defined as parallel planes proximal or distal from the annulus. Abbreviated dimensions refer to those in Figure 1.2.

	Height (mm)	Virtual derived area diameter (mm)
LVOT	-5	22.9 ± 3.2
Annulus (L_{aa})	0	23.3 ± 2.2
Right coronary ostium (L_{ca-aa})	16.7 ± 3.6	
Left coronary ostium (L_{ca-aa})	14.4 ± 3.6	
Sinus	21.9 ± 3	31.4 ± 14
Sino-tubular junction (L_{stj})		28 ± 3
Ascending aorta	30	29.3 ± 3.5

A prosthesis whose EOA is too low relative to a patient's requirements will cause excessive transvalvular gradients, and possible patient-prosthesis mismatch. The EOA at a specific

pulse rate and stroke volume is a function of both the leaflet dynamics and the geometric orifice area of the valve. Geometric orifice area and internal orifice diameter of a valve are functions of valve design and position. However, the influence of valve diameter in determining proper function is often overlooked, due to the lack of consistency in sizing the prosthesis and annulus (Diab et al., 2011; Ruzicka et al., 2009).

International standards dictate that the labelled size of a valve should take a patient-centred approach. This requires that the labelled size is equivalent to the measured tissue annulus diameter (TAD), for example, a “size 23” valve will fit a patient with a 23 mm TAD (International Standards Organisation, 2005).

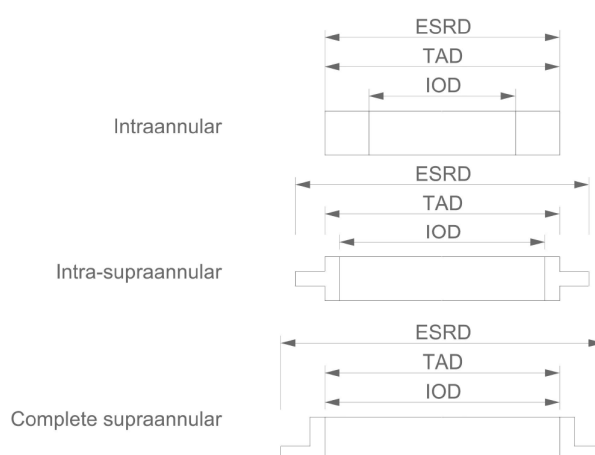


Figure 5.2: Definition of dimensions for three types of valve positioning: intraannular, intra-supraannular and complete supraannular. ESRD - external sewing ring diameter, IOD - internal orifice diameter, and TAD - tissue or aortic annulus diameter.

Although the ISO definition is clear, there are several complicating factors. The tissue annulus diameter is defined as the minimum aortic diameter of the aortic root. During imaging measurements, the vessels grow and contract with pressure, leading to a diameter variation of at least 10% (though this decreases with age) (Kalath et al., 1986). To compound the problem, conventional echocardiographic measurements are limited by their 2 dimensional nature, which means that the resulting image may lie out of plane with the annulus centre resulting in underestimation of the TAD (Cerillo et al., 2012).

During surgery, it should be possible to make static, direct measurements. However, though the aortic annulus is often spoken of as if there is a distinct ring, in practise this is far from the case, and simple measurements presuming a uniform diameter can be unreliable (Ho, 2009). The most consistent method of measurement should use flat-head candles, as opposed to Hegar dilators, which may overestimate the TAD (Azarnoush et al., 2013).

The sewing ring is used to secure a surgical valve in position. In bioprosthetic and mechanical valves, the sewing ring is typically fabricated from a Dacron[®] or Gore-Tex[®] mesh. As described in Section 1.8, interfaces between different materials can often be the weakest link in a valve. The delamination at the interface in the valve designed by Gallocher et al. (2006) was the cause of valve failure. If possible, it might be preferable to fabricate the sewing ring and stent cylinder from the same material to avoid joins.

Stasiak et al. (2014) considered the suitability of oriented styrenic BCPs $10 \times 5 \times 0.35$ mm for use in the sewing ring by passing a single suture through the sheet, 2 mm from its edge. When polystyrene cylinders were oriented parallel to the direction of strain, samples of SI-BS19 could withstand 3 MPa and 500% strain; when oriented perpendicular, they also supported 3 MPa, but reached 700% strain. A fully sutured sewing ring made from SI-BS19 could support 75 N. A valve must be able to support approximately 7.5 N. The strength of styrenic BCP is comparable to other clinically used materials; chemically treated, sutured, calf pericardium which is used in cardiac bioprostheses, is able to withstand 2.6 to 7.6 MPa, depending on treatment method (García Páez et al., 2000).

5.1.4 Leaflet design

In Chapter 2 I ignored leaflet shape in my material performance index. Although leaflet shape may only have higher order effects on the material performance index, it is still an important part of the overall valve performance. The first descriptions of native leaflet geometry were made over 2300 years ago, yet they continue to be refined. The shape of a leaflet can be described using a combination of 3D surfaces, generally consisting of cylinders, cones, spheres and other real quadric surfaces, or with other mathematical forms. I searched the literature for descriptions of the native valve shape, and proposals of more effective shapes. The results of this search are summarised in Table 5.3. For the nomenclature used to describe the parts of the leaflet, refer to Figure 1.3a.

Table 5.3: Surfaces used to describe the shape of a trileaflet aortic valve.

Shape	Notes (native description or proposed design)	Source
Spherical portion - semilunar	Native	Philistion of Locir (c.427-c.347 BC) in (Bezuidenhout and Zilla, 2014)
Sigmoid	Native	Erasistratus of Ceos (c.304-c.250 BC) in (Bezuidenhout and Zilla, 2014)
Hemispheres	Native	Leonardo da Vinci (1452-1519) in (Bezuidenhout and Zilla, 2014)
3 interlocking circles	Native	Retzius (1843) in (Bezuidenhout and Zilla, 2014)
‘Cone’ shaped and ‘dome’ shaped		(Ghista and Reul, 1983; Roe et al., 1966)
Paraboloids of revolution with foci at leaflet base		(Leat and Fisher, 1994; Mercer et al., 1973)
Semi-dome shaped / triangular	Proposed polymeric	(Mohri et al., 1973)
2 radii of curvature over 2 subtended angles (general Gaussian)	Native	Chong et al. (1973), Kim et al. (1991)
Elliptic paraboloid	Bioprosthetic	(Hamid et al., 1986)
‘Jellyfish’ perforated disk with polymeric flaps	Polymeric, not a trileaflet	(Imachi et al., 1989)

Table 5.3 continued.

Shape	Notes (native description or proposed design)	Source
Cylindrical form, conical when open (see Figure 5.3)	Native, then widely used in pericardial valves.	(Labrosse et al., 2006; Thubrikar and Klemchuk, 1990)
Determined by fractal structure of fibres	Native	(Peskin and McQueen, 1994)
Alpharabola	Polymeric	(Leat and Fisher, 1994)
Conic	Approximated bovine pericardial, to make polymeric	(Mackay et al., 1996)
Spherico-hyperbolic	Polymeric	(Butterfield et al., 2001)
Elliptico-hyperbolic conicoid	Polymeric	(Butterfield et al., 2001)
Offset hyperboloid of revolution	Native, to make polymeric valve.	(Jiang et al., 2004)
Set of parabolae	Polymeric, used for Aortech valve.	(Beith, 2006)
Bezier curves with de Casteljau algorithm	Polymeric, by <i>in silico</i> optimisation.	(Mohammadi et al., 2009; Mohammadi and Mequanint, 2011)
3 intersecting cylinders to define each leaflet	Polymeric, by <i>in silico</i> optimisation.	(Burriesci et al., 2010)

Table 5.3 continued.

Shape	Notes (native description or proposed design)	Source
Hemicylindrical	Proposed polymeric.	Wisman et al. in Bezuidenhout and Zilla (2014)
Translated hyperbolic curve swept through quartic radial curve	Polymeric, by <i>in silico</i> optimisation.	(Gharaie and Morsi, 2015)

In Table 5.3, the valve shapes evolve over time from descriptions of the native valve, through to proposed polymeric trileaflet designs and their optimisation. The most clear distinction that can be made is between leaflets which are purposefully designed to have a single degree of curvature (Gaussian curvature = 0) when open, versus those with positive Gaussian curvature. Notably, the shape described by Thubrikar and Klemchuk (1990) is designed as a single section of a cylinder when open, thus it can be cut from a flat sheet and mounted to an appropriate stent (Figure 5.3). The energy required to reverse the curvature of a cylinder is less than that required for a sphere, which should reduce the pressure and time required to open a cylindrical form valve. On the other hand, diastolic stresses are reported to be lower in spherically shaped valves (Liu et al., 2007b). To date, few designs have been tested against one another *in vitro*, making direct comparisons difficult. It is certain that material and form are intrinsically linked. Thus, if the material is not perfectly biomimetic, a perfectly biomimetic form is unlikely to be necessary to create an optimal valve.

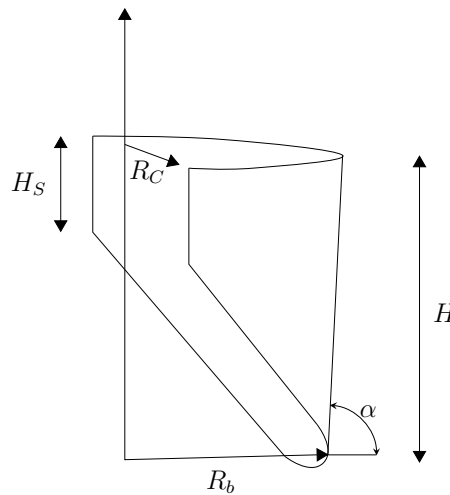


Figure 5.3: Open form of the valve designed by Thubrikar and Klemchuk (1990). Each leaflet can be cut from a single, flat sheet, and can be described by 5 parameters.

The effect that leaflet design has upon durability and haemodynamics of the valve are summarised in Table 5.4 by the type of feature. In general, a change in any feature results in opposite effects on durability and haemodynamics. Each of the 5 features identified in Table 5.4 could be a parameter used to optimise the valve's performance. Translation of each of these features to quantitative parameters would result in a large number of variables, and an optimisation problem far beyond the scope of this chapter.

The Thubrikar and Klemchuk (1990) shape is attractive due to its simple cylindrical geometric surface when open, meaning that it should require a reduced pressure to reverse its curvature and can be formed from a flat sheet. However, the pure cylinder is only

the case for the open valve, and upon closure it forms a coaptation region which is not cylindrical. This coaptation region is necessary for proper functioning of the valve; without a significant coaptation area the valve will not form a good seal (Loerakker et al., 2013; Thubrikar and Klemchuk, 1990).

Table 5.4: Design features for heart valve leaflets.

Feature	Effect of parameter increase on valve stresses	Effect of parameter increase on haemodynamics
Leaflet thickness	Reduced stresses	Inferior haemodynamics (Bernacca et al., 2002; Rahmani et al., 2012).
Stent height / profile	Reduced valve stresses (particularly at commissures) (Chandran et al., 1991; Hamid et al., 1986).	Inferior haemodynamics, possible interference with nearby structures (Chandran et al., 1991). Reduced likelihood of prolapse (Labrosse et al., 2006).
Stent flexibility	Reduced valve stresses at commissures (Chandran et al., 1991; Christie and Barratt-Boyes, 1991), but can cause leaflet bunching if severe (Vesely, 2003).	Problematic if asymmetry causes prolapse of a single leaflet (Vesely, 2003).
Depth/sag of belly and free edge	Reduced stresses (Vesely, 2003)	Cylindrical valves (zero belly) require less energy to reverse curvature (Liu et al., 2007b).
Coaptation area	Can increase radial strain (Loerakker et al., 2013).	Reduced regurgitation.
Angle/distance between leaflets at commissure		Opens more easily. Closing and sealing more difficult.

A polymeric valve can be manufactured in any state between fully open and fully closed. An advantage of forming a valve in a partially open state (Rottenberg et al., 2000), is to reduce opening forces and flexural strain between the open and closed positions (Jansen et al., 1991). However, this can lead to poor closing characteristics; Leo et al. (2006) performed hydrodynamic and PIV testing of the Aortech valves which had failed *in vivo* due to thrombus formation at the commissure. These valves were formed with various leaflet thicknesses and degrees of openness. While thickness dominated the performance, the neutral open state of the valve also led to regurgitant flows during closing which

contributed to the high shear, thrombus-inducing regions at the commissures. As such, the valve should be formed with a neutral state near to the closed position, and designed to have reasonable leaflet coaptation during diastole. This is not possible using a single cylindrical surface as proposed by Thubrikar and Klemchuk (1990), which lead Burriesci et al. (2010) to propose, and optimise, an alternative geometry based purely upon cylindrical surfaces.

Burriesci et al. (2010) performed *in silico* optimisation and *in vitro* evaluation of their valve formed from cylindrical surfaces, with reference to the much tested and published Aortech valve (Wheatley et al., 1998). The optimisation considered five geometric parameters, though it did not include leaflet thickness, which was uniformly set to $100\text{ }\mu\text{m}$, and used a linear material with a modulus of 45 N mm^{-2} . The optimised valve performed significantly better than the reference valve in hydrodynamic tests in measures of pressure drop, *EOA*, energy loss, regurgitation, and leakage. The von Mises stresses during diastole were also lower for the optimised valve. The optimised cylindrical valve shape which was proposed, has gone on to be used in the Triskele valve (which is currently in animal trials). Based upon this study I selected this leaflet shape, which I hereafter refer to as the cylindrical form valve. Using a 3D CAD package I reproduced the shape and added a stent and sewing ring to produce the valve shown in Figure 5.4, .

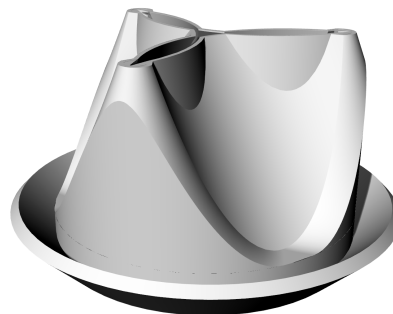


Figure 5.4: Trial prosthetic heart valve design, the “cylindrical form valve”, based upon the leaflet form proposed by Burriesci et al. (2010).

I compared the cylindrical form valve to the design proposed by Zaffora (2011). This design was based upon a leaflet belly with a spherical form, and a commissure/leaflet-stent boundary region with a cylindrical form, whose construction is similar to that described in Section 5.2.1. A fibre orientation optimisation had been previously performed on this valve (Serrani et al. Submitted). Prior to commencing this project the Structure Materials group at the University of Cambridge and Politecnico di Milano produced a prototype valve based upon the design of Zaffora (2011). This preliminary geometry is

shown in Figure 5.5. This valve was characterised by having a particularly high profile, which resulted in poor hydrodynamics during *in vitro* testing. A new design, with a lower profile, was proposed (Figure 5.5). This leaflet form is hereafter referred to as the spherical form valve.

The cylindrical and spherical form valves will now be manufactured, tested, and compared.

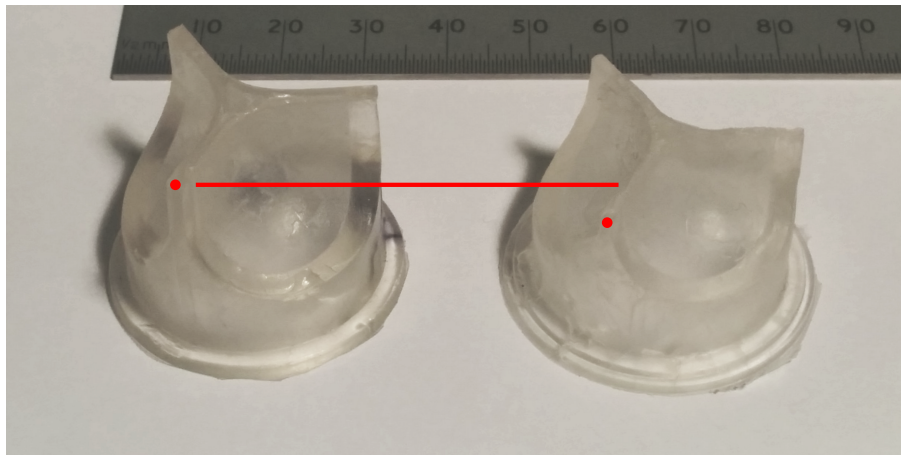


Figure 5.5: The original and updated spherical form valve designs. The valve on the left is the initial valve, which has a high profile. The valve on the right is the updated low profile valve design. The red line indicates the height of the nearest commissure in the updated valve. Both valves were fabricated by compression moulding and have internal diameters of 22 mm.

5.2 Materials and methods

5.2.1 Valve design

The cylindrical and spherical form valves were designed using Rhino3D® (McNeel, Seattle, WA, USA), a Non-Uniform Rational B-Splines (NURBS) based CAD package. The visual programming add-on package Grasshopper® was used for parametric manipulation of the shapes.

Cylindrical form valve

A valve based entirely upon cylindrical surfaces, as described by Burriesci et al. (2010) was used as a shortlisted design. Dimensions optimised by the authors are indicated in Figure 5.6. The height of the valve is 15 mm and diameter 22 mm. The bulk of the leaflet

is defined by a cylinder of diameter 22 mm inclined at 33.4° to the vertical. The coaption region is defined by two cylinders also of diameter 22 mm inclined at 10.9° to the vertical. The intersection between the coaption and main cylinders lies on a plane 0.4 mm from the leaflet reflection plane and at an angle of 0.63° . The stent cylinder and posts were designed with a thickness of 2.5 mm, as shown in Figure 5.4. The leaflet thickness was set to 0.3 mm.

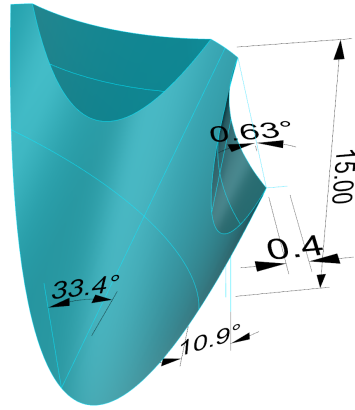


Figure 5.6: Construction dimensions for the ventricular surface of the cylindrical form valve, based upon the leaflet optimised by Burriesci et al. (2010). The surface is constructed with cylinders of 22 mm diameter, which is equivalent to the valve's internal diameter.

Spherical form valve

The spherical form valve was proposed by Zaffora (2011) (Figure 5.7). A 120° segment of a hemisphere is extruded radially, to form a spherical belly and cylindrical sides (for more details see Appendix C.1). The spherical and cylindrical diameters used for construction were set to 22 mm. Leaflet thickness was set to 0.3 mm; and the commissural distance (spacing between aortic surfaces of the leaflets, d_{com}) was minimised to 0.7 mm, with manufacturing constraints providing the minimum thickness. At the commissures, the ventricular sides of the leaflets are separated by 0.1 mm. The form of this leaflet approximates that of a standard bioprosthetic valve.

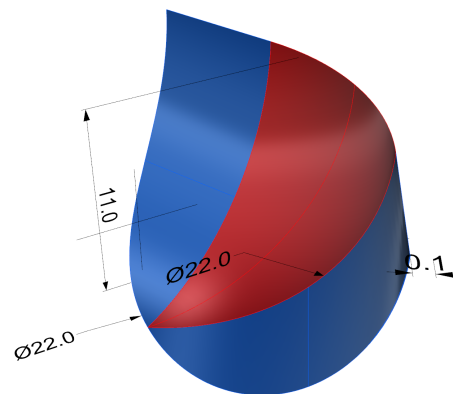


Figure 5.7: Construction dimensions for ventricular surface of the spherical form valve, based upon the leaflet proposed by Zaffora (2011). The valve has an internal diameter of 22 mm. A 120° segment of a 22 mm diameter hemisphere (red) is extruded radially, to form the cylindrical sides (blue). The ventricular sides of the leaflets are separated by 0.1 mm at the commissures.

5.2.2 Prototype valve fabrication

Valve performance is dependent on the triad of valve design, material, and manufacturing. As the aim of this chapter is to select a valve design for final manufacture, I chose to use the previously selected material and a preferred means of manufacture during selection. In Chapter 2 I selected polystyrene-*block*-polyethylene-polypropylene-*block*-polystyrene with 22wt% of polystyrene (SEPS22). Injection moulding is commonly used to process thermoplastics and so a bench-top injection moulding process was used to form the prototype valves.

The geometry of the mould to make the spherical form valve was relatively straightforward to machine. The male part was CNC machined from stainless steel, and the female part spark eroded (Cambridge Reactor Design Ltd., Cambridgeshire, UK). The geometry of the mould for the cylindrical form valve was more complex. The prototype tool was manufactured by rapid additive manufacturing, involving direct metal laser sintering (EOSINT M280) with an aluminium alloy AlSi₁₀Mg, by 3T RPD Ltd. (Berkshire, UK). Post-processing involved the addition of mould alignment pins and smoothing the mould surfaces using a spray paint that was applied by brush.

A bench-top injection moulding apparatus was used to fill the mould cavities. Polymer pellets were manually compacted after heating in an oven at 160 °C for 10 minutes. The compacted pellets were loaded into the injection moulder's barrel (ϕ 25 mm, 100 mm

length). The polymer melt passes through 30 mm of connecting tubing before entering the die. The die is mounted in a purpose-built frame with a 4-point hand clamping system to clamp the tool without polymer leakage. The barrel and mould were heated with band heaters and the tube with flexible cable heaters to 160 °C. Pressure was recorded at the barrel exit to indicate when filling of the barrel was complete.

Rigid stent

After hydrodynamic testing was completed, the valves were modified by placing small holes at the top of the stent posts through which a rigid metal ring was passed. The metal ring eliminated bending of the stent during diastole. The performance of the valves was reassessed in a second set of hydrodynamic tests.

Leaflet thickness variation

In another set of hydrodynamic tests the leaflet thickness was modified. The average leaflet thickness was varied by applying layers of spray-on paint to the male and female moulds to reduce the thickness of the cavity.

5.2.3 Hydrodynamic performance

The hydrodynamic performances of the valves were assessed using a pulse duplicator. This consists of a servo-electrically controlled pump, driving a membrane which imitated the ventricular wall. As illustrated in Figure 5.8, valves were mounted at the inlet and exit of the ventricular chamber. The test valve was placed at the exit and a bileaflet mechanical valve at the inlet. The exiting fluid passes through resistance, compliance, and reservoir units before completing the loop. The system is described in detail by Lanzarone et al. (2009). The servo-electric drive was programmed such that the systolic flow rate followed the Swanson and Clark waveform (Swanson and Clark, 1977), and the diastolic flow rate was reproduced by a modified Talukder and Reul flow rate waveform (Talukder and Reul, 1978).

The valves are mounted in straight perspex tubing, of diameter 35 mm.

Pressure measurements are made 35 mm upstream and 105 mm downstream from the test valve (140PC pressure sensors, Honeywell Inc.[®], Freeport, IL, USA). Ultrasonic measurements of the flow rate were made 70 mm before the test valve using a transit-time ultrasound flowmeter (HT110 series, Transonic Systems Inc.[®], Ithaca, NY, USA). Data

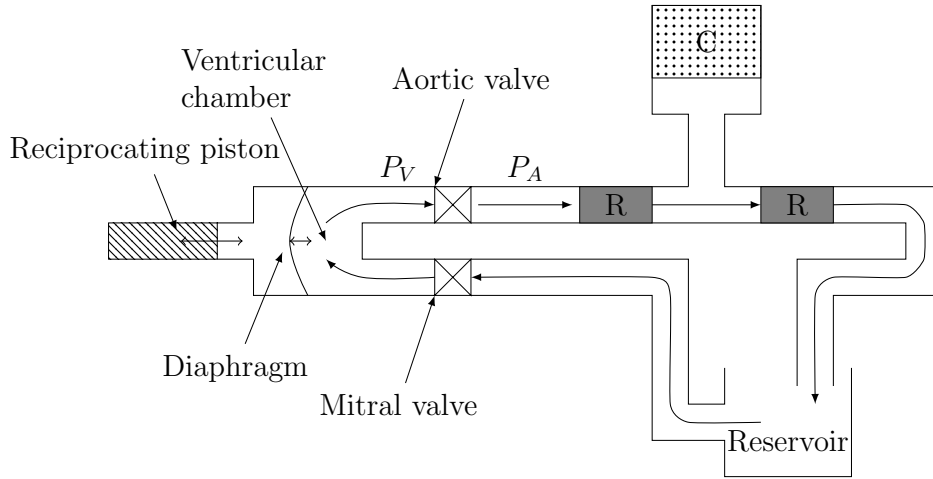


Figure 5.8: Schematic of the pulse duplicator set up. The resistance and compliance units are indicated by ‘R’ and ‘C’, respectively. Pressure measurements were made at P_V and P_A .

was recorded at a frequency of 200 Hz using LabView, and analysed using MATLAB (Mathworks, MA, USA).

Tests were made in accordance with ISO 5840. Measurements to assess EOA_G are carried out at 120 mmHg, 70 BPM at flow rates of 2, 3.5, 5, and 7 l min^{-1} . Regurgitation is assessed with diastolic pressure differences of 80, 120 and 160 mmHg, at 45, 70 and 120 BPM.

Leaflet dynamics were viewed axially downstream from the valve. Images were collected at 25 Hz.

5.2.4 Finite element modelling

The geometries were updated after the hydrodynamic tests for the final valve design. Finite element modelling was used to compare the peak leaflet stresses in the valve before and after the update. The models were run by Dr Marta Serrani using a previously validated model.

A uniform pressure load was applied on the aortic surface of the leaflet up to 135 mmHg to simulate a physiological backpressure during the closing phase. A quasi-static loading condition was assumed (Haj-Ali et al., 2008; Luo et al., 2003; Sun et al., 2005); the nonlinear implicit finite element algorithm provided by ABAQUS was used to solve the numerical problem. The hyperelastic Mooney-Rivlin constitutive model was used to model the polymer, and is described in detail in Appendix E. The isotropic material

parameters which are shown in Table 5.5 were based upon the mechanical properties of SEPS22 which were collected in Chapter 2.

Table 5.5: Mooney-Rivlin parameters optimised for the tensile strain energy density of SEPS22.

	c_1	c_2	k_4
Isotropic	0.3	0.36	n/a

5.3 Results

Pulsatile testing was performed on both valves at a range of cardiac outputs, diastolic pressure drops, and pulse rates. Figure 5.9 shows that the EOA_G of the cylindrical form valves was greater than the spherical form valves, except for at a cardiac output of 7 l min^{-1} . The EOA_G of both valves increased with cardiac output, as the leaflets are opened further by higher flow rate.

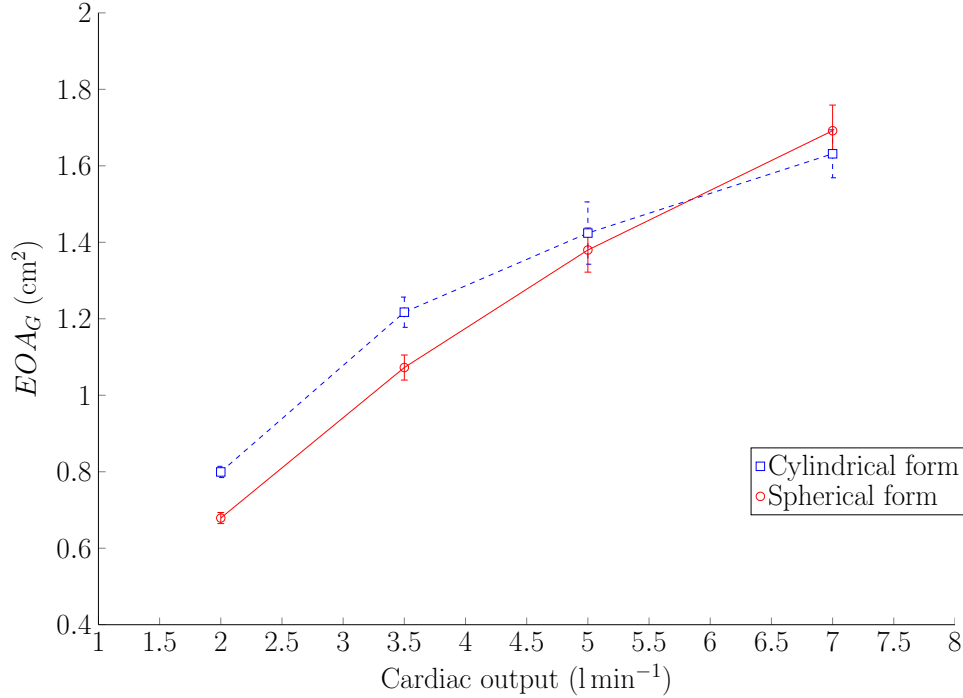


Figure 5.9: EOA_G measurements of both valve forms at a range of cardiac outputs. The cylindrical form valves have a greater effective orifice area at low cardiac outputs, but at 7 l min^{-1} the spherical valve is superior.

Cylindrical form valves were more regurgitant at all pulse rates and diastolic pressure drops (Figure 5.10). In general, spherical form valve regurgitation increased with in-

creasing diastolic pressure, suggesting that there may be some leakage through the closed valve. Regurgitation through the cylindrical form valve remained constant with increasing diastolic pressure drops, and analysis of the flow profile indicated that regurgitation is dominated by flow during closing.

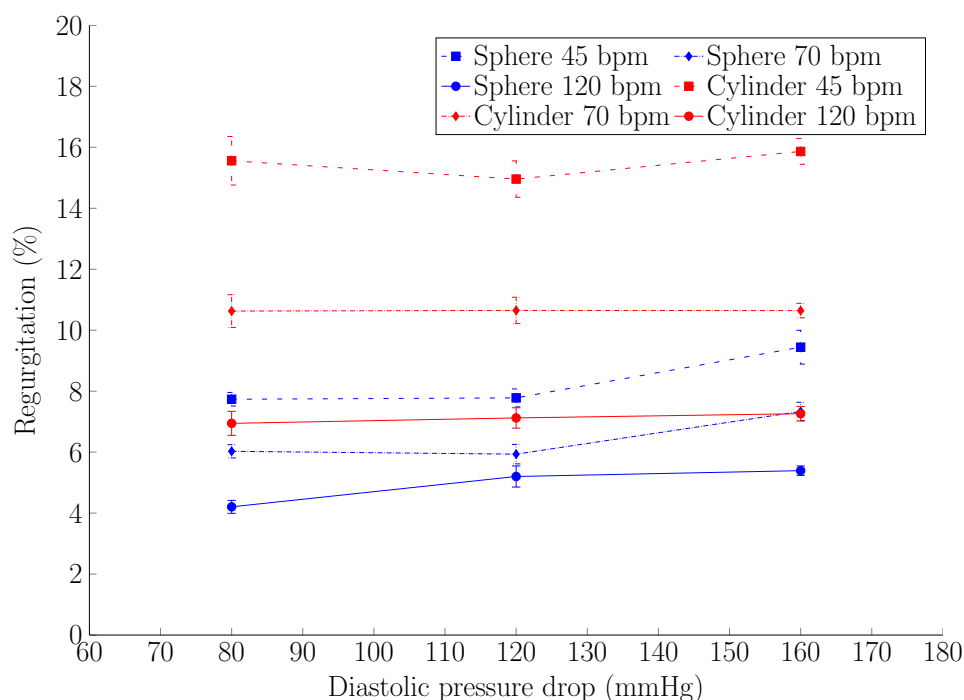


Figure 5.10: The spherical form valves are less regurgitant than the cylindrical form valves at all diastolic pressure drops.

Although energy loss is rarely used in the clinic, it is a valuable measure for making proper comparisons between valves. In the data presented here, the cylindrical form valve had a superior EOA_G , but the spherical form valve was superior in terms of regurgitation. Figure 5.11 shows energy loss, which reconciles EOA and regurgitation to yield an overall performance measure. The spherical valve had a lower energy loss than the cylindrical form valve at all flow rates except at 3.5 l min^{-1} . Despite the spherical valve fulfilling the ISO standard (evaluated at 5 l min^{-1}), 17% of energy imparted on the fluid by the ventricle was lost passing through the valve. At less efficient flow rates, up to 30% of the energy was lost.

Energy is lost over the valve during forward flow and when retrograde flow is resisted. In Figure 5.12 the relative contributions of systole and diastole to energy loss are shown. Clearly, the high energy loss of the cylindrical form valve at low flow rates is associated with regurgitation (dashed red line). The cylindrical form valve functions less efficiently during systole at high flow rates, suggesting that the valve is behaving differently which could be due to a laminar turbulent transition. For the spherical form, valve diastole and

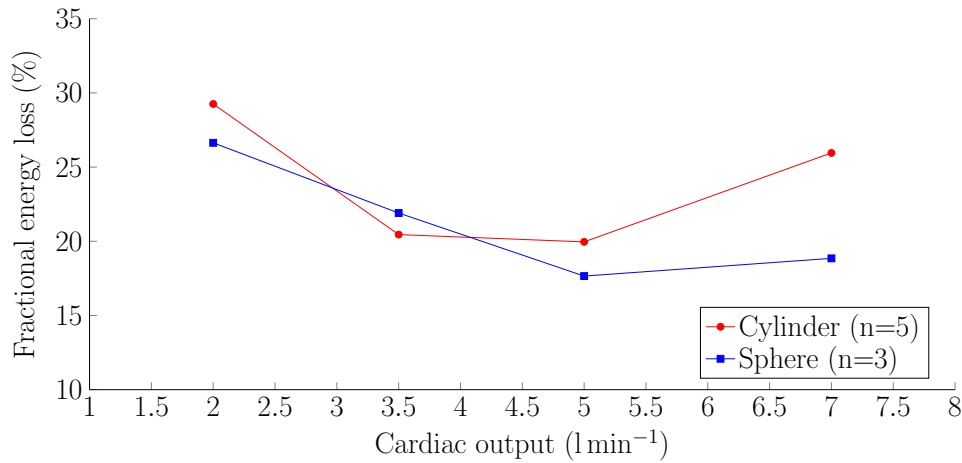


Figure 5.11: Energy loss over both types of valve tested in the pulsatile flow. There is a greater fraction of energy lost over the cylindrical form valve than over the spherical form valve at all flow rates except 3.5 l min^{-1} . The valves are most effective at 5 l min^{-1} .

systole contribute equally to the inefficiencies of the valve.

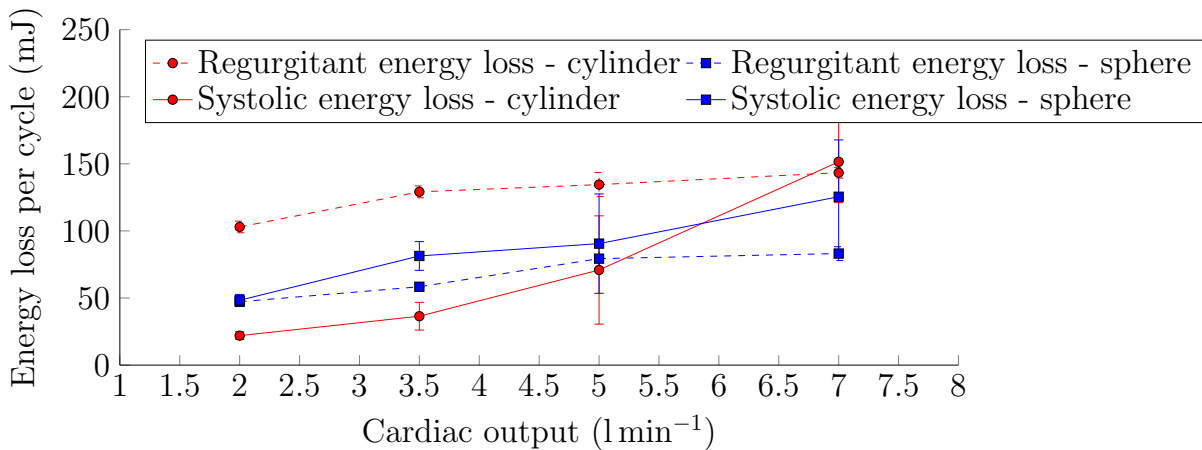


Figure 5.12: Energy loss per cycle for regurgitant (dashed lines) and systolic (solid lines) cases as a function of cardiac output for both forms of valve. The inefficiencies of heart valves occur during both diastole and systole. Energy loss in the cylindrical form valve (red lines) is dominated by the poor closing behaviour, whilst in the spherical valve (blue lines) the energy loss is equally split between systole and diastole over the range of flow rates.

Images of the leaflet dynamics of the valves during systole are shown in Figures 5.13 and 5.14. The cylindrical form valve, at 5 l min^{-1} , is more stable when open (images 3 to 5). In contrast, the spherical form valve appears to be unstable in the open phase, and is not able to fully reverse the curvature of two of its leaflets. The fully open (lower) leaflet of the spherical valve also seems to have a “tongue”, where the free edge opens further than the leaflet belly. This may indicate that, rather than fully reversing, the sphere has

formed a saddle.

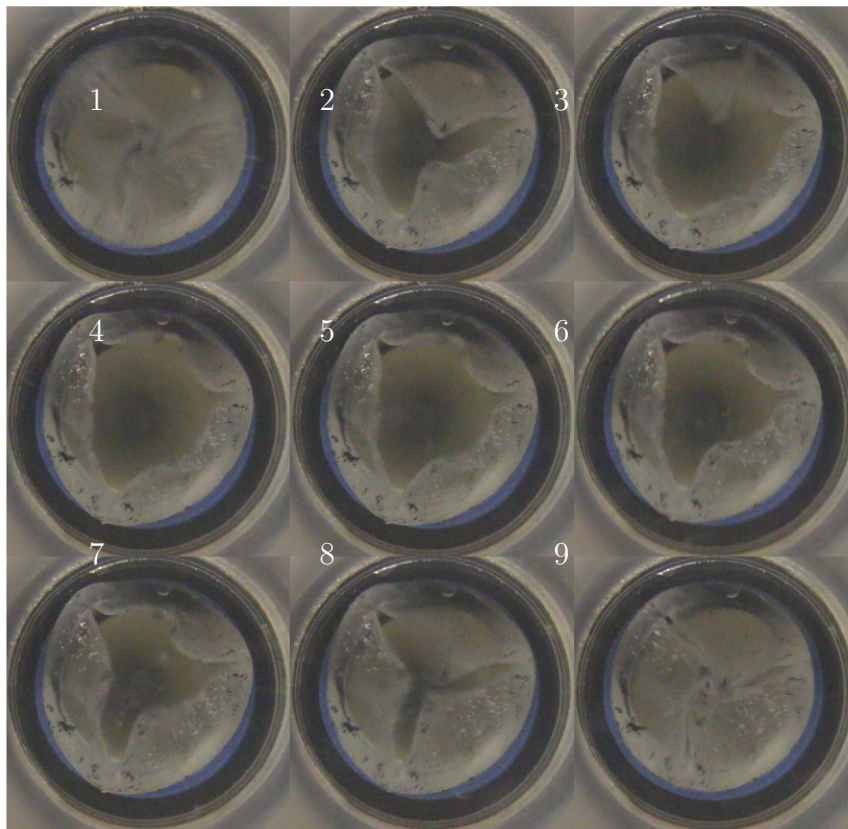


Figure 5.13: Images taken (at 25 Hz) during the systolic phase for a cylindrical form valve (51 min^{-1} , 70 BPM).

The spherical form valve during diastole is shown in Figure 5.15 to demonstrate the deformation of the stent posts (in images 2 to 10). The bending causes the leaflets to twist at the free edge centre.

5.3.1 Variation in leaflet thickness

I modified the spherical leaflet form mould to produce a selection of valves with differing leaflet thicknesses. It was not possible to achieve large uniform changes in leaflet thickness, and I could only achieve a $50\text{ }\mu\text{m}$ difference between the maximum and minimum mean thicknesses. Nonetheless, there was a correlation between leaflet thickness and the maximum pressure required to open the valve, as shown in Figure 5.16a. There were no correlations between mean leaflet thickness and other important performance parameters, such as effective orifice area (EOA_G) and energy loss (E_{loss}); however the sample size was

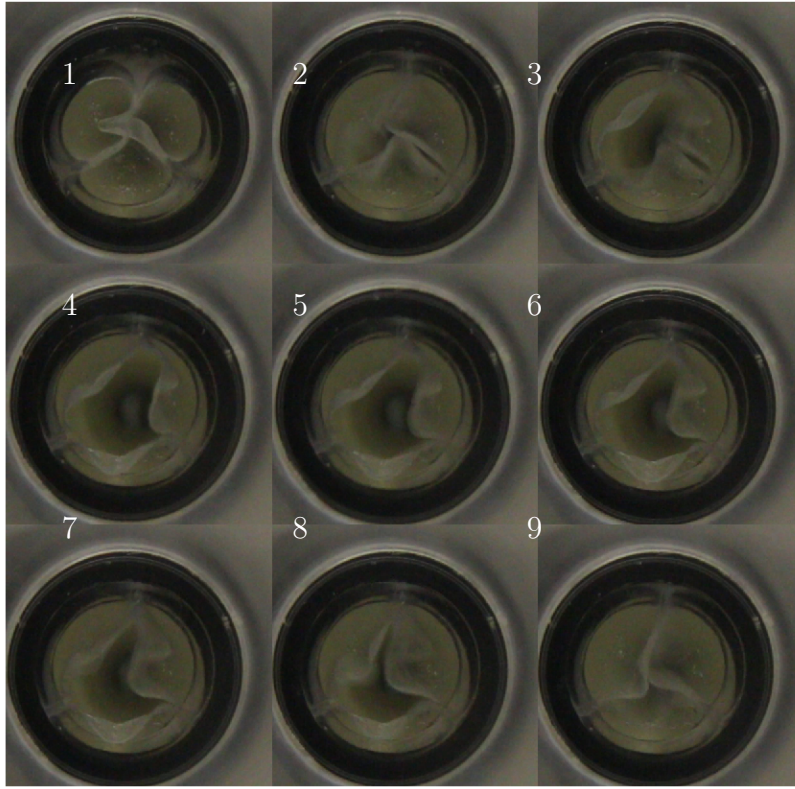


Figure 5.14: Images taken (at 25 Hz) during the systolic phase, for a spherical form valve (51min^{-1} , 70 BPM). There appears to be a flow instability through the orifice causing the leaflet to oscillate between images.

limited. Transvalvular pressure gradient (TPG_{max}) varied from 21 to 40 mmHg without a significant effect on EOA_G , suggesting that all valves reached a similar geometric orifice area (GOA) once the leaflet curvature had reversed (Garcia et al., 2004).

The variation in thickness between leaflets meant that the leaflets did not open simultaneously. Furthermore, at low cardiac outputs one, and occasionally two, leaflets did not open. All three leaflets should open at low, as well as high, cardiac outputs. Figure 5.16b shows that leaflets with a thickness greater than $325\mu\text{m}$ may not open at low cardiac outputs. This provides an *upper bound* for leaflet thickness for this form of valve when made with SEPS22. However, it may be necessary to further decrease leaflet thickness for all 3 leaflets to open at *all* cardiac outputs.

The upshot of the non-uniform changes in leaflet thickness was that it was possible to observe the effect of spatial variations in leaflet thickness on transvalvular opening pressure. Figure 5.17 shows the results of a covariance analysis on the spatially variant leaflet thickness measurements and TPG_{max} .

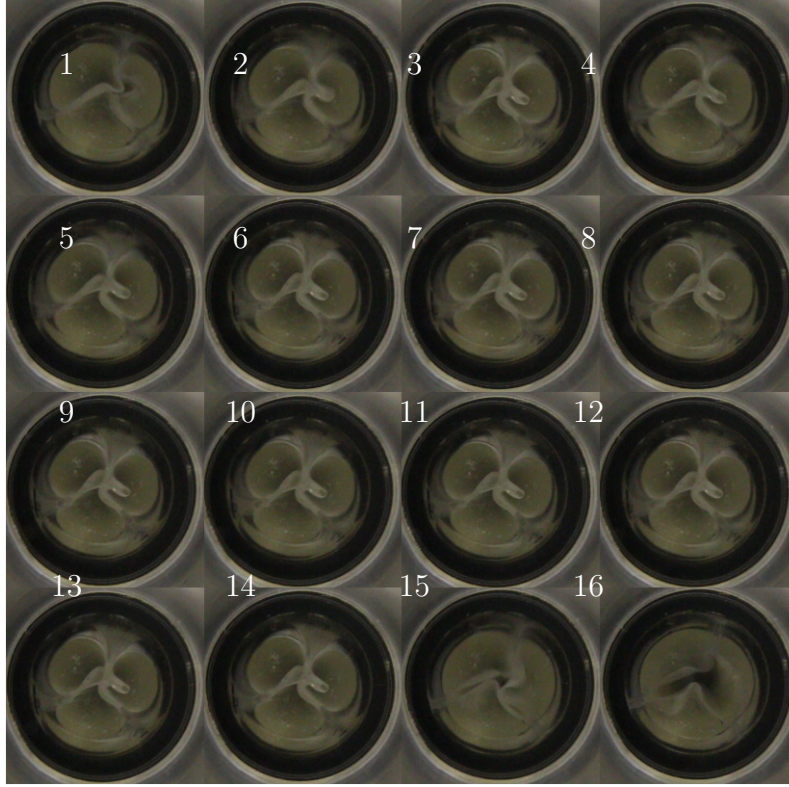


Figure 5.15: Images taken (at 25 Hz) during the diastolic phase, for a spherical form valve. (51 min^{-1} , 70 BPM).

Covariance, σ_{cov} , is a marker of the degree of linear dependence between N random variables, calculated as:

$$\sigma_{cov}(X, Y) = \sum_{i=1}^N \frac{(x_i - \bar{x})(y_i - \bar{y})}{N - 1} \quad (5.6)$$

Where x_i and y_i are observations of parameters X and Y . \bar{x} and \bar{y} are the mean values. In the covariance matrix, the diagonal components, $i = j$, are the variance of the variables, and the off-diagonal components, $i \neq j$, are the covariances relating one variable to another. If the $X = Y$ then $\sigma_{cov}(X, Y) = \sigma_X^2$, where σ is variance. A higher covariance indicates a higher degree of correlation between the two variables, where one is perfect correlation. X was taken to be TPG_{max} , and Y to be the leaflet thickness measurements.

Figure 5.17b shows the covariance value for each location on the leaflet. A large, positive value (≤ 1) indicates a positive correlation between thickness and TPG_{max} . The thickness of the free edge near to the commissures is the most important leaflet dimension during opening. The images of the spherical valve when open (Figure 5.14) support this

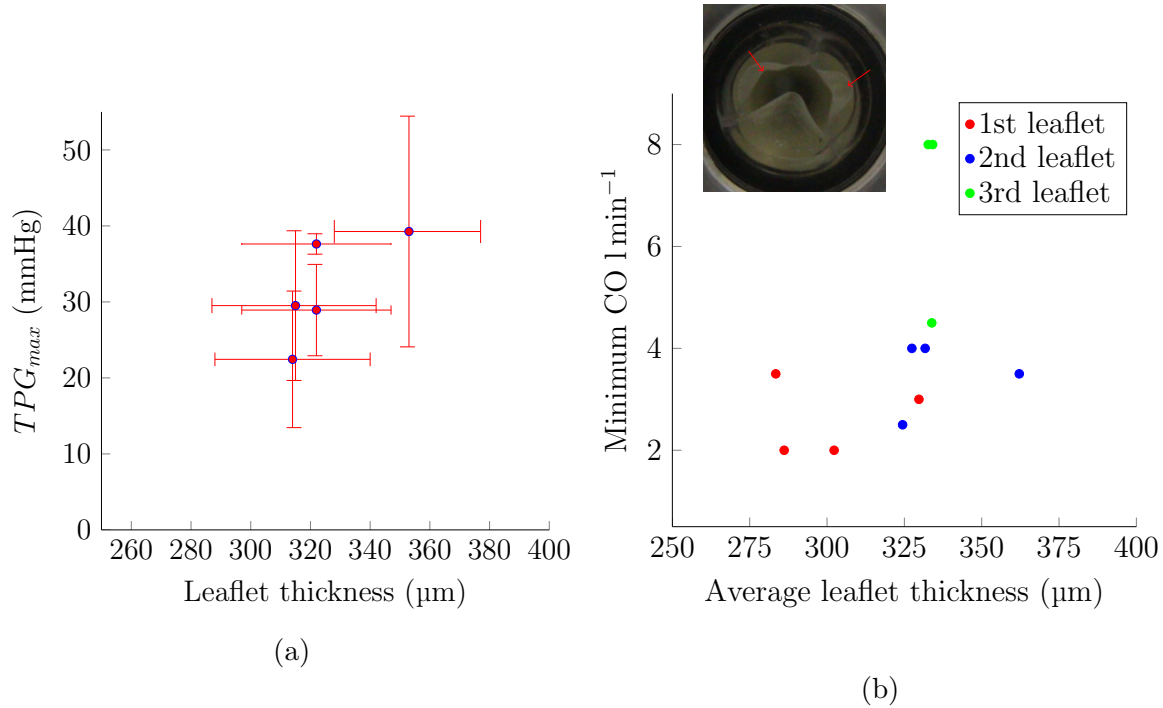


Figure 5.16: (a) The effect of leaflet thickness on the maximum transvalvular pressure which is reached during opening of the spherical form valve. (b) The minimum cardiac output (2, 3.5, 5, or 7 l min^{-1} , at 120 mmHg) required to open the 1st, 2nd, and 3rd leaflets. The thickness measurements are average values taken from 7 points on each leaflet (a) and opening was determined from videos taken at each cardiac output. The inset shows the case where two leaflets have opened, and one remained closed during systole.

proposition, as they show the fully open valve to have its tightest bend in the region in which the “free edge left” and “free edge right” measurements were made. Importantly, the highest diastolic stresses are also located near to the commissures, indicating that for a uniformly thick leaflet, the leaflet thickness used in the material performance index in Chapter 2 applies to this location.

The same analysis was performed for the cylindrical form valve, though there was no correlation between leaflet thickness (which varied over 70 μm) and TPG_{max} , nor any positive linear dependencies (covariants) between spatial thickness variation and TPG_{max} . The cylindrical form leaflet has a greater GOA than the spherical form leaflet, as a result of the leaflet curvature fully reversing. As such, the tightest radius of curvature when open was found along the stent-leaflet boundary. As the thickness measurements were made using a micrometer (of diameter 8 mm), they were not sensitive to small variations in thickness along the stent-leaflet boundary.

The overall performance of the cylindrical form valve in terms of energy loss was dominated by closing performance. A covariance analysis between leaflet spatial thickness

and regurgitation found no significant linear dependencies.

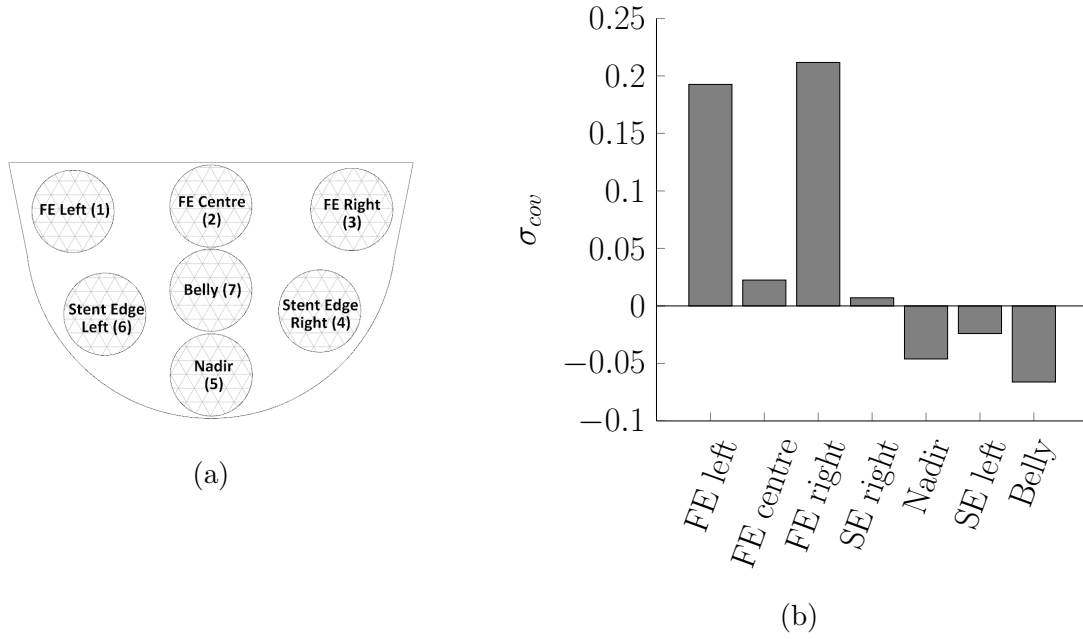


Figure 5.17: (a) shows the locations of measurements for spatial variation in the thickness of heart valve leaflet. (b) shows the covariance matrix values ($i \neq j$) of leaflet thickness and TPG_{max} (5 valves, 15 leaflets). FE refers to the free edge in this figure, and SE to the stent-leaflet boundary.

5.3.2 Stent post stiffness

During diastole the posts of all valves were deflected, leading to an increase in coaptation between the leaflets, but also causing them to assume a very different geometry. To address this issue I fabricated a new valve in which the stent posts were radially fixed using a metal ring. This eliminated the deflection of the posts, as shown in Figure 5.18. Stent post fixing did not have any influence upon the EOA_G of the valves (Figure 5.19), but led to a large improvement in regurgitation, as shown in Figure 5.20. It is unlikely that the ring significantly influenced the flow field downstream of the valve.

A summary of the results, relevant to the fulfilment of the ISO standards, is shown in Table 5.6. All valves fulfilled the ISO standards for EOA_G of being greater than 1 m^2 . With respect to the limit for regurgitation, the cylindrical form valve was only marginally acceptable once the stent was stiffened (which was accompanied by a 9% drop in EOA_G). The spherical valve was acceptable with both flexible and rigid stent posts. These results can be directly compared to a clinically available bioprosthetic reference valve which was previously tested. The bioprosthesis was superior to the polymeric prostheses in measures



Figure 5.18: Five images during diastole of the spherical form valve with fixed stent posts at 51 min^{-1} and 70 BPM. There is no difference in the position of the commissures between the images, indicating that there was no post deflection. The ring appears as a silver circle.

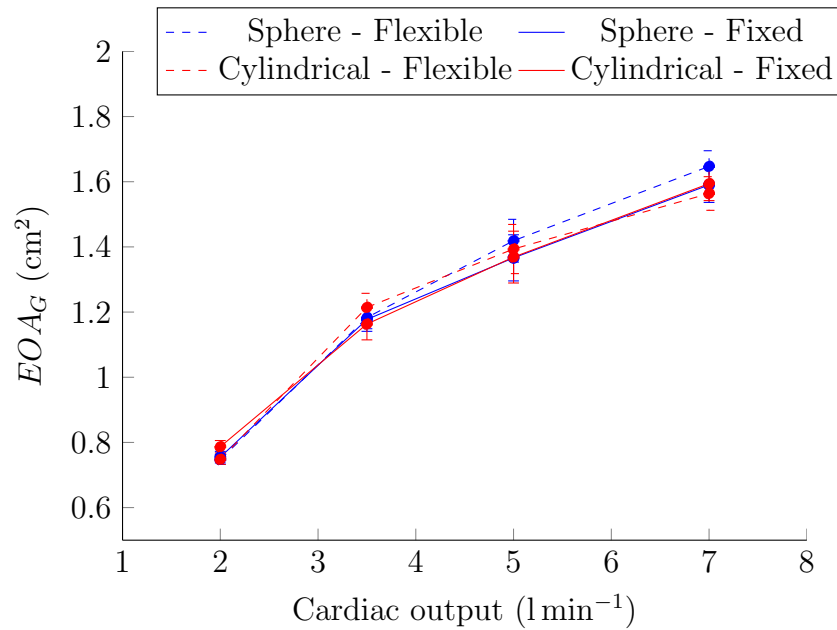


Figure 5.19: Effect of limiting radial deflection on the EOA_G of spherical and cylindrical form valves.

of both EOA_G and regurgitation. However the orifice area may partly be aided by the slightly larger internal diameter of the valve (23 mm vs. 22 mm), though the valve was mounted with a 22 mm collar such that the geometric orifice area when open was equal.

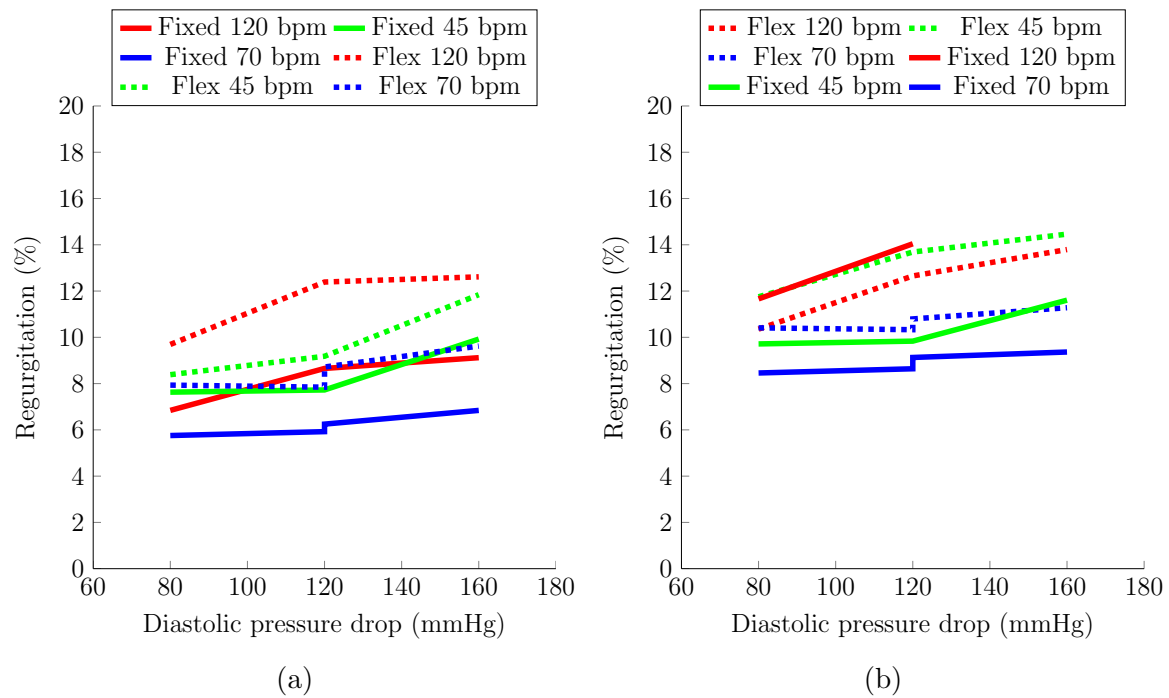


Figure 5.20: Regurgitation of the spherical (a) and cylindrical (b) form valves, with (solid) and without (dashed) radial fixation of the stent posts, during pulsatile testing. The valves were tested at three pulse rates (red, green, blue) and at three diastolic pressure gradients. The radial fixation of the stent leads to significantly less regurgitation for both valve forms.

Table 5.6: Summary of hydrodynamic data for the tested valves, under the ISO 5840 standard conditions of 5 l min^{-1} , 70 BPM, 120 mmHg. (n) indicates the number of valves of each type that were tested.

Valve	TAD (mm)	EOA (cm^2)	Regurgitation (%)
ISO5840 Standard (n)	23	≥ 1.00	≤ 10
Spherical form, unstented (4)	22	1.36 ± 0.05	9.32 ± 0.12
Spherical form, fixed stent (2)	22	1.27 ± 0.07	7.45 ± 0.14
Cylindrical form, unstented (6)	22	1.41 ± 0.08	17.8 ± 0.13
Cylindrical form, fixed stent (2)	22	1.28 ± 0.10	9.71 ± 0.29
Bioprosthesis - 3000 PERIMOUNT Magna Aortic 25 (previously tested in system)	23 ^a	1.63	4.66 ± 0.34
Bioprosthesis - 3000 PERIMOUNT Magna Aortic 25 (<i>in vivo</i> data, (Botzenhardt et al., 2005))	21-23	2.09 ± 0.55	3.33 ± 1.15

^amounted with 22 mm collar.

5.4 Discussion

I proposed two designs of polymeric prosthetic heart valve. One is characterised by being formed from a spherical surface, the other from cylindrical surfaces. In hydrodynamic tests the cylindrical form valve achieved a greater EOA_G , to the detriment of regurgitation. The cylindrical form valve was based upon the design of Burriesci et al. (2010) who optimised the design *in silico*, and verified *in vitro*, against the Aortech valve. In their *in vitro* hydrodynamic tests, using valves of equivalent diameter, at 51min^{-1} , 70 BPM and 100 mmHg mean arterial pressure, the EOA_G of the design was 3.34cm^2 and regurgitation 10.8%, with a 12.1% energy loss. In my experiments, with a flexible stent I recorded an EOA_G of 1.4cm^2 , and once the stent was fixed radially, regurgitation was reduced to 9.7%. The performance of the prototype valve tested here is inferior to that tested by Burriesci et al. (2010) due to the prototype's higher energy loss. The large disparity may be attributed to a combination of differences (this report vs. Burriesci et al. (2010)):

- Testing systems (custom tester vs. Vivitro commercial tester),
- Mode of manufacture (injection moulding vs. dip casting),
- Leaflet thickness ($300\text{ }\mu\text{m}$ vs. $100\text{ }\mu\text{m}$),
- Material (SEPS22 (modulus $\sim 8\text{ MPa}$) vs. silicone (modulus $\sim 45\text{ MPa}$)).

Despite these differences, it is interesting to refer the final two points back to the hypothesis made in Section 2.1.5 and Equation (2.2). I related leaflet thickness and modulus to the force required to open a leaflet. In summary, $\frac{P_{max}}{t^3 E}$ is equal to some constant K_v . For the stiffer, thinner silicone valve, K_v is $400\text{ mmHg}/(\text{N mm})$, while for the softer, thicker, SEPS22 valve, K_v is $300\pm 145\text{ mmHg}/(\text{N mm})$. These are remarkably similar given the approximations that have been made, indicating that the assumptions made in Section 2.1.5 were reasonable.

The superior EOA_G of the cylindrical form valve came at the expense of unacceptable regurgitation. Regurgitation was dominated by retrograde flow during closing, rather than leaking. This suggests that the valve had adequate coaptation between leaflets, but was not able to close quickly enough. *In vivo*, closing is initiated by the vortices in the sinuses of Valsalva (Peacock, 1990; Tien et al., 2014; Van Steenhoven and Van Dongen, 1979), which were not present in this *in vitro* hydrodynamic testing system and could influence closing dynamics. Contrary to the *in vivo* results, De Paulis et al. (2005) found no change in valve behaviour when they compared valved conduits with and without pseudo-sinuses *in vitro*.

The high regurgitation is likely to be connected to the neutral shape that the valve assumes. When unloaded, the angle between the leaflets at the commissure ($2\theta_c$) is 0° for the spherical form because a finite space is required between the leaflets to form them without having to separate them after moulding. In the cylindrical valve this angle can be as much 12° . A small commissural angle has the disadvantage of reduced *GOA* and increased leaflet stresses when open, but the advantage of reduced regurgitation. Leo et al. (2005) performed a thorough velocity field analysis (using laser doppler velocimetry and particle image velocimetry) of a mechanical valve and three versions of a prototype Aortech polymeric valve. *In vivo* trials of the Aortech valve had failed with thrombi forming on the inside of the stent post, and as such the investigators paid particular attention to commissure design. The various Aortech prototypes were characterised by having different θ_c . Although larger θ_c aided opening without detriment to regurgitation, retrograde jets during closing were observed with laser doppler velocimetry, which may have contributed to the *in vivo* failure of the design.

The spherical form valve, without modification, would fulfil the ISO 5840 criteria and this was necessary for progression to an animal and clinical trial. The cylindrical valve fulfilled the ISO criteria but only marginally once the valve had been modified. As such, the spherical form valve was selected for further design iterations and testing.

My study has been valuable in demonstrating the advantages and shortcomings of a valve manufactured from single material. The major shortcoming of the single material valve was the excessive bending of the stent posts. In general, the quality of the valve was good as only one valve broke during testing (due to a visible, pre-existing flaw). The use of direct metal laser sintering to fabricate a mould tool for the production of prototype, injection moulded, polymeric prosthetic heart valves is the first reported in the literature. A functioning valve was produced. The surface was considerably rougher than that of the stainless steel mould so some differences in performance may be attributed to manufacturing. The rougher surface is most likely to affect durability, as flaws may grow from the surface.

5.4.1 Design improvements

Regurgitation was much reduced when the stent posts were fixed radially. Furthermore, significant deflection of the posts led to a markedly different leaflet conformation during diastole, potentially making the optimised anisotropy irrelevant. Several options existed to alleviate this issue:

- Increase the radial thickness of the stent.

- Increase the circumferential thickness of the stent.
- Increase the stiffness by:
 - increasing the PS content (through multi-step injection moulding),
 - using a stiffer material (and thus making a valve with material interfaces).
- Reduce the profile (height) of the valve.
- Suture the commissure or stent post to the aortic wall - like the Sorin Freedom Solo (running suture) or Medtronic 3f (tab at commissure) bioprostheses.

Given the desire to produce a single material valve, which would not need material interfaces or sutures, the first two options were initially pursued.

Increases in the thickness of the stent brought two design constraints into consideration: potential interference with the coronary arteries; and a difference between the external sewing ring diameter (ESRD) and TAD (=internal orifice diameter, IOD). I added the maximum possible expansion to the stent post's axial cross section, as shown in Figure 5.21. The construction steps are shown in Appendix C. The sewing ring extends around the complete circumference of the valve, allowing sutures to be placed at all positions. The valve continues to be made from a single material, including leaflets, stent, and sewing ring.

In the hydrodynamic tester the sewing ring was rigidly fixed in place. This may be a poor representation of the physiological case as during the cardiac cycle the nadirs and commissures of the native valve are highly mobile. Dagum et al. (1999) placed radio opaque markers at the commissures and nadirs of the aortic valve of a sheep. They observed heterogeneous and asymmetric changes in shape. During diastole, 3.7, 10.3 and 11.1% diameter increases at the posterior, right and left sectors, respectively, were observed. Up to 6° of torsion was also observed, and a diameter increase of between 16 and 40% at the sinotubular junction (Dagum et al., 1999; Thubrikar and Klemchuk, 1990). The authors also stress the importance of matching dynamics of valvular implants with those of the aortic root. The use of SEPS22 for the stent posts and sewing ring may allow the valve to flex with the aortic root, in a more physiological manner than current prostheses with stiff stent posts and sewing rings.

The benefit of the change in stent post design was confirmed using a structural finite element (FE) model as shown in Figure 5.22. The maximum stress moved from the middle of the stent-leaflet boundary towards the commissure, and was also reduced by 46%. This reduction in maximum stress is beneficial because small amount of flexibility

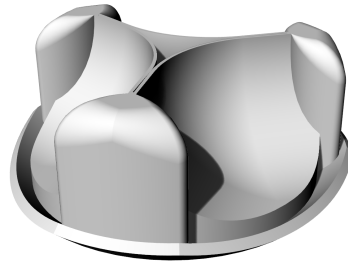


Figure 5.21: CAD image of the updated valve design consisting of spherical form leaflets, enlarged stent posts and a sewing ring for supra-annular implantation.

can significantly reduce the stresses in the leaflet during diastole, increasing the durability of the valve (Krucinski et al., 1993).

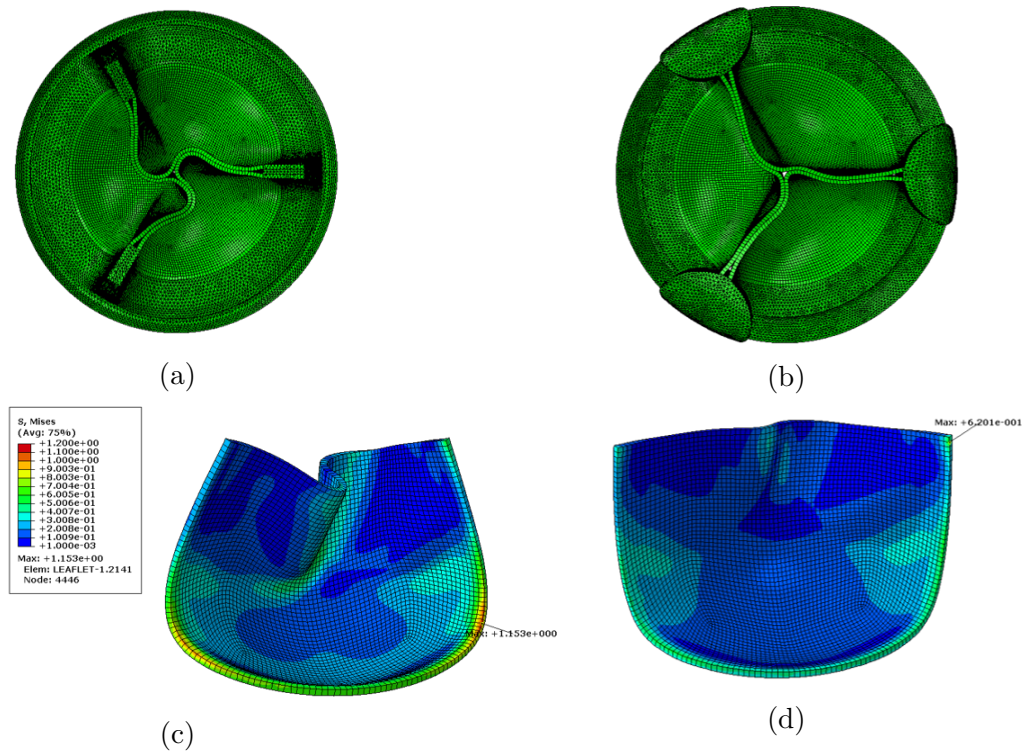


Figure 5.22: FE modelling of the old (a and c) and new (b and d) stent post designs when loaded to 95 mmHg. Images (a) and (b) are viewed axially during diastole. Images (c) and (d) show the von Mises stresses in a single leaflet of each valve. The new stent post design reduces the deflection of the posts and deformation of the leaflets compared to the old. Note that the stress concentrates ($\sigma_{max} = 1.15 \text{ MPa}$) near to the base of the stent post in (c), but the stress is reduced ($\sigma_{max} = 0.62 \text{ MPa}$) and across the stent-leaflet boundary in (d). Modelling and images courtesy of Dr Marta Serrani.

5.5 Conclusion

I fabricated and hydrodynamically tested two types of valve, referred to as spherical form and cylindrical form, which had fundamentally different leaflet designs were evaluated. The spherical form valve has a more conventional leaflet shape, akin to a bioprosthesis, while the cylindrical form valve uses only cylindrical surfaces to reduce the pressure required to reverse the leaflet's curvature. I manufactured both valves from SEPS22 by injection moulding. The valves were then tested in a hydrodynamic pulsatile tester. The cylindrical valve had a greater EOA_G but suffered from unacceptable regurgitation, due to its slow closing. The spherical form valve had a lower EOA_G , and less regurgitation, and fulfilled the ISO standard on both counts. Both valves were inferior to a standard bioprosthesis with respect to hydrodynamic performance.

The original valve designs suffered from excessive deflection of their stent posts and commissures during diastole, which was improved when the posts were radially fixed in place. An updated valve design was proposed in which the most notable feature was an enlargement of the stent posts. Based upon FE modelling, this design resulted in less deflection of the stent posts and commissures and a more stable deformation of the leaflets. This design will be taken forward for final manufacture and testing in the following chapters.

Chapter 6

Valve fabrication

6.1 Introduction

The aim of this chapter is make the valve with a bioinspired orientation. Polymers can be shaped into nearly any 3D form, and some of the properties of the final product can be very dependent on the processing of the source polymer. In this chapter I review the methods which have been used to form polymer-based products, particularly polymeric heart valves, and I consider alternative means for controlling the orientation of cylindrical PS domains. I go on to propose a processing method and I experimentally evaluate its ability to orient domains in a simple geometry. This leads to the development of a model which can be used to design the process to achieve bioinspired orientation in the polymeric heart valve leaflets. Finally, a means of processing and tool design is selected, and the final valve is manufactured.

The most crucial part of a valve is the leaflets, in which the highest diastolic stresses can be found at the leaflet-stent boundary. Bioinspired orientation can be used to reduce these stresses and increase the durability of the valve. Zaffora (2011) optimised the orientation of anisotropy in a polymeric leaflet. The distribution of the optimised orientation was shown in Figure 1.12. In summary, near to the free edge the optimised orientation is horizontal and parallel to the free edge. Moving towards the nadir, the oriented fibres form arcs across the leaflet, with each arc following a similar shape to that of a cable suspended between the stent-leaflet boundaries.

One criteria upon which polymers were shortlisted in Chapter 2 was on their rubbery mechanical properties at room temperature and pressure. In order to permanently change the shape of these polymers the conditions must be changed. If the polymer can be

dissolved, it becomes a viscous solution for solvent, dip, or film casting. In film casting, the solvent is evaporated from the polymer solution while on a flat plate to leave a thin film of polymer. Alternatively, a shaped mandrel can be used, which is dipped into solution, the solvent is evaporated, and the polymer is then detached from the mandrel. Depending on the viscosity, mould shape and position, and atmospheric conditions, the resultant thickness from a single dip can be changed. Repeat dips can then be used to build up the desired thickness (Daebritz et al., 2004b). This process generally results in very few flaws in the polymer, which contributes to the good durability results which have been recorded for dip cast valves (Bezuidenhout and Zilla, 2014). However, it is unattractive from a manufacturing standpoint due to long processing times, the use of non-biocompatible solvents, and the difficulty of maintaining consistency (Leat and Fisher, 1995). Polymer solutions can also be used to coat fabrics or other substrates; SIBS-toluene solution was used to coat polyester fabric, which was trialled *in vivo* but was unsuccessful due to SIBS-polyester dehiscence (Gallocher, 2007).

The absence of major flaws in solvent cast polymers is a significant advantage, so the issues of consistency in leaflet thickness can be overcome by forming simple flat sheets. Rather than using a shaped mandrel (in the desired shape), solvent cast films of a constant thickness can be cut to the desired shape, and solvent bonded to a pre-fabricated frame. Small changes can then be made to the leaflet geometry by subsequent thermo-forming. Unfortunately the solvent bonding of the leaflet to the stent is prone to causing defects which may lead to failure (Leat and Fisher, 1995).

Polymers that are hard to process using temperature or dissolution, ePTFE for example (which cannot be solvent cast), can also be manipulated as flat sheets which are then sutured to a stent. ePTFE valves tested *in vivo* had poor durability and calcified (Nistal et al., 1990). Alternatively, one end of a cylinder can be split into three flaps which are folded upon themselves, and sutured to form three leaflets within the cylinder. This method saw successful clinical use in the less strenuous pulmonary position (Ando and Takahashi, 2009).

Electrohydrodynamic hot jet plotting could provide a means of directly printing polymers with exceptional resolution ($<10\mu\text{m}$). However, the experience of the UCL group with electrohydrodynamic atomisation suggests that this technology is yet to reach maturity (Reade, 2009). The Fraunhofer Institute, in collaboration with the Helmholtz-Institute for Biomedical Engineering of RWTH Aachen University, fabricated polycarbonate-urethane venous valves using a dropwise method. Dissolved polymers, of varying hardness, deposited in drop volumes of 2 to 60 nl, then allowing the solvent to evaporate in order to build up a complete valve (Bezuidenhout and Zilla, 2014).

Alternatively, polymers can be manipulated at elevated temperatures. Compression moulding requires a male (core) and female (cavity) mould, between which a block of polymer is placed. The mould is then compressed, causing the molten polymer to fill the cavity. The earliest silicone valves made by Roe et al. (1966) were compression moulded at 180 °C, followed by a 4 h cure at 200 °C. Later designs used silicone in plaster moulds, filled by evacuating air or centrifugation followed by room temperature curing (Chetta and Lloyd, 1980). Claiborne et al. (2013b) also compression moulded uncrosslinked xSIBS in an evacuated, five part aluminium mould at 260 °C, to initiate Diels-Alder crosslinking. They were successful at producing valves, though further results - especially durability - have not yet been reported for this valve. Whilst it is relatively easy to reliably reproduce the temperature conditions during compression moulding, it is hard to control the flow field within the cavity, and ensure complete filling of complex parts.

Injection moulding can overcome these limitations. Injection moulding involves the compression and heating of polymer pellets in a barrel, before injection into a mould cavity. The mould can then be split, the part ejected, and the process repeated. Injection moulding tools can have intricate, accurate, and complex geometries, which are reproducibly and rapidly filled without need for toxic solvents. Various patents suggest that injection moulding has been used to produce polymeric valves (Bernacca et al., 2009; Bluestein et al., 2013a; Campbell et al., 2004; Chinn, 2002; Pietsch et al., 1988), though few have reported the results - if of course the valves were made that way. Mackay (1992) recognised the advantages of injection moulding for polymeric valves, and fabricated moulds for the Glasgow PU valve. Unfortunately they could not achieve consistently thin leaflets, due to poor tooling and air bubbles in the mould, limiting the durability of the valve. Sacristan et al. (2003) produced injection moulded silicone trileaflet valves in a conduit for use in ventricular assist devices. This has certainly been a successful avenue of use for injection moulded valves, as the process is very cost effective, and the durability limit of these valves is rarely approached as the ventricular assist devices are only for short term use.

6.1.1 Orientation of polystyrene domains

As well as processing the polymer into the form of the prosthesis, the aim of this thesis is to orient the stiff polystyrene (PS) cylinders of the BCP into a bioinspired orientation. The selected BCP self-assembles into cylinders at room temperature. During solvent casting, entropic forces dominate, causing microphase separated cylinders to be randomly oriented, however, it may be possible to seed the microphase separation, causing it to grow

in a quasi-crystalline manner. In the same manner that a bubble of steam will form at a defect in a pot of water, or a salt will crystallise at a flaw in a substrate, the formation of microphase separations in BCPs can also be initiated. By chemically or topographically patterning the surface of a BCP (solution) it is possible to seed a crystalline “flaw” from which a regular microphase structure can grow. PS cylinder arrays in thin films of SBS BCP can be oriented perpendicular or parallel to the surface, depending on the strength of the surface field. Unfortunately, predictions and experiments can only propagate this orientation up to approximately 10 (parallel oriented cylinder) layers from the surface (Sakurai, 2008). The use of a selective solvent and fast evaporation can result in cylinders which are well oriented perpendicular to the surface (Phillip et al., 2010). While these effects continue to be useful in other applications, they are not a realistic means for achieving orientation across the leaflets of a BCP prosthetic heart valve.

It is also possible to orient microdomains under the influence of an external electrical or magnetic field. Microphase separation leads to spatial variation in the dielectric constant, meaning that domains can order parallel to the electric field. However, the electric field is limited in power due to dielectric breakdown. To overcome the electric field limitation, a magnetic field can be used. However, magnetic fields are less efficient at orientation, and so the lowest strength field which has successfully been used to orient microphases was 1.8 T (Liedel et al., 2012; Sakurai, 2008).

The most widely studied method of microdomain orientation is using mechanical force fields. When the temperature is above T_m (melting temperature) but below T_{ODT} (order-disorder transition temperature) the domains can be moved and deformed. The use of shear and extensional deformations to align microphase domains of BCPs was first recorded by Keller et al. (1970). Cylindrical BCPs orient in the direction of extension when in polymer melts (Castelletto and Hamley, 2004; Fang et al., 2009; Stasiak et al., 2010) and solutions (Hamley, 2000), though high strain rates (20 s^{-1}) decrease the quality of alignment (Carastan et al., 2013). Continuous shear leads to orientation perpendicular to the shear gradient - in the direction of flow - while oscillatory shear causes microdomains to orient perpendicular to the shear gradient, to parallel, and back to perpendicular as frequency is increased (Chen et al., 1997; Morozov and Fraaije, 2002).

Injection moulding has the potential to reproducibly fabricate complex parts within the necessary tolerance, and also leads to shear and extensional forces which can be used to orient PS cylinders. Given these two points, I selected injection moulding as a means of producing bioinspired, polymeric prosthetic heart valves.

A polymer injection moulding tool with the necessary tolerances to make a prosthetic heart valve generally costs upwards of £5k, and so, it is unwise to design and develop a

tool without a reasonable understanding of the polymer characteristics and mould flow patterns. Thus I begin this chapter by describing polymers that I injected into a simple test geometry to determine how shear and stretch influence the cylinder orientation. Along with these observations, the melt rheology of the polymer was characterised, before developing a model for the orientation of PS domains during moulding. The model is validated in a valve test geometry and then the model is used to inform the design of the final tool. Finally, a valve is injected and the orientation is evaluated.

6.2 Point injection

In an injection moulder used in production (as Figure 6.1) the following steps take place:

1. The solid polymer (in pellet, powder or crumb form) is compacted using a rotating screw in the barrel.
2. The compacted polymer is melted as it advances along the heated barrel.
3. The screw stops rotating, and is rammed along the barrel, ejecting polymer from the nozzle of the barrel, into the injection moulding tool.
4. Polymer passes through the sprue bushing, along a runner or runners, and through a gate or gates, into the cavity.
5. If the tool has been heated intentionally or by the injected polymer, it is cooled and the part solidifies.
6. The tool is split along the parting line.
7. The (moulded polymer) part is ejected or manually removed from the tool.

For prototyping, I reproduced this process on a bench top scale:

1. Polymer pellets heated in an oven.
2. Heated pellets compacted and cooled.
3. Compacted block placed in barrel of extruder.
4. Barrel and tool heated.
5. A ram used to push the polymer melt from the barrel into the cavity of the tool.
6. Tool removed from the moulder, cooled, and the part removed.

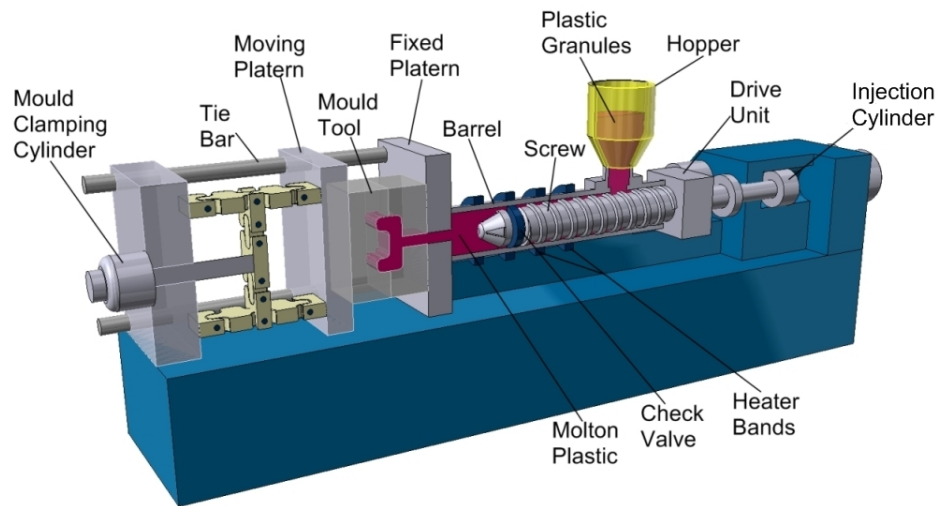


Figure 6.1: Schematic of injection moulder. Taken from rutlandplastics.co.uk.

A gate is the inlet for polymer into the cavity. If the gate is oriented perpendicular to a thin cavity (such as heart valve leaflet) the polymer will diverge in a scenario referred to as *radial flow*. To simulate radial flow in a preliminary experiment, one of the shortlisted polymers considered in Chapter 2, SIS30, was injected at 160 °C via a 1 mm diameter gate into the centre of two stainless steel parallel circular plates each of diameter 80 mm whose separation could be set in order to achieve a range of sample thicknesses. The injection was performed using a manual hydraulic press, in which the injection rate was manual so subject to variation in control. The plates were cooled from 160 °C to 40 °C under running water over approximately one minute after the completion of injection. The time taken to perform the injection was recorded, and the volumetric injection rate inferred. Two injection rates and three sample thicknesses were tested, as summarised in Table 6.1.

Table 6.1: Injection rates and sample thickness for point injected specimens of SIS30.

Code	Injection rate ($\text{m}^3 \text{s}^{-1}$)	Sample thickness (mm)
A	$7 \pm 2 \times 10^{-8}$	0.95 ± 0.05
B		0.45 ± 0.02
C		0.23 ± 0.03
D	$2 \pm 0.5 \times 10^{-8}$	0.97 ± 0.05
E		0.44 ± 0.02
F		0.30 ± 0.02

6.2.1 Structure analysis by small angle X-ray scattering

Cylindrical PS domain orientation leads to anisotropic mechanical properties. In this chapter I investigate whether these can be harnessed to produce a bioinspired prosthesis, as described in Section 1.10.1. It was not feasible to perform tensile testing to evaluate the mechanical anisotropy on small samples, such as parts of the leaflets, so alternative means of characterising the orientation were needed. The spacing of the PS domains in my samples is of the order of 10 nm, whose structure can only be analysed using X-rays or neutrons. Stasiak et al. (2010) showed that mechanical properties are strongly correlated with small angle X-ray scattering (SAXS) analysis, making it an appropriate means of assessing orientation. This method utilises Bragg's law, whereby a crystalline solid scatters electromagnetic radiation such that different path lengths result in constructive or destructive interference at a detector. Bragg's law describes the case of constructive interference where d is the distance between crystal planes, θ is the scattering angle, λ is the wavelength, and n is the order of the scattering peak:

$$2d\sin\theta = n\lambda \quad (6.1)$$

Thus the crystal plane spacing and orientation can be calculated using monochromatic irradiation and a detector covering a range of angles.

The orientation of the domains in the point-injected samples was evaluated by SAXS using a synchrotron source of X-rays, at the I22 beamline at the Diamond Light Source, Harwell Science and Innovation Campus, UK. The energy used was 12.4 keV (0.1 nm) with 6 m between the sample and the RAPID 2D detector. The sample was irradiated with a rectangular beam whose full width (at half maximum of the Gaussian distribution) was $320 \times 80 \mu\text{m}$, allowing spatial mapping of the orientation in small samples to be performed. The integrated SAXS patterns were processed using OriginPro 9.0 (OriginLab, MA, USA).

As depicted in Figure 6.2, the samples were moved relative to the beam, to collect patterns at points at various radii, with the beam in the Z-axis direction. A radial section was cut, of thickness $\sim 1 \text{ mm}$, and the beam oriented in the plane of the sample. SAXS patterns were recorded every 1 mm across the sample when the beam was in the Z-axis direction; and every 0.1 mm for scans through the thickness of the sample, along the Z axis.

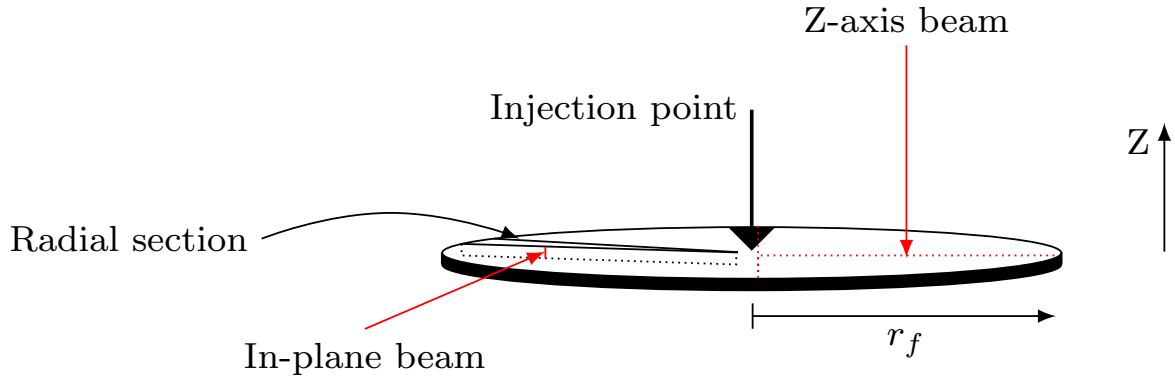


Figure 6.2: The beam was oriented in the Z direction for SAXS scanning of the disc of radius r_f along the X and Y axes. A radial section was removed from the disc and the beam oriented along the Y-axis, for scanning at an array of Z positions through the sample. Red dots indicate the approximate position of measurements which were made radially and along the Z axes.

6.2.2 Results

It was a surprise to observe that the cylindrical PS domains of the injection moulded discs did not orient solely in the direction of flow (Fang et al., 2009; Stasiak et al., 2010). In fact, a bimodal distribution of orientations was observed; as indicated by the SAXS pattern and azimuthal integration shown in Figure 6.3. The 1st order peak corresponds to a domain spacing of 27 nm, and the higher order peaks occur at $\sqrt{3}$ and $\sqrt{7}$, indicating that the PS cylinders are arranged in a hexagonal structure (Stasiak et al., 2010, 2009). Bi-directional orientation is evident across the entirety of all six samples, and the orientation is symmetric across the sample.

Azimuthal peak broadening at full width half maximum ($FWHM$) was used as a measure of the degree of anisotropy for the two reflections at 90° and 180° . In Figure 6.4, the radial and circumferential cylinder orientation is plotted as vectors, in the X and Y directions across the sample. The length of the vector is proportional to $1/FWHM$. Close to the injection point (within 5 mm) there is some variation in the degree of anisotropy and orientation of the domains, which is associated with the development of flow from the gate. At larger radii, the degree of anisotropy in the radial and circumferential orientations was high throughout the sample, and did not vary significantly with position.

The samples were scanned with the beam oriented in the plane of the sample, as shown in Figure 6.5. The pattern varies with position, and is approximately symmetric across the centre line of the sample, indicating that the bimodal orientation was layered, with remarkably good segregation between the circumferentially and radially oriented layers. At some depths, ± 0.2 mm for example, radial and circumferential patterns are visible.

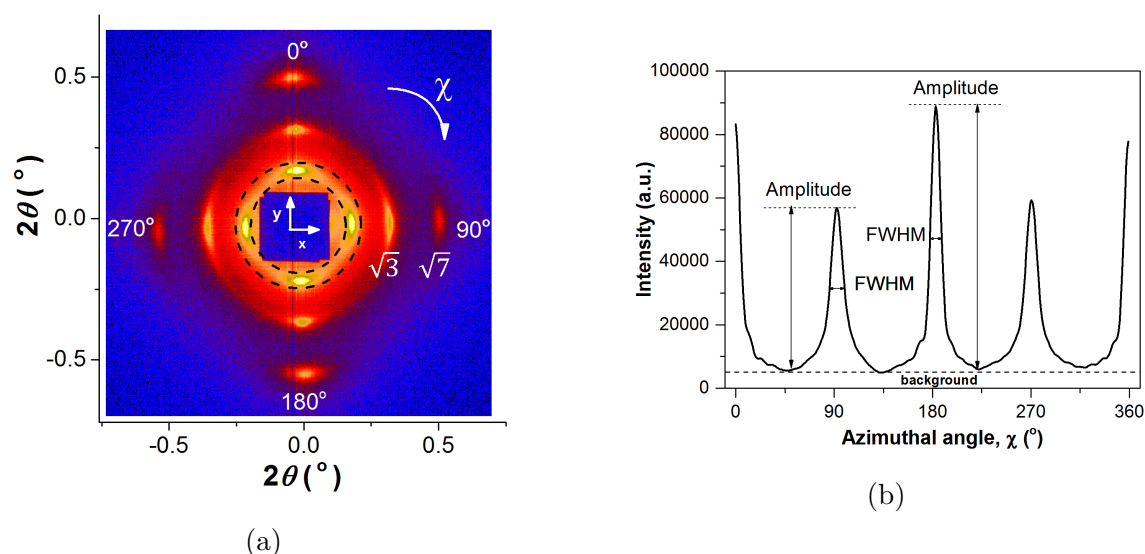


Figure 6.3: (a) SAXS pattern from a Z-axis beam through a 0.95 mm thick sample injected at $7 \times 10^{-8} \text{ m}^3 \text{ s}^{-1}$. The four innermost peaks (indicated by - - - at $2\theta = 0.2^\circ = \theta_1$) correspond to the first order of scattering from a biaxial arrangement of cylinders. The peaks at $2\theta = 0.35^\circ = \theta_1\sqrt{3}$ and $2\theta = 0.53^\circ = \theta_1\sqrt{7}$ correspond to reflections from other planes of the hexagonally structured cylinders (this arrangement is shown in Figure 6.5c). (b) shows the azimuthal integration of the diffraction space in (a) in the region marked by - - -. The amplitude and full width half maximum are marked. These data were processed by Dr Joanna Stasiak.

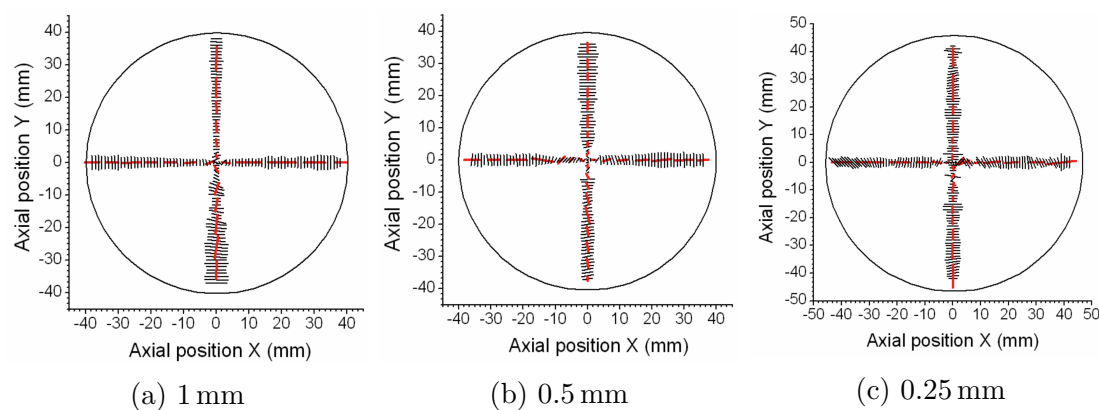
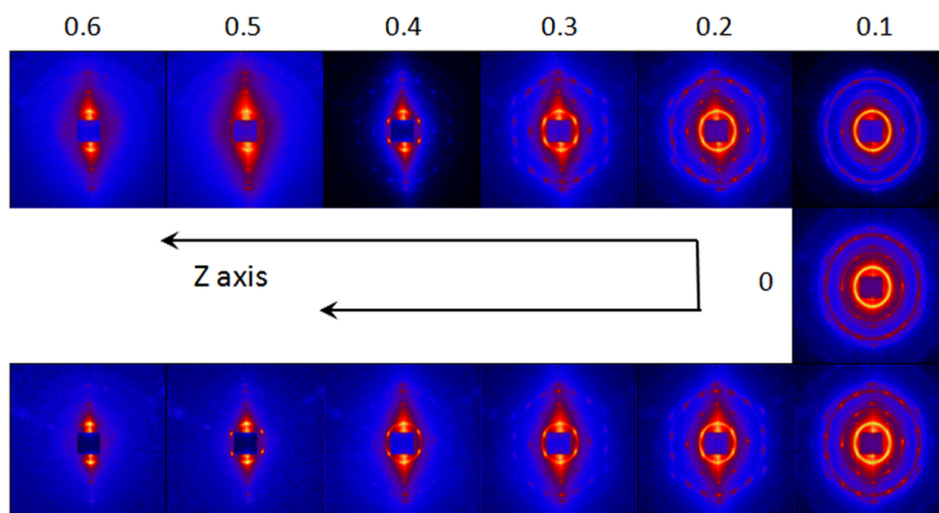


Figure 6.4: SAXS mapping of the orientation of PS domains in thin discs (1, 0.5, 0.25 mm thick). The length of each tick mark corresponds to the azimuthal integration of each peak. The origin of the X and Y axes was located at central injection point of each sample. This data was processed by Dr Joanna Stasiak.

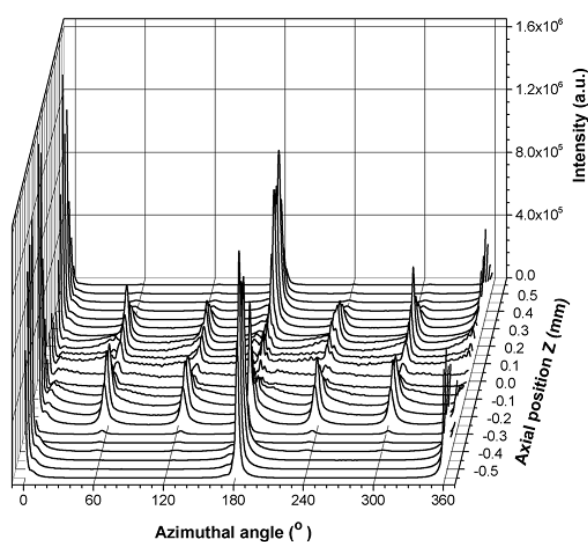
This is due to the finite thickness of the beam which passed through both layers simultaneously. In the centre of the sample there is an isotropic region, as indicated by the circular scattering pattern at depths of 0 and ± 0.1 mm.

X-rays are scattered from all the crystal planes in an oriented PS sample. The (110), (101), and (011) planes have a normalised spacing of 1; the (121), (211), and (112) planes have a $\sqrt{3}$ spacing; and the (123) and corresponding planes have a $\sqrt{7}$ spacing (Honeker and Thomas, 2000). These are marked in Figure 6.3a for the pattern from the Z-axis beam. The corresponding peaks were found in the patterns for the in-plane beam aligned with the hexagonally arranged PS cylinders (0.3 mm depth in Figure 6.5a). The sum of the first order peak areas for reflections from each set of planes was compared. The peaks found at a normalised spacing of 1 accounted for 98% of the first order scatter. Thus, when the beam is oriented in the Z-direction, the quantity of radial and circumferential orientation can be compared by looking at the peaks arising due to scattering from the planes of the unit cell ((110), (101), and (011)).

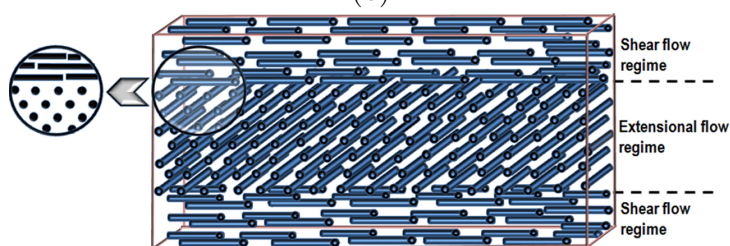
I measured the thickness of the radial and circumferential layers when the sample was scanned with the beam oriented in the plane of the sample. This was compared to the area of the radial and circumferential peaks when the Z-axis beam was scattered. The magnitude of the radial and circumferential peak areas was a function of the beam's angle of incidence on the crystal planes, however the ratio of the radial and circumferential peak areas from the Z-axis beam matched the thickness of the radial and circumferential layers when they were measured using the in-plane beam in 9 samples.



(a)



(b)



(c)

Figure 6.5: (a) SAXS pattern for an in-plane beam at 13 depths (z positions) in a sample. (b) Azimuthal integration of the first order peaks for an in-plane beam through a sample of thickness 0.95 mm and injected at $7 \times 10^{-8} \text{ m}^3 \text{ s}^{-1}$. The larger peaks at 0° and 180° correspond to the radially oriented cylinders in the skin regions, and the six smaller peaks correspond to the circumferentially cylinders in the core. (c) is a schematic of the bimodal structure of PS cylinders. The detail shows the hexagonal arrangement of cylinders. This data was processed by Dr Joanna Stasiak.

6.3 Flow characterisation

It is known that deformations during flow can control PS domain orientation. To predict these deformations I needed to relate the fluid stresses and deformations through a constitutive model. In this section I progressively test the suitability of more complex constitutive models to evaluate their accuracy in describing the polymer's melt behaviour.

Rheological measurements are performed in standard geometries to determine the parameters of the constitutive models, before being tested in the radial flow scenario. In the radial flow geometry the equations may be solved analytically for some constitutive models, otherwise finite element (FE) methods were considered. With an accurate constitutive model, the velocity field under a set of process conditions can be predicted, from which it should be possible to predict the orientation of PS cylinders. A schematic of the radial flow geometry, which contains the nomenclature used in the subsequent analyses, is shown in Figure 6.6.

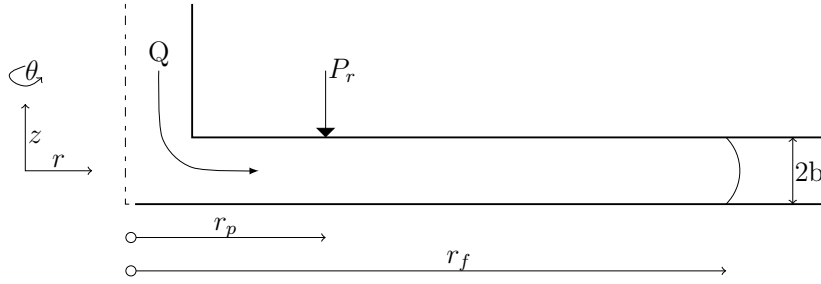


Figure 6.6: Schematic of radial flow from a point injection, using cylindrical coordinates. Q is the flow rate through the gate, P_r is the pressure reading taken at radius r_p , $r_f = f(t)$ is the edge of the disc/flow, and b is the half-thickness of the disc.

6.3.1 Generalised Newtonian Flow

Generalised Newtonian models are the simplest constitutive relations which may be able to adequately describe the flow field. In this analysis incompressibility, rotational symmetry, constant density, and no wall slip are assumed (Winter, 1975):

$$\nabla \cdot \vec{v} = 0 \quad (6.2)$$

$$\vec{v} = (v_r(r, z), 0, 0) \quad (6.3)$$

$$\frac{\partial}{\partial \theta} = 0 \quad (6.4)$$

$$\rho = \text{constant} \quad (6.5)$$

$$v_r(r, \theta, \pm b) = 0 \quad (6.6)$$

where \vec{v} is the velocity vector, ρ is the density, and θ , r , and z are the axes defined in Figure 6.6. Using assumptions 6.2, 6.3, and 6.4, which correspond to continuity, pure radial flow, and symmetry, v_r varies with z and r as:

$$v_r = \frac{f(z)}{r} \quad (6.7)$$

And so the rate of strain tensor, $\dot{\gamma}$, where (1, 2, 3) correspond to (r, θ, z) is, (Winter, 1975);

$$\dot{\gamma} = \nabla \vec{v} + (\nabla \vec{v})^t = \begin{bmatrix} -2r^{-2}f & 0 & r^{-1}f' \\ 0 & 2r^{-2}f & 0 \\ r^{-1}f' & 0 & 0 \end{bmatrix} \quad (6.8)$$

where $f' = df/dz$. Given an inflow of Q and half-thickness of b , f is solved to give the velocity gradients:

$$\nabla \vec{v} = \frac{3Q}{8\pi r b} \begin{bmatrix} -\frac{1}{r} \left(1 - \frac{z^2}{b^2}\right) & 0 & -\frac{2}{b} \left(\frac{z}{b}\right) \\ 0 & \frac{1}{r} \left(1 - \frac{z^2}{b^2}\right) & 0 \\ 0 & 0 & 0 \end{bmatrix} \quad (6.9)$$

It is immediately obvious that at the walls ($z = b$) there are no elongational deformations (diagonal components), only shear, while at the midplane ($z = 0$) there is pure extensional flow, and no shear.

Equation (6.9) can be integrated to yield an expression for v_r :

$$v_r = \frac{3Q}{8\pi r h} \left(1 - \frac{z^2}{b^2}\right), \quad v_\theta = v_z = 0 \quad (6.10)$$

Using conservation of momentum:

$$\rho \left[\frac{\partial \vec{v}}{\partial t} + \vec{v} \cdot \nabla \vec{v} \right] = \rho \mathbf{g} + \nabla \cdot \boldsymbol{\sigma} \quad (6.11)$$

where $\boldsymbol{\sigma}$ is the total stress tensor, and $\boldsymbol{\sigma} = -P_H \mathbf{I} + \boldsymbol{\tau}$, where P_H is the hydrostatic pressure, \mathbf{I} is the identity matrix, and $\boldsymbol{\tau}$ is the shear stress tensor. The Navier-Stokes equation in cylindrical coordinates, for the radial component with inertial elements neglected, is formed:

$$\frac{\partial P}{\partial r} = \eta \left[\frac{1}{r} \frac{\partial}{\partial r} \left(r \frac{\partial v_r}{\partial r} \right) - \frac{v_r}{r^2} + \frac{1}{r^2} \frac{\partial^2 v_r}{\partial \theta^2} - \frac{2}{r^2} \frac{\partial v_\theta}{\partial \theta} + \frac{\partial^2 v_r}{\partial z^2} \right] \quad (6.12)$$

Taking assumptions 6.2 to 6.6, flow rate Q , and also assuming a Newtonian fluid of constant viscosity η ,

$$\tau = \eta \dot{\gamma} \quad (6.13)$$

where τ is the shear stress and $\dot{\gamma}$ is the shear rate. The pressure at radius r_p , can be calculated by integrating the above expression and substituting r for r_f , which is the instantaneous radius of the polymer disc as it expands.

$$P(r_p) - P(r_f) = 2\eta \left[\frac{2}{r_p} - \frac{2}{r_f} - \frac{3Q}{8\pi b^3} (\ln r_p - \ln r_f) \right] \quad (6.14)$$

However, in most cases real fluids are not Newtonian. The first deviation from the aforementioned behaviour which I will consider is a variation in viscosity. As well as the constant viscosity expressions shown above, Winter (1975) also derived an analytical solution for a power law fluid, where η is a function of shear rate $\dot{\gamma}$:

$$\eta = m\dot{\gamma}^{n-1} \quad (6.15)$$

where m is the consistency index and n is the power index. This can account for a monotonically increasing or decreasing viscosity. Assuming that the r -components of the normal stress components cancel, the radial pressure gradient is a function of r only, and $\dot{\gamma} = |\dot{\gamma}_{rz}|$. Then, the velocity field can be obtained:

$$v_r(r, z) = \frac{Q}{4\pi b r} \frac{2n+1}{n+1} \left[1 - \left(\frac{z}{b} \right)^{\frac{1+n}{n}} \right] \quad (6.16)$$

And also the pressure at r_p , if the disc has an outer radius of r_f :

$$P(r_p) - P(r_f) = \left(\frac{2n+1}{n} \frac{Q}{\pi r_f 4b^2} \right)^n \frac{m r_f}{b(1-n)} \left[1 - \left(\frac{r_p}{r_f} \right)^{1-n} \right] \quad (6.17)$$

Experimental materials and methods

Rheological characterisation of the selected molten polymer, SEPS22, was carried out using a stress controlled Bohlin CVO rheometer with both smooth and roughened stainless steel parallel plates (\varnothing 25 mm). Steady shear viscometry was performed at 130, 150, 170 and 190 °C.

Previously (in Section 6.2), the injection moulding apparatus was incapable of sustaining a consistent and controllable flow. To validate the orientation model I used a BOY 22D

injection moulder (BOY Ltd, Northants, UK) (as shown in Figure 6.7). The moulder consists of a 32 mm diameter barrel, and screw with 80 mm of travel. The barrel has four heating regions from hopper to nozzle, which were set to 80, 110, 130 and 150 °C. I designed and constructed a custom riser and plate assembly which could be heated and cooled using integrated electric cartridge heaters and water cooling channels. The dimensions of the cavity are set by a stainless steel sheet, allowing arbitrary sheet thicknesses and 2D shapes to be moulded. In these experiments a circular cavity with a radius of 100 mm and thickness of 0.7, 1, and 1.5 mm were used.



Figure 6.7: BOY 22D injection moulder used for making flat discs.

The plates were heated to 150 °C and injected using the back pressure control mode, at various pressures, from 25 to 95% of the maximum 800 bar barrel pressure. A pressure line connects to the mould cavity at radius $r_p = 45$ mm, and leads to the pressure gauge (Terwin 2000, 500 bar range). The vertical portion of the line is filled with hydraulic oil, though the remaining 10 mm cannot be filled with oil as it is horizontal, and so becomes filled with the melted polymer upon injection.

Experimental results

When stress-controlled rheometric testing was performed with smooth plates the polymer disc slipped, so roughened plates were used for the shear rheology characterisation. Steady shear rheology is shown in Figure 6.8, with the data fitted to a power law model (Equation (6.15)) the melt is clearly shear-thinning. The decreasing shear rate sweeps had

a lower viscosity than the increasing ones, indicating some thixotropy (time dependence of viscosity), but this was small compared to the sample-to-sample variation.

I also considered the effect of temperature on the polymer rheology; viscometry data for steady shear at 130, 150, 170 and 190 °C is shown in Figure 6.9. The viscosity is highest at 130 °C, decreases to a relatively constant value between 150 and 170 °C, before increasing at 190 °C, likely due to oxidation of the polymer.

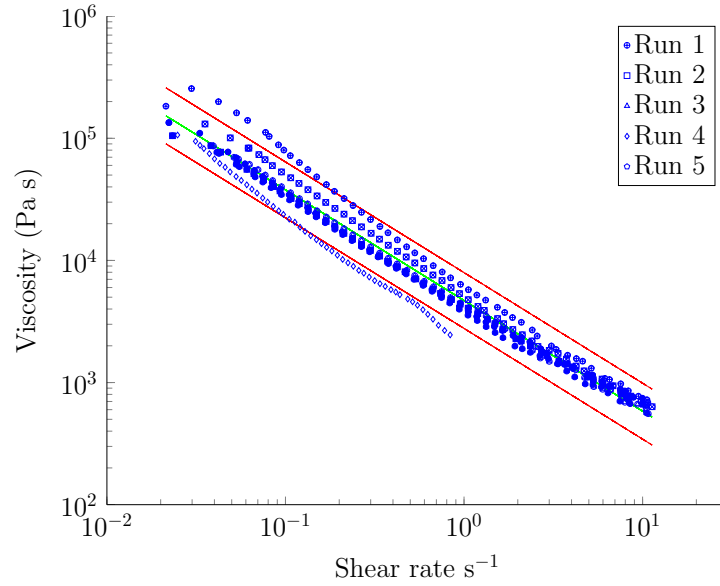


Figure 6.8: 5 runs of steady shear sweeps of SEPS22 at 150 °C, with increasing shear rates (empty symbols); and 4 decreasing (filled symbols). The increasing and decreasing shear rates are nearly coincident, so are hard to distinguish. The data is fitted to a power law model (green), and the 95% confidence interval limits are shown (red). The power law index is $n = 0.094(0.082, 0.106)$, and consistency factor $m = 4696(2430, 9072)$ (95% c.i.).

The polymer melt was injected into the cavity at 150 °C. Figure 6.10 shows an example of the screw position and pressure trace that were obtained during injection. An initial rapid increase in pressure is recorded at the gauge as the polymer melt fills a short section of the pressure gauge line. Subsequent analyses were based upon the pressure trace in region (e), which was extrapolated back to an initial time at which the polymer reached the pressure gauge at r_p . Despite operating at 95% of the moulder's maximum injection pressure, the high viscosity of the polymer leads to modest injection speeds, and long processing times. Higher temperatures would reduce processing times, but run the risk of degradation (Figure 6.9). In future it may be possible to inject under a nitrogen atmosphere to reduce degradation.

The polymer in the pressure line takes over 2 h to relax - a significant time in comparison to the time taken to inject the polymer. The ratio of the material's relaxation time to the

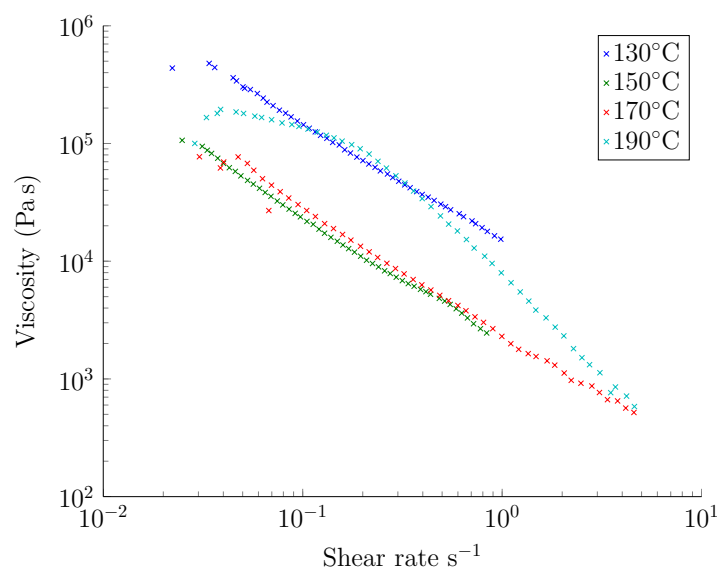


Figure 6.9: Steady shear sweeps of SEPS22 at 130, 150, 170 and 190 °C.

processing time, is termed the Deborah number (De). High Deborah numbers indicate that elastic and solid-like characteristics are important.

In Figure 6.11 the experimental data is compared to the pressure predicted using Equations 6.10 and 6.17. The experimental data reaches significantly higher pressures than the power law and Newtonian models predict. In general, the experimental pressure is approximately double the pressure that is predicted by the power law model. A power law fluid would lead to a more linear increase in pressure due to the reduced viscosity at higher shear rates, which we might find in the early part of the injection. Given the discrepancy, it is appropriate to consider more representative rheological models which might produce a closer fit to the experimental data, allowing the velocity field to be predicted, and thus orientation, more accurately.

All of the rheological measurements that have been made thus far were taken in a parallel plate geometry, which produces shear without extension. A complete description of a fluid must be valid in both shear and extension; however it is impossible to produce steady and spatially uniform extensional flows (Petrie, 2006), making extensional rheometry the ugly cousin of shear rheometry. Instead, the next level of complexity accounts for the viscoelasticity of polymers.

6.3.2 Viscoelasticity

Newtonian behaviour would have made analysis easier but was clearly not the best description for this polymer melt. The elastomeric properties of polymers are important at

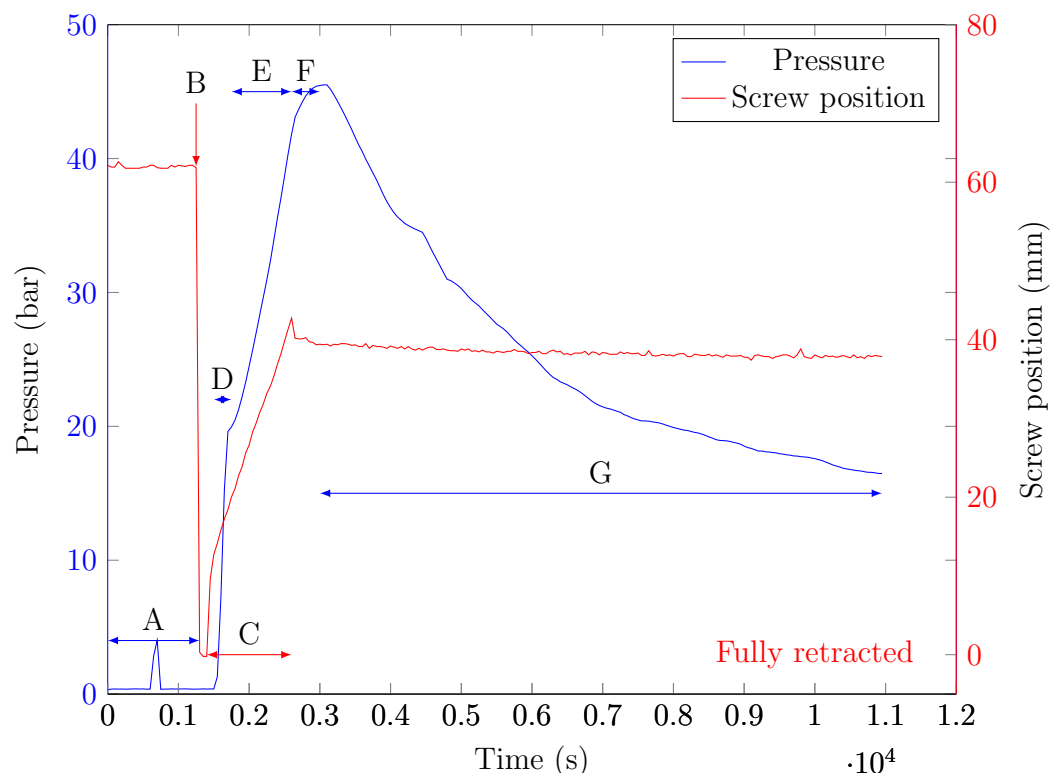


Figure 6.10: Example of the pressure and screw position data collected during injection moulding of a disc. The tool is held at 150 °C throughout the procedure. The pressure gauge is stabilised at A, before the screw is retracted and loaded at B. A constant back-pressure is applied to the screw C forcing the polymer into the disc cavity. The polymer melt reaches the pressure gauge line, which it must fill D, before the radial flow continues E, until the cavity is filled. The screw is halted, though the pressure at the gauge continues to increase F as the movement is propagated through the nozzle and down the runner. The tool is left at temperate for 2 h over which time the polymer relaxes G.

melt temperatures, and so these must be accounted for during processing. The simplest way to incorporate elastic behaviour into the constitutive fluid model is to assume that the current stress in a fluid is linearly related to its strain history, meaning that the stress and strain responses are separable. To assess the relative contributions of elastic and viscous properties oscillatory rheology measurements were performed.

The amplitude sweep data are shown in Figure 6.12a. As amplitude increases, the elastic and viscous moduli are invariant up to 5.5% deformation at which point the rheometer's torque limit is reached and the rheometer cannot complete the test. Linear viscoelastic measurements can be performed up to 5% strain.

Frequency sweep testing was performed at 1% strain, well within the linear region of viscoelasticity and torque limit of the machine. The frequency sweep shown in Figure 6.12 demonstrates that at the temperature of interest, 150 °C, the elastic contribution to

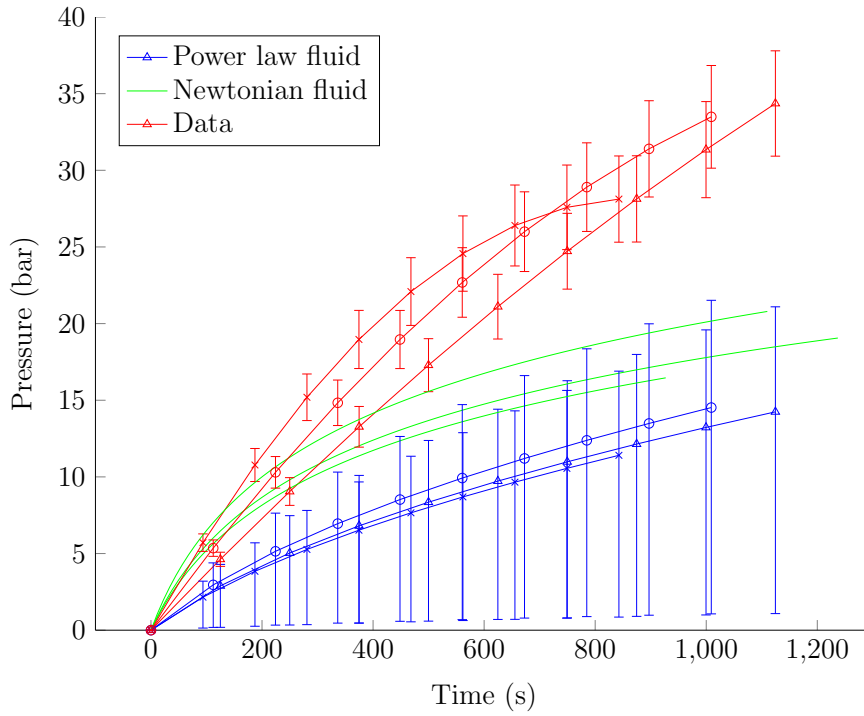


Figure 6.11: Experimental data ($n=3$, \triangle , \times , \circ) vs. predictions based upon generalised Newtonian models for point injection (region (e) in Figure 6.10). Pressure is measured at $r_p = 45$ mm, and the predicted pressures are based upon the results of equations 6.10 and 6.17, given the measured experimental flow rates. The power law model is based upon the rheological data presented in Figure 6.8 and the Newtonian model assumes a viscosity of 10 kPa. The error bars of the power law model are based upon the confidence limits of the data shown in Figure 6.8.

viscosity is greater than the viscous contribution, at all measured shear rates. As such the Weissenberg number ($\frac{\text{viscous forces}}{\text{elastic forces}}$) is large - suggesting solid-like behaviour as associated with the high Deborah number in Figure 6.10. For reference, the wall shear rate in the radial flow scenario with a typical $Q = 2 \times 10^{-8} \text{ m}^3 \text{ s}^{-1}$, reaches approximately 2.5 s^{-1} . The complex viscosity (Figure 6.12c) exhibited shear thinning behaviour, which followed a power law at low temperatures, similar to the result of the steady shear experiments (Figure 6.8). However, comparison of the steady and dynamic data also indicates that the Cox-Merz rule (Equation (6.18)) is not valid for these flows:

$$\eta(\dot{\gamma}) = \eta^*(\omega) \text{ when } \dot{\gamma} = \omega \quad (6.18)$$

Indicating that high steady shear rate viscosity cannot be predicted based upon high frequency oscillatory rheometry. The melt appears more viscous during small oscillations than during the large deformations found in continuous shear, which may be due to the breakdown of the self-assembled microstructure (Djabourov et al., 2013).

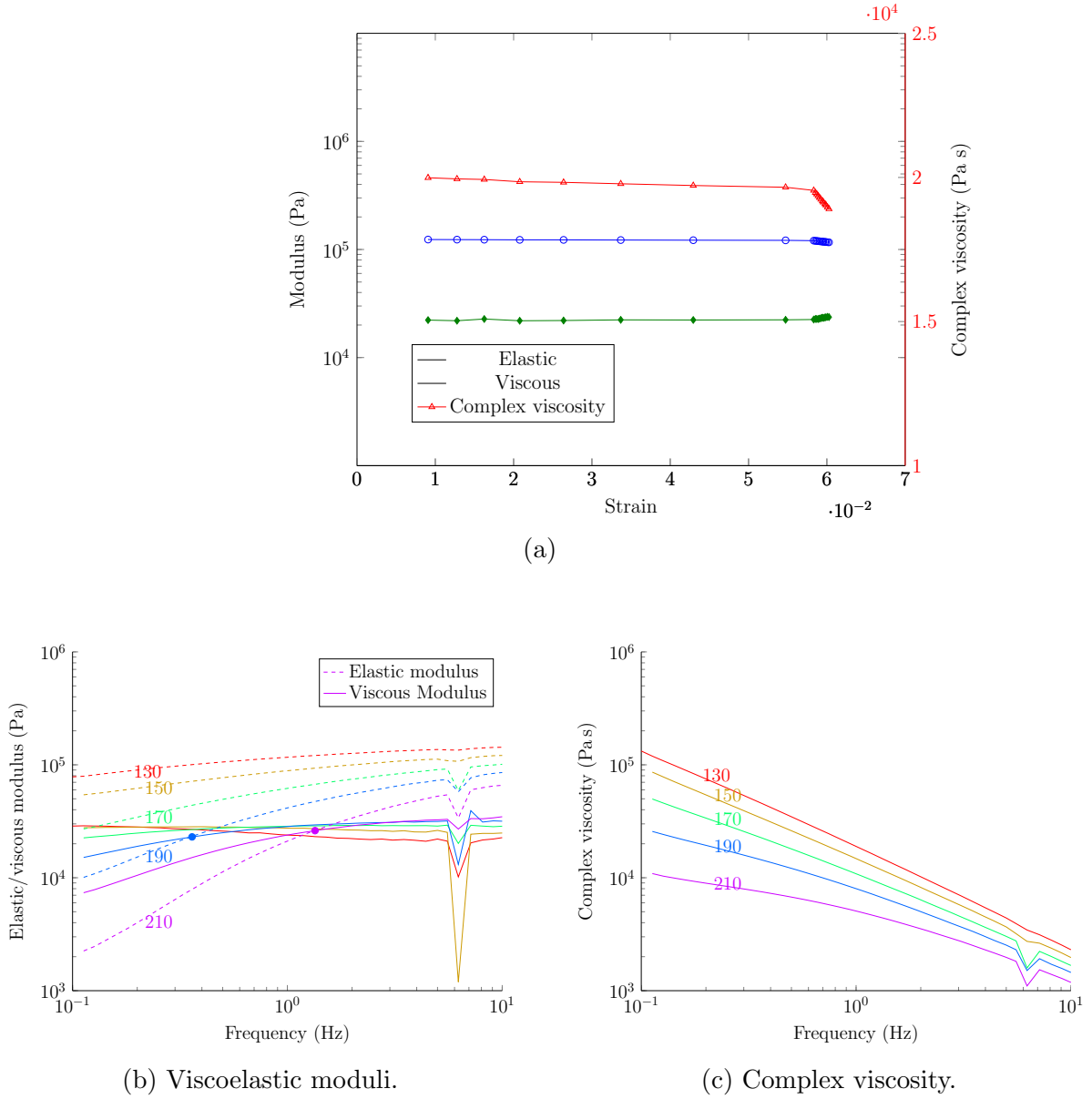


Figure 6.12: Parallel rough plate oscillatory shear of SEPS22 melt; (a) shows an amplitude sweep at 130 °C and 1 Hz. The elastic modulus $G' = \frac{\sigma_0}{\epsilon_0} \cos \delta$ and viscous modulus $G'' = \frac{\sigma_0}{\epsilon_0} \sin \delta$, where δ is the phase shift between stress and strain. (b) and (c) are frequency sweeps, at 1% strain (ϵ_0), at temperatures from 130 to 210 °C. Crossover points for sweeps at 190 and 210 °C are marked with •. There is a systematic error in the data point collected at 6.25 Hz, which can be attributed to a changeover in the rheometer's stress transducer at this frequency. Complex viscosity is calculated as $\eta^* = \frac{\sqrt{G'^2 + G''^2}}{\omega}$.

Non-linearity

The polymer melt undergoes significant deformation during injection moulding, and the Weissenberg and Deborah numbers are both large, so non-linear viscoelastic models may be more appropriate for modelling the flow of the fluid. A first order fluid model where

no elastic effects are considered is Newtonian; adding two elastic terms results in a (non-linear) third order fluid (Bird et al., 1987):

$$\begin{aligned}\boldsymbol{\tau} = & -\alpha_1 \dot{\boldsymbol{\gamma}} + \alpha_2 \frac{\mathcal{D}}{\mathcal{D}t} \dot{\boldsymbol{\gamma}} - \alpha_{11} (\dot{\boldsymbol{\gamma}} \cdot \dot{\boldsymbol{\gamma}}) \\ & - \alpha_3 \frac{\mathcal{D}^2}{\mathcal{D}t^2} \dot{\boldsymbol{\gamma}} \\ & + \alpha_{12} \left[\dot{\boldsymbol{\gamma}} \cdot \left(\frac{\mathcal{D}}{\mathcal{D}t} \dot{\boldsymbol{\gamma}} \right) + \left(\frac{\mathcal{D}}{\mathcal{D}t} \dot{\boldsymbol{\gamma}} \right) \cdot \dot{\boldsymbol{\gamma}} \right] \\ & - \alpha_{1:11} (\dot{\boldsymbol{\gamma}} : \dot{\boldsymbol{\gamma}}) \dot{\boldsymbol{\gamma}} + \dots\end{aligned}\quad (6.19)$$

Where the first line corresponds to the Newtonian case, and in which the substantive/total derivative is:

$$\frac{\mathcal{D}}{\mathcal{D}t} \dot{\boldsymbol{\gamma}} = \frac{\partial \dot{\boldsymbol{\gamma}}}{\partial t} + \mathbf{v} \cdot \boldsymbol{\nabla} \dot{\boldsymbol{\gamma}} + \frac{1}{2} (\boldsymbol{\omega} \cdot \dot{\boldsymbol{\gamma}} - \dot{\boldsymbol{\gamma}} \cdot \boldsymbol{\omega}) \quad (6.20)$$

The α constants are related to the viscometric functions during steady shear flow by:

$$\eta = -\frac{\tau_{yx}}{\dot{\gamma}} = \alpha_1 - 4(\alpha_3 - 2\alpha_{1:11}) \dot{\gamma}^2 \quad (6.21a)$$

$$\Psi_1 = -\frac{\tau_{xx} - \tau_{yy}}{\dot{\gamma}^2} = \frac{N_1(\dot{\gamma})}{\dot{\gamma}^2} = 2\alpha_2 \quad (6.21b)$$

$$\Psi_2 = -\frac{\tau_{yy} - \tau_{zz}}{\dot{\gamma}^2} = \frac{N_2(\dot{\gamma})}{\dot{\gamma}^2} = -\alpha_2 + \alpha_{11} \quad (6.21c)$$

The first and second normal stress coefficients, Ψ_1 and Ψ_2 , only arise in viscoelastic fluids. Ψ_1 and Ψ_2 are calculated from the normal stress differences N_1 and N_2 . N_1 is most easily obtained with a cone and plate rheometer, as the shear rate is independent of radius (Macosko, 1994). The normal stress difference is evaluated from the normal plate force (F_z) as:

$$N_1(\dot{\gamma}) = \frac{2F_z}{\pi R_{cp}^2} \quad (6.22)$$

Where R_{cp} is the radius of the cone and plate. The non-homogeneous shear distribution of the parallel plate rheometer allows the second normal stress difference to be evaluated:

$$N_1(\dot{\gamma}) - N_2(\dot{\gamma}) = \frac{F_z}{\pi R_{pp}^2} \left(2 + \frac{d \ln F_z}{d \ln \dot{\gamma}_{pp}} \right) \quad (6.23)$$

Where R_{pp} is the radius of the parallel plates and $\dot{\gamma}_{pp}$ is the shear rate at the edge of the plates.

Bird et al. (1987) solved the radial flow problem for the constitutive model in Equation (6.19) using perturbation methods, to yield equations for the radial (with coefficients up to r^{-5} term) and axial (up to r^{-6}) velocity profiles during steady, creeping flow.

The pressure drop between some point r_p and the edge of the disc r_f , which is assumed to be at zero gauge pressure, is given by:

$$P(R_p) - P(R_f) = \left(3R_f \ln \frac{R}{R_f} \right) \left(1 + \frac{3}{10} \frac{\left(\frac{R_f}{R} \right)^2 - 1}{R_f \ln \left(\frac{R_f}{R} \right)} \left[(5A_2 - 3A_{11}) - \frac{6}{7}Re - 9R_f (A_3 - 2A_{1:11}) \right] + \dots \right)$$

Where $R = \frac{r}{b}$ is dimensionless radius, and the constants A_2, A_3, A_{11}, A_{12} , and $A_{1:11}$ depend on the viscometric parameters (Co and Bird, 1977). The terms in $[]$ brackets arise from the normal stresses, inertia, and non-Newtonian viscosity, respectively.

Experimental Materials and Methods

The viscometric parameters for SEPS22 were evaluated using an Ares strain controlled rheometer (TA Instruments, DE, USA). A shear rate sweep was performed with the parallel plates (25 mm diameter), and a steady shear rate step with the cone and plate fixture (25 mm diameter and 0.1 rad cone), at 150 °C. 0.7 to 1.5 mm samples were stamped from injection moulded discs. The samples were placed in the rheometer for 30 min to equilibrate and relax.

The velocity and pressure profile equations were solved using MATLAB r2014a (Mathworks, MA, USA).

Experimental results

The viscosity of a 6 constant 3rd order fluid (Equation (6.21a)) consists of a zero-shear rate viscosity and a $(\alpha_3 - 2\alpha_{1:11}) \dot{\gamma}^2$ term. Unfortunately a second order polynomial $(A + B\dot{\gamma}^2)$ to describe viscosity is inappropriate for this polymer melt; no value of B can produce the correct viscosities. As such, a constant viscosity of 10 kPa.s was used, as in the original Newtonian model. In fact, a $\dot{\gamma}^{-1}$ term (as seen in Equation (6.15)) would be necessary to accurately describe the viscosity.

The 1st normal stresses were collected using the cone and plate rheometer (Figure 6.13). Unfortunately it was hard to contain the sample within the rheometer plates for long durations. Given the difficulty of sample containment and normal stress measurement it is remarkable that a $\dot{\gamma}^2$ relationship - that may be used in Equation (6.22) - fits so closely to the 1st normal stresses (Figure 6.13b).

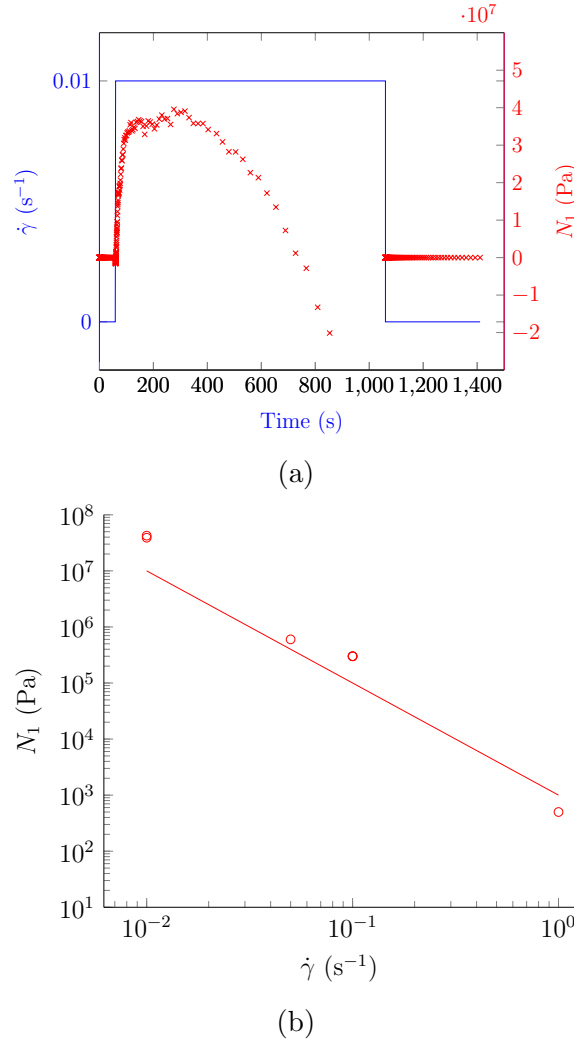
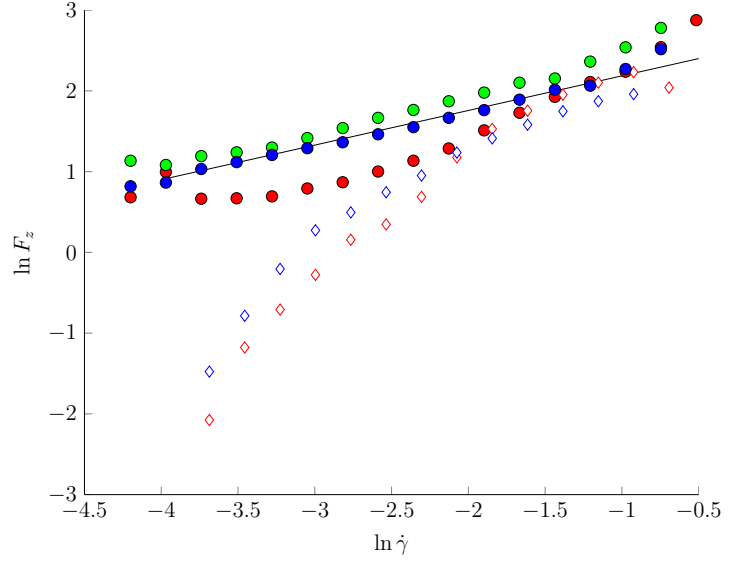


Figure 6.13: 1st normal stresses during pulse shear for SEPS22 at 150 °C, calculated using Equation (6.22). (a) shows the 1st normal stress during a step up and step down in shear rate with the cone and plate rheometer. Sample containment was lost after approximately 300 s. (b) shows the 1st normal stress during 5 pulse shear rates. The line corresponds to the relationship $N_1 = 1000\dot{\gamma}^{-2}$, for use in Equation (6.21b).

The difference between the 1st and 2nd normal stresses was determined using the parallel plate rheometer. There is some disparity in normal stress between the upward and downward sweeps at low shear rates, likely due to memory effects. As such, the upward sweep gradient was used, $\frac{d \ln F_z}{d \ln \dot{\gamma}} = 0.5$ and $F_z = 20\dot{\gamma}$, in Equation (6.23), to yield $N_1(\dot{\gamma}) - N_2(\dot{\gamma}) = 1 \times 10^5 \dot{\gamma}$. Unfortunately, this does not fit so cleanly with the form of the 2nd normal stress coefficient (Equation (6.21c)), in which $\Psi_2 = N_2/\dot{\gamma}^2$. And so assuming an average shear rate of 1 s⁻¹, $\Psi_2 = 1 \times 10^5$. Also, there is a difference in viscosity measured with this rheometer, and previously measured using the stress controlled Bohlin, in Section 6.3.1, possibly due to the need to use rough plates in the previous, stress-controlled experiment.

Figure 6.14: The difference between the 1st and 2nd normal stresses during shear rate sweeps (up \circ and down \diamond) in the parallel plate rheometer for 3 runs (red, green, blue). The data is plotted as a natural logarithm with a line of gradient 0.5 fitted to the upward sweep, for use in Equation (6.23). Sample containment was lost during the downward sweep in the second (green) run.



These values were used to determine the constants $\alpha_1, \alpha_2, \alpha_3, \alpha_{11}$, and $\alpha_{1:11}$, equal to 1×10^4 , 5×10^2 , -1.5×10^{-6} , -9.95×10^4 , and 0, respectively.

The 3rd order viscoelastic model predicts a significantly greater pressure drop than the equivalent viscosity Newtonian model (Figure 6.15) making it a more accurate model for this flow. The 3rd order model is only evaluated up to $r_f = 0.1$ m, after which the cavity should be filled. The initial experimental pressure spike was due to the polymer filling the horizontal portion of the pressure line. Flashing (overfilling) of the cavity may explain the higher pressures recorded at the end of the run. If the 3rd order analytical model were able to take into account the shear thinning viscosity (rather than assuming a constant viscosity), a more accurate prediction of pressure would be expected.

6.3.3 Computational modelling

Taking account of normal stresses in the analytical model was another step closer to understanding the behaviour of the SEPS polymer melt, however it still led to a 30% discrepancy compared to the experimental data. Furthermore, to model the flow in the complex 3D heart valve geometry a viscoelastic model should be implemented in a finite element (FE) solver. I considered three options: the (viscoelastic) White-Metzner and Giesekus models, and (generalised Newtonian) Carreau-Bird model.

The White-Metzner model describes low shear rate viscoelasticity using the following relation:

$$\boldsymbol{\sigma} + \lambda_r \nabla \boldsymbol{\sigma} = 2\eta_v \dot{\boldsymbol{\gamma}} \quad (6.24)$$

where $\boldsymbol{\sigma}$ is the total stress tensor, λ_r is the relaxation modulus, η_v is the viscosity, and $\dot{\boldsymbol{\gamma}}$

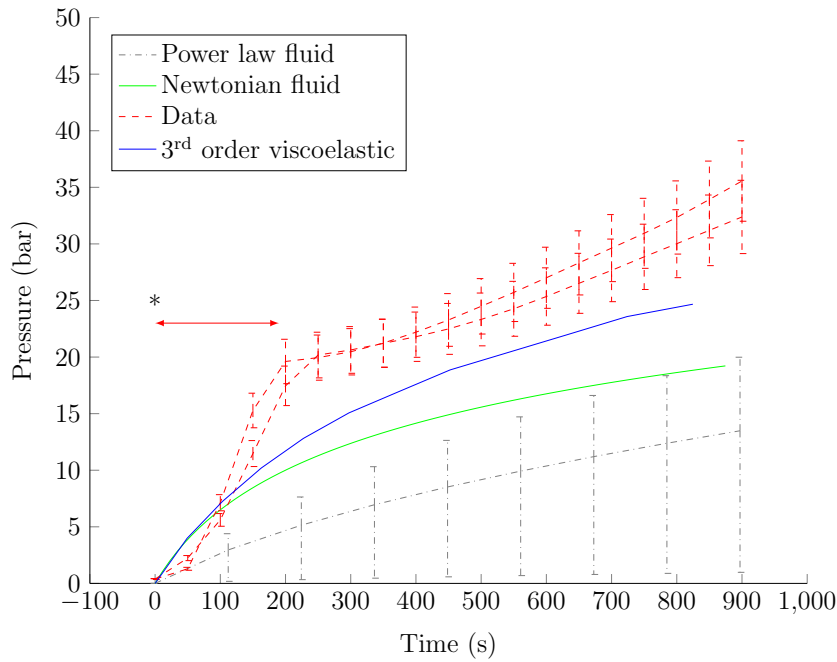


Figure 6.15: Comparison of raw pressure data with the predicted pressure using a Newtonian, power law, and a 3rd order viscoelastic model. The spike in pressure due to filling of the pressure line is indicated by *.

is the shear rate. In Equation (6.24), the viscosity and relaxation modulus follow power law relations:

$$\eta_v(\dot{\gamma}) = (\eta_0 - \eta_\infty)(1 + m_v^2 \dot{\gamma}^2)^{\frac{n_v-1}{2}} + \eta_\infty \quad (6.25)$$

$$\lambda_r(\dot{\gamma}) = m_\lambda \dot{\gamma}^{n_\lambda-1} \quad (6.26)$$

Where η_0 and η_∞ are the zero and infinite shear rate viscosities, respectively. m_v and n_v are the viscoelastic viscosity power law consistency factor and index respectively, and m_λ and n_λ are the viscoelastic relaxation modulus power law consistency factor and index respectively. No purely viscous contribution to the stress tensor was used, as this is associated with very fast relaxation modes in polymer solutions.

The power law viscosity parameters as previously reported (Figure 6.8) were used: $m_v = 4696$ and $n_v = 0.094$.

During steady shear the first normal stress for a White-Metzner fluid is calculated as (Morrison, 2001):

$$\Psi_1(\dot{\gamma}) = 2\eta_v(\dot{\gamma})\lambda_r(\dot{\gamma}) \quad (6.27)$$

And the second normal stress, $\Psi_2 = 0$. Using the shear sweep data from Figure 6.14 yielded $m_\lambda = 1.122$ and $n_\lambda = 2.906$.

I also tested the applicability of the Giesekus model (Giesekus, 1982) to the polymer melt. More realistic constitutive models, such as the one proposed by Giesekus, consider the polymer chains as dumbbells which are deformed during flow. The upper-convected

Maxwell equation considers a dumbbell in a dilute solution, Giesekus extended this equation to model dumbbells which are surrounded by dumbbells, which impart anisotropic drag on each other. This results in a non-separable constitutive model, which has a quadratic stress tensor term, and non-zero normal stresses (Larson, 1988). The constitutive equation of the Giesekus model is:

$$\frac{\boldsymbol{\tau}}{\lambda} + \frac{\partial \boldsymbol{\tau}}{\partial t} + \mathbf{v} \nabla \boldsymbol{\tau} - \left((\nabla \mathbf{v})^T \boldsymbol{\tau} + \boldsymbol{\tau} (\nabla \mathbf{v}) \right) = \frac{\eta_0}{\lambda} \dot{\boldsymbol{\gamma}} - \frac{a}{\eta_0} \boldsymbol{\tau} \cdot \boldsymbol{\tau} \quad (6.28)$$

Where a is the mobility parameter, which represents the anisotropy of hydrodynamic drag on the polymer molecule (Bird and Wiest, 1985).

During steady shear the viscosity η is given by;

$$\eta(\dot{\gamma}) = \frac{\eta_0(1 - n_2)}{1 + (1 - 2a)n_2} \quad (6.29)$$

Where n_2 and Λ are given by:

$$n_2 = \frac{1 - \Lambda}{1 + (1 - 2a)\Lambda} \quad (6.30)$$

$$\Lambda = \sqrt{\frac{\sqrt{1 + 16a(1 - a)\lambda^2\dot{\gamma}^2} - 1}{8a(1 - a)\lambda^2\dot{\gamma}^2}} \quad (6.31)$$

The first normal stress difference, N_1 , during steady shear, is:

$$N_1 = 2\lambda\eta_0 \frac{n_2(1 - an_2)}{\lambda^2 a(1 - n_2)} \quad (6.32)$$

And the analytical form of the second normal stress difference, N_2 is:

$$N_2 = \frac{-aN_1}{2} \frac{(1 - n_2)}{1 - an_2} \quad (6.33)$$

When implementing the Geisekus model in an finite element solver, convergence can be promoted by decomposing the stress tensor into viscoelastic and purely viscous components, such that $\boldsymbol{\tau} = \boldsymbol{\tau}_E + \boldsymbol{\tau}_V$, where $\boldsymbol{\tau}_E$ is equal to $\boldsymbol{\tau}$ in Equation (6.28), and the purely viscous component $\boldsymbol{\tau}_V = 2\eta_0\eta_r\dot{\boldsymbol{\gamma}}$, where η_r is some viscosity ratio, preferably greater than 0.11 (ANSYS, 2012).

Using the parallel plate rheometry shear sweep data the Giesekus model was fitted using the 4 parameters shown in Table 6.2. The parameters were optimised for viscosity, using OriginPro 9 (MA, USA). The viscosity ratio, η_r , was bounded between 0.11 and 1, and

the upper limit of α was set to 0.5 due to convergence difficulties in ANSYS when using higher values.

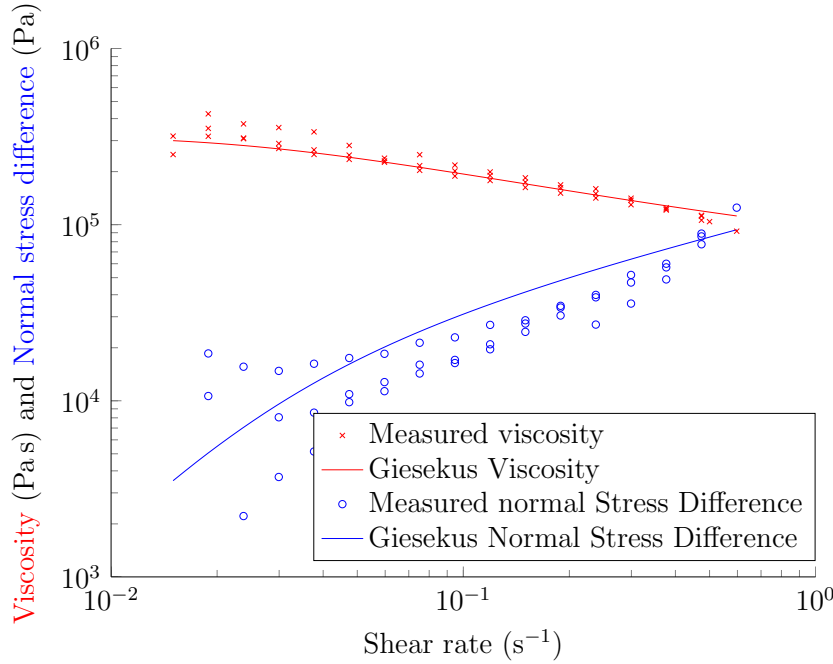


Figure 6.16: Increasing shear rate sweep in the parallel plate rheometer with the results of the Giesekus model fitted to the data using equations 6.29, 6.32 and 6.33, with the parameters as listed in Table 6.2.

Table 6.2: Parameters used in the Giesekus model (Equation (6.28)) for fitting to shear viscometry and then subsequently used in the FE model.

Parameter	Value	Unit
η_0	3.2×10^5	Pa s
α	0.4	-
λ	30	s
η_r	0.15	-

In contrast to the parallel plate shear rate sweep data which was collected with rough plates (Figure 6.8), the data shown in Figure 6.16 shows a zero shear rate limit. This is appropriate for a (Newtonian) Bird-Carreau model fit to this data:

$$\eta = \eta_\infty + (\eta_{b0} - \eta_\infty) \left(1 + (\lambda_b \dot{\gamma})^2\right)^{\frac{n_b-1}{2}} \quad (6.34)$$

Where η_∞ is the infinite shear rate viscosity, η_{b0} is the zero shear rate viscosity, λ_b and n_b is the power law index for the Bird-Carreau model; which were set as shown in Table 6.3.

Table 6.3: Parameters used in the Bird-Carreau model (Equation (6.34)) for fitting to shear viscometry (Figure 6.8) and then subsequently used in the FE model.

Parameter	Value	Unit
η_{b0}	3.5×10^5	Pa s
η_{∞}	1×10^2	Pa s
λ_b	40	s ²
n_b	0.61	-

Finite element analysis

ANSYS Polyflow (PA, USA) is a powerful FE solver which is capable of solving the aforementioned differential equations. Large values of the Weissenberg number, which imply strong memory effects, invoke the use of an evolving function - even during steady simulations - to promote convergence when using the White-Metzner fluid model. Evolution gradually increases the flow rate, to ensure convergence. The initial flow rate is set such that the Weissenberg number is less than 0.3 (ANSYS, 2012).

For the FE model, an axisymmetric geometry was assumed, as shown in Figure 6.17. The segment is $5^\circ \times 0.7 \text{ mm} \times 100 \text{ mm}$. A hard, unbiased, tetrahedral mesh was used. The FE solver, with a Newtonian constant viscosity model, was checked for mesh insensitivity. The following results are reported for a mesh consisting of 20 elements radially, 10 through the thickness, and 3 across the segment.

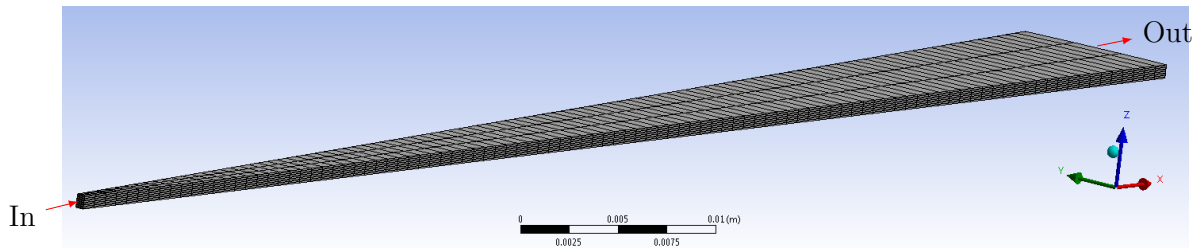


Figure 6.17: Mesh of the injection moulding disc segment. A fully developed flow enters the model from the left, and exits from the right. The top and bottom surfaces have no slip constraints, and each side surface has a symmetric constraint.

Results

The actual and predicted pressure measurements for the analytical model, FEM and experimental data are shown in Table 6.4. The constant viscosity of the Newtonian model is certainly inappropriate for modelling the system. The addition of Newtonian shear thinning behaviour results in a pressure drop $1/3$ the magnitude of the experimental

case. As such, viscoelasticity and the addition of normal stresses are necessary to account for higher pressure. The Giesekus model, however, overestimates the pressure drop; which may be due to the overestimation of normal stresses when the model parameters are optimised based upon the viscosity (Figure 6.16), and also due to the constraint on α in Equation (6.28) which was required for convergence. Furthermore, while the Giesekus model very often provides an excellent fit to data in shear flow, its performance in extension is known to be inferior. In particular, Larson (1988) reported that Giesekus does not predict strain softening in biaxial extension.

Table 6.4: Comparison of pressure drops between $P(r = 0.045) - P(r = 0.1)$ as recorded and predicted using analytical and FE models.

Model	Shear thin- ning?	Viscoelastic / normal stresses?	ΔP (bar)
Experimental data	✓	✓	35
Newtonian analytical			19
Power Law analytical	✓		12.5
3 rd order analytical		✓	25
FEM Newtonian			19
FEM Power-law	✓		8
FEM Carreau-Bird	✓		100
FEM Giesekus	✓	✓	67

The velocity profiles are compared at $r = 0.045$ m, when $r_f = 0.1$ m, as shown in Figure 6.18. The analytical and FE power law models display characteristic plug-like flow profiles. The Carreau-Bird and viscoelastic models have profiles which are similar to the constant viscosity Newtonian model, but the maximum velocity is lower. The Giesekus and Carreau-Bird models predict a lower maximum velocity than the other models.

The constant viscosity Newtonian model had remarkably similar results in comparison to the more complex models: it was fortuitous that at the tested shear rates the variable viscosity was similar to the constant viscosity. This may not occur in future injection scenarios, so it is necessary to use the variable viscosity models.

The 3rd order fluid model had the closest pressure fit, but is not available in FE software, so was not used. This left the FE power-law, Carreau-Bird, and Giesekus models. The introduction of normal stresses in the Giesekus model went some way to accounting for the pressure drop. However, the Giesekus model had poor stability in the FE solver at different processing conditions and convergence could not be guaranteed.

The power-law model produced the least accurate prediction of pressure drop, and the

velocity profile was also very different to all other models. On the other hand, the Bird-Carreau led to a similar velocity profile to the (accurate) Giesekus model, despite its overestimation of pressure. The stability of the problem in the FE solver was much better, allowing it to be used to model flows in complex meshes. As a consequence, the Bird-Carreau model was selected for further modelling. In other instances where normal stresses are important for describing the behaviour of interest, extrudate swell during extrusion for example, the Bird-Carreau would not be deemed suitable.

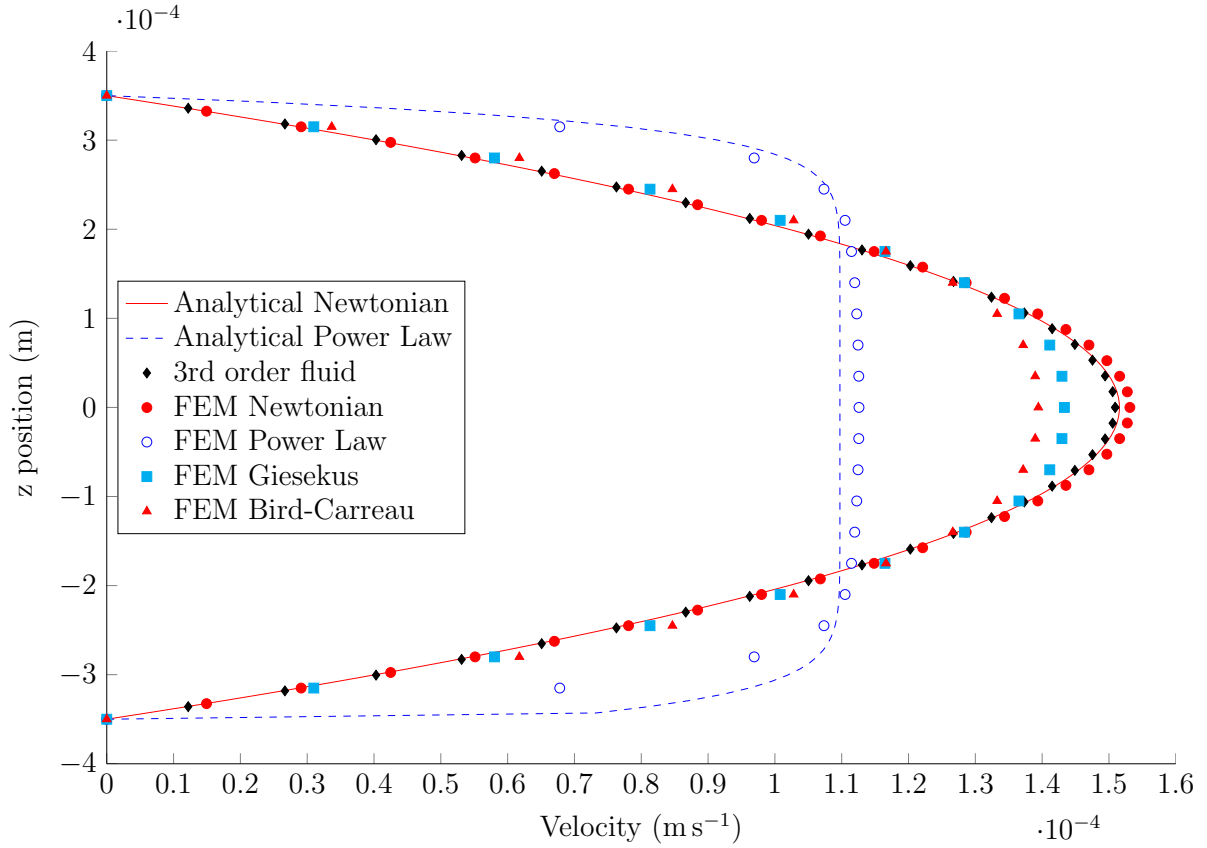


Figure 6.18: Velocity profiles for $r = 0.045$ m, when $r_f = 0.1$ m, with $Q = 2 \times 10^{-8} \text{ m}^3 \text{ s}^{-1}$, based upon the analytical and FE models.

All of the models considered in this chapter, even Giesekus', assume an isotropic viscosity. Given that SEPS22 is moulded below the order-disorder transition temperature, and the polymers are anisotropic, it is likely that the viscosity is also anisotropic. Particularly in mixed flow scenarios (elongation and shear), the models are unlikely to provide a completely accurate description of the flow.

6.4 Orientation modelling

6.4.1 Background

I previously selected force fields as the preferred means of orienting the BCP domains. Preliminary experimentation yielded an unexpected phenomenon during slow point injection between plates - biaxial orientation of the BCP cylinders. My search of the relevant literature indicated that although both shear and stretch are widely recorded as mechanisms for the orientation of cylinders in BCPs, the scenario where both deformations are competing for dominance is rare.

Trebbin et al. (2013) worked with aqueous solutions of amphiphilic BCP micelles, which are liquid at room temperature and are significantly less viscous than the polymer melts which I have considered. The BCP micelles form semi-flexible anisotropic particles with a diameter of 25 nm and length of several μm . Between 5 and 30% wt/wt the particles have a nematic arrangement, which makes them a model solution for carbon nanotubes, fibrous proteins, rod-like nanoparticles and DNA.

The authors flowed the solution in a microfluidic channel, which had curved and contraction-expansion flow features, while simultaneously performing SAXS and polarized optical microscopy. Generally, the micelles oriented in the direction of flow, due to the shear gradient. However, during expansion of the flow channel, shear and extensional forces competed. In the central region of the flow, during expansion, the extensional forces dominated and the authors observed a region of orientation perpendicular to the flow direction.

The 2D flow field was obtained using particle image velocimetry, and the flow was also computationally modelled. Trebbin et al. (2013) compared the extension and shear rates using the ratio:

$$C_s = \frac{\dot{\varepsilon}}{\dot{\gamma}} \quad (6.35)$$

here $\dot{\varepsilon}$ is the extension rate, calculated as:

$$\dot{\varepsilon} = 6 \frac{III\dot{\gamma}}{II\dot{\gamma}} \quad (6.36)$$

The shear rate is:

$$\dot{\gamma} = \sqrt{2II\dot{\gamma}} \quad (6.37)$$

Where $II\dot{\gamma} = \text{tr}(\dot{\gamma}^2)$ and $III\dot{\gamma} = \det(\dot{\gamma})$ are the second and third invariants of the strain rate tensor respectively.

In the experimental setup of Trebbin et al. (2013), the critical value of C_s was determined to be 0.14, such that regions in which $C_s > 0.14$ contained micelles oriented parallel to flow, and where $C_s < 0.14$, micelles were oriented perpendicular to the direction of flow. They also noted that the shear thinning nature was an important characteristic of the Newtonian fluid for accurately equating the modelling and experimental results.

I sought to determine whether a similar shear-extension critical value might also be applicable to the the BCP melt flow and able to predict the layered structure which I observed (in Section 6.2.2). Furthermore, Trebbin et al. (2013) made some inroads into predicting orientation, but their analysis is somewhat limited as it assumes that extension always results in orientation perpendicular to the direction of flow (though extension may also be in the direction of flow). As such, an alternative model is proposed.

Finally, while perpendicular orientation has not been previously observed in phase separating BCP, it does occur in short fibre polymer composites, for which various modelling strategies do exist. To reduce computational load, modelling of the flow through thin cavities has used the Hele-Shaw approximation:

$$\frac{\partial}{\partial x} \left(S \frac{\partial P}{\partial x} \right) + \frac{\partial}{\partial y} \left(S \frac{\partial P}{\partial y} \right) = 0 \quad (6.38)$$

Where $S = \int_0^h z^2 / \eta dz$, and h is the cavity thickness in the z direction, which reduces the flow equations to 2D. However, such a formulation would be incapable of predicting a layered structure, as previously observed and which I aim to predict. And so, with greater computational power, 3D simulations may be pursued (Vlachopoulos and Strutt, 2003).

Thus far, it has been assumed that orientation can be described by a single vector which, for a single, rigid fibre or cylinder, is indeed the case. However, within a finite fluid element containing many fibres it is more appropriate to describe orientation with a probability distribution. However, the probability distribution is cumbersome, and is hard to mathematically manipulate, particularly as a function of flow during processing. As such, orientation tensors are often employed.

The components of orientation tensors are equivalent to the coefficients of a Fourier series expansion of the probability distribution function. Symmetric second and fourth order tensors are generally used to describe the orientation. Fibres are transported convectively, while shear and stretch reorient fibres. Advani (1987) derived the equations of change, referred to as the Tucker-Folgar equation, for the orientation tensors during flow. Theoretically, with a valid flow field and complete fibre information, including the fibre

aspect ratio, density, and a connectivity parameter, orientation can be predicted. The Tucker-Folgar equations require a closure approximation to be solved, and unfortunately the solution is dependent on the choice of closure method. Models for the prediction of short-fibre orientation during injection moulding, can be found in commercial software. However, in this chapter, attention is focussed upon simple orientation models, the “scalar” model, previously proposed in Equation (6.35) and Section 6.4.2, and a “vectorial” model which I propose in Section 6.4.4.

In this chapter there is no substantial motivation to use a probability distribution to describe orientation, particularly as the anisotropic basis for the hyperelastic material model used to predict strain energy density in the heart valve requires a definite vector orientation. Therefore, a definite vector basis is used to describe orientation in this chapter.

The radial flow geometry is also taken as a simple injection case for polymer composites. In most commercial scenarios, polymer composites are injected into cold injection moulding tools (below the glass transition temperature). In these cases the orientation is dominated by the flow patterns in the advancing polymer front. Hot polymer is convected from the core layers to the skin layer where it cools, in a process described as fountain flow. The rolling of the polymer composite has been shown to improve orientation at the wall through a combination of shear and extension, though also this contributes to built in stresses (Mavridis, 1988).

6.4.2 Orientation model

It is well known that shear causes cylindrical BCP domains to align in the direction of flow, and extension causes the cylinders to align in the principal direction of extension. Thus, the formulation proposed by Trebbin et al. (2013), in Equation (6.35), could be used to predict orientation. Equation (6.35) determines the dominant mechanism for orientation. If shear dominates, $C_s > C_{sC}$, where C_{sC} is a critical value of the ratio of shear to stretch rate. Where shear dominates, at the walls of a mould for example, cylinders are oriented in the direction of flow, and their orientation vector, \vec{a} , is given by:

$$\vec{a} = \vec{\gamma} = \frac{\vec{v}}{|\vec{v}|} \quad (6.39)$$

In thin, divergent flows stretch occurs perpendicular to the flow direction - as previously observed in the radial flow scenario and the channels of Trebbin et al. (2013) - and so the orientation direction when stretch dominates, $C_s < C_{sC}$, can be calculated based upon

the surface normal, n , and velocity vectors:

$$\vec{a} = \vec{\varepsilon} = \frac{\vec{n} \times \vec{v}}{|\vec{n} \times \vec{v}|} \quad (6.40)$$

In all instances the orientation vectors, \vec{a} , are defined over a hemisphere, such that:

$$\vec{a} = -\vec{a} \quad (6.41)$$

The fibres are assumed to be inertia-less, which is a reasonable assumption in a creeping flow. Convection of fibres is also neglected, so their orientation history is not taken account of, which may be a more significant shortcoming of the model.

6.4.3 Methods

Injection moulding was performed using the same apparatus and methods as previously described in Section 6.3.1. Three disc thicknesses, 0.7, 1.0 and 1.5 mm, were injected, at 3 injection rates from 2.5 to 250 mm³ s⁻¹. The final radii of each disc was between 50 and 100 mm.

Previously, in Figure 6.5, I showed that the biaxial SAXS pattern which can be observed when the X-ray beam passes through the thickness of a sample (Z-axis beam, see Figure 6.2) is due to a layered arrangement of oriented cylinders. The X-ray beam has a finite thickness, with a Gaussian distribution that has a full width half maximum of less than 230 μm , and root mean square of less than 100 μm (Bruker Nanostar SAXS). When the thickness of the beam is small in comparison to the sample's thickness (1 mm) distinct skin and core layers of orientation are visible when viewed in the plane of the sample (see Figure 6.2).

Radiation passing through a crystalline structure is scattered, leading to interference at the detector. The scattering angle is related to the crystal spacing by Bragg's Law (Equation (6.1)), and the *amount* of radiation which is scattered is a function of the crystal quality and thickness. The full width at half maximum of a peak is related to the size of the crystalline domains (Borsali and Pecora, 2008), while the peak area is proportional to quantity of crystalline material aligned correctly to give Bragg interference at the detector (Fratzl et al., 2013).

Two rows of SAXS measurements (at 5 mm spacing) were made on a radial strip cut from each sample (as indicated in results Figure 6.21a), using a Bruker Nanostar with CuK α radiation (Materials Science and Metallurgy, University of Cambridge). The az-

imutally integrated patterns were analysed using the MATLAB Peakfit function. A Gaussian/Lorentzian blended curve with a flat baseline correction was fitted to the peaks. The peaks were integrated, indicating the amount of orientation in each direction.

6.4.4 Results

I applied the proposed orientation models to the velocity field predicted by the Giesekus and Carreau-Bird FE models. Figure 6.19a shows how the calculated extension and shear rates vary through the thickness of the disc. The shear rate is highest at the walls, and decreases to zero at the midplane (Figure 6.19a). The rate of extension is greater in the core than in the skin regions of the disc. The ratio of extension to shear, C_s , is shown in Figure 6.19b.

C_s is large at the wall, and decreases towards the midplane. At the midplane, where both the shear and extension rates are calculated to be zero, their ratio is undefined. This singularity arises due to the formulation of the extension rate (Equation (6.36)). In the skin region, the extension type is uniaxial, whereas at the midplane the extension type is planar. If the strain rate is decomposed into its components and simplified (Equation (6.42)) it becomes clear that the conventional formulation of strain rate also depends on the shearing components ($\dot{\gamma}_{ij}, i \neq j$), which are zero at the midplane. As such, planar stretch is incompatible with a 3D formulation of the stretch rate.

$$\dot{\epsilon} = -6 \frac{\dot{\gamma}_{22} \dot{\gamma}_{31}^2}{\dot{\gamma}_{11} \dot{\gamma}_{22} - \dot{\gamma}_{31}^2} \quad (6.42)$$

Vectorial analysis

In response to the singularity of the standard shear and stretch formulations at $z = 0$, I proposed an alternative method. The extensional and shear components of the velocity gradient tensor can be extracted as follows:

$$\nabla \vec{v} \cdot \begin{bmatrix} 1 & 0 & 0 \\ 0 & 1 & 0 \\ 0 & 0 & 1 \end{bmatrix} = \nabla \vec{v} \cdot \mathbf{I} = \begin{bmatrix} \frac{\partial u}{\partial x} \\ \frac{\partial v}{\partial y} \\ \frac{\partial w}{\partial z} \end{bmatrix} = \vec{\epsilon}_v \quad (6.43)$$

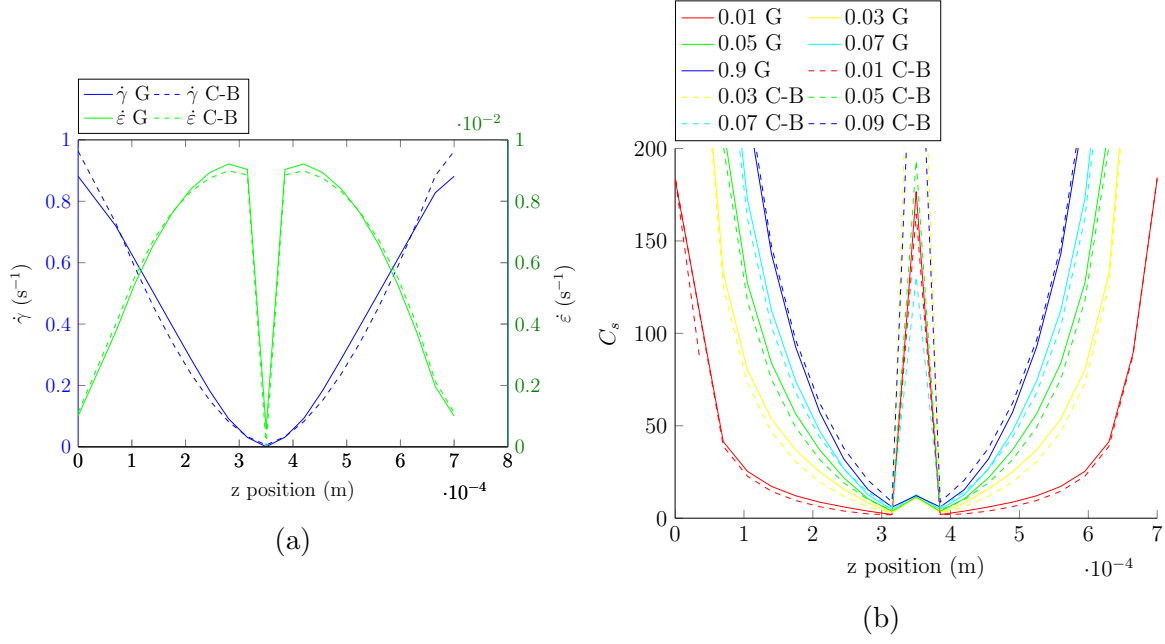


Figure 6.19: (a) The shear ($\dot{\gamma}$) and extension ($\dot{\epsilon}$) rates at a radius of 0.045 m, of a disc of $r_f = 0.1$ m, and (b) the ratio of extension to shear rate (C_s) at various radii, based upon the velocity field predicted by the Giesekus (solid lines) and Carreau-Bird (dashed lines) FE models.

$$\vec{\gamma}_v = \nabla \vec{v} \cdot (1 - \mathbf{I}) = \begin{bmatrix} \frac{\partial u}{\partial y} + \frac{\partial u}{\partial z} \\ \frac{\partial v}{\partial x} + \frac{\partial v}{\partial z} \\ \frac{\partial w}{\partial x} + \frac{\partial w}{\partial y} \end{bmatrix} \quad (6.44)$$

Where $\vec{\epsilon}_v$ is the extension vector and $\vec{\gamma}_v$ is the shear vector, and \mathbf{I} is the identity matrix. As before, the magnitude of the stretch and shear vectors can be compared to determine the dominant deformation:

$$C_v = \frac{|\vec{\gamma}_v|}{|\vec{\epsilon}_v|} \quad (6.45)$$

Plots of $\vec{\gamma}_v$, $\vec{\epsilon}_v$, and C_v shown in Figure 6.20. All 3 parameters have the same form as their scalar equivalent in the skin regions. However, at the core of the sample $\vec{\epsilon} > 0$, and so C_v is definite. While the vectorial model makes more physical sense at the sample's midplane, it only works for uniaxial flows, so cannot be used for modelling the complex valvular geometries. Away from the midplane, the vectorial and scalar models have a similar form.

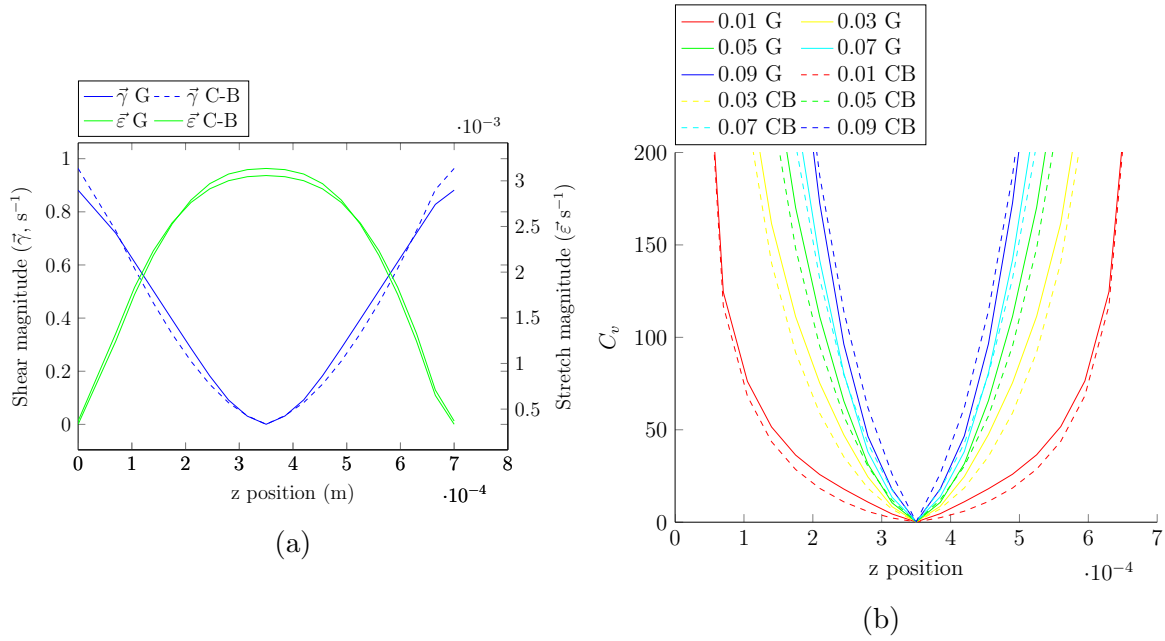


Figure 6.20: The vectorial shear ($|\vec{\gamma}_v|$) and extension ($|\vec{\epsilon}_v|$) rates in the disc ($r_f = 0.1$ m), at a radius of 0.045 m (a), and the ratio of extension to shear rate (C_v) (b) at various radii, based upon the velocity field predicted by the Giesekus (solid lines) and Carreau-Bird (dashed lines) FE models.

SAXS orientation maps

Figure 6.21 shows results of a SAXS array scan of a radial segment of a sample. The bimodal orientation which was reported in Section 6.2.2 is clearly evident in this sample, though there is a variation in the direction of orientation along the sample (6.21a). The magnitude of the peak areas change across the samples, possibly due to the angle of incidence of the X-ray beam with respect to the crystal planes, and inhomogeneities in the polymer due to variable cooling. When the peak area is considered as a fraction of the *total* peak area, the proportion of radially oriented phase remains stable ($60 \pm 10\%$) along the radius of the sample shown in Figure 6.21b.

At the edge of the sample the orientation vectors are not radial and circumferential, which may be due to the flow not being perfectly circular when it reaches the edge of the cavity, thus causing it not to flow solely in the radial direction as it fills the cavity.

Ten flow rate and disc thickness combinations were injected for SAXS scanning. There was some variation in sample size, as not all samples filled the cavity. In these instances, the flow may have slowed, particularly at larger radii, possibly reducing the quality of the orientation. The SAXS measurements were grouped, and averaged, at four radii: 0 to 25, 25 to 50, 50 to 75, and 75 to 100 mm. The SAXS patterns were then evaluated against

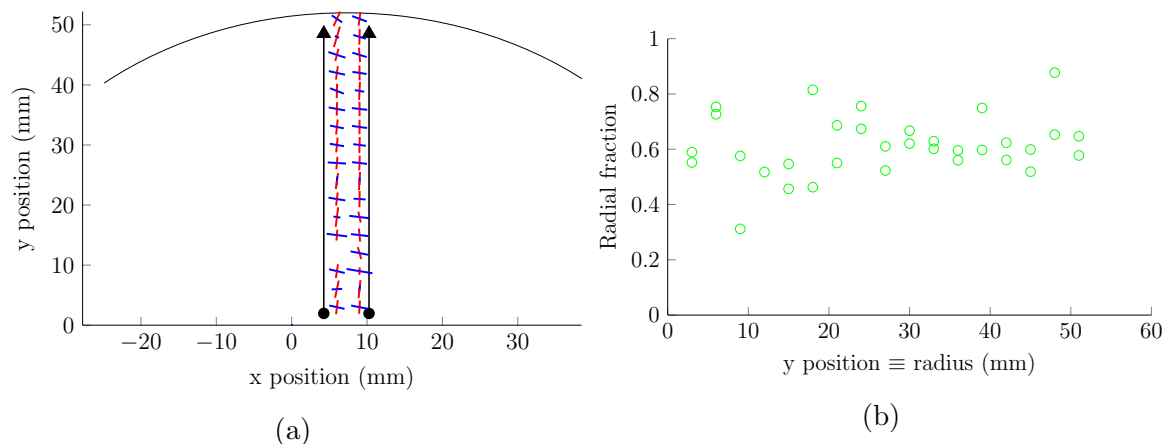


Figure 6.21: (a) SAXS scan of a segment of disc with the cylinder orientation marked. The length of the vector is proportional to the peak area. The black arc indicates the outer radius of the disc and the arrows indicate the direction of flow (a). (b) shows the peak area as a function of radius in a sample (for the sample shown in (a)). The radial peak is calculated from the average area of the two peaks which corresponds to the cylinders oriented radially, and Peak 2 to those oriented circumferentially. The radial peak fraction is calculated as a proportion of the sum of the peak areas at each point. In this sample the radial orientation dominates.

their orientation predictions based upon the Carreau-Bird flow field and scalar prediction model (Section 6.4.2). The ratio of stretching deformation to shear deformation (C_s) is calculated throughout the flow field based upon Equation (6.35). I hypothesised that orientation is stretch controlled below a critical magnitude of C_s , which I will refer to as C_{sC} , allowing the orientation to be predicted for each modelled flow field.

Figure 6.22 shows the fraction of points which were predicted incorrectly as a function of C_{sC} . At low values of C_{sC} the sample is predicted to contain purely circumferential orientation, while at high values the sample is predicted to contain purely radial orientation. These plots indicate that at a variety of process conditions, and throughout the radial geometry, a *constant* value of C_{sC} can be used to predict orientation.

Figures 6.22a to 6.22d are combined to produce a plot where the maximum recorded error between any single experiment and simulation is shown as a function of C_{sC} . Figure 6.24a also indicates that the optimal value of C_{sC} for the SEPS22 flow at 150 °C is 3. Furthermore, among the flows tested in this batch of experiments, orientation was predicted correctly in 85% of the sample (by volume). In the *worst* case, orientation was *correctly* predicted in over 70% of the sample (by volume).

There still remains the question of whether there is a physical significance to $C_{sC} = 3$. Figure 6.23 shows the magnitude of extensional and shear deformations at the critical value of C_s , demonstrating that extension is more efficient at orienting PS cylinders than

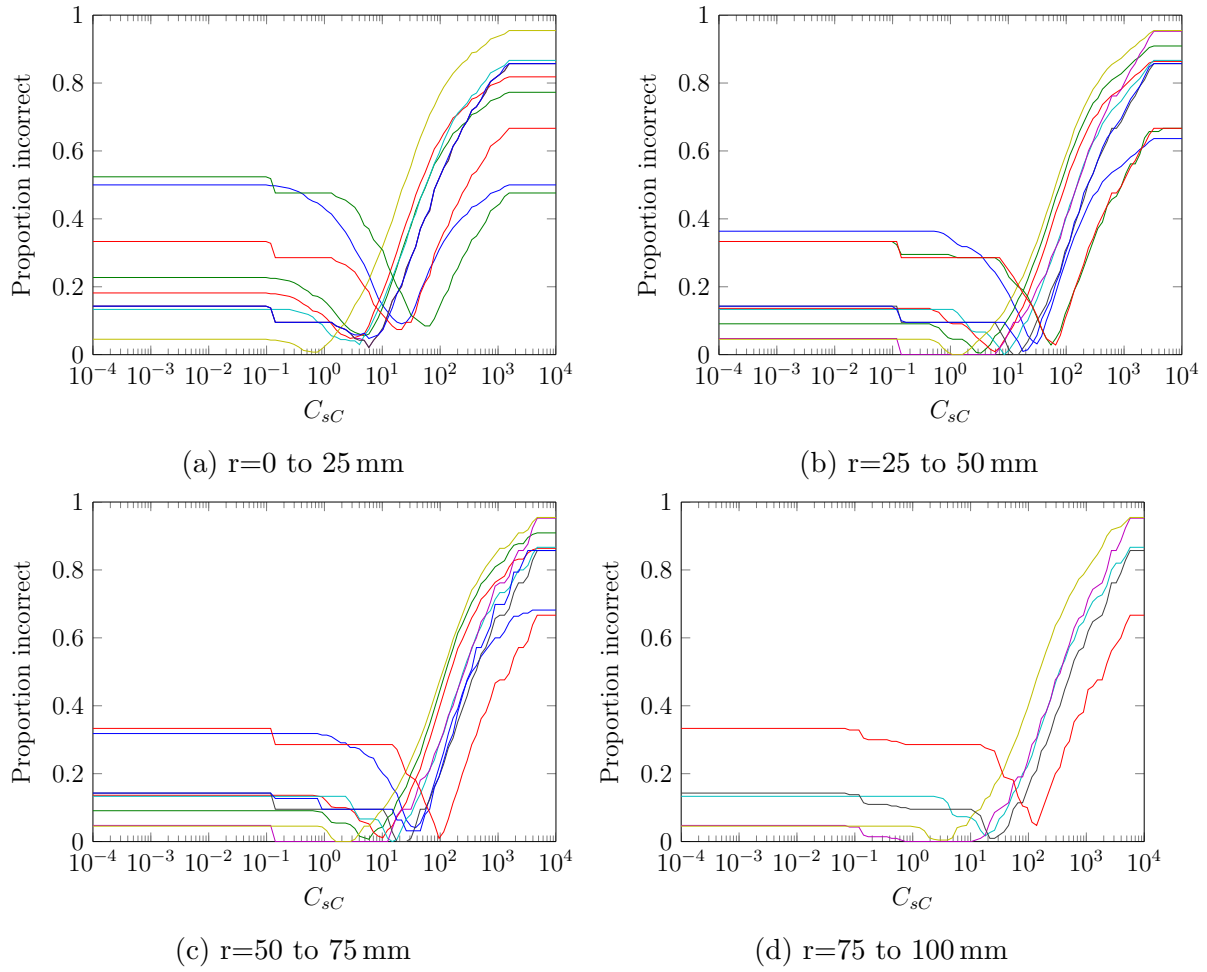


Figure 6.22: Number fraction of points for which orientation were predicted incorrectly based upon the given value of C_{sC} . Each line corresponds to a different sample. Radial orientation dominates in nearly all samples, and so the incorrect proportion is low for low values of C_{sC} .

shear is. Further work is need to assess the significance of C_{sC} in the Tucker-Folger equation (Advani, 1987). Although not shown here, I also calculated the critical ratio (C_{vC}) of vectorial extension ($\vec{\varepsilon}_v$) and shear ($\vec{\gamma}_v$) proposed in Section 6.4.4, to be 10.

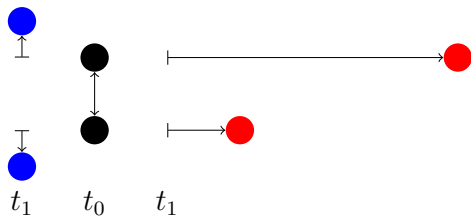


Figure 6.23: Schematic to illustrate the power of stretch over shear. Given 2 fluid elements separated by 1 unit (black ●); after 1 time unit (from t_0 to t_1) the elements are separated by stretching (blue ●), or by shearing (red ●) deformations. The illustrated deformations are for flow scenarios where $C_{vC} = 10$. Stretch is a more efficient means of orientation than shear.

I compared the predicted orientation distribution with the measured orientation. In

Figure 6.24b, the proportion of radial orientation is mapped as a function of injection rate and thickness. Greater disc thicknesses promote circumferential orientation, while higher flow rates promote radial orientation. In Figure 6.24b, a 100-fold reduction in flow rate only reduces the fraction of radial orientation by 2%, while a 2-fold change in thickness leads to a 10% change in radial orientation.

Several samples were injected at a higher temperature (170 °C and 190 °C). In these samples there was a lower fraction of radial orientation compared to samples injected at the same rate, but at lower temperatures. Without further work, it is unclear whether temperature solely changes the polymer's rheology and thus flow field, or whether C_{sC} may also vary with temperature.

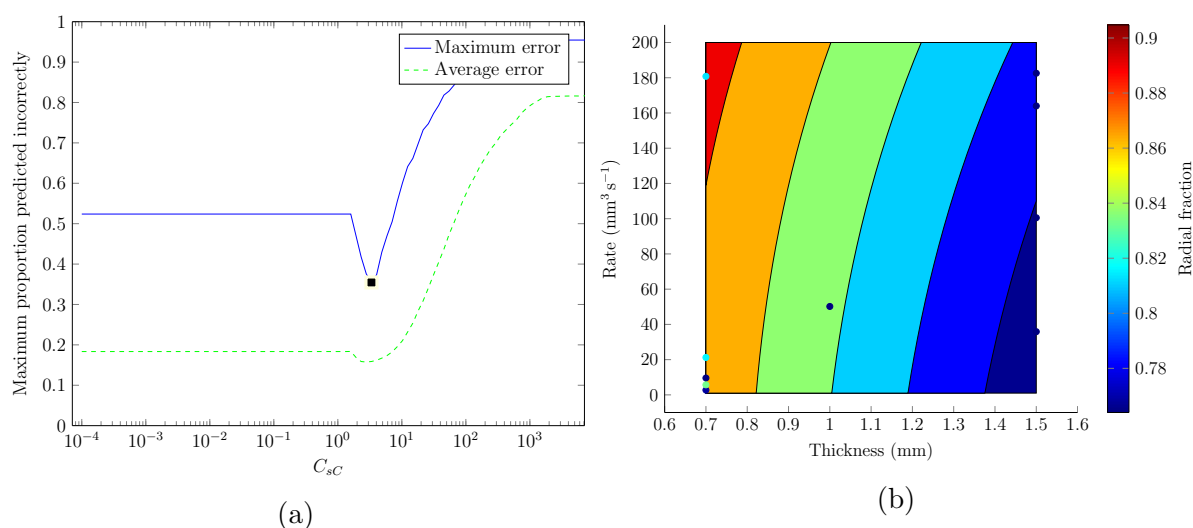


Figure 6.24: (a) shows the maximum and average proportion of incorrectly predicted orientations amongst all samples shown in Figure 6.22. The optimal value of C_{sC} is marked with ■, at $C_{sC} = 3$. (b) is a contour plot of orientation in the thickness-rate space when injection moulding a disc of SEPS22 at 150 °C. The contours are based upon the scalar orientation model, using the flow field predicted by the Carreau-Bird model. Scatter marks indicate experimental values whose orientation was evaluated by SAXS.

6.5 Controlling orientation in the injection moulded valve

Thus far, I have shown that flow fields can be used to control the orientation in a simple injection moulded part. These findings are now to be translated to a prosthetic heart valve, such that the leaflets have a *bioinspired* orientation of PS cylinders.

The spherical form valve, as previously described in Section 5.2, was used for testing the control of orientation in a sample part. For the production of prototype valves, the

Table 6.5: Processing conditions for injection of valves.

Gate position	Total flow rate ($\text{mm}^3 \text{s}^{-1}$)	Leaflet flow rate ($\text{mm}^3 \text{s}^{-1}$)
Free Edge	17.1	5.7
Commissure	11.3	3.8
Free Edge Centre	6	2

bench top injection moulding apparatus was adapted from that used in Section 6.2 to inject discs. A custom aluminium mount was made for the stainless steel valve tool, consisting of four locking screws for clamping the tool onto the injection plate. Three injection plates were fabricated such that various gate (inlet) positions could be tested. The injection scenarios were referred to as Free Edge (FE), Commissural (C), and Free Edge Centre (FEC), which are illustrated in Figure 6.25. The cavity was vented through the sewing ring and injection was continued until a steady flow (flash) through the vents developed. The benchtop injection moulding apparatus has limited control of injection rate or pressure, nor was I able to record the pressure during injection. Instead, the barrel position was recorded with respect to time, yielding the flow rates shown in Table 6.5. After injection, the tool was removed from the injection moulder and cooled by direct contact with running water.

The leaflets were dissected from the valve and mounted on a frame which flattened them such that the X-ray beam passed perpendicular to the sample. SAXS was used to assess the spatial distribution of PS cylinders across the leaflets. SAXS was performed on beamline I22 at Diamond Light Source, Harwell Science and Innovation Campus, UK. The peak integration method previously described, was used to assess orientation.

Concurrently, based upon the processing conditions used to inject the valves, the leaflet orientation was *predicted*. This provided a test of the orientation model in a complex geometry. The Carreau-Bird rheological model for the polymer melt, as determined in Section 6.3.3, was used to model the flow field. Using the scalar orientation model, which I validated for the simple geometry in Section 6.4.4, the orientation of PS cylinders in the leaflet was predicted. The cavity was assumed to be axisymmetric with order 3, with the flow rate into each valve given in Table 6.5. A uniform leaflet thickness of $400 \mu\text{m}$ (as measured in the final parts) was used in the simulations. The geometry was meshed using 184,218 elements. Hard edge sizing was used to produce bricks in the leaflet, with 40 elements through the leaflet's thickness, and tetrahedral elements in the bulk of the stent.

To indicate the distribution of orientation across the leaflet and through its thickness, the orientation fields are shown at 6 depths (0, 40, 80, 120, 160, and $200 \mu\text{m}$) within each

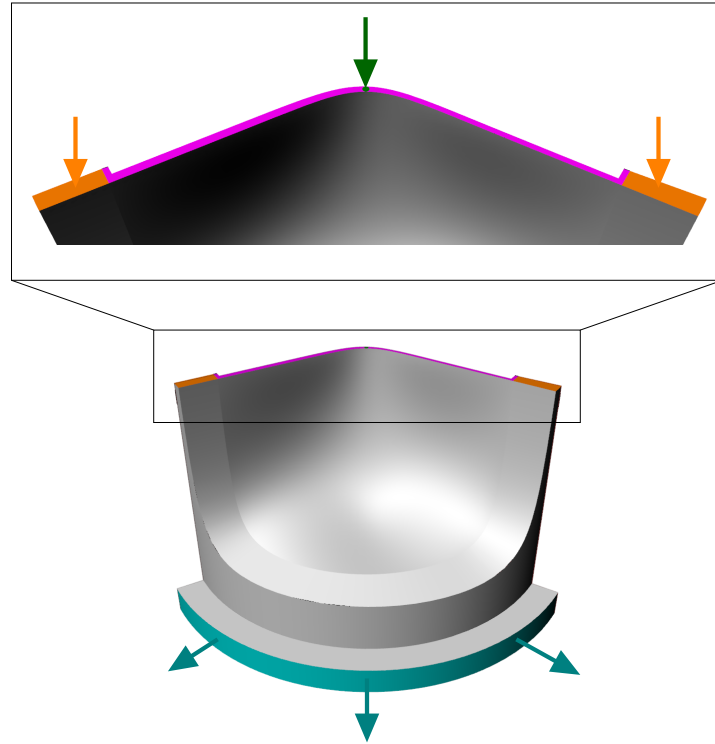


Figure 6.25: Schematic of inflows and outflows from the valve cavity, used experimentally and computationally. The inset details the gate (inlet) positions: **orange** indicates commissural (C) injection, the **green** indicates Free Edge Centre (FEC) injection, and Free Edge (FE) injection occurs through the combination of **orange**, **green** and **pink**. The outlet is indicated by the **cyan** region.

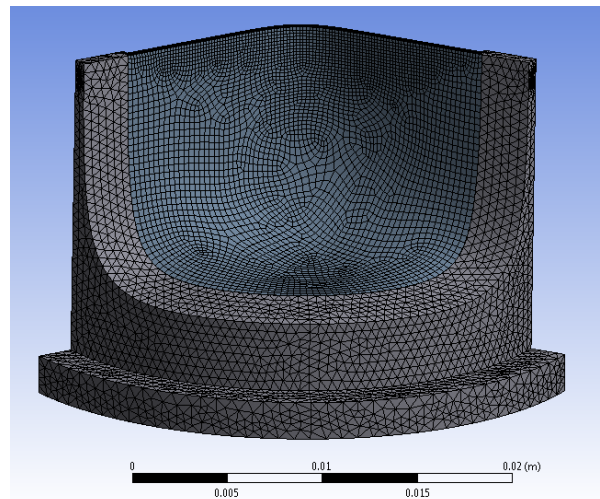


Figure 6.26: 184,218 elements were used to model the flow through the valve cavity. Bricks were used to model the thin surface of the leaflet, while tetrahedral elements were used to model the stent. There were 40 mesh elements through the thickness of the leaflet

leaflet. The regions near to the wall of the cavity are referred to as *skin* regions, while the central regions are referred to as the *core*.

6.5.1 Results

The polymer flows from the commissures in the C injection scenario (Figure 6.27). The melt then simultaneously flows down the stent posts and grows from the sides of the leaflet towards the centre. In the centre of each leaflet the flows from the commissures meet, before flowing towards the nadir, resulting in shear-induced vertical orientation in the centre of the leaflet. In the core regions of the leaflet there is some stretch-induced orientation (as indicated by the presence of blue vectors in Figures 6.27e and 6.27f). In Figure 6.27e stretching arises near to the commissures as the flow diverges to flow along the free edge and down to the nadir. In Figure 6.27f there is stretching at the base of the leaflet, presumably due to flow passing out of the leaflet and back into both the stent post (right and left of image) and stent cylinder (centre of image). Curiously, there are some stretch vectors to be found in the centre of the leaflet. The high magnitude of stretch - relative to the magnitude of shear - is likely to arise due to the convergence of flows from the free edge as they are redirected down the leaflet. As such, it is highly unlikely that cylinders would actually be oriented horizontally in this region, as the principal stretch direction is in fact in the *direction* of flow, highlighting a shortcoming of the scalar orientation model.

The SAXS map of a representative leaflet injected from the commissures is shown in Figure 6.27g: in these images biaxial orientation appears as a cross, as opposed to the layer by layer representation in Figure 6.27. Biaxial orientation is present in the SAXS map of the leaflet, though rarely are the two orientations perpendicular to one another. There appears to be a dominance of horizontal orientation at the sides of the leaflet, which was not the case in the computational predictions. SAXS scanning perpendicular to the leaflet is unable to determine whether orientation has arisen due to shearing or stretching deformations. It is interesting to note that the modelling predicts a region of horizontal orientation near the base of the leaflet (Figure 6.27f), which is also present in the SAXS map of the leaflet.

The prediction of orientation as a result of injection from the free edge is shown in Figure 6.28. In this case the flow travels vertically down the leaflet, gradually fanning out to enter the stent posts. This fanning does result in stretching deformations which led to horizontal orientation in the core regions of the leaflet (6.28e and 6.28f). The large inflow area provided little resistance to flow in comparison to the FEC scenario, and as control of the injection rate was limited, there was a relatively high flow rate through the valve (see Table 6.5). Higher flow rates promote orientation in the direction of flow, and thus at lower flow rates it may be possible to produce more circumferential orientation. Regardless, the orientation at the sides of the leaflet is dominated by shear at all depths.

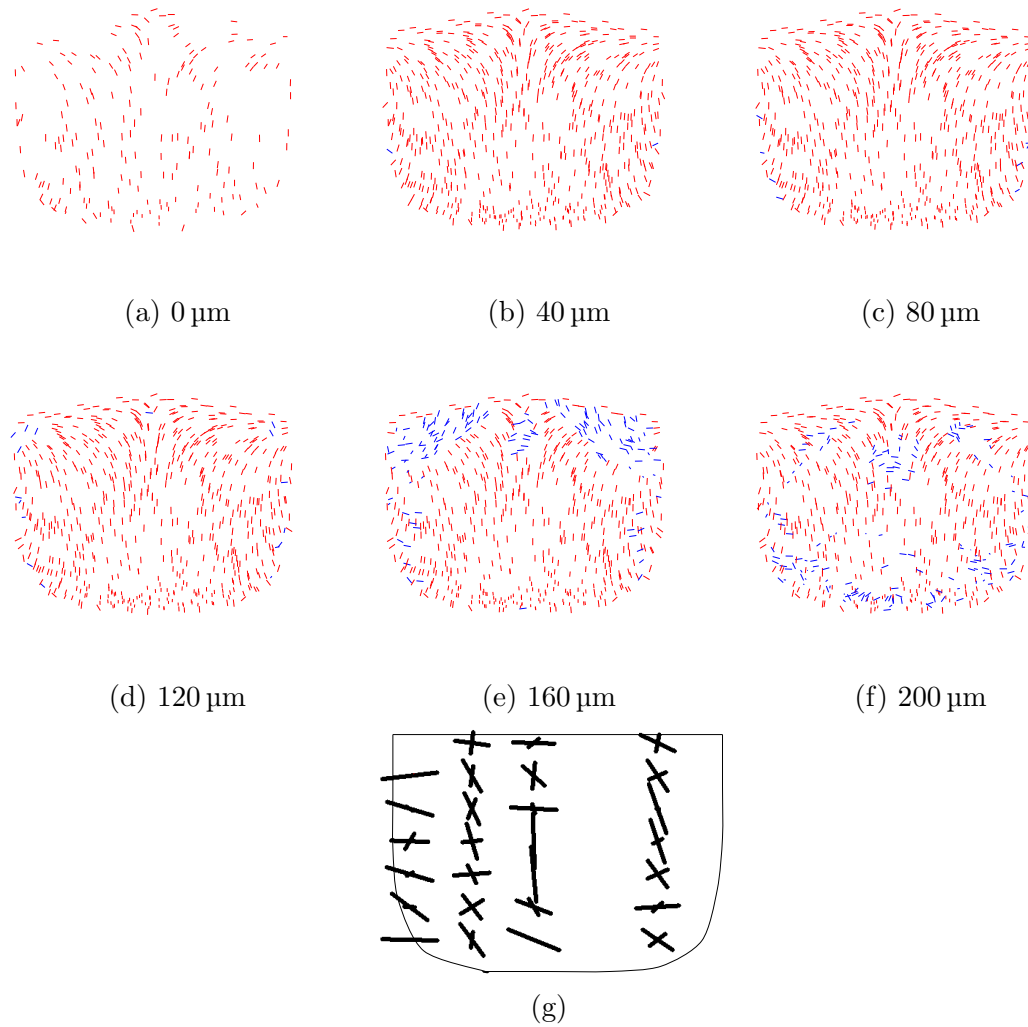


Figure 6.27: (a) to (f) Predicted orientation at various depths through the leaflet (total thickness $400\mu\text{m}$) for the C injected valve. The tick marks have been normalised, but as the plot is a 2D projection of 3D space some appear shorter than expected. The red marks correspond to cylinders oriented by shear deformations, and blue to orientation by extension. (g) is a representative SAXS maps of the orientation in injection moulded leaflets. PS cylinders are predominantly horizontal at the leaflet edge, but also exhibit significant biaxial orientation near the centre.

Contrary to the predicted orientation, the SAXS map displayed in Figure 6.28g has very little biaxial orientation. The orientation of the centre of the leaflet is predominantly vertical, and it fans on either side, in agreement with the orientation of the skin regions, but the stretch oriented core region does not seem to be present. On the left of the leaflet some horizontal orientation was recorded, this column of SAXS scans may be due to the X-ray beam passing through the stent post at a non-perpendicular incidence. The nadir of the leaflet has a large amount of horizontal orientation, possibly arising due to X-rays

passing through the stent cylinder.

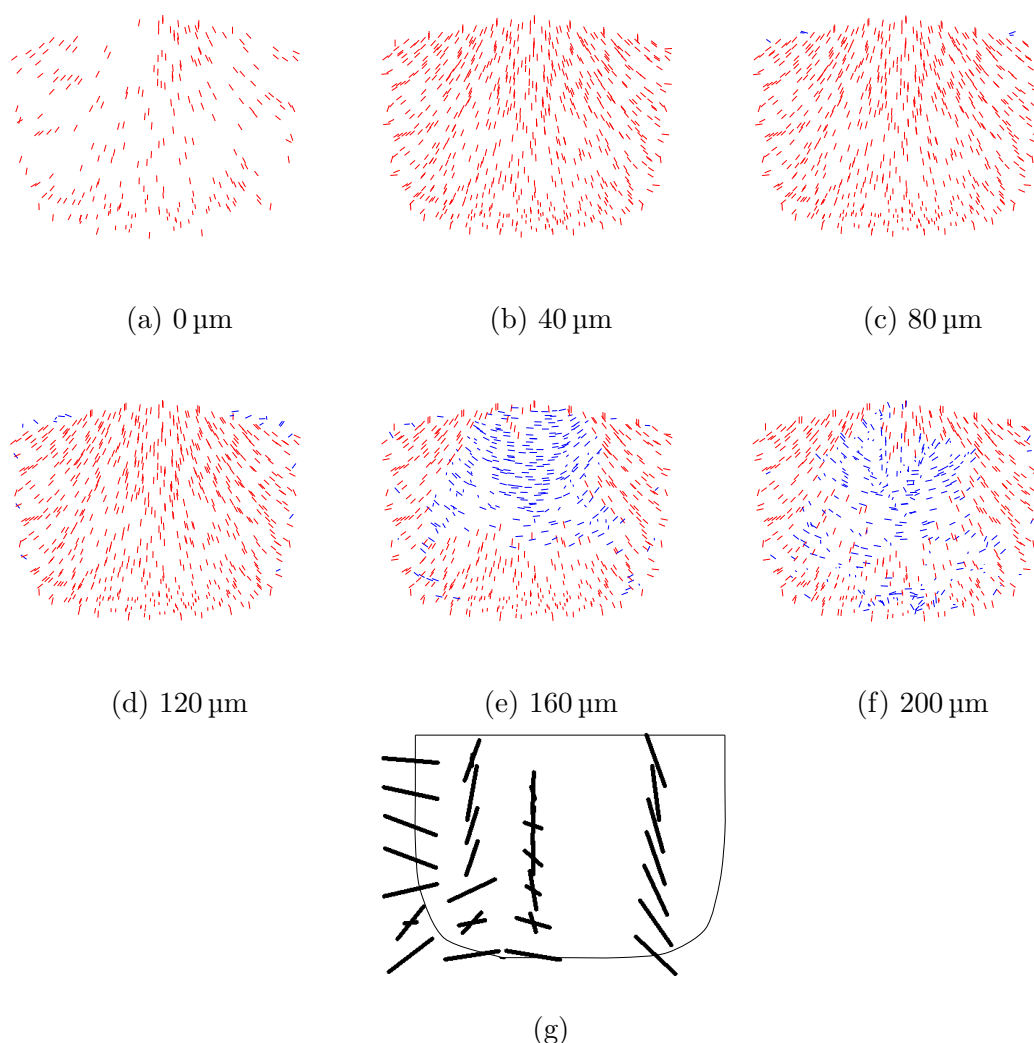


Figure 6.28: (a) to (f) shows predicted orientation at various depths within the leaflet (total thickness 400 μm) for the FE injected valve. The tick marks have been normalised, but as the plot is a 2D projection of 3D space some appear shorter than expected. The red marks correspond to cylinders oriented by shear deformations, and blue to orientation by extension. (g) representative SAXS maps of the orientation in injection moulded leaflets. PS cylinders in the free edge injection results in predominantly vertical orientation in the centre of the leaflet, fanning to horizontal at the sides.

Locating the gate at the centre of the free edge of the leaflet (FEC, Figure 6.29) led to a flow most similar to radial flow, where the flow diverges in a thin disc. In contrast to the perpendicular flow into the disc geometry, here the polymer melt enters the cavity without changing its direction of flow. Therefore, the flow quickly assumes a steady profile, producing the characteristic layered biaxial structure with approximately 50% circumferential orientation near to the gate. As the flow grows radially, the orientation

near to the free edge is horizontal. At all points along the leaflet-stent boundary, the flow crosses perpendicular (though this might not be immediately apparent from the 2D projection of the 3D leaflet).

The SAXS mapping of the FEC leaflet is shown in Figure 6.29g. The leaflet is dominated by uniaxial orientation in the horizontal direction. Some biaxial regions are found nearer to the free edge. The dominance of horizontal orientation may have been aided by restrictions to the outflow near the nadirs due to the arrangement of the heaters - so polymer had to flow towards the commissures.

In summary, the orientation model is able to predict PS cylinder orientation in complex geometries. For each of the injection conditions the orientation of shear aligned vectors are accurately predicted by the model. Cylinders which are oriented by stretch (and lead to a biaxial layered structure) are also predicted. However, their exact orientation is not always correct, nor is their fraction.

As may be apparent from the SAXS maps, referencing the maps to the leaflet was not a trivial task. There were various confounding factors: the leaflet must be flattened to ensure that the beam passes perpendicular to the surface. Flattening and mounting the leaflet required the edges of the leaflet to be gripped, without the grips intersecting the X-ray beam. To achieve this, the leaflet had to be dissected to include some of the stent post and stent base; which are much thicker than the leaflet and hard to cut accurately. Consequently, a reference point cannot be accurately determined on the leaflet.

For mapping of the final valve (as shown at the end of this Chapter) a purpose built mounting frame was cut from perspex such that the leaflets can be accurately mounted and referenced.

6.5.2 Discussion

Using the basic assumption that shear results in PS cylinder orientation in the direction of flow, and stretching leads to orientation perpendicular to flow, the orientation distribution was predicted for a complex form. In the skin layers (0 to 80 μm), the PS domains orient in the direction of flow. When injection is slow, stretching dominates in the core of the thin sections.

In this section the flow fields predicted by the FE solver were assumed to be valid: no further pressure or velocity field measurements were made. Shear rates were in the previously tested range of rheometric data. The shortcomings of the scalar orientation model to determine orientation were highlighted by the predicted orientation in the commissural

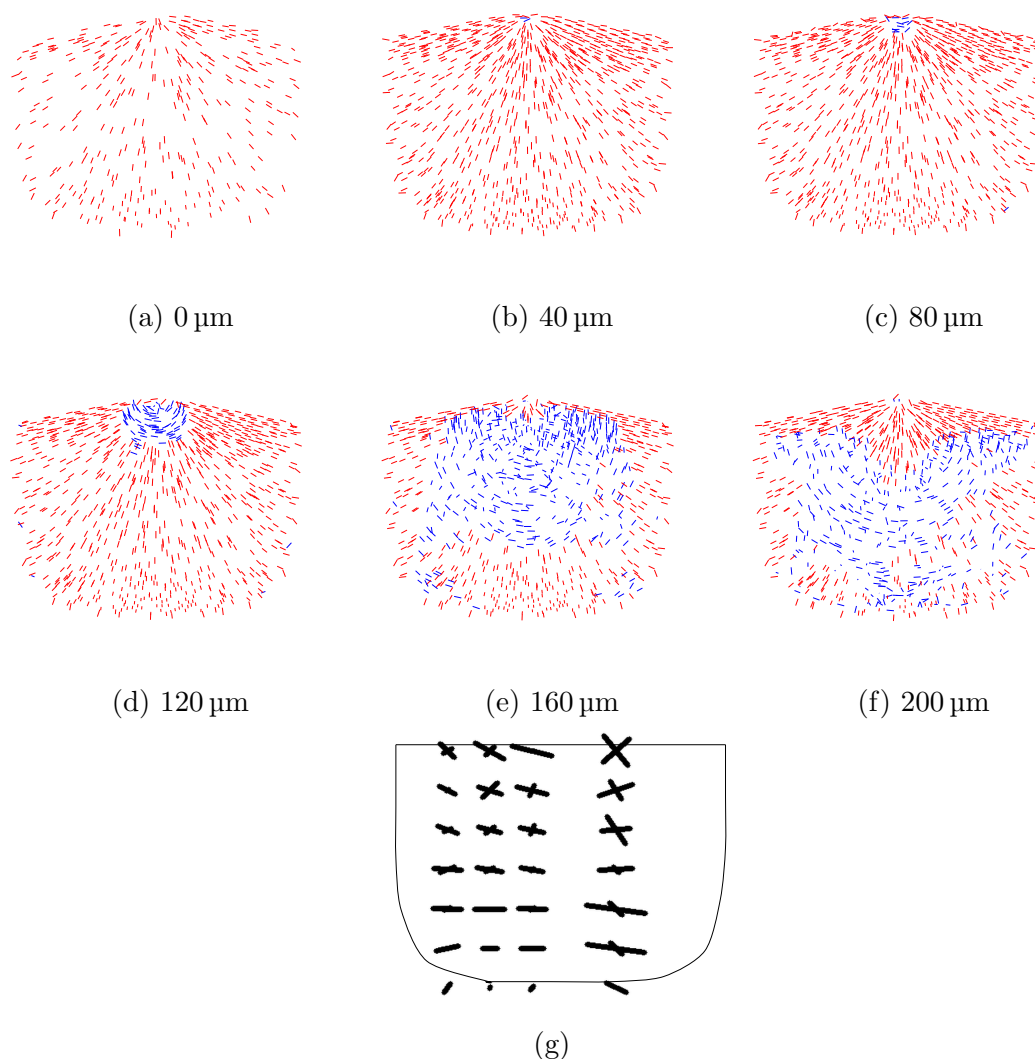


Figure 6.29: Predicted orientation at various depths within the leaflet (total thickness $400\text{ }\mu\text{m}$) for the FEC injected valve. The tick marks have been normalised, but as the plot is a 2D projection of 3D space some appear shorter than expected. The red marks correspond to cylinders oriented by shear deformations, and blue to orientation by extension. (g) shows a representative SAXS map of the orientation in injection moulded leaflets. PS cylinders in the FEC injection results in horizontal orientation throughout the leaflet, with biaxial orientation present near to the centre and free edge.

injection scenario (Figure 6.27). At the centre of the free edge the flows from each commissure converge, leading to an acceleration and stretch in the direction of flow (down the leaflet). The positively extending component of this stretch is not perpendicular to the flow, as assumed by the scalar model, and is thus unlikely to lead to biaxiality. In the SAXS mapping (Figure 6.27g) there is some biaxial orientation on the left and right sides of the leaflet which is caused by the flows from the left and right commissures which diverge before reaching the centre of the leaflet.

Inspection of the SAXS maps indicates that the biaxial orientations do not always lie perpendicular to one another. This demonstrates that the assumption of orthogonal orientation is inappropriate for fully describing biaxial orientation. The Advani-Tucker tensor orientation model (Advani, 1987) would be able to describe such behaviour, as well as predict the quality of orientation - which I did not consider here. In Figures 6.27 to 6.29, 3D vectors in 3D space are projected to a 2D surface, making it tricky to compare orientations between the computational prediction and SAXS maps. Future work would quantitatively evaluate the difference in orientation between cases.

The purpose of testing various gate positions, both computationally and experimentally, was to inform the design of the bioinspired valve. The most crucial part of a valve is the leaflets, in which the highest diastolic stresses can be found at the leaflet-stent boundary. Zaffora (2011) optimised the orientation of anisotropy to reduce these stresses. The distribution of the optimised orientation was shown in Figure 1.12. In summary, near to the free edge the optimised orientation is horizontal, and parallel to the free edge. Moving towards the nadir, the oriented fibres form arcs across the leaflet, with each arc following a similar shape to that of a cable suspended between the stent-leaflet boundaries.

The optimised orientation shares many characteristics with the natural leaflet, which is shown in Figure 1.7. The natural leaflet has predominantly horizontal orientation, and continuous collagen fibres stretch from the leaflet-stent boundary to the centre of the leaflet where they bundle to form the fibrous Nodule of Arantius. In both the optimised polymeric and natural valve the fibres approximate to arcs. The natural valve, however, has another interesting characteristic. Collagen fibres also run between the horizontal collagen bundles, approximately 45° to the horizontal. This morphology is particularly evident in the photograph of a stained porcine valve published by Sauren (1981) (page 14). More recently, various authors have used microscope imaging (Marom et al., 2013; Rock et al., 2014), and small angle light scattering (Sacks et al., 1997; Sellaro, 2003) to detect the orientation of collagen bundles. Their studies on porcine valves¹ also clearly show the dominance of horizontal fibres, with further fibres passing between bundles at 45° , or oriented vertically from the nadir of the leaflet (particularly evident in the right coronary leaflet in Rock et al. (2014)). 3 mechanisms of branching were identified (tree-like, pinnate and fan-like), indicating that the collagen bundles branch in response to a variety of biomechanical cues.

If the presence of biaxial orientation in the native leaflet has some mechanical purpose, it

¹It is worth noting that the main difference between the porcine and human aortic valve is the relative sizes of the cusps; the non-coronary cusp is largest in humans, while the right coronary cusp is largest in pigs (Sim et al., 2003). No differences in collagen arrangement have been noted.

may be advantageous to reproduce this in the bioinspired BCP valve proposed here. The FEC gate position (with slow injection) promotes biaxial orientation of PS cylinders in the leaflet, with the core orientation following the desirable arcs across the leaflet, and the skin orientation perpendicular. However, there is little consensus among the literature regarding the *purpose* of collagen fibre branching and biaxial orientation in the natural leaflet. In all likelihood, collagen growth and orientation is a result of biomechanical influences which ‘fine-tune’ the structure (to the individual) over time (Rock et al., 2014). Given this uncertainty, it would be naïve to design for biaxial orientation on a bioinspired basis alone.

At high injection rates from a point, when biaxial orientation does not occur, the FEC gate position would lead to orientation extending radially from the centre of the free edge. Along the free edge of the leaflet the orientation would be horizontal, while in the centre of the leaflet the orientation would be vertical. The diastolic load must be transferred from the leaflet to the stent. As such, it is unsurprising to observe that in both the optimised and native leaflets the fibres are close to perpendicular to the stent-leaflet boundary when they cross it. This suggests that even without biaxial orientation FEC injection would be desirable.

There are considerations beyond orientation to be made when designing an injection moulding tool. There is an array of guidelines for tool design which often recommend that the following considerations should be made (Cracknell and Dyson, 1993; Eastman, 2011; Proto Labs Ltd., 2010):

- To reduce sinkage and warpage;
 - eliminate thick walls,
 - maintain constant wall thickness,
 - core out large volumes.
- Avoid wall thicknesses ≤ 0.5 mm.
- Reduce sharp corners.
- Include draft to aid part removal from tool (no vertical sides).
- Gate away from thin edges to avoid break during gate trimming.
- Maintain proper cooling of cores.

Some sources do recommend that gating into thin sections should be avoided as it leads to high shear rates, higher injection pressures, and difficulty in filling thick sections (East-

man, 2011). However, the proposed low processing rate (injection velocity and unit production) negates the first two reasons, and the small part size counters the final one. In fact, gating into the thick stent would carry the risk of not completely filling the thin leaflet.

After injection, cooling, and part ejection the sprue must be removed from the part. Tool design guidelines warn of the risk of part damage during this trimming step. However, as this process will be performed by hand, and without time pressure, the risk is reduced. Furthermore, across the leaflet the greatest stresses are found at the leaflet-stent boundary, while in the leaflet centre they are low. As such, the centre of the leaflet is a less critical region for stress reduction.

The FE injection scenario is an unconventional means of gating a tool because there is no thin sprue of polymer which can be trimmed off. The FE injection would require significant post-processing to remove the ‘runner’ and ‘gate’ material. On the other hand, the C and FEC gate positions each fill the cavity from 3 locations. Consequently the melt flow from each gate must meet and join in the part. This meeting line is referred to as the *weld line*. The weld line may be a source of flaws from which cracks could grow. In the C injection scenario the weld lines occur down the centre of each leaflet, whereas in the FEC scenario welding takes place in the stent posts.

In an alternative injection scenario, which was not considered here, the gates could be located close to the nadir of each leaflet. Like the FEC scenario, injection at the nadirs would also allow control of radial and circumferential orientation in the ideal directions. However, the sprue would be perpendicular to the leaflet’s surface, meaning that a small nipple would be left after trimming, which may affect the dynamic behaviour of the leaflet. Also, the radial flow geometries considered earlier also have a perpendicular sprue, which is likely to cause the less developed orientation close to the gate. Thus, it is preferable for the inlet flow to be in a similar direction to the cavity flow, as found for the other gate positions.

In summary, the FEC injection allows for a large degree of control over the orientation in the leaflet, which can be tuned to mimic the biological and optimised orientations. The FE scenario was not able to produce the necessary horizontal orientation. The C gate location can produce appropriate orientation in the critical regions of the leaflet (the stent boundary), but it led to a weld line in the centre of the leaflet. Therefore, the FEC gate position was selected for the final tool.

6.6 Final valve injection

In Chapter 5 I proposed a final design for the polymeric prosthetic heart valve. Compared to the prototype valves tested in Chapters 5 and 6 (Figure 6.25 for example), the final design (Figure 5.21) is characterised by having thicker stent posts and a lower profile (due to the reduced distance between the nadir and sewing ring). The stent posts were thickened to reduce their deflection during diastole, and the valve's profile was lowered to avoid obstruction of the coronary arteries.

6.6.1 Methods

Modelling

The transient mould filling process was modelled using Autodesk Simulation Moldflow Adviser 2015. The viscometric data was matched to the previously used Carreau-Bird model (Table 6.3), as Moldflow adviser uses the Cross model as opposed to the Carreau-Bird model. The values of the parameters and side-by-side comparison of the two models is shown in Appendix D. The cavity filling was modelled using an injection rates of $5 \text{ mm}^3 \text{ s}^{-1}$ and $95 \text{ mm}^3 \text{ s}^{-1}$.

Manufacture

The injection moulding tool for the final valve was manufactured by Kelland Precision Tooling Ltd. (Huddersfield, UK). The injection was performed at the Bradford Centre for Polymer Micro and Nano Technology using a Fanuc Roboshot S-2000i30B, a servo-hydraulic moulder, allowing for greater control of the injection rate and reducing the likelihood of contamination - particularly from hydraulic oil.

Upon consultation with the animal house regarding pig sizes, two valve sizes were manufactured to accommodate the variation in aortic root sizes. The valves were sized for tissue annulus diameters (TAD) of 21 mm and 23 mm with supra-annular placement, such that the TAD corresponds to the internal orifice diameter of the valve. Both valves were designed with a leaflet thickness 0.3 mm. The injection moulding tool contained a cavity for each valve, meaning that both valves were injected simultaneously.

The parts were injected at a ram velocity of 0.5 mm s^{-1} , corresponding to each cavity being filled at $95 \text{ mm}^3 \text{ s}^{-1}$.

The tool was heated using cartridge heaters, and contained integrated cooling channels, for the mould to be cooled over approximately 180 s.

The leaflet orientation was mapped with SAXS using a Bruker Nanostar (at Materials Science and Metallurgy, University of Cambridge), using the same analysis methods as previously described.

6.6.2 Results

Modelling

The transient injection process is shown as a sequence of images in Figure 6.30. In comparison to the prototype results presented in Section 6.5.1, the tool is not overfilled and there is no steady flash from the mould. In comparison to conventional injection moulding processes, the injection is slow.

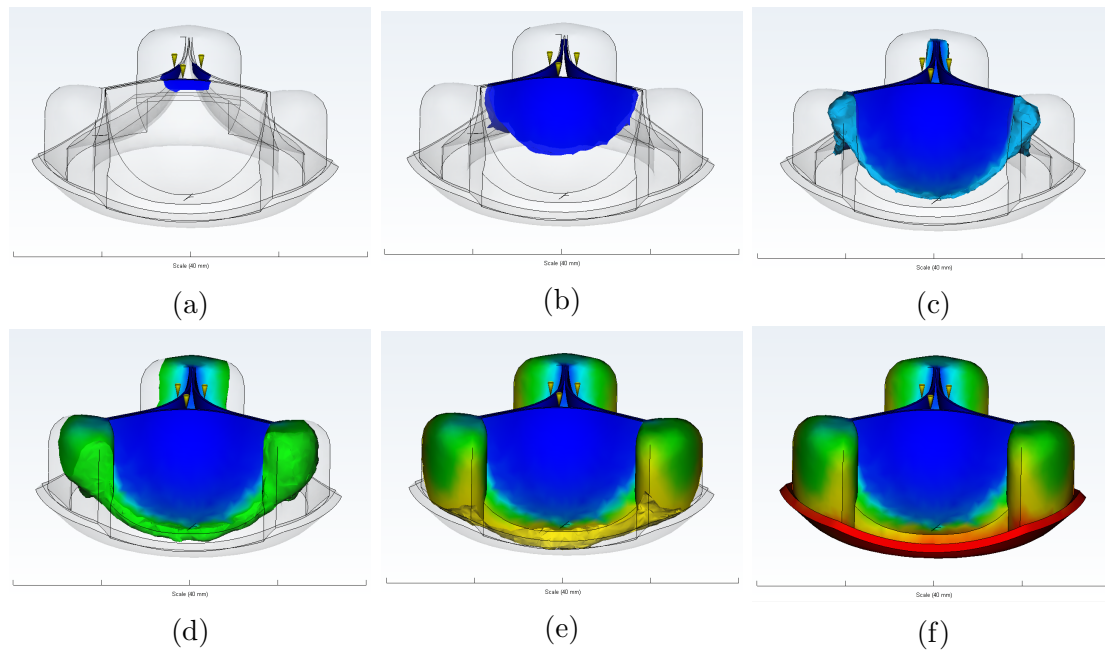


Figure 6.30: Modelling of the cavity filling process for the final valve at $5 \text{ mm}^3 \text{ s}^{-1}$. The images are taken at 150 s intervals. The colour corresponds to the polymer's residence time in the cavity, with blue for short, green for medium, red for long. First, the leaflets are filled; second, the stent posts; and finally the sewing ring. There were no differences in the flow patterns for injection at $5 \text{ mm}^3 \text{ s}^{-1}$ and $95 \text{ mm}^3 \text{ s}^{-1}$.

Manufactured valves

The surface finish quality of the final injected valves was excellent (Figure 6.31). Remnants of the weld line were visible in the stent, though with no flaws or cracks visible to the naked eye.

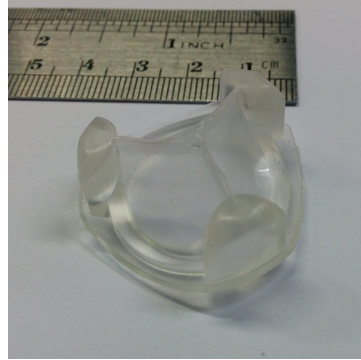


Figure 6.31: Final injection moulded valve.

The leaflets of the final valves were dissected from the stent body and mapped using SAXS. The maps of 6 leaflets are shown in Figure 6.32. There was negligible biaxial orientation in these leaflets as the injection rate was quicker than the prototype valves. However, compared to the previous FEC injection the shear induced orientation at the sides of the leaflet is more horizontal. In the 2D projection of the leaflets a horizontal orientation at the sides matches the optimised distribution well. In the centre of the leaflet the orientation is vertical. While this is contrary to the designed result, it is not an immediate worry as the stress in the centre of the leaflet is approximately 20 to 40% of the stress found at the sides. There would, however, be some second order effects which would influence the stress distribution. This issue is considered in Chapter 7.

6.7 Conclusion

In this chapter I aimed to manufacture a prosthetic heart valve with bioinspired orientation. In an initial study, discs of BCP were injected from a central point. Although most authors have observed that PS cylinders orient in the direction of flow, using SAXS I observed a layered biaxial structure where the skin layers are oriented radially and the core circumferentially.

I proposed that the biaxial structure forms as a result of the competition between stretching and shearing deformations. To predict the velocity field during injection moulding I characterised the melt rheology of the selected polymer, SEPS22. SAXS measurements

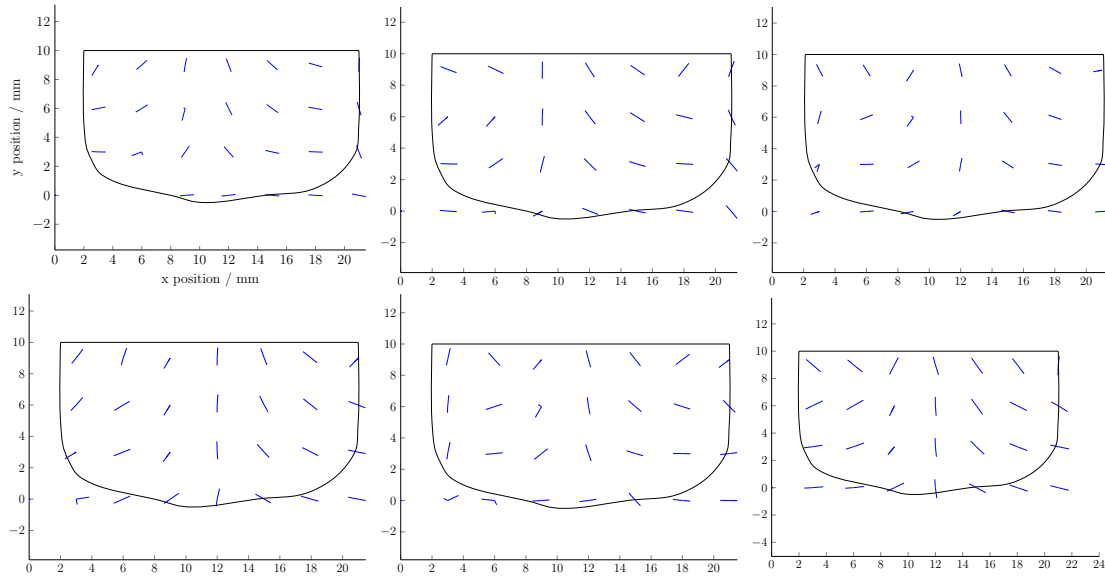


Figure 6.32: SAXS mapping of six leaflets from injection moulded valves.

were made upon injection moulded discs to determine the proportion of radial orientation. Using the velocity field and SAXS measurements, a critical value of the ratio of shear rate to stretch rate was determined, which could be used to predict biaxial orientation.

A bench-scale injection moulding process was built to test various gate positions from which to inject the heart valve. Three scenarios were tested: injection along the free edge, from the commissures, and from a point at the centre of the free edge (FEC). Injection from the FEC position was most successful at promoting biaxial orientation at low flow rates.

In the final valve design, the FEC gate position led to the bioinspired orientation of PS cylinders in the critical side regions of the leaflet, as characterised by Figure 6.32.

Chapter 7

Valve testing

7.1 Introduction

Successful design of a novel heart valve is characterised by lifelong durability of the valve and without the need for anticoagulant therapy. These characteristics informed the search for and selection of new materials in Chapter 2. Physiological opening and closing of the valve is necessary for the avoidance of anticoagulant therapy. In Chapter 5 I used hydrodynamic testing to compare two prototype leaflet designs, resulting in the selection of the one with a spherical leaflet form. I hypothesised that lifelong durability might be aided by a bioinspired orientation of stiff PS cylinders in the leaflets of the prosthetic polymeric valve. In Chapter 6 I designed a novel injection moulding process which achieved this orientation.

In Chapters 3 and 4 the material (isolated from the valve) was subject to chemical and biological forces. Chapter 3 showed that the material's biocompatibility was good. Chapter 4 showed that the material calcified less than a biological reference, but that the combination of calcification and mechanical fatigue may be a failure route, which should be considered in further testing.

A point has now been reached at which it is appropriate to test the final valve, for the characteristics of lifelong durability without the need for anticoagulant therapy. In this chapter hydrodynamic and durability testing will be performed.

7.2 Hydrodynamics

In general, adequately sized trileaflet valves with good hydrodynamics and made from haemocompatible materials do not require anticoagulation. As the haemocompatibility of the coated and uncoated materials is adequate (Chapter 3), the hydrodynamic parameters of the final valve design will be tested with respect to ISO 5840 in this section.

7.2.1 Materials and methods

The same pulse duplication methods as described in Chapter 5 were used to assess the hydrodynamic performance of the valve. These tests were performed by Mr de Gaetano at Politecnico di Milano, Milan, Italy.

Valves were manufactured from SEPS22, as described in Section 6.6. Unfortunately, the injection moulding tool resulted in valves with too thin leaflets. In particular, the leaflets were specified to have a uniform thickness of 300 μm . Using a micrometre the minimum leaflet thickness was 240 μm at one of the stent-leaflet boundaries. Using a microscope the minimum leaflet thickness at the commissure was 150 μm . Nevertheless the valves were made sufficiently well for meaningful hydrodynamic testing. Over ten valves were made and three were used for hydrodynamic testing.

7.2.2 Results

The effective orifice area, EOA_G (Equation (5.3)); the mean systolic pressure difference, MSPD; and regurgitation of the valve were evaluated, over a minimum of 10 cycles for 3 valves. The results are reported in Table 7.1.

The final valve design exceeded the hydrodynamic ISO 5480 standard for a 23 mm valve. Compared to the prototype valves previously tested in Chapter 5, the final valve design had a greater EOA_G and lower regurgitation than both the spherical and cylindrical form prototype valves.

The hydrodynamic performance was probably aided by the unintentionally thinner leaflets which allowed the leaflets to open and close more easily. At the conclusion of Chapter 5, the valve design had been updated by increasing the thickness of the stent posts. This change resulted in less deflection of the posts.

Table 7.1: Valve performance and minimum ISO performance parameters, at a cardiac output of 5 l min^{-1} , 70 BPM, and 120 mmHg. Results are reported as mean \pm range.

Parameter	23 mm polymeric valve (n=3)	ISO 5480 standard
EOA_G (cm^2)	1.59 ± 0.02	≥ 1
MSPD (mmHg)	6.83 ± 0.18	
Regurgitant volume (ml/stroke)	5.06 ± 0.61	
Regurgitation (%)	8.71 ± 0.99	≤ 10

7.3 Valve fatigue testing

The long term survival of a prosthetic heart valve can be tested under *in vitro* conditions. In accordance with the ISO 5840 standard, rigid valves must survive 400 million cycles, and flexible valves must survive 200 million cycles, equivalent to approximately 11 and 5.5 years, respectively, in a human.

As discussed in Section 2.1.5, it is possible to reduce the time for fatigue testing by increasing the frequency. However, the maximum testing frequency is dependent on the type of valve and tester. In particular, the valve should open and close completely, leaflet dynamics should be physiological, and viscoelastic materials should not be tested above the frequency at which they undergo a β or glass transition (20 or 80 Hz for SIBS30 when tested in Section 2.1.5). Testing performed at a frequency between 60 and 200 BPM is referred to as quasi-real time durability testing, and a pulsatile tester (as used for hydrodynamic testing) can be used. Accelerated fatigue testing takes place at higher frequencies (300 to 1800 BPM) using specialised accelerated testers.

7.3.1 Materials and methods

For this valve, quasi-real time durability testing was performed using the pulsatile tester as previously described (Section 5.2.3). Tests were performed using the pulse duplicators by me at the Department of Chemical Engineering and Biotechnology, University of Cambridge, UK; and by Francesco de Gaetano at LaBS, Politecnico di Milano, Milan, Italy. The tests were performed at frequencies of 135 and 200 BPM, and at a cardiac output of 5 l min^{-1} , as detailed in Table 7.2.

ISO 5840 recommends that sinusoidal oscillations are used in an accelerated fatigue tester. In the quasi-real time test, a modified flow curve was used such that the diastolic period lasted for 50% of the cycle, and the pressure variation was approximately sinusoidal at

the valve.

Survival of a valve is defined as the valve supporting a transvalvular pressure gradient during diastole (TPG_d) of at least 100 mmHg, for at least 10% of the cycle period and for at least 95% of the number of cycles survived.

7.3.2 Results

The pulse duplicator flow loops (particularly the Cambridge setup) were not well suited for use at 200 BPM, which led to a diastolic overpressure. I recorded the maximum transvalvular pressure that was reached during diastole, $(TPG_d)_{MAX}$, as well as the transvalvular pressure supported for 10% or more of the cycle, $(TPG_d)_{10}$, according to ISO 5840. The large diastolic overpressure led to the large difference between $(TPG_d)_{MAX}$ and $(TPG_d)_{10}$. The large distance between the mitral valve and ventricle probably contributed to the overpressure.

All valves failed having performed fewer than 200 million cycles, thus failing ISO 5840. Failure occurred when the valves were unable to support the diastolic pressure difference, due to tears in the leaflets, or holes forming in the leaflets, as shown in Figure 7.1. The diastolic overpressure differed between testing systems. Higher pressures were associated with reduced valve lifetimes.

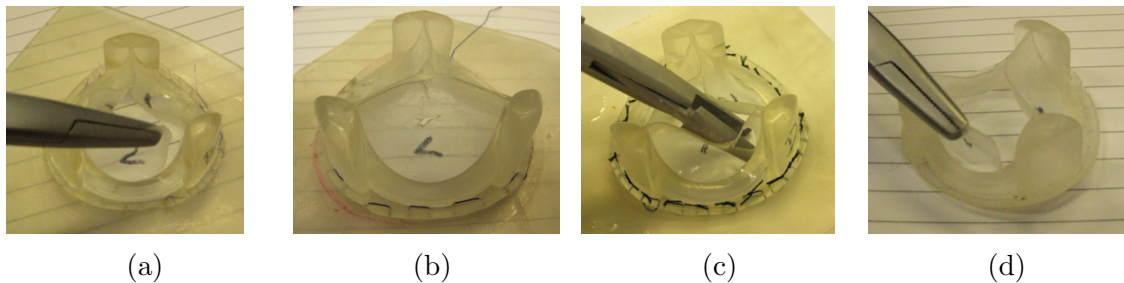


Figure 7.1: Images of failed valves. Valves (a), (b), and (d) failed at the leaflet stent boundary, and valve (c) failed with a hole at the centre of one leaflet. Images (a) to (d) correspond to valves B, C, D, and F in Table 7.2.

7.3.3 Discussion

The injection moulding tool, and thus the valves which it produced were not within tolerance. In particular, the leaflets were specified to have a uniform thickness of 300 μm . Using a micrometre and light microscopy, the actual leaflet thickness was measured. With the micrometre, the minimum thickness was 240 μm , on one of the stent-leaflet

Table 7.2: Quasi-real time durability testing results for SEPS22 valves. TPG_d is the transvalvular pressure gradient during diastole, where $_{10}$ indicates that TPG_d is sustained for at least 10% of the cycle, as per the ISO standard, and $_{MAX}$ is the maximum TPG_d in a cycle.

Valve	Testing Location	Size (mm)	$(TPG_d)_{10}$ (mmHg)	$(TPG_d)_{MAX}$ (mmHg)	Frequency (BPM)	Lifetime (10^6 cycles)
1	Milan	23	92	163	200	2.0
2	Milan	23	100	190	200	4.6
3	Milan	23	111	172	200	3.5
B	Cambridge	23	120	150	135	0.39
C	Cambridge	23	145	190	200	0.58
D	Cambridge	23	130	185	200	2.0
F	Cambridge	21	145	373	200	1.7

boundaries. By light microscopy the minimum thickness was $150\mu\text{m}$. The microscope measurement is likely to be a more accurate value, assuming that the minimum thickness was found at the commissures. The micrometre was less sensitive to fine spatial variations in thickness as it had a diameter of 8 mm.

Testing was performed in distilled water, so calcification did not accelerate failure. The diastolic overpressure may have contributed to the acceleration of failure.

The remainder of this chapter will analyse the cause of failure, and possibilities for future improvements.

7.4 Failure analysis

In Chapter 2, fracture mechanics methods were used for the comparative assessment of material fatigue. Previously, and in parallel, Zaffora (2011) and Serrani et al. (submitted) have used FE modelling to evaluate valve designs and to optimise PS cylinder orientation. In this section, experimental fatigue and FE modelling will be combined to help determine the cause of failure. Materials, processing and leaflet form shall be considered as I seek to determine whether the durability of the valve could achieve a level of acceptability.

7.4.1 FE modelling

The FE model was constructed and run by Dr Serrani. The FE model was previously validated by comparing the deflection of the stent posts to pulsatile testing results. The

modelling of the valve was performed using an anisotropic hyperelastic model without viscoelasticity. The base of the sewing ring was constrained vertically and the outside edge was constrained radially.

Dr Serrani used the Mooney-Rivlin model for strain energy, ψ . A derivation of this model is shown in Appendix E. Assuming incompressibility:

$$\psi = c_1(I_1 - 3) + c_2(I_2 - 3) + k_4 \log^2 \sqrt{I_4}, \quad (7.1)$$

where c_1 , c_2 , and k_4 are material parameters, and k_4 is associated with the orientation. I_1 , I_2 , and I_4 are the 1st, 2nd, and pseudo-4th (Equation (E.5)) invariants of the Cauchy-Green stress tensor, \mathbf{C} . The material parameters were fitted to the experimental data, which was previously presented in Section 2.3.3 for SEPS22, to give the values shown in Table 7.3.

Table 7.3: Mooney-Rivlin parameters optimised for the tensile strain energy density of SEPS22

	c_1	c_2	k_4
Anisotropic	0.15	0.15	1.62

A comparison of the strain energy density as a function of strain for the computational and for the fatigue model is shown in Figure 7.2a. Unfortunately, the Mooney-Rivlin formulation has no damage, Mullins, or memory components, meaning that it is not a good fit to the experimental data.

The stress strain data for the fatigue model was collected using oscillations at increasing steps of maximum strain. Higher strains probably cause breakage of the PS cylinders, so that the cyclic stress strain curves that reach higher maximum strains do not pass through the same points as those that reached lower maximum strains. This “strain softening” or breakage is reversible, but only once samples are left for at least an hour to recover.

Although Mooney-Rivlin is widely used for elastomeric materials, it is impossible for it to fit the experimental data shown here. The differential of the strain energy with respect to strain should give the stress-strain relationship. However, the best fit line to the experimental data for strain energy density when stretched parallel to the cylinders (solid red) is nearly linear with respect to strain, indicating that stress would be independent of strain.

The leaflet stress is approximately equal regardless of the constitutive model that is used, because the leaflets must support the same pressure load (assuming that the leaflets are

the same thickness). The effect of the difference between the modelled and actual strain energy density in the valve will be that regions of low stress will, in reality, be stiffer and have a higher strain energy density than the model predicts, as shown by the plot of strain energy density against stress (Figure 7.2b). Future work will need to implement damage or memory components to account for this effect.

The geometry of the valve in the model was modified to account for the tooling inaccuracies. In the *actual* valve geometry the leaflet thickness reached a minimum of $150\text{ }\mu\text{m}$ at the stent leaflet boundary, as indicated in Figure 7.2c. The *actual* orientation of PS cylinders was used, as mapped using SAXS and shown in Figure 6.32. The *designed* valve geometry, where leaflet thickness was a constant $300\text{ }\mu\text{m}$, was also modelled with the *actual* and *optimised* orientations, for comparison.

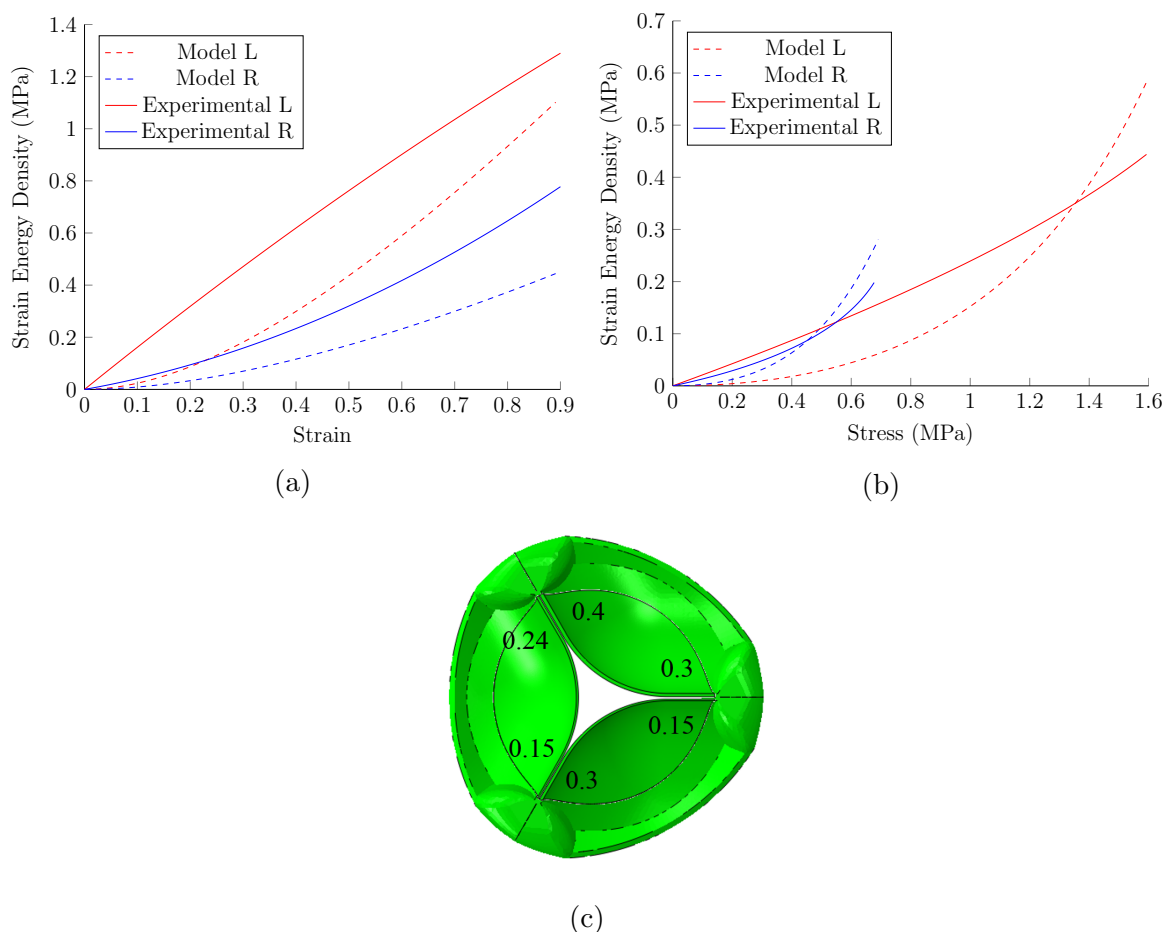


Figure 7.2: Comparison of the Mooney-Rivlin formulation for strain energy density and experimental data with a quadratic fit. (a) shows strain energy density against strain, and (b) against stress. L indicates stretching parallel to the PS cylinder orientation; R, perpendicular. (c) Axial view of 3D CAD model of valve marked with the measured leaflet thicknesses (mm) at the commissures from the *actual* valve geometry.

Results

The results of the FE simulation are shown in Figure 7.3. The von Mises and strain energy density maxima were located at the leaflet-stent boundary, and at the centre of the leaflet which was folded. These maxima support the failure locations of the actual valves shown in Figure 7.1.

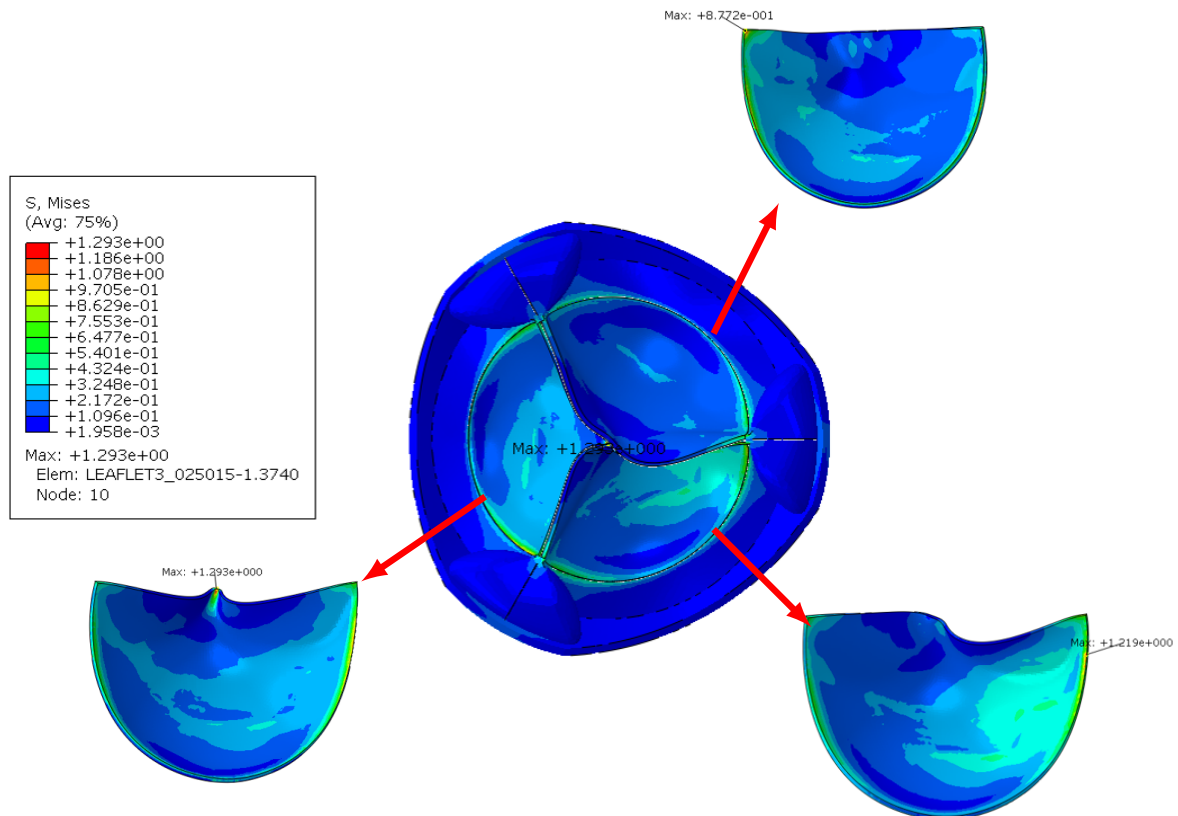


Figure 7.3: Results of the FE simulation showing von Mises stress during diastole in the final valve when loaded to 60 mmHg. The maximum stress is marked for each leaflet, 1.29 MPa in the lower left leaflet, 1.22 MPa in the lower right, and 0.87 MPa in the upper right. The maximum stress is located at the leaflet-stent boundary in the right leaflets, and in the centre of the left leaflet. This figure was produced by Dr Serrani.

The maximum predicted strain energy density in the valve as a function of the applied pressure is shown in Figure 7.4. The *actual* valve FE model did not converge up to 120 mmHg, and so higher pressure results could only be obtained by extrapolation. A quadratic fit was used for the extrapolation, which is appropriate given that stress in the leaflet is directly proportional to the transvalvular pressure (if there are no large leaflet deformations), and there is an approximately quadratic relation between stress and strain energy density for these materials.

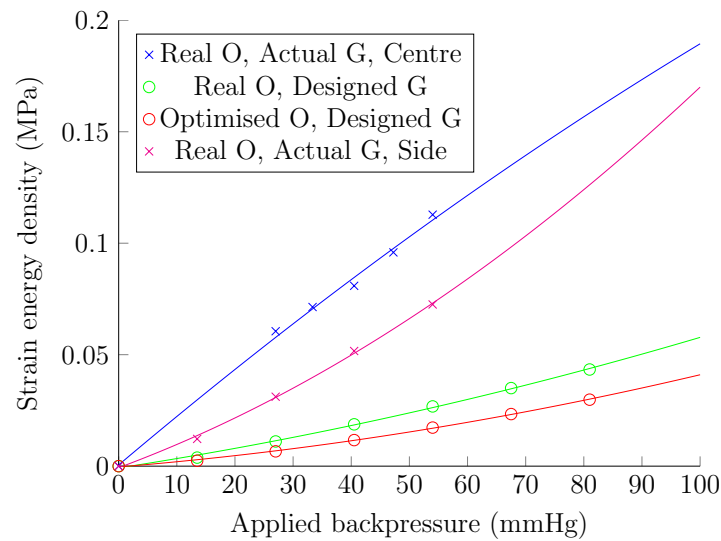


Figure 7.4: Maximum strain energy density in the valve as a function of applied pressure in the FE simulation. Orientation is abbreviated to O, geometry is abbreviated to G. Centre and side refer to the elements containing the maximum strain energy density at the centre and at the side of leaflet, respectively, as shown in Figure 7.3. Simulations were performed by Dr Serrani.

7.4.2 Fracture mechanics to crack nucleation

In Chapter 2, fracture mechanics was used for the comparative assessment of material fatigue, but for absolute predictions of fatigue other parameters must also be considered.

Mechanical fatigue failure in polymers occurs through the growth of flaws to become cracks which then cause catastrophic tearing. When strained uniaxially, crack growth rate is determined by the size of the crack, the material properties, and strain energy density. Lifetime prediction based on fracture mechanics methods assumes that:

1. Flaws grow independent of one another,
2. The growth of naturally occurring flaws is determined by the same parameters that determine the growth of artificial cracks in test pieces,
3. The flaws have a high enough population density such that a flaw above the critical size is likely to be found in a region of high stress (Kingston and Muhr, 2012).

The physical validity of the assumptions has been assessed using micro computed tomography imaging (Le Gorju Jago, 2008). Flaws initially grow independently, before coalescence causes rapid increases in the size of cracks. Furthermore, stress concentrations may not necessarily occur in the same region as the largest flaws. As it would be impossible to know the precise 3D description of all flaws and compute their growth in a

FE model, fatigue life predictions use an *effective flaw size* parameter.

In Chapter 2 an industry standard effective flaw size of 40 μm was used. To determine the effective flaw size in SEPS22 samples, a crack nucleation test is used. This consists of cyclically straining tensile bar samples without any pre-cracks until they fail.

First, I investigated the role of processing and orientation on material fatigue. The crack growth tests were performed on isotropic (solvent cast) samples, and perpendicular to the PS cylinder orientation to supplement the measurements made parallel to the PS cylinder orientation in Section 2.3.5. Second, I determined the actual effective flaw size in SEPS22, by performing crack nucleation tests on oriented samples (parallel and perpendicular), and solvent cast samples. Third, the crack growth parameters were evaluated when the polymer was submerged in buffer solution. These experiments were used to construct an *absolute* fatigue model, which was compared to the FE modelling and experimental valve fatigue data.

Materials and methods

Samples of oriented SEPS22 were manufactured via compression moulding, as previously described (Section 2.2). SEPS22 sheets were also formed using solvent casting. SEPS22 pellets were dissolved in toluene at 10w/v% before drying in a flat-bottomed Teflon[®] coated vessel.

The macroscopic crack growth rates for SEPS22 R (perpendicular) and SEPS22 SC (solvent cast - isotropic) were determined as previously described (Section 2.2.4).

Tensile bar samples (with dimensions shown in Figure 2.10a) were cut from the polymer sheets parallel (L) and perpendicular (R) to the PS cylinder orientation. PS cylinders were randomly oriented in the solvent cast (SC) samples.

The tensile bars were then cyclically strained using the Texture Analyser (Stable Microsystems, Surrey, UK). Nine samples could be simultaneously tested using wide, rubber coated grips. Initial flaws grew to form cracks and caused failure in the tensile bars.

For the assessment of crack growth rate in representative environmental conditions, the crack growth setup was modified by Eugenia Biral, under my supervision. The new setup allowed samples to be strained and crack position monitored whilst immersed. The crack growth rate was measured for solvent cast samples of SEPS22 in tris-buffered solution (Fisher Scientific, Loughborough, UK).

Results

The power law model was fitted to the crack growth data for SEPS22 L, R, and SC. The power law coefficients, B , and exponents, F , are reported in Table 7.4.

Equation (2.14) is used to connect the macroscopic fracture mechanics model with crack nucleation in the tensile bars. Assuming a final crack size for failure of $300\text{ }\mu\text{m}$ (the tensile bar and leaflet thickness), the effective initial flaw size for use in Equation (2.14) was calculated. This is reported in Table 7.4.

The effective flaw sizes of SEPS22 ranged between 253 and $291\text{ }\mu\text{m}$. Natural rubber is reported to have an effective flaw size of approximately $70\text{ }\mu\text{m}$ (Zarrin-Ghalami and Fatemi, 2012).

A comparison of the fracture mechanics and crack nucleation lifetime predictions is shown in Figure 7.5. This figure demonstrates that failure is not isotropic for the range of strain energy densities shown. At a given strain energy density, a BCP strained parallel to the PS cylinders has a greater lifetime than when strained perpendicular. This means that optimal orientation in a polymeric prosthetic heart valve has two benefits: the strain energy density is reduced (Section 1.10.1) and the lifetime at a given strain energy density is greater.

The fracture mechanics lifetime prediction for the parallel samples has a steeper gradient in the log-log plot than the other material. This is likely to be a result of the strain-softening of the sample. The samples have a “memory” of the maximum strain that they have reached, consistent with the Mullins effect (Diani et al., 2009). The lifetime of the isotropic samples is greater than expected, probably due to the low flaw size associated with this processing method.

Table 7.4: Fracture mechanics crack growth parameters and calculated effective flaw sizes, based upon a $a_f = 300\text{ }\mu\text{m}$. NR refers to natural rubber, with the values shown below reported by Zarrin-Ghalami and Fatemi (2012). The crack growth parameters for SEPS22 SC in buffer were determined by Eugenia Biral.

Material	F	B	$(a_0)_{a_f=300}\text{ (}\mu\text{m)}$
SEPS22 L	3.83	8.3×10^{-6}	291
SEPS22 R	1.8	1.84×10^{-5}	253
SEPS22 SC	2.51	9.87×10^{-6}	260
SEPS22 SC (in buffer)	2.55	1.35×10^{-5}	-
NR	2	4×10^{-5}	70

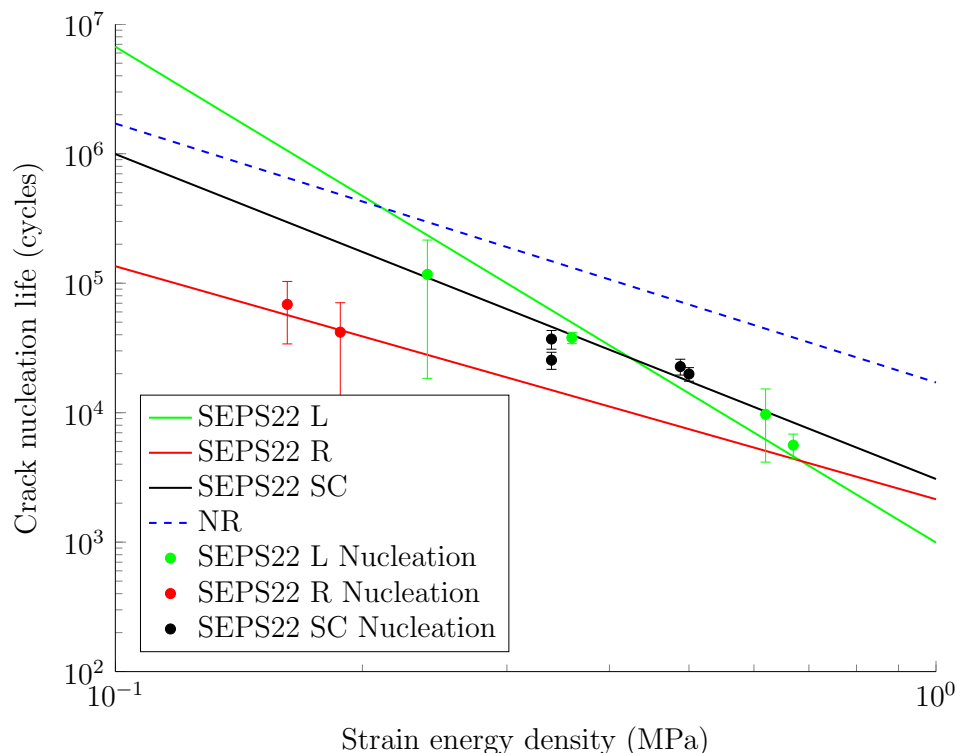


Figure 7.5: Comparison of the fracture mechanics and crack nucleation lifetime predictions as a function of strain energy density in a uniaxial tensile bar. Crack growth parameters and flaw sizes are those listed in Table 7.4, and the NR model is based upon the data collected by Zarrin-Ghalami and Fatemi (2012) for natural rubber. Each crack nucleation point corresponds to the mean lifetime and standard deviation of 9 samples.

A comparison of crack growth rates for SEPS22 SC in air and buffered solution is shown in Figure 7.6. There was no significant difference between the crack growth rates in the different environments. The values of B and F are reported in Table 7.4.

The lifetime of the valves which underwent fatigue testing was then compared to the result of the FE modelling and fatigue prediction, as shown in Figure 7.7. The predicted lifetime, when the maximum strain energy density is calculated based upon the valve being loaded $(TPG_d)_{10}$, is less than an order of magnitude different from all the experimental results. The stress-strain model for the material does not contain strain softening terms, which accounts for some of the discrepancy in experimental and model data in Figure 7.2a. Furthermore, the fatigue crack model assumes that a critically sized flaw can be found in the high stress region. The small region of high stress decreases the likelihood of this occurring, though future analyses could make use of Weibull analysis to determine the probability of a critically sized flaw occurring in the volume of interest.

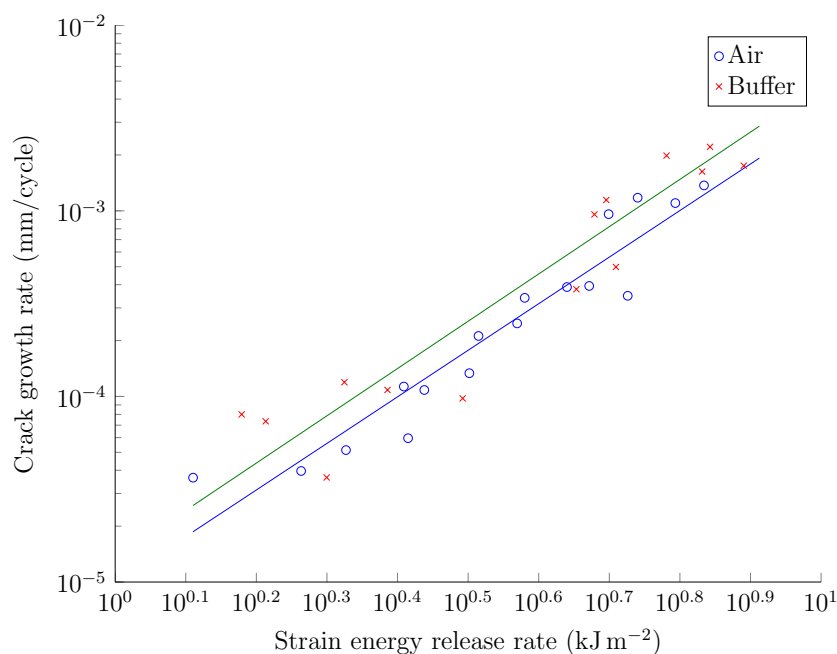


Figure 7.6: A comparison of crack growth rates for SEPS22 when in air and when submerged in tris-buffered solution (data collected by Eugenia Biral).

Discussion

With reference to Table 7.4, there is a large disparity in the initial flaw size between the value for natural rubber reported by Zarrin-Ghalami and Fatemi (2012), and that calculated for SEPS22. Furthermore the effective flaw size in these experiments did vary depending on the value of the failure crack size (a_f), to which it was similar. Zarrin-Ghalami and Fatemi (2012) on the other hand reported that the results were relatively unaffected by the value of a_f , however they performed their crack nucleation testing with 1 mm thick samples. Natural rubber is the best characterised elastomer, but it can behave quite differently to other elastomers. In particular, natural rubber strain crystallises which improves the fatigue life. It also has a good fatigue life without requiring filler particles.

Kingston and Muhr (2012) performed macroscopic crack growth and crack nucleation studies on natural and styrene-butadiene rubber containing filler particles. In their experiments, unfilled natural rubber had a small and invariant effective flaw size (10 – 50 μm), as also observed by (Choi and Roland, 1996; Lake and Thomas, 1967), whereas the effective flaw size of the *filled* natural and styrene-butadiene rubbers varied with applied strain. At large strains (> 200%) the effective flaw size was greater than 200 μm , though at low strains it was similar to the invariant natural rubber flaw size, 10 – 15 μm . They concluded that when fatigue life is low, steady-state crack growth rate may not be a valid

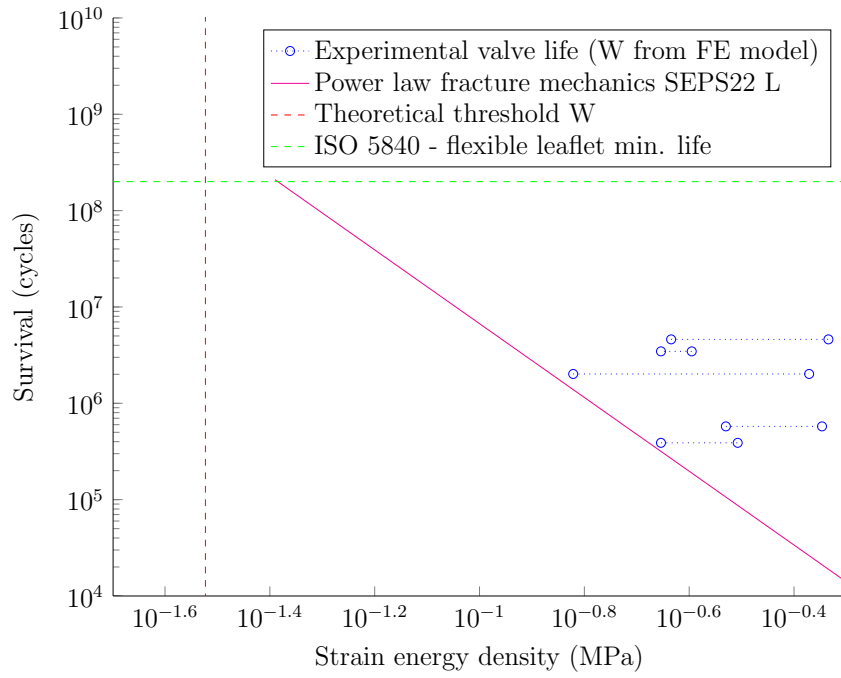


Figure 7.7: The power law SEPS22 fatigue model plotted together with the predicted maximum strain energy density in the failed valves as predicted from the FE model. Each valve consists of two points: the strain energy density was calculated based upon $(TPG_d)_{10}$ and upon $(TPG_d)_{MAX}$. The ISO 5840 standard for the minimum valve lifetime is plotted, as well as the theoretical threshold strain energy density, based upon $T_0 = 0.02 \text{ kJ m}^{-2}$, $k_g = 2.5$, and a constant effective flaw size of $250 \mu\text{m}$ (see Section 7.4.2 for more information).

assumption for filled materials (Kingston and Muhr, 2012).

Despite not being a “filled” rubber - in the conventional sense of the word - the PS BCP tested here have large effective flaw sizes. Such behaviour has been associated with conventional filled elastomers at high strains. A full fatigue model would require a non-steady state crack growth, and a greater range of strain energy densities to be considered.

It was not possible - in a reasonable time period (less than 1 month) - to achieve statistically significant measures of fatigue life greater than 5×10^5 cycles in a crack nucleation study. Thus it was not possible to validate whether the BCPs had a smaller effective flaw size at lower strain energy densities. Further work would require the testing equipment to be able to operate at higher frequencies.

In future, the crack growth rate and crack nucleation tests will need to be run at lower strain energy densities. This would move out of the power law region of polymer crack growth, and into region (2), according to Figure 2.8. When the tearing energy is less

than T_0 , and in the absence of ozone, the crack growth rate tends to zero, and fatigue life becomes infinite. In region (2), crack growth follows:

$$\frac{dc}{dN} = A \left(\frac{T_{max} - T_0}{T_{ref}} \right) \quad (7.2)$$

where T_{ref} is generally taken to be 1 kJ m^{-2} (Mars and Fatemi, 2003), and A is a material parameter. T_0 is thus the maximum tearing energy for theoretical infinite fatigue life. Physically, T_0 corresponds to the energy required to break monomer-monomer bonds at the crack tip, and is controlled by the number of monomers between crosslinks and the monomeric bond strength. Experimental data found T_0 to be between 0.02 and 0.07 kJ m^{-2} for a variety of rubbers. The similarity between materials was probably due to the monomer bonds being of the same type (C–C) (Lake and Thomas, 1967). If the threshold tearing energy, $T_0 = 0.02 \text{ kJ m}^{-2}$, is converted to a uniaxial strain energy density using Equation (2.12), the minimum threshold strain energy density can be calculated. Assuming that the geometric parameter $k_g = 2.5$ and the effective flaw size was constant, $250 \mu\text{m}$, gave W_0 approximately equal to 0.03 MPa . This value provides a theoretical lower limit for the strain energy density for infinite fatigue life, and is plotted on Figure 7.7.

In Figure 7.7, the experimental valve lifetimes are all greater than the predicted lifetimes, regardless of whether $(TPG_d)_{10}$ or $(TPG_d)_{MAX}$ is used to predict the strain energy density in the valve. This difference cannot be attributed to the difference between the constitutive relation used in the FE model and experimental data, as shown in Figure 7.2b, as this disparity predicts that the strain energy density in the FE model should underestimate the actual strain energy density.

The disagreement is likely to be a result of the difference in volume between the tensile bars used to determine the effective flaw size and the region of high stress along the stent-leaflet boundary. The likelihood of finding a flaw above the critical size is much greater for the tensile bars as they had a volume of approximately 60 mm^3 , where as the elements along the stent-leaflet boundary occupied a maximum of 3 mm^3 . I also attributed the longer-than-expected valve lifetimes to the smooth finish of the valve moulding tool in comparison to the mould used to form the compression moulded tensile bars for fatigue testing.

The power law model predicts that the ISO standard may be reached for this valve design with a strain energy density greater than T_0 . The predicted maximum strain energy density for the *designed* valves with *actual* and *optimised* orientation predicts a lifetime of 3×10^7 and 1×10^8 , respectively. Though closer to, these do not exceed the

ISO standards, so indicate that, if the fatigue models are correct, further optimisation of leaflet form and thickness are necessary. Generally, the fatigue curves diverge (upwards) from the power law model before reaching T_0 , increasing the likelihood that the valves may survive.

In Chapter 2 material cyclic fatigue was compared based upon the power law model. Figure 7.7 shows that the power law model may be valid when the ISO standard is reached (noting that the model has not yet been validated past 5×10^6 cycles). This indicates that it was appropriate to use the power law model to compare fatigue life to select materials to produce for successful heart valves.

I found it surprising to discover that the effective flaw size was so large for the BCP. In conventional rubbers, such as natural rubber and styrene-butadiene rubber, the largest flaws arise due to the presence of fillers. The BCP does not contain carbon black filler which would normally be approximately $200 \mu\text{m}$, from which flaws can often grow to cracks (Mars and Fatemi, 2002), and so I hypothesised that BCP flaws were due to non-homogeneous orientation and frozen-in stresses during cooling.

To investigate these hypotheses I performed a high resolution SAXS mapping of a tensile bar sample and polarised light stress analysis, which I followed by cyclic fatigue testing. Using the same methods previously described, tensile bar samples with parallel orientation were scanned using the Bruker Nanostar SAXS. Peak width was used as a measure of the quality of orientation.

SAXS is based on scattering of X-rays from crystal planes. As such, the orientation of planes with respect to the beam's angle of incidence can affect the amount of scattering. Nevertheless, all three samples shown in Figure 7.8 (d, e, and f) were found to be inhomogeneous in their orientation quality.

I also took photoelastic images of the same samples when they were strained. When polarised light is passed through some materials the electromagnetic wave components are resolved along the two principle stress directions and each component experiences a different refractive index. The two components interfere, leading to a photoelastic fringe pattern. The relative retardation of the components is a function of the stress in the material.

The photoelastic images are shown in Figure 7.8 (a, b, and c). There is a variation in colour across the tensile bar samples, indicating that the stress state also varies. After imaging, the samples were cyclically strain until failure. The point at which they failed is marked upon the images. In sample (b) the failure point is certainly at a stress concentration. In samples (a) and (c) there may be stress concentrations associated with

the failure point. Stress and orientation quality do not appear to match one another. Future work should involve annealing the polymer to reduce frozen in stresses.

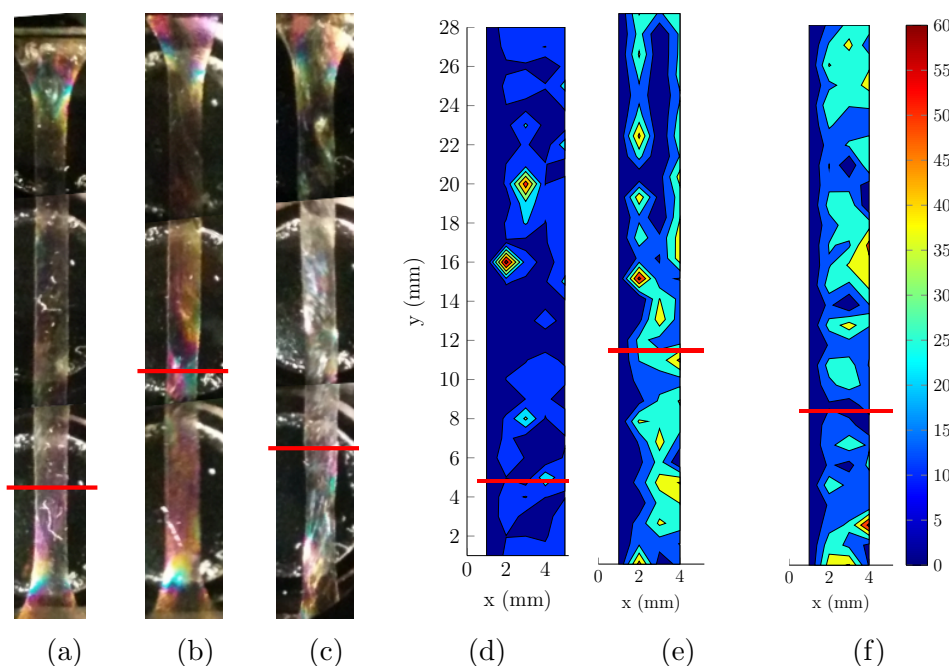


Figure 7.8: (a), (b), and (c): Birefringence of strained SEPS22 samples marked (-) with the point at which fatigue failure occurred. Failure occurred for samples (a), (b), and (c) after 2809, 6977, and 8104 cycles, respectively. (d), (e), and (f) are the SAXS peak width maps of the same SEPS22 samples, unstrained and before fatigue testing. The peak width is measured in degrees, so the maximum peak width was 60° .

Dr Stasiak performed light microscopy of solvent cast samples, and samples injection moulded in the aluminium moulds in Chapter 6. A selection of these images are shown in Figure 7.9. Both the compression (a) and injection (b) moulded samples have visible surface features with dimensions of approximately $10\text{ }\mu\text{m}$. The parallel features on the injection moulded samples probably originate from the machining of the mould. The solvent cast material (c) appears to have a much smoother surface. The large surface flaws on the moulded samples are likely to have increased the effective flaw size.

7.5 Conclusion

The final valve was tested for hydrodynamic and fatigue performance *in vitro*. The valve had acceptable hydrodynamic performance, in accordance with ISO 5840, and was superior to the prototype valves tested in Chapter 5. The effective orifice area of the 23 mm valve was $1.59 \pm 0.02\text{ cm}^2$, and regurgitation was $8.71 \pm 0.99\%$. The fatigue performance

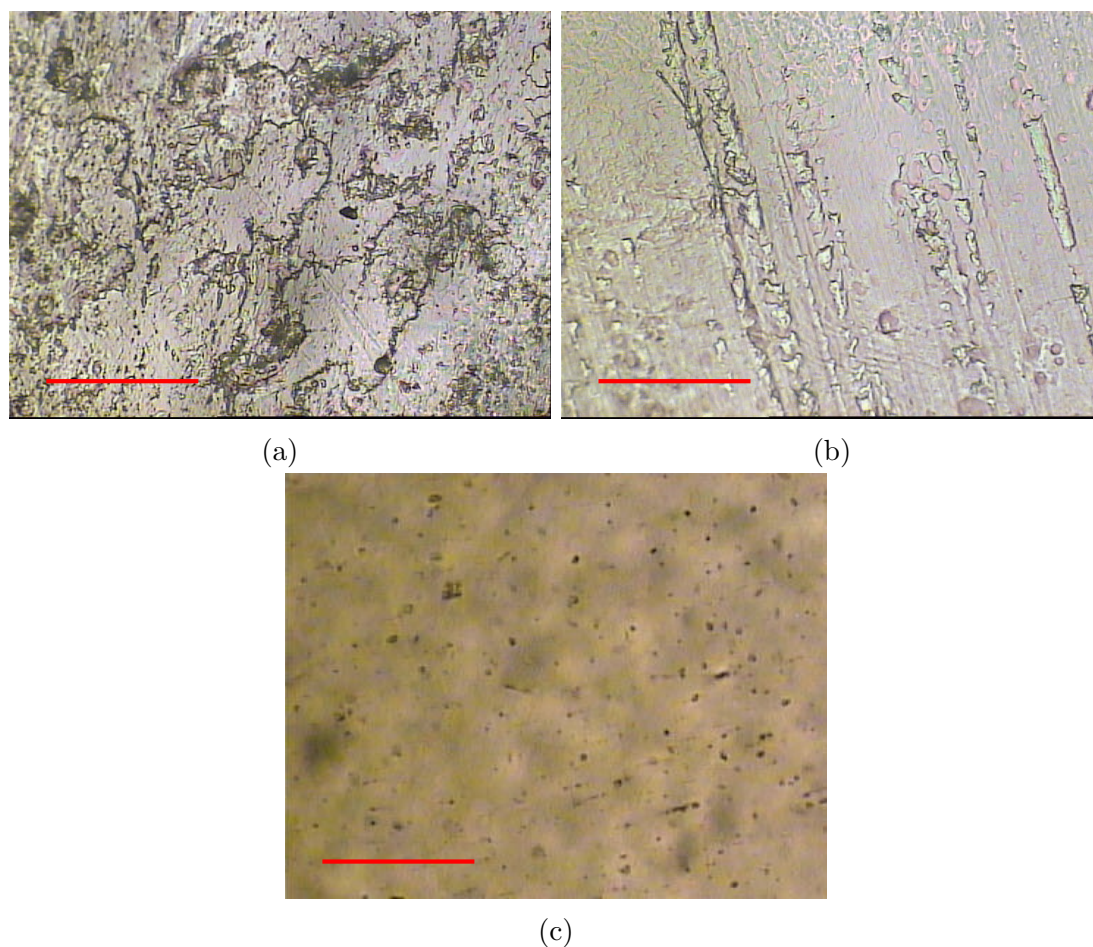


Figure 7.9: Light microscopy of the surface of SEPS22 processed into sheets by (a) compression moulding, (b) injection moulding, and (c) solvent casting. The red scale bar indicates 100 μm .

was unacceptable for a flexible leaflet valve, as the valves only survived for approximately 4×10^6 cycles at 100 mmHg.

Tears in the leaflets of the valves were concentrated at the leaflet stent boundary, where inaccuracies in tool manufacture had led to a thinning of the leaflets. A FE model of the *designed* and *actual* valve geometries, with the actual PS cylinder orientation used in both cases, was used to assess the strain energy density when loaded during diastole. The strain energy density was compared to an experimental fatigue model for the material.

Based upon a power law for the growth of cracks, I constructed fatigue models for SEPS22 strained parallel and perpendicular to the PS cylinders, and isotropic SEPS22. The effective flaw size was determined using crack nucleation tests. The fatigue of oriented PS BCP was anisotropic because fatigue life varies according to whether strained parallel or perpendicular to the PS cylinders. The effective flaw size of SEPS22 was considerably larger than that of natural rubber, possibly indicating that microphase-separating BCPs

behave like filled elastomers.

Combining the absolute fatigue model and FE simulations led to a predicted fatigue life of 5×10^5 cycles for the *actual* valve at 100 mmHg, which was significantly lower than recorded value, although in remarkably good agreement given the simplifications inherent in the model. The maximum strain energy density in the *designed* valve was considerably lower, and the predicted fatigue life of a correctly moulded valve could reach 1×10^8 cycles. This, however, is beyond the validated range for the fracture mechanics model.

Chapter 8

Concluding remarks

8.1 Conclusions

The ideal prosthetic heart valve has lifelong durability without the need for anticoagulant therapy. A prosthesis must contend with a complex biological, chemical, and mechanical environment, and for a valve design to be successful, the intrinsically connected triad of materials, processing, and valve form must work in harmony.

Since the early years of cardiac surgery polymers have been candidate materials for use in the ideal prosthetic heart valve, but none have yet succeeded. The choice of material informs the design, and so design optimisation must start with being able to select *optimal* materials. Acceptable durability and haemodynamics in a prosthetic heart valve invokes the use of materials that are both durable and flexible.

I presented a set of criteria based upon chemical stability and mechanical properties for selecting materials for use in a polymeric prosthetic heart valve. A material performance index uses the leaflet's thickness as the design variable, while the material properties of modulus and fatigue stress are combined in the ratio $\frac{E_{flex}}{\sigma_f^3}$, such that superior materials have a lower performance index. For the rapid evaluation of new materials I proposed the use of fracture mechanics methods for the prediction of the cyclic fatigue stress, σ_f , which enables evaluation of the mechanical properties in up to two days.

The method is a general and quantitative means of rapidly assessing materials for use in a polymeric prosthetic heart valve, and could also be used for other applications requiring both flexibility and durability. Although valve design is driven by the choice of material, this method allows design and material to be de-coupled, making screening quicker and more efficient.

The native heart valve has a collagen architecture which contributes to its durability. The anisotropy of collagen has inspired other researchers to embed strong fibres into polymer leaflets, but these have failed due to delamination and dehiscence. I proposed that a set of block copolymers (BCPs) which self-assemble at the nano-scale to form stiff PS cylinders in a rubbery bulk and can be processed to yield mechanically anisotropic materials which could mimic the anisotropic properties of the native heart valve.

I tested the stability of a shortlist of BCPs under accelerated degradation conditions (ISO 10993:13). This indicated that the unsaturated BCPs (SIS18, SIS30, and SI/BS19) were more susceptible to degradation. The saturated BCPs (SIBS30, SEBS20, SEBS29, and SEPS22) met the *in vitro*, qualitative requirements of ISO 10993:13 for long term implantable materials.

I evaluated the mechanical properties of the polymers to generate the material performance index. The saturated BCPs could be ranked in increasing order of preference as: SEBS20, SEBS29, SEPS22, and SIBS30. Unfortunately, SIBS30 suffered from severe shrinkage during moulding which led to visible flaws, and so it had to be eliminated from the shortlist. When PS cylinders were well oriented SEPS22 and SIBS30 had superior performance indices relative to a reference polyurethane material that had previously been tested for prosthetic heart valve leaflets. As a consequence, SEPS22 was selected for further testing and use in valve design.

A review of the literature showed a wide range of leaflet designs for polymeric prostheses, two were selected for detailed evaluation. One of these was based upon *cylindrical* surfaces (Burriesci et al., 2010), and the other based upon *spherical* surfaces (Zaffora, 2011). Prototype valves were injection moulded from SEPS22 and their hydrodynamics tested *in vitro*. The cylindrical valve had a greater effective orifice area but unacceptable regurgitation. The spherical valve had a lower effective orifice area, but less regurgitation and, in total, a lower energy loss over the valve. Only the spherical form valve complied with the prosthetic heart valve International Standard for hydrodynamics (ISO 5840), and so this design was selected for use in the final valve. The design was improved by increasing the thickness of the stent posts which reduced their deflection during diastole. In terms of hydrodynamics, I acknowledge that the polymeric prostheses were inferior to a similarly sized Perimount Magna reference bioprosthesis, which could be addressed in future.

In the experiments that I performed, when the thickness of leaflets made from SEPS22 (without optimised orientaiton) was greater than 325 μm , all three leaflets did not consistently open at flow rates greater than or equal to 21 min^{-1} , so the leaflets were designed with a thickness of 300 μm . The hydrodynamic results for the spherical valve also in-

licated that the maximum transvalvular pressure gradient during opening was strongly correlated with the thickness of the leaflets near to the commissures. Although variations in thickness across the leaflet were beyond the scope of this thesis, this provides an interesting direction for further optimisation of the leaflet design.

Injection moulding was proposed as a means to orient the stiff PS cylinders and thus manufacture the prostheses with a bioinspired orientation. Thin discs of cylinder forming BCPs were injection moulded isothermally. Using small angle X-ray scattering (SAXS), a novel structure in which the PS cylinders formed a layered biaxial structure, was observed. I hypothesised that this structure was formed by the force field during injection, and so determined a constitutive and orientation model for the BCP.

I characterised the rheology of the polymer melt, and made pressure measurements on the discs during injection moulding. The Giesekus and 3rd order fluid viscoelastic constitutive models provided the best description of the flow and pressure field during injection. The generalised Newtonian Carreau-Bird model also provided an acceptable description of the velocity field. The third order model was not available in the FE software, and the Giesekus model was not stable over the range of processing conditions, so I selected the Carreau-Bird model to describe the velocity field. I proposed that the ratio of shear-to-extensional deformations ($C_s = \frac{\dot{\gamma}}{\dot{\epsilon}}$) could be used to predict the layered biaxial orientation during point injection of discs, with shear resulting in orientation in the direction of flow and extension resulting in orientation perpendicular to flow.

Nine discs were injection moulded and the ratio of radial to circumferential orientation was assessed using SAXS. Based upon a comparison of the flow field and the SAXS data, a constant critical value of $C_{sC} = 3$ correctly predicted orientation in 85% of the samples (by volume). In more complex shapes, such as the heart valve, the model was an acceptable predictor of biaxial orientation.

A combination of modelling (using the Carreau-Bird model and shear-extension ratio) and bench-scale injection moulding was used to determine a point at which to inject the valves. Three injection scenarios were considered: injection from the commissures, along the full length of the free edge, and from points at the centre of the free edge of each leaflet. Injection from the centre of the free edge of each leaflet allowed a bioinspired orientation to be produced (which was mapped using SAXS). Low flow rates led to a layered biaxial structure which mimicked the major bundles of collagen across the leaflet and interconnections between the bundles. At high flow rates, the critical regions of the leaflet (at the stent-leaflet boundary) contained PS cylinders in the optimal orientation which, according to the FE model, reduced the average and maximum stresses in the valve relative to the isotropic case.

The haemocompatibility of BCPs of types SI/BS19, SIS30, SIBS30 and SEPS22 were assessed in comparison to expanded polytetrafluoroethylene (ePTFE), polyester (PES), and bovine pericardium (BP) graft materials. Haemocompatibility was assessed by rotating them in modified Chandler loops at physiological shear rates, while in contact with fresh human blood. In measures of coagulation and thrombogenicity, the BCPs were better than PES, but worse than ePTFE and BP. In measures of inflammation, the BCPs and ePTFE were better than PES and BP. A heparin coating was applied to SEPS22, that improved the material and made it superior to all of the reference materials in terms of coagulation, thrombogenicity, and inflammation.

The durability of the heparin coating was tested by dynamically straining the material in buffered solution for 3 weeks. XPS and water contact angle measurements indicated that there was only a small loss of heparin from the surface. However, immersion in an oxidising solution did lead to destruction of the coating. The direct contact viability of murine fibroblasts (L929) upon SEPS22 and heparin coated SEPS22 was superior to PTFE, PES, BP, and the control samples. With respect to haemocompatibility and cell viability, uncoated SEPS22 would be satisfactory, but coating with heparin would make it an excellent material for use in the prosthetic heart valve.

The crystallisation of calcium-phosphate on the native heart valve, bioprostheses, and polymeric prostheses can cause their failure. The candidate BCPs were tested using a device which flexed the materials while they were submerged in calcifying solution. The BCPs calcified less than the glutaraldehyde-fixed pericardium reference, but calcification was shown to increase the flexural stiffness of statically calcified polymers, and accelerate failure of the BCPs when they were dynamically flexed.

Surprisingly, heparin coating improved the durability of SEPS22 in both calcifying and non-calcifying solutions. Despite the high electronegativity of heparin, it also led to a small reduction in calcification. The higher surface roughness of uncoated SEPS22 may account for this difference. Contrary to earlier hypotheses (Imachi et al., 2001), I found that calcium-phosphate crystals did not localise to surface cracks.

Two sizes of aortic prosthesis were manufactured by injection moulding, for use with aortic root annulus diameters of 21 and 23 mm. The valves were tested *in vitro* according to ISO 5480 with a sample size of three. The effective orifice area of the valve was $1.59 \pm 0.02 \text{ cm}^2$, which was greater than the standard 1 cm^2 . Regurgitation was 8.71 ± 0.99 which was less than the 10% maximum. Seven valves survived approximately 4×10^6 cycles at 100 mmHg, which was less than the minimum standard of 2×10^8 cycles. Therefore hydrodynamics were satisfactory, but durability was unacceptable. The leaflets of the valve were thinner than intended (due to inaccurate tooling), which was a

major contributor to the premature fatigue failure.

My study of crack nucleation indicated that the effective flaw size was several orders of magnitude larger than expected. Large effective flaw sizes have also been recorded for filled rubbers, suggesting that the phase-separated PS domains have an effect similar to that of filler particles. Frozen-in stresses were identified in compression moulded polymers, and non-homogeneous orientation was also observed. Both contributed to the concentration of stresses and growth of flaws.

By extrapolating the fatigue prediction and using the results of FE analysis, I predicted that correctly manufactured polymeric valves could theoretically reach 3×10^7 cycles. Furthermore, if the orientation could be optimised, 1×10^8 cycles could be reached. These values are short of the ISO 5840 standard for flexible leaflet valves but, crucially, this prediction is based upon a logarithmic extrapolation of the fracture mechanics model so lifetimes may be greater than predicted as the strain energy density approaches the threshold value for crack growth. Understanding of the failure mechanisms is still at an early stage, indicating that further work is required, first, to reduce the strain energy density in the leaflet, and second, to validate the fatigue model at lower strain energy densities. This work has definitely established that there is still potential for bioinspired polymeric prostheses to overcome the issues of durability and need for anticoagulation with further development.

8.2 Further work

The next stages in development of a polymer prosthetic heart valve should focus on increasing durability to a level equivalent to ten or more years operation in a person. In the following sections, I present strategies for improving durability of the valve and SEPS22 BCP material. I will go on to detail several necessary, interesting, and potentially fruitful avenues for investigation.

In parallel with the valve development, future work should monitor the progression of other solutions to heart valve disease. In particular, the arrival of new oral anticoagulants could reduce the drawbacks associated with mechanical heart valves. Some of the latest oral anticoagulants have been licensed by the FDA with the potential to supersede warfarin. The thrombin inhibitor, dabigatran; and factor Xa inhibitors, rivaroxaban, apixaban, and edoxaban. In the case of dabigatran, it is contraindicated for use in patients with mechanical heart valves after a trial of 252 patients was halted due to an excess of ischaemic strokes and bleeding events (Yeh et al., 2015).

To overcome the durability issues associated with bioprostheses, new processing methods were developed and implemented in the early 2000s. *In vivo* durability data is still being collected on these valves. Improvements are anticipated and the recommended age for a bioprosthesis could fall further below the current 60 years (Vyavahare et al., 1997a).

The greatest shift in prosthetic heart valve technology in the past decade has been to transcatheter implantation. Most recently, TAVI has shown benefits in comparison to surgical replacement in low-risk, as well as high-risk patients older than 70 years (Thyregod et al., 2015). Once safety is shown to be sufficient for younger patients to receive TAVI, then data can be collected on the actual durability of valves. Modelling suggests that crimping the tissue reduces the lifetime by 50% (Martin and Sun, 2015). Polymeric materials have the potential to overcome the issues of durability in transcatheter bioprostheses, but the effects of crimping will need to be tested.

8.2.1 Valve design

I concluded Chapter 7 with the prediction that a valve manufactured with uniformly thick leaflets, could allow the valve to reach 3×10^7 cycles at 100 mmHg for the *actual* orientation and 1×10^8 cycles if the *optimised* orientation of PS domains were achieved. Accelerated testing should be used to verify such long lifetimes.

In order to reach the ISO 5840 minimum lifetime, I predict that the maximum strain energy density in leaflets made from oriented SEPS22 will need to be reduced to below 0.04 MPa. This assumes that the power law model provides a minimum limit to the lifetime, which is a good assumption when the threshold strain energy release rate, T_0 , is approached. The maximum strain energy density should also occur at a point in the valve where the principal strain direction is aligned with the PS cylinder orientation.

In order to achieve the predicted minimum lifetime a number of aspects warrant further investigation. The threshold strain energy density has only been calculated theoretically. To determine this experimentally will require tensile and fatigue testing equipment that can reach frequencies higher than 1 Hz. Further fatigue testing of the material will also reveal whether the effective flaw size varies with strain for phase separating BCP, and thus improve the accuracy of the fatigue model.

During my testing of the BCP in aqueous solutions, I observed under SEM a surface mud-cracking pattern. Further investigation of this effect is recommended as it may play a role in the formation of flaws in the material.

Strain energy density in the valve was evaluated using FE simulations, but the material

model lacked a memory component. A more accurate lifetime prediction will be possible once strain memory (a form of the Mullins effect) is incorporated. Leaflet thickness is the primary determinant of strain energy density in the leaflet, and the pressure required to open the valve. In this thesis, a maximum leaflet thickness was determined by extrapolation from hydrodynamic testing, but this thickness did not result in an adequate lifetime for the valve. Incorporating fluid-structure interactions into a hyperelastic, viscoelastic, anisotropic FE model is a large step for modelling, but would allow the maximum leaflet thickness to be determined.

Alternatively, improving the accuracy of the material lifetime model and valve strain energy density constitutive equation would allow the current FE model of diastolic loading to determine a minimum leaflet thickness, which could then be tested *in vitro*.

In Section 5.3.1 I evaluated the effect of variations in thickness across the leaflet on the pressure required to open the valve. The thickness at the commissures of the spherical valve was found to have the most influence on the valve opening. There are likely to be strong benefits from optimising spatial variations in the leaflet thickness, which could be performed using FE modelling, but would require a fluid-structure interaction model needed to simulate the opening of the valve.

8.2.2 Materials and processing

In Chapter 2, the BCP SIBS30 could not be selected because of cracking and shrinkage which occurred during melt processing. However it had the best material performance index so its deficiencies should be investigated. If higher temperatures could be used during injection moulding, possibly by using a nitrogen atmosphere to reduce oxidation, it may be possible that a lengthy annealing process could reduce the shrink-associated cracking. A longer annealing process would also be likely to benefit the SEPS22 material, in which stress concentrations were evident.

In Chapter 6 I reported a novel biaxial orientation phenomenon. While this was not pursued for the final injection, it would be of considerable interest to investigate the fatigue properties of the layered material. Furthermore, I drew many analogies between the PS cylinder BCP and conventional short-fibre filled composite polymers. In particular, the biaxial orientation may also be modelled using the Tucker-Folgar equation. The Tucker-Folgar equation contains parameters used to describe the aspect ratio of fibres and the strength of interactions between the fibres, which I would expect to be quite different for the BCP in comparison to conventional composites (Advani, 1987; Chung and Kwon, 2002; Park and Park, 2011).

To achieve mechanical anisotropy in the materials used in this thesis, I employed a BCP which phase separated. Further improvement of the materials might be possible by investigating the association between material performance and molecular architecture. In particular, molecular weight is a strong determinant of polymer mechanical properties, and may influence the modulus and fatigue life differently, thus allowing the material performance index to be improved. It would also be worthwhile to assess the performance index of the BCP materials once they have been chemically crosslinked (Ducrot et al., 2014).

Microphase separation in BCP leads to a form of physical crosslinking, in this case between PS domains. Crosslinking is greater in a triblock copolymer relative to a diblock copolymer, as the links are domain-bulk-domain, rather than just domain-bulk. Considering an ABA triblock copolymer, where A forms cylinders or spheres in a bulk of B; each single chain starts in a cylinder, enters the bulk, and may either bridge to another cylinder, or loop to the same cylinder, as illustrated in Figure 8.1. The proportion of chains which display bridging is approximately 37 to 50% (Karatasos et al., 2000).

Drolet and Fredrickson (2001) investigated whether the bridging fraction could be increased in pentablock copolymers (ABABA) to improve BCP toughness. They performed a theoretical optimisation of the bridging fraction when the size of the central block (ABABA) is varied while keeping the total ratio of block A to B constant. As the ratio of central block to end blocks was increased, the bridging fraction increased from 0.25 to 0.67. If SEPSEPS could be synthesized (instead of SEPS), it may be possible to improve durability.

If crosslinking is used to improve durability, it is important to check whether the modulus is changed, and thus whether the material performance index is improved. It is certainly possible that when some materials are crosslinked, the toughness can be increased with no change in stiffness. Li et al. (2014) tuned the chain length of hybrid alginate-polyacrylamide hydrogels to produce materials with a higher fracture energy without changing the elastic modulus.

Much of my thesis has been based upon mimicking the anisotropy of the native valve. In a slightly different approach, the strain dependent mechanical properties could be mimicked. In particular, opening and closing a valve only requires small leaflet strains, but loading a valve during diastole leads to greater strains. The native valve has a highly non-linear stress-strain response, as shown in Figure 1.8. Once the strain reaches 8%, the leaflet's stiffness increases up to 300-fold. Copying this non-linear stress-strain behaviour could produce an optimal valve.

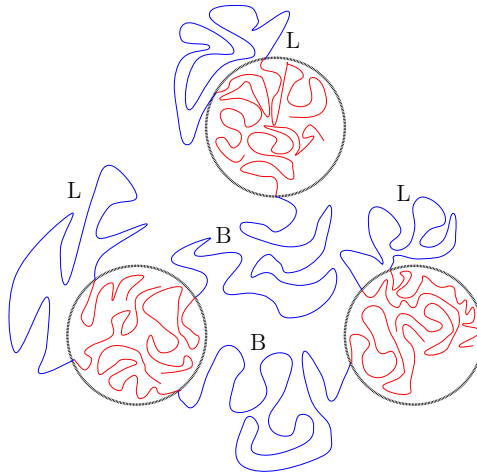


Figure 8.1: Bridging (B) and looping (L) in ABA triblock copolymers.

Textiles have been proposed for prosthetic valves as they are easy to bend, but strong when loaded in tension. Unfortunately they failed due to textile wear and tissue ingrowth (Heim et al., 2014). A possible alternative could be the use of liquid crystal elastomers, which could be tuned to be isotropic when unstrained and become nematic upon strain. For example, with the aim of making general tissue replacement materials, Agrawal et al. (2013) coupled liquid crystal mesogens to poly(hydrogenmethysiloxane), the materials hardened under dynamic compressive strain.

Appendix A

Valve development flow chart

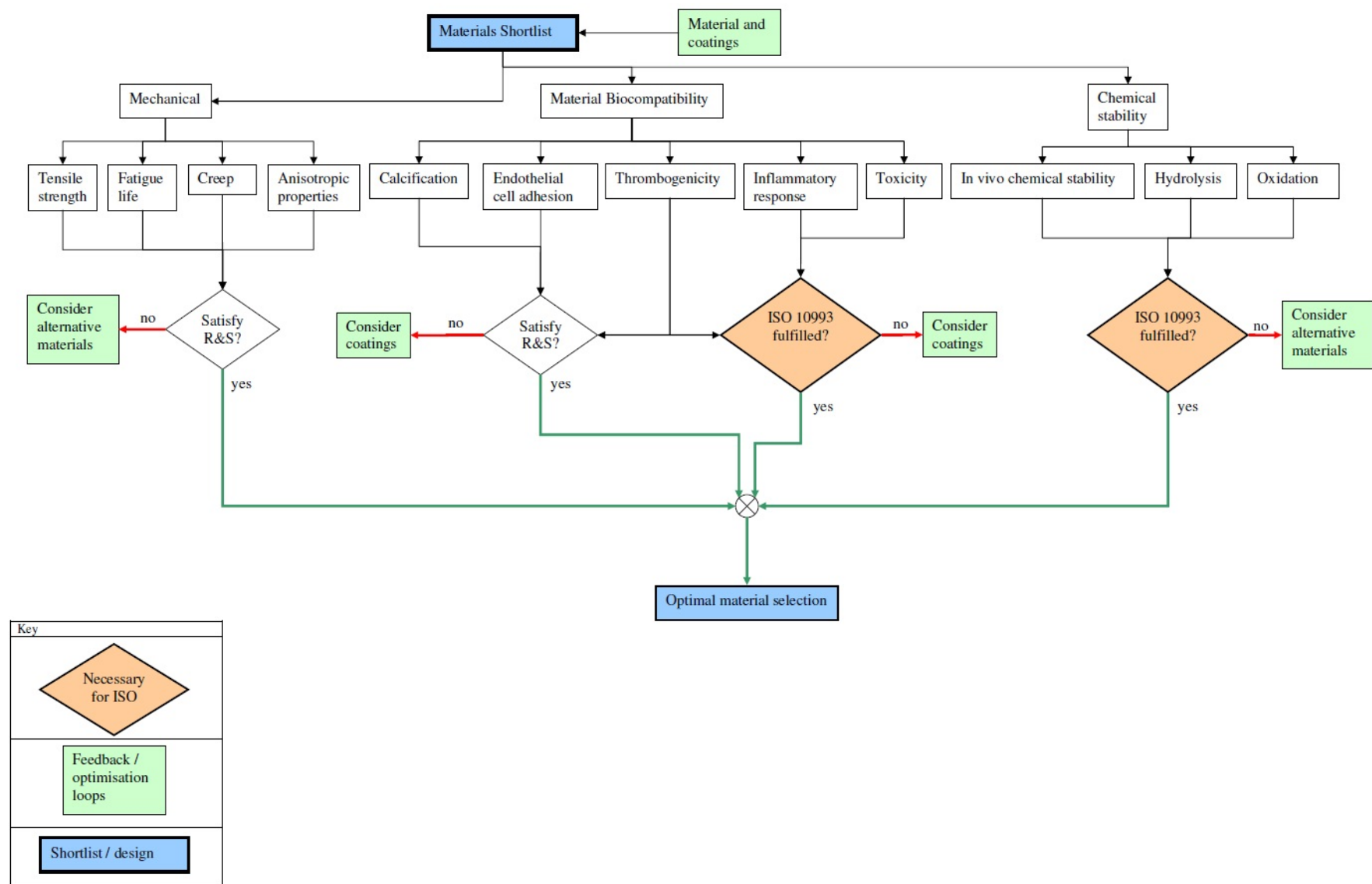


Figure A.1: Flow chart for the selection of a polymeric material for use in a prosthetic heart valve.

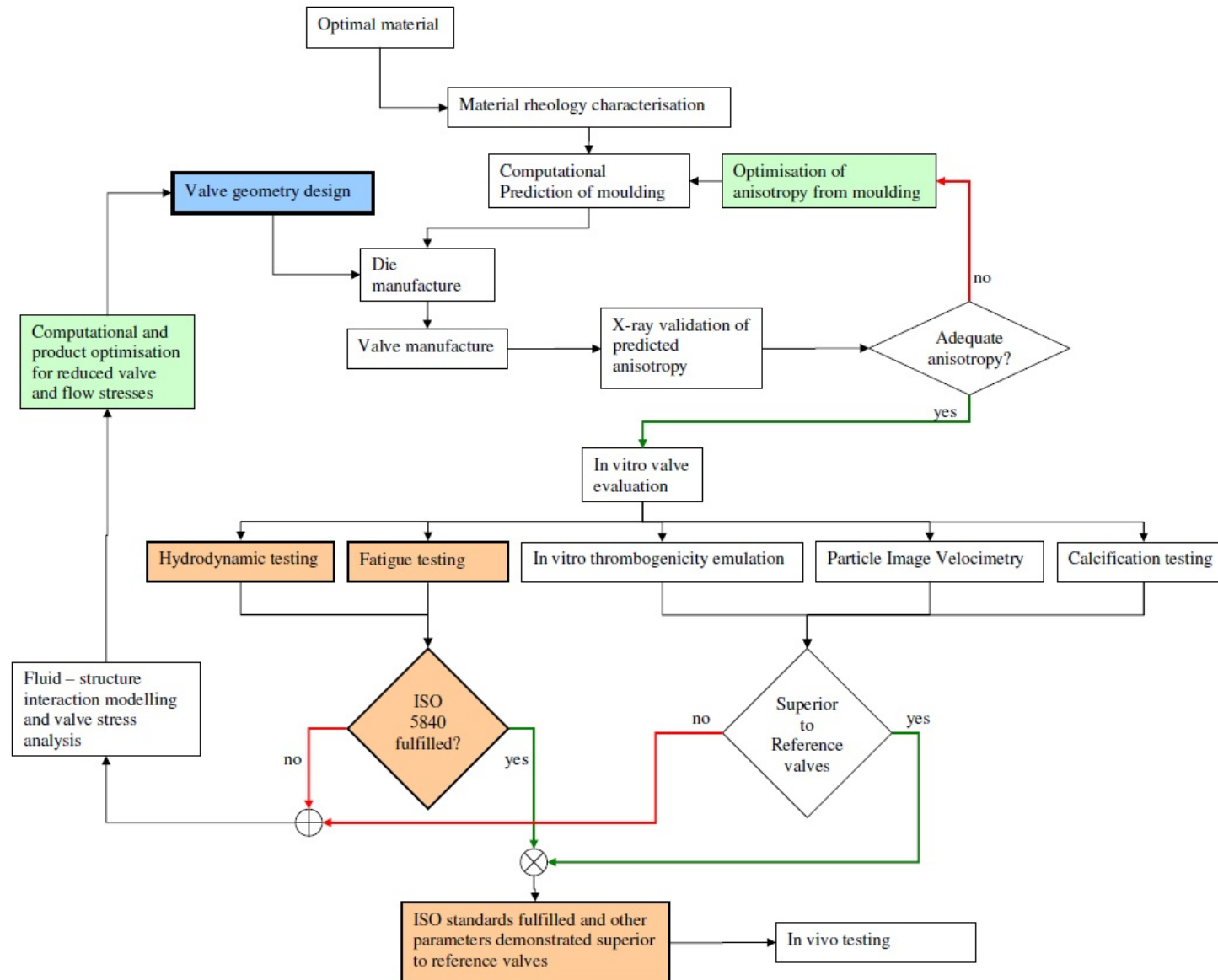


Figure A.2: Flow chart for the design of a polymeric prosthetic heart valve.

Appendix B

Derivation of performance indices for material selection

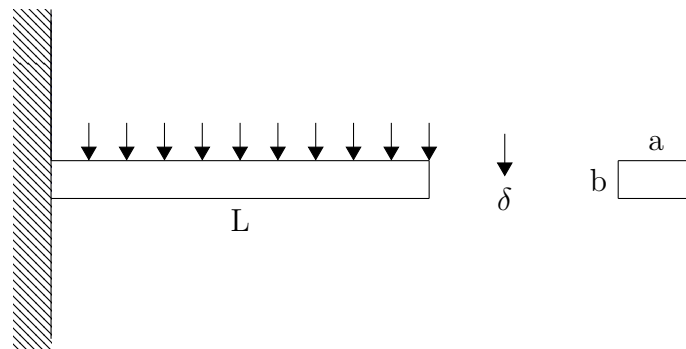


Figure B.1: Schematic of a uniformly loaded simple beam, with a fixed end. The beam has length L , width a , and depth b . The deflection when loaded is δ .

Given the task of designing an aeroplane wing. The wing might be thought of as a simple beam which is fixed at one end, and is uniformly loaded along its length, as indicated in figure B.1. As a designer (and a passenger!) my primary concern is that the tip of the wing does not deflect too much. A large deflection would be likely to disrupt the aerodynamics, and in the worst case might even cause the wing to fail. The deflection of the wing might be expressed using equation B.1, where δ is the deflection at the unsupported end, P_w is the load which is uniformly distributed across the wing, l is the length of the wing, E is the Young's Modulus of the material and I is the second moment of area of the wing, which, for a simple rectangular wing (for the sake of simplicity) would be $\frac{ab^3}{12}$ where a is the width of the wing and b is the depth of the wing.

$$\delta = \frac{P_w l^3}{8EI} \quad (\text{B.1})$$

Now, given the above equation, there might be several strategies available to minimise the deflection. Let us assume that the load to be supported (our plane and passengers), the length (maybe by the size of the hangar) and the width of the wing (aerodynamics) are set, which leaves us with the material stiffness and the wing's depth to alter. Our discerning designer, and passenger, would be quick point out that the weight of the wing is also quite important; too heavy and the wing must then support even more of its own weight. The weight of a simple rectangular wing is:

$$W = abl\rho g \quad (\text{B.2})$$

where ρ is the density of the material and g is the constant of gravitational acceleration. Like baggage weight limits, there is a wing weight limit and so when combined with our previously constrained variables, the product $b\rho$ becomes equal to some constant. Equations B.1 and B.2 can now be combined in equation B.3, with the set parameters and variable parameters grouped:

$$\delta = \frac{2P_w l^6 a^2 g^3 \rho^3}{2W^3 E} \quad (\text{B.3})$$

Equation B.3 tells us that if compare 2 materials, if one is more dense, then a wing made from this material must be thinner. For the thinner wing to achieve the same deflection that material must be stiffer. If we group together the set parameters and the deflection we have a bundle of 'design' terms which amount to a *performance index*, I_W .

$$I_W = \frac{\rho^3}{E} \quad (\text{B.4})$$

Minimising I_W would reduce deflection, or alternatively allow us to make our wing longer, or support a greater load. Based upon a physical and a mechanical property of a material we can now compare the likelihood that they would make a good aeroplane wing. Furthermore, if we wanted to search the complete material space, we could plot all materials on a graph of $\log E$ versus $\log \rho$. On such a graph, with logarithmic scales, we could draw lines of gradient 3 upon which materials with equal I_W would lie. The free searching method is delightfully elegant, but we must be mindful that design can rarely be bundled into 2 or 3 material properties, and other, often qualitative measures must also be considered.

Appendix C

Construction of the final valve

Table C.1: Steps in the construction of the final spherical valve geometry

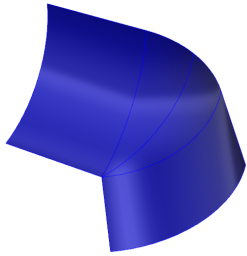
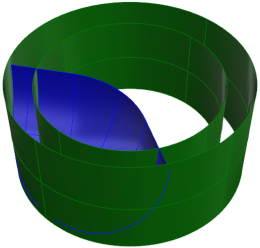
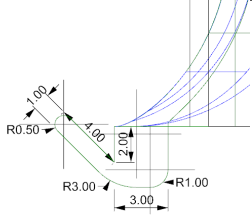
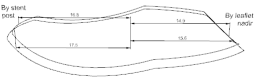
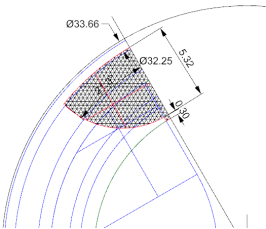
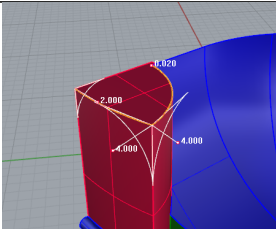
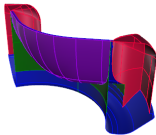
	Sphere of radius equal to TAD
	Sphere centre located on $r_{TAD} + \sin(d_{com})$
	$StentID = TAD$, $stentOD = r_{TAD} + 3$
	Sewing ring design, giving maximum ESRD=33.66 mm

Table C.1 continued.

	<p>The outer edge of the sewing ring skirts the outside of the stent with a 1 mm of clearance, and the leaflet nadirs with 2 mm of clearance. This minimises the sewing ring area whilst allowing space for suturing.</p>
	<p>Half stent cross section design. Leaves 1 mm radial space to the edge of the SR. Each stent occupies 42.6°. A minimum of space is left between the stent edge and the commissure to promote opening whilst providing a tight seal during closing (0.1 mm).</p>
	<p>Fillets: 0.02 at commissure, to 4 mm, to 2 mm at stent post centre. 1 mm down radial corners</p>
	<p>The aortic surface of the valve is mirrored, repeated rotationally, and then <i>closed</i>. The body is then <i>shelled</i> to produce a constant thickness leaflet which extends to the stent.</p>

Appendix D

Cross model

The Cross model was matched to the Carreau-Bird model for SEPS22. The Cross model viscosity is expressed as:

$$\eta = \frac{\eta_{0W}}{1 + \left(\frac{\eta_{0W}\dot{\gamma}}{\tau_W} \right)^{1-n_W}} \quad (\text{D.1})$$

Where η_{0W} , is the zero shear rate viscosity; τ_W , is the critical stress level for transition to shear thinning; and n_W , is the power law index in the Cross model. The Cross model predicts a zero-shear viscosity and transition region, and further parameters can also be implemented to account for the pressure and temperature variation of viscosity. To fit to the previously used Carreau-Bird model, Cross-WLF parameters were selected as shown in Table D.1. The Carrea-Bird and Cross model viscosities are shown in Figure D.1. For the range shown, they match well.

Table D.1: Cross model fitting parameters for SEPS22 at 150 °C

η_{0W}	$3.6 \times 10^5 \text{ Pa s}$
n_W	0
τ_W	$5 \times 10^4 \text{ Pa}$

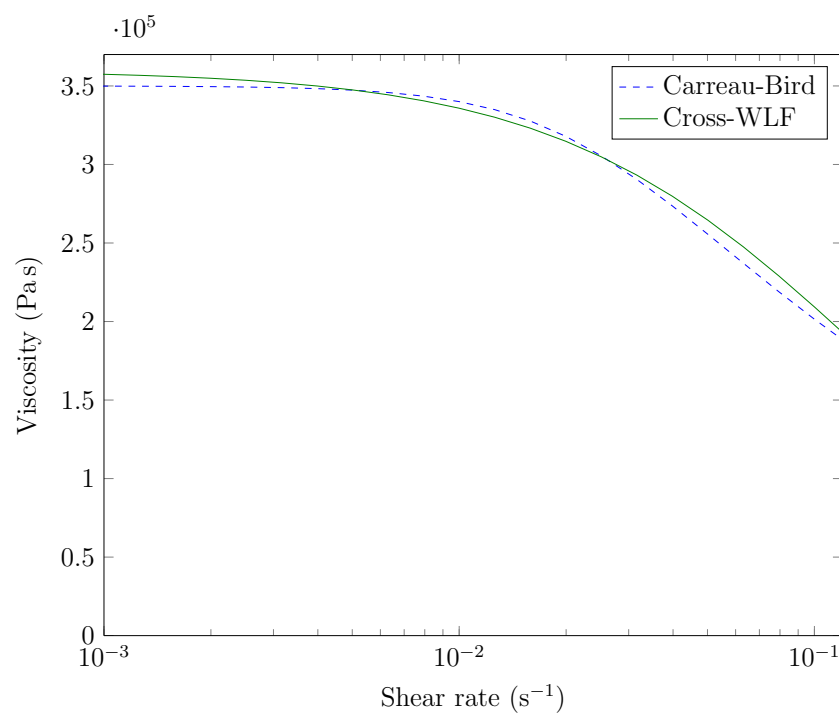


Figure D.1: Comparison of the Carreau-Bird and Cross model viscosities.

Appendix E

Mooney-Rivlin model

Mooney-Rivlin is a hyperelastic model which can be used to describe elastomer behaviour. The strain energy, ψ , is defined as follows:

$$\psi = \psi(\mathbf{C}) - p(\mathbf{J} - 1) \quad (\text{E.1})$$

Where \mathbf{C} is the Cauchy-Green tensor, p is the hydrostatic pressure, and \mathbf{J} is the volume ratio, which is assumed to equal to 1 for an incompressible material.

The strain energy can be separated into an isotropic and anisotropic portion:

$$\psi(\mathbf{C}) = \psi_{iso}(\mathbf{C}) + \psi_{aniso}(\mathbf{C}) \quad (\text{E.2})$$

For the isotropic part of the potential, the strain energy can be expressed in terms of its invariants:

$$\psi_{iso} = \psi_{iso}(I_1, I_2) = c_1(I_1 - 3) + c_2(I_2 - 3) \quad (\text{E.3})$$

Where c_1 and c_2 are material parameters.

The anisotropic contribution of ψ is expressed as:

$$\psi_{aniso} = \psi_{aniso}(I_4) = k_4 \log^2 \sqrt{I_4} \quad (\text{E.4})$$

Where k_4 is a material parameter, and the 4th invariant, I_4 takes into account the cylinders' orientation (vector \mathbf{a}):

$$I_4 = \mathbf{a} \cdot \mathbf{C} \mathbf{a} \quad (\text{E.5})$$

In summary, the strain energy function is:

$$\psi = c_1(I_1 - 3) + c_2(I_2 - 3) + k_4 \log^2 \sqrt{I_4} - p(J - 1) \quad (\text{E.6})$$

The parameters were optimised for SEPS22 to yield the values shown in Table E.1

Table E.1: Mooney-Rivlin parameters optimised for the tensile strain energy density of SEPS22

	c_1	c_2	k_4
Anisotropic	0.15	0.15	1.62
Isotropic	0.3	0.36	n/a

Bibliography

- Advani, S. G. (1987). The Use of Tensors to Describe and Predict Fiber Orientation in Short Fiber Composites. *Journal of Rheology*, 31(8):751.
- Agrawal, A., Chipara, A. C., Shamoo, Y., Patra, P. K., Carey, B. J., Ajayan, P. M., Chapman, W. G., Verduzco, R., and Rafael (2013). Dynamic Self-Stiffening in Liquid Crystal Elastomers Aditya. *Nature Communications*, 23(4):1739–51.
- Ainslie, K., Thakar, R., Bernards, D., and Desai, T. (2009). Inflammatory Response to Implanted Nanostructured Materials. In *Biological Interactions on Materials Surfaces*, chapter 18, pages 355–371. Springer US.
- Akat, K., Borggreffe, M., and Kaden, J. J. (2009). Aortic valve calcification: basic science to clinical practice. *Heart*, 95(8):616–23.
- Akins, C. W., Travis, B., and Yoganathan, A. P. (2008). Energy loss for evaluating heart valve performance. *The Journal of thoracic and cardiovascular surgery*, 136(4):820–33.
- Alexander, K., Clarkson, J., Bishop, D., and Fox, S. (2001). Good Design Practice for Medical Devices and Equipment: A Framework. Technical report, University of Cambridge and Cambridge Consultants.
- Alferiev, I., Stachelek, S. J., Lu, Z., Fu, A. L., Sellaro, T. L., Connolly, J. M., Bianco, R. W., Sacks, M. S., and Levy, R. J. (2003). Prevention of polyurethane valve cusp calcification with covalently attached bisphosphonate diethylamino moieties. *Journal of biomedical materials research. Part A*, 66(2):385–95.
- Allison, B. C., Applegate, B. M., and Youngblood, J. P. (2007). Hemocompatibility of hydrophilic antimicrobial copolymers of alkylated 4-vinylpyridine. *Biomacromolecules*, 8(10):2995–2999.
- Amado, E. and Kressler, J. (2011). Triphilic block copolymers with perfluorocarbon moieties in aqueous systems and their biochemical perspectives. *Soft Matter*, 7(16):7144.
- Amann, K. (2008). Media calcification and intima calcification are distinct entities

- in chronic kidney disease. *Clinical Journal of the American Society of Nephrology : CJASN*, 3(6):1599–605.
- Amiji, M. and Park, K. (1993). Surface modification of polymeric biomaterials with poly(ethylene oxide), albumin, and heparin for reduced thrombogenicity. *Journal of biomaterials science. Polymer edition*, 4(3):217–234.
- Anderson, G. H., Hellums, J. D., Moake, J., and Alfrey, C. P. (1978). Platelet response to shear stress: changes in serotonin uptake, serotonin release, and ADP induced aggregation. *Thrombosis research*, 13(6):1039–1047.
- Anderson, H. (1981). Normal and Abnormal Mineralization in Mammals. *ASAIO Transactions*, 27:702–708.
- Anderson, J., Cook, G., Costerton, B., Hanson, S., Hensten-Pettersen, A., Jacobsen, N., Johnson, R., Mitchell, R. N., Pasmore, M., Schoen, F. J., Shirtliff, M., and Stoodley, P. (2004). Host reactions to biomaterials and their evaluation. In Ratner, B. D., Hoffman, A. S., Schoen, F. J., and Lemons, J. E., editors, *Biomaterials Science*, chapter 4, pages 293–354. Elsevier, 2 edition.
- Anderson, J. M. (2001). Biological responses to materials. *Annual review of materials research*, 31:81–110.
- Andersson, J. and Andersson, J. (2003). Complement Activation Triggered by Biomaterial Surfaces. *Medicine*.
- Ando, M. and Takahashi, Y. (2009). Ten-year experience with handmade trileaflet polytetrafluoroethylene valved conduit used for pulmonary reconstruction. *Journal of Thoracic and Cardiovascular Surgery*, 137(1):124–131.
- Andrews, R. K., Lopez, J. a., and Berndt, M. C. (1997). Molecular mechanisms of platelet adhesion and activation. *International Journal of Biochemistry and Cell Biology*, 29(1):91–105.
- ANSYS (2012). ANSYS POLYFLOW User’s Guide.
- Ashby, M., Bréchet, Y., Cebon, D., and Salvo, L. (2004). Selection strategies for materials and processes. *Materials & Design*, 25(1):51–67.
- ASTM International (2002). Flexural Properties of Unreinforced and Reinforced Plastics and Electrical Insulating Materials.
- Azarnoush, K., Pereira, B., Dualé, C., Dorigo, E., Farhat, M., Innorta, A., Dauphin, N., Geoffroy, E., Chabrot, P., and Camilleri, L. (2013). Comparison between three types

- of stented pericardial aortic valves (Trivalve trial): study protocol for a randomized controlled trial. *Trials*, 14:413.
- Bach, D. S. (2010). Echo/Doppler Evaluation of Hemodynamics After Aortic Valve Replacement. Principles of Interrogation and Evaluation of High Gradients. *JACC: Cardiovascular Imaging*, 3(3):296–304.
- Balachandran, K., Sucosky, P., and Yoganathan, A. P. (2011). Hemodynamics and mechanobiology of aortic valve inflammation and calcification. *International journal of inflammation*, 2011:15.
- Bar-Cohen, Y. (2005). Biomimetics: mimicking and inspired-by biology. *Smart Structures and Materials*, 5759:1–8.
- Bates, F. S. and Fredrickson, G. H. (1990). Block copolymer thermodynamics: theory and experiment. *Annual review of physical chemistry*, 41:525–57.
- Beith, J. G. (2006). Valve.
- Belanger, M.-C. and Marois, Y. (2001). Hemocompatibility, Biocompatibility, Inflammatory and in Vivo Studies of Primary Reference Materials Low-Density Polyethylene and Polydimethylsiloxane : A Review. *Journal of Biomedical Materials Research*, 58(5):467–477.
- Berlin, D. B., Davidson, M. J., and Schoen, F. J. (2014). The power of disruptive technological innovation: Transcatheter aortic valve implantation. *Journal of Biomedical Materials Research Part B: Applied Biomaterials*, pages n/a–n/a.
- Bernacca, G., Fisher, A., Wilkinson, R., Mackay, T., and Wheatley, D. (1992a). Calcification and stress distribution in bovine pericardial heart valves. *Journal of Biomedical Materials Research*, 26(7):959–66.
- Bernacca, G., Mackay, T., and Wheatley, D. (1992b). A dynamic in vitro method for studying bioprosthetic heart valve calcification. *Journal of Heart Valve Disease*, 1(1):115–30.
- Bernacca, G., Mackay, T., Wilkinson, R., and Wheatley, D. (1995). Calcification and fatigue failure in a polyurethane heart valve. *Biomaterials*, 16(4):279–285.
- Bernacca, G. M., Haworth, W. S., O’connor, B., and Wheatley, D. J. (2009). Method of manufacture of a heart valve prosthesis.
- Bernacca, G. M., O’Connor, B., Williams, D. F., and Wheatley, D. J. (2002). Hydrody-

- namic function of polyurethane prosthetic heart valves: influences of Young's modulus and leaflet thickness. *Biomaterials*, 23(1):45–50.
- Bernacca, G. M. and Wheatley, D. J. (1999). Surface modification of polyurethane heart valves: effects on fatigue life and calcification. *International Journal of Artificial Organs*, 21(12):814–9.
- Bertazzo, S., Gentleman, E., Cloyd, K. L., Chester, A. H., Yacoub, M. H., and Stevens, M. M. (2013). Nano-analytical electron microscopy reveals fundamental insights into human cardiovascular tissue calcification. *Nature materials*, 12(6):576–83.
- Bezuidenhout, D. and Zilla, P. (2014). Flexible Leaflet Polymeric Heart Valves. *Cardiovascular and Cardiac Therapeutic Devices: Studies in Mechanobiology, Tissue Engineering and Biomaterials*, 15:93–129.
- Bird, R., Armstrong, R., and Hassager, O. (1987). *Dynamics of Polymeric Liquids. Volume 1. Fluid Mechanics*. Wiley-Interscience, 2 edition.
- Bird, R. B. and Wiest, J. M. (1985). Anisotropic Effects in Dumbbell Kinetic Theory. *Journal of Rheology*, 29(5):519.
- Bleiziffer, S., Eichinger, W. B., Hettich, I., Guenzinger, R., Ruzicka, D., Bauernschmitt, R., and Lange, R. (2007). Prediction of valve prosthesis-patient mismatch prior to aortic valve replacement: which is the best method? *Heart (British Cardiac Society)*, 93(5):615–20.
- Bluestein, D., Claiborne, T. E., and Slepian, M. (2013a). Polymeric Heart Valve.
- Bluestein, D., Einav, S., and Slepian, M. J. (2013b). Device thrombogenicity emulation: a novel methodology for optimizing thromboresistance of cardiovascular devices. *Journal of Biomechanics*, 46:338–344.
- Bodnar, E. and Frater, R. (1992). *Replacement Cardiac Valves*. McGraw-Hill.
- Boloori Zadeh, P., Corbett, S. C., and Nayeb-Hashemi, H. (2013). Effects of fluid flow shear rate and surface roughness on the calcification of polymeric heart valve leaflet. *Materials Science & Engineering. C, Materials for Biological Applications*, 33(5):2770–5.
- Borsali, R. and Pecora, R. (2008). *Soft Matter Characterization*. Springer Netherlands.
- Botzenhardt, F., Eichinger, W. B., Bleiziffer, S., Guenzinger, R., Wagner, I. M., Bauernschmitt, R., and Lange, R. (2005). Hemodynamic Comparison of Bioprostheses for

- Complete Supra-Annular Position in Patients With Small Aortic Annulus. *Journal of the American College of Cardiology*, 45(12):2054–2060.
- Bourantas, C. V., Van Mieghem, N. M., Farooq, V., Soliman, O. I., Windecker, S., Piazza, N., and Serruys, P. W. (2013). Future perspectives in transcatheter aortic valve implantation. *International Journal of Cardiology*, 168(1):11–18.
- Braune, S., Grunze, M., Straub, A., and Jung, F. (2013). Are there sufficient standards for the in vitro hemocompatibility testing of biomaterials? *Biointerphases*, 8(1):30.
- Brockbank, K. G. M. and Song, Y. C. (2003). Mechanisms of bioprosthetic heart valve calcification. *Transplantation*, 75(8):1133–5.
- Bronzino, J. D. (2000). *The Biomedical Engineering Handbook*. Springer, 2 edition.
- Bruck, S. (1991). Biostability of materials and implants. *Journal of Long-term Effects of Medical Implants*.
- Brydson, J. (1995). *Thermoplastic Elastomers: Properties and Applications*. iSmithers Rapra Publishing, volume 81 edition.
- Buellesfeld, L., Stortecky, S., Kalesan, B., Gloekler, S., Khattab, A. a., Nietlispach, F., Delfine, V., Huber, C., Eberle, B., Meier, B., Wenaweser, P., and Windecker, S. (2013). Aortic root dimensions among patients with severe aortic stenosis undergoing transcatheter aortic valve replacement. *JACC: Cardiovascular Interventions*, 6(1):72–83.
- Burriesci, G., Marincola, F. C., and Zervides, C. (2010). Design of a novel polymeric heart valve. *Journal of medical engineering & technology*, 34(1):7–22.
- Butcher, J. T., Simmons, C. A., and Warnock, J. N. (2007). Review : Mechanobiology of the Aortic Heart Valve. *Journal of Heart Valve Disease*, 17:62–73.
- Butterfield, M., Wheatley, D., Williams, D., and Fisher, J. (2001). A new design for polyurethane heart valves. *Journal of heart valve disease*, 10(1):105–10.
- Cacciola, G., Peters, G. W., and Baaijens, F. P. (2000). A synthetic fiber-reinforced stentless heart valve. *Journal of biomechanics*, 33(6):653–8.
- Campbell, L. A., Moe, R., and Sarnowski, E. J. (2004). Method of manufacturing a prosthetic heart valve.
- Carabello, B. a. (2002). Evaluation and management of patients with aortic stenosis. *Circulation*, 105(15):1746–1750.

- Carastan, D. J., Amurin, L. G., Craievich, A. F., Gonçalves, M. D. C., and Demarquette, N. R. (2013). Morphological evolution of oriented clay-containing block copolymer nanocomposites under elongational flow. *European Polymer Journal*, 49(6):1391–1405.
- Castelletto, V. and Hamley, I. (2004). Morphologies of block copolymer melts. *Current Opinion in Solid State and Materials Science*, 8(6):426–438.
- Cerillo, A. G., Mariani, M., Berti, S., and Glauber, M. (2012). Sizing the aortic annulus. *Annals of cardiothoracic surgery*, 1(2):245–56.
- Chakraborty, S., Bag, S., Pal, S., and Mukherjee, A. K. (2006). Structural and microstructural characterization of bioapatites and synthetic hydroxyapatite using X-ray powder diffraction and Fourier transform infrared techniques. *Journal of Applied Crystallography*, 39(3):385–390.
- Chandran, K. B., Kim, S. H., and Han, G. (1991). Stress distribution on the cusps of a polyurethane trileaflet heart valve prosthesis in the closed position. *Journal of biomechanics*, 24(6):385–95.
- Charnley, J. (1963). Tissue reactions to polytetrafluoroethylene. *Lancet*, December(28):1379.
- Chen, Z. Z., Kornfield, J., and Smith, S. (1997). Pathways to Macroscale Order in Nanostructured Block Copolymers. *Science*, 277(5330):1248–1253.
- Chenoweth, D. E. (1987). Complement Activation in Extracorporeal Circuits. *Annals of the New York Academy of Sciences*, 516:306–313.
- Cherepanov, G. (1967). Crack propagation in continuous media. *Journal of Applied Mathematics and Mechanics*, 31(3):503–512.
- Chetta, G. and Lloyd, J. (1980). The Design, Fabrication and Evaluation of a Trileaflet Prosthetic Heart Valve. *Journal of Biomechanical Engineering*, 102(1):8.
- Chinn, J. A. (2002). Polymeric heart valve fabricated from polyurethane/polysiliconeurethane blends.
- Cho, H. H.-j. H.-j. and Kim, H.-s. H. (2009). Osteopontin: a multifunctional protein at the crossroads of inflammation, atherosclerosis, and vascular calcification. *Current Atherosclerosis Reports*, pages 206–213.
- Cho, K., Jang, W. J., Lee, D., Chun, H., and Chang, Y. W. (2000). Fatigue crack growth of elastomers in the swollen state. *Polymer*, 41(1):179–183.

- Choi, I. S. and Roland, C. M. (1996). Intrinsic Defects and the Failure Properties of cis-1,4-Polyisoprenes. *Rubber Chemistry and Technology*, 69(4):591–99.
- Chong, K. P., Wieting, D. W., Hwang, N. H. C., and Kennedy, J. H. (1973). Stress Analysis of Normal Human Aortic Valve Leaflets during Diastole. *Artificial Cells, Blood Substitutes and Biotechnology*, 1(2):307–321.
- Christensen, K., Larsson, R., and Emanuelsson, H. (2001). Heparin coating of the stent graft effects on platelets, coagulation and complement activation. *Biomaterials*, 22:349–355.
- Christie, G. W. and Barratt-Boyes, B. G. (1991). On stress reduction in bioprosthetic heart valve leaflets by the use of a flexible stent. *Journal of Cardiac Surgery*, 6(4):476–81.
- Christie, G. W. and Barratt-Boyes, B. G. (1995). Age-dependent changes in the radial stretch of human aortic valve leaflets determined by biaxial testing. *The Annals of Thoracic Surgery*, 60:S156–9.
- Chung, D. H. and Kwon, T. H. (2002). Fiber orientation in the processing of polymer composites. *Korean-Australia Rheology Journal*, 14(4):175–188.
- Claiborne, T., Xenos, M., Sheriff, J., Chiu, W., Soares, J., Alemu, Y., Gupta, S., Judex, S., Slepian, M., and Bluestein, D. (2013a). Toward Optimization of a Novel Trileaflet Polymeric Prosthetic Heart Valve via Device Thrombogenicity Emulation. *ASAIO Journal*, 59(3):275–83.
- Claiborne, T. E., Girdhar, G., Gallocher-Lowe, S., Sheriff, J., Kato, Y. P., Pinchuk, L., Schoepfhoerster, R. T., Jesty, J., and Bluestein, D. (2011). Thrombogenic potential of Innovia polymer valves versus Carpentier-Edwards Perimount Magna aortic bioprosthetic valves. *ASAIO journal (American Society for Artificial Internal Organs : 1992)*, 57(1):26–31.
- Claiborne, T. E., Sheriff, J., Kuetting, M., Steinseifer, U., Slepian, M. J., and Bluestein, D. (2013b). In vitro evaluation of a novel hemodynamically optimized trileaflet polymeric prosthetic heart valve. *Journal of Biomechanical Engineering*, 135(2):1–8.
- Clark, M. A., Arnold, S. V., Duhay, F. G., Thompson, A. K., Keyes, M. J., Svensson, L. G., Bonow, R. O., Stockwell, B. T., and Cohen, D. J. (2012). Five-year clinical and economic outcomes among patients with medically managed severe aortic stenosis: Results from a medicare claims analysis. *Circulation: Cardiovascular Quality and Outcomes*, 5(5):697–704.

- Co, A. and Bird, R. B. (1977). Slow viscoelastic radial flow between parallel disks. *Applied Scientific Research*, 33(5-6):385–404.
- Cohn, L. H., Collins, J. J., DiSesa, V. J., Couper, G. S., Peigh, P. S., Kowalker, W., and Allred, E. (1989). Fifteen-year experience with 1678 Hancock porcine bioprosthetic heart valve replacements. *Annals of surgery*, 210(4):435–442; discussion 442–443.
- Corden, J., David, T., and Fisher, J. (1995). In vitro determination of the curvatures and bending strains acting on the leaflets of polyurethane trileaflet heart valves during leaflet motion. *Proceedings of the Institution of Mechanical Engineers*, 209(4):243–53.
- Cracknell, P. and Dyson, R. (1993). *Handbook of Thermoplastics Injection Mould Design*. Springer, 1 edition.
- Cribier, A., Eltchaninoff, H., Bash, A., Borenstein, N., Tron, C., Bauer, F., Derumeaux, G., Anselme, F., Laborde, F., and Leon, M. B. (2002). Percutaneous transcatheter implantation of an aortic valve prosthesis for calcific aortic stenosis: First human case description. *Circulation*, 106(24):3006–3008.
- Daebritz, S. H., Fausten, B., Hermanns, B., Franke, A., Schroeder, J., Groetzner, J., Autschbach, R., Messmer, B. J., and Sachweh, J. S. (2004a). New flexible polymeric heart valve prostheses for the mitral and aortic positions. *The Heart Surgery Forum*, 7(5):E525–32.
- Daebritz, S. H., Fausten, B., Hermanns, B., Schroeder, J., Groetzner, J., Autschbach, R., Messmer, B. J., and Sachweh, J. S. (2004b). Introduction of a flexible polymeric heart valve prosthesis with special design for aortic position. *European Journal of Cardiothoracic Surgery : Official Journal of the European Association for Cardiothoracic Surgery*, 25(6):946–52.
- Dagum, P., Green, G. R., Nistal, F. J., Daughters, G. T., Timek, T. A., Foppiano, L. E., Bolger, A. F., Ingels, N. B., and Miller, D. C. (1999). Deformational Dynamics of the Aortic Root Modes and Physiologic Determinants. *Circulation*, 100(Supplement 2):54–62.
- D’Arcy, J., Prendergast, B., and Chambers, J. (2011). Valvular heart disease: the next cardiac epidemic. *Heart*, 97(2):91–93.
- Dasi, L. P., Simon, H. A., Sucusky, P., and Yoganathan, A. P. (2009). Fluid mechanics of artificial heart valves. *Clinical and experimental pharmacology & physiology*, 36(2):225–37.
- De Hart, J., Peters, G., Schreurs, P., and Baaijens, F. (2004). Collagen fibers reduce

- stresses and stabilize motion of aortic valve leaflets during systole. *Journal of Biomechanics*, 37(3):303–311.
- De Paulis, R., Schmitz, C., Scaffa, R., Nardi, P., Chiariello, L., and Reul, H. (2005). In vitro evaluation of aortic valve prosthesis in a novel valved conduit with pseudosinuses of Valsalva. *Journal of Thoracic and Cardiovascular Surgery*, 130(4):1016–1021.
- Demer, L. L. and Tintut, Y. (2008). Vascular calcification: pathobiology of a multifaceted disease. *Circulation*, 117(22):2938–48.
- DeYoreo, J. J. and Vekilov, P. G. (2003). Principles of Crystal Nucleation and Growth. *Reviews in Mineralogy and Geochemistry*, 54(1):57–93.
- Diab, M., Peter, J., Faerber, G., Bothe, W., Lemke, S., Breuer, M., and Doenst, T. (2011). Sizing strategy is a major determinant for postoperative pressure gradients in commonly implanted stented tissue valves. *Circulation*, 124:A16654.
- Diani, J., Fayolle, B., and Gilormini, P. (2009). A review on the Mullins effect. *European Polymer Journal*, pages 601–612.
- Djabourov, M., Nishinari, K., and Ross-Murphy, S. B. (2013). *Physical Gels from Biological and Synthetic Polymers*. Cambridge University Press.
- Doehring, T. C., Kahelin, M., and Vesely, I. (2005). Mesostructures of the Aortic Valve. *Journal of heart valve disease*, 14(5):679–686.
- Dorozhkin, S. V. (2009). Calcium Orthophosphates in Nature, Biology and Medicine. *Materials*, 2(2):399–498.
- Drolet, F. and Fredrickson, G. H. (2001). Optimizing chain bridging in complex block copolymers. *Macromolecules*, 34(15):5317–5324.
- Du Bois, D. and Du Bois, E. F. (1916). A Formula To Estimate The Approximate Surface Area If Height And Weight Be Known. *Archives of Internal Medicine (Chic)*, XVII(6_2):863–871.
- Ducrot, E., Chen, Y., Bulters, M., Sijbesma, R. P., and Creton, C. (2014). Toughening elastomers with sacrificial bonds and watching them break. *Science (New York, N.Y.)*, 344(6180):186–9.
- Eastman (2011). Eastman polymers processing and mold design guidelines. Technical report, Eastman Chemical Company, Kingsport, TN.
- Ebewele, R. (2000). *Polymer Science and Technology*. CRC Press.

- Edwin, F., Tettey, M., Aniteye, E., Tamatey, M., Sereboe, L., Entsua-Mensah, K., Kotei, D., and Baffoe-Gyan, K. (2011). The development of cardiac surgery in West Africa—the case of Ghana. *The Pan African medical journal*, 9:15.
- Egan, K. P., Kim, J. H., Mohler, E. R., and Pignolo, R. J. (2011). Role for circulating osteogenic precursor cells in aortic valvular disease. *Arteriosclerosis, Thrombosis, and Vascular Biology*, 31(12):2965–2971.
- Ehrenstein, M. R., Jury, E. C., and Mauri, C. (2005). Statins for atherosclerosis - as good as it gets? *The New England Journal of Medicine*, 352(1):73–5.
- El Fray, M. and Altstädt, V. (2003a). Fatigue behaviour of multiblock thermoplastic elastomers. 1. Stepwise increasing load testing of poly(aliphatic/aromatic-ester) copolymers. *Polymer*, 44(16):4635–4642.
- El Fray, M. and Altstädt, V. (2003b). Fatigue behaviour of multiblock thermoplastic elastomers. 2. Dynamic creep of poly(aliphatic/aromatic-ester) copolymers. *Polymer*, 44(16):4643–4650.
- El Fray, M. and Altstädt, V. (2004). Fatigue behaviour of multiblock thermoplastic elastomers. 3. Stepwise increasing strain test of poly(aliphatic/aromatic-ester) copolymers. *Polymer*, 45(1):263–273.
- El Fray, M., Prowans, P., Puskas, J. E., and Altstädt, V. (2006). Biocompatibility and fatigue properties of polystyrene-polyisobutylene-polystyrene, an emerging thermoplastic elastomeric biomaterial. *Biomacromolecules*, 7(3):844–50.
- El-Hamamsy, I. and Poirier, N. C. (2013). What is the role of the Ross procedure in today's armamentarium? *The Canadian journal of cardiology*, 29(12):1569–76.
- Engberg, A. E., Rosengren-Holmberg, J. P., Chen, H., Nilsson, B., Lambris, J. D., Nicholls, I. a., and Ekdahl, K. N. (2011). Blood protein-polymer adsorption: Implications for understanding complement-mediated hemoincompatibility. *Journal of biomedical materials research. Part A*, pages 74–84.
- Erlenkötter, A., Endres, P., Nederlof, B., Hornig, C., and Vienken, J. (2008). Score model for the evaluation of dialysis membrane hemocompatibility. *Artificial organs*, 32(12):962–9.
- Fang, L., Wei, M., Shang, Y., Jimenez, L., Kazmer, D., Barry, C., and Mead, J. (2009). Surface morphology alignment of block copolymers induced by injection molding. *Polymer*, 50(24):5837–5845.

- Farzaneh-Far, A., Proudfoot, D., Shanahan, C., and Weissberg, P. (2001). Vascular and valvar calcification: recent advances. *Heart*, 85(1):13–7.
- Fisher, L. and Termine, J. (1985). Noncollagenous proteins influencing the local mechanisms of calcification. *Clinical Orthopaedics and Related Research*, 200(November):362.
- Fratzl, P. (2008). *Collagen: Structure and Mechanics*. Springer Science and Business Media, LLC.
- Fratzl, P., Dunlop, J. W. C., and Weinkamer, R. (2013). *Materials Design Inspired by Nature: Function Through Inner Architecture*, volume 1. Royal Society of Chemistry.
- Gallegos, R., Rivard, A., Suwan, P., Black, S., Bertog, S., Steinseifer, U., Armien, A., Lahti, M., and Bianco, R. (2006). In-vivo experience with the Triflo trileaflet mechanical heart valve. *Journal of heart valve disease*, 15(6):791–9.
- Gallocher, S. L. (2007). *Durability Assessment of Polymer Trileaflet Heart Valves*. PhD thesis, Florida International University.
- Gallocher, S. L., Aguirre, A. F., Kasyanov, V., Pinchuk, L., and Schoephoerster, R. T. (2006). A Novel Polymer for Potential Use in a Trileaflet Heart Valve. *Journal of Biomedical Materials Research. Part B Applied Biomaterials*, 79(2):325–334.
- Garcia, D. and Kadem, L. (2006). Orifice Area, Effective Orifice Area, or Gorlin Area? *Journal of Heart Valve Disease*, 15(5):601–8.
- Garcia, D., Pibarot, P., Landry, C., Allard, A., Chayer, B., Dumesnil, J. G., and Durand, L.-G. (2004). Estimation of aortic valve effective orifice area by Doppler echocardiography: effects of valve inflow shape and flow rate. *Journal of the American Society of Echocardiography*, 17(7):756–765.
- García Páez, J. M., Herrero, E. J., San Martín, A. C., García Sestafe, J. V., Téllez, G., Millán, I., Salvador, J., Cordon, A., and Castillo-Olivares, J. L. (2000). The influence of chemical treatment and suture on the elastic behavior of calf pericardium utilized in the construction of cardiac bioprostheses. *Journal of Materials Science: Materials in Medicine*, 11(5):273–277.
- Gardner, R. (1974). An examination of the fluid mechanics and thrombus formation time parameters in a Chandler rotating loop system. *Journal of Laboratory and Clinical Medicine*, 84(4):494–508.
- Gent, A. N., Lindley, P. B., and Thomas, A. G. (1965). Cut Growth and Fatigue of Rubbers. I. The Relationship between Cut Growth and Fatigue. *Rubber Chemistry and Technology*, 38(2):292–300.

- Ghanbari, H., Kidane, A. G., Burriesci, G., Ramesh, B., Darbyshire, A., and Seifalian, A. M. (2010). The anti-calcification potential of a silsesquioxane nanocomposite polymer under in vitro conditions: potential material for synthetic leaflet heart valve. *Acta Biomaterialia*, 6(11):4249–60.
- Gharaie, S. H. and Morsi, Y. (2015). A novel design of a polymeric heart valve. *International Journal of Artificial Organs*, 38(5):259–70.
- Gharib, M., Kremers, D., Koochesfahani, M. M., and Kemp, M. (2002). Leonardo’s vision of flow visualization. *Experiments in Fluids*, 33(1):219–223.
- Ghista, D. and Reul, H. (1983). Advances in Cardiovascular Physics, Part 1 Modelling. In *Cardiovascular Engineering*, page 230. S. Karger.
- Giachelli, C. M., Speer, M. Y., Li, X., Rajachar, R. M., and Yang, H. (2005). Regulation of vascular calcification: roles of phosphate and osteopontin. *Circulation Research*, 96(7):717–22.
- Giesekus, H. (1982). A simple constitutive equation for polymer fluids based on the concept of deformation-dependent tensorial mobility. *Journal of Non-Newtonian Fluid Mechanics*, 11(1-2):69–109.
- Girdhar, G., Xenos, M., Alemu, Y., Chiu, W.-C., Lynch, B. E., Jesty, J., Einav, S., Slepian, M. J., and Bluestein, D. (2012). Device thrombogenicity emulation: a novel method for optimizing mechanical circulatory support device thromboresistance. *PloS one*, 7(3):e32463.
- Goffin, Y., Van Hoeck, B., Jashari, R., Soots, G., and Kalmar, P. (2000). Banking of Cryopreserved Heart Valves in Europe: Assessment of a 10-year Operation in the European Homograft Bank (EHB). *Journal of Heart Valve Disease*, 9(2):207–14.
- Golander, C.-G. and Larsson, R. (1986). Surface modified solid substrate and a method for its preparation.
- Goldbarg, S. H., Elmariah, S., Miller, M. a., and Fuster, V. (2007). Insights into degenerative aortic valve disease. *Journal of the American College of Cardiology*, 50(13):1205–13.
- Golomb, G. and Wagner, D. (1991). Development of a new in vitro model for studying implantable polyurethane calcification. *Biomaterials*, 12(May):397–405.
- Gonzalez-Alvarez, a., Arellano, M., Diat, O., Legrand, J. F., and Piau, J. M. (2004). Elongational properties and crystallization of poly (isobutylene) melts probed by synchrotron radiation. *Revista Mexicana de Fisica*, 50(5):506–514.

- Goosen, M. F. A. and Sefton, M. V. (1979). Heparinized Styrene-Butadiene-Styrene Elastomers. *Journal of Biomedical Materials Research*, 13:347–364.
- Granta Design Ltd. (2003). Materials Database.
- Griffith, A. (1921). The Phenomena of Rupture and Flow in Solids. *Philosophical Transactions of the Royal Society A: Mathematical, Physical and Engineering Sciences*, 221(582-593):163–198.
- Gupta, M. (2001). Simulation of planar entrance flow using strain-rate-dependent shear and elongational viscosities. *Journal of reinforced plastics and composites*.
- Haj-Ali, R., Dasi, L. P., Kim, H. S., Choi, J., Leo, H. W., and Yoganathan, A. P. (2008). Structural simulations of prosthetic tri-leaflet aortic heart valves. *Journal of Biomechanics*, 41(7):1510–1519.
- Hamid, M., Sabbah, H., and Stein, P. (1986). Influence of stent height upon stresses on the cusps of closed bioprosthetic valves. *Journal of biomechanics*, 19(9):759–769.
- Hamley, I. W. (2000). Effect of shear on ordered block copolymer solutions. *Current opinion in Colloid & Interface Science*, 5:342 – 350.
- Hamley, I. W. (2004). *Developments in block copolymer science and technology*. John Wiley & Sons, Inc.
- Hamon, R. F., Khan, a. S., and Chow, a. (1982). The cation-chelation mechanism of metal-ion sorption by polyurethanes. *Talanta*, 29(4):313–26.
- Han, D. K., Park, K., Park, K. D., Ahn, K. D., and Kim, Y. H. (2006). In vivo biocompatibility of sulfonated PEO-grafted polyurethanes for polymer heart valve and vascular graft. *Artificial Organs*, 30(12):955–959.
- Harada, N. S., Oyama, H. T., Bartoli, J. R., Gouvea, D., Cestari, I. a., and Hui Wang, S. (2005). Quantifying adsorption of heparin on a PVC substrate using ATR-FTIR. *Polymer International*, 54(1):209–214.
- Harasaki, H., Moritz, A., Uchida, N., Chen, J.-F., McMahon, J. T., Richards, T. M., Smith, W. A., Murabayashi, S., Kambic, H. E., Kiraly, R. J., and Nosé, Y. (1987). Initiation and Growth of Calcification in blood pumps. *ASAIO Transactions*, 33(3):643–648.
- Hastings, G. (1992). *Cardiovascular Biomaterials*. Springer-Verlag London Limited, London, UK.

- Hathcock, J. J. (2006). Flow effects on coagulation and thrombosis. *Arteriosclerosis, thrombosis, and vascular biology*, 26(8):1729–37.
- Haworth, W. W. S. (1978). Testing of Materials for Artificial Heart Valves. *British Polymer Journal*, 10(4):297–301.
- Hayes, M., Edwards, D., and Shah, A. (2015). *Fractography in Failure Analysis of Polymers*. William Andrew.
- Heim, F., Gasser, B., Khoffi, F., and Blondel, P. (2014). Textile heart valve: first in-vivo experiment in the aortic position. *Journal of heart valve disease*, 23(3):316–8.
- Helske, S. and Kupari, M. (2007). Aortic valve stenosis: an active atheroinflammatory process. *Current Opinion in Lipidology*, 18(5):483–491.
- Hermans, H., Herijgers, P., Holvoet, P., Verbeken, E., Meuris, B., Flameng, W., and Herregods, M.-C. (2010). Statins for calcific aortic valve stenosis: into oblivion after SALTIRE and SEAS? An extensive review from bench to bedside. *Current Problems in Cardiology*, 35(6):284–306.
- Heron, M., Hoyert, D. L., Murphy, S. L., Xu, J., Kochanek, K. D., and Tejada-Vera, B. (2009). Deaths: final data for 2006. *National vital statistics reports : from the Centers for Disease Control and Prevention, National Center for Health Statistics, National Vital Statistics System*, 57(14):1–134.
- Hilbert, S., Ferrans, V., Tomita, Y., Eidbo, E., and Jones, M. (1987). Evaluation of explanted polyurethane trileaflet cardiac valve prostheses. *Journal of Thoracic and Cardiovascular Surgery*, 94(3):419–29.
- Ho, S. Y. (2009). Structure and anatomy of the aortic root. *European journal of echocardiography : the journal of the Working Group on Echocardiography of the European Society of Cardiology*, 10(1):i3–10.
- Hoerstrup, S. P., Sodian, R., Sperling, J. S., Vacanti, J. P., and Jr, J. E. M. (2000a). Engineered Heart Valves. *Tissue Engineering*, 6(1):75–85.
- Hoerstrup, S. S. P., Sodian, R., Daebritz, S., Wang, J., Bacha, E. A., Martin, D. P., Moran, A. M., Guleserian, K. J., Sperling, J. S., Kaushal, S., Vacanti, J. P., Schoen, F. J., and Mayer, J. E. (2000b). Functional living trileaflet heart valves grown in vitro. *Circulation*, 102:Iii–44–Iii–49.
- Hoffman, D., Sisto, D., Yu, L., Dahm, M., and Kolff, W. (1991). Evaluation of a Stented Polyurethane Mitral Valve. *ASAIO Transactions*, 37(3):M354–5.

- Holzapfel, G. a., Gasser, T. C., and Ogden, R. W. (2000). A new constitutive framework for arterial wall mechanics and a comparative study of material models. *J. Elasticity*, 61(8):1–48.
- Honeker, C. C. and Thomas, E. L. (2000). Perpendicular deformation of a near-single-crystal triblock copolymer with a cylindrical morphology. 2. TEM. *Macromolecules*, 33(25):9407–9417.
- Hong, J., Larsson, A., Ekdahl, K. N., Elgue, G., Larsson, R., and Nilsson, B. (2001). Contact between a polymer and whole blood: Sequence of events leading to thrombin generation. *Journal of Laboratory and Clinical Medicine*, 138(2):139–145.
- Hopkins, R. a. (2006). Bioprosthetic valves and laudable inflammation? *Circulation*, 114(4):261–264.
- Hukins, D. W. L., Mahomed, A., and Kukureka, S. N. (2008). Accelerated aging for testing polymeric biomaterials and medical devices. *Medical engineering & physics*, 30(10):1270–4.
- Hulme, A. and Cooper, J. (2012). Life prediction of polymers for industry. *Sealing technology*, (September):8–12.
- Imachi, K., Abe, Y., Matsuura, H., Iwasaki, K., Son, Y.-p., and Kouno, A. (2001). A new hypothesis on the mechanism of calcification formed on a blood-contacted polymer surface. *Journal of Artificial Organs*, 4(1):74–82.
- Imachi, K., Mabuchi, K., Chinzei, T., Abe, Y., Imanishi, K., Yonezawa, T., Maeda, K., Suzukawa, M., Kouno, A., Oho, T., Fujisama, I., and Alsumi, K. (1989). In Vitro and In Vivo Evaluation of a Jellyfish Valve for Practical Use. *ASAIO Transactions*, 35(3).
- International Standards Organisation (2005). Cardiovascular implants - Cardiac valve prostheses.
- ISO (2010). Biological evaluation of medical devices - Part 13: Identification and quantification of degradation products from polymeric medical devices (ISO 10993-13:2010).
- Iung, B. (2003). A prospective survey of patients with valvular heart disease in Europe: The Euro Heart Survey on Valvular Heart Disease. *European Heart Journal*, 24(13):1231–1243.
- Iung, B., Cachier, A., Baron, G., Messika-Zeitoun, D., Delahaye, F., Tornos, P., Gohlke-Bärwolf, C., Boersma, E., Ravnaud, P., and Vahanian, A. (2005). Decision-making in elderly patients with severe aortic stenosis: Why are so many denied surgery? *European Heart Journal*, 26(24):2714–2720.

- Lung, B. and Vahanian, A. (2011). Epidemiology of valvular heart disease in the adult. *Nature reviews. Cardiology*, 8(3):162–172.
- Jansen, J., Willeke, S., Reiners, B., Harbott, P., Reul, H., Lo, H. B., Daebritz, S. H., Rosenbaum, C., Bitter, A., Ziehe, K., Rau, G., and Messmer, B. J. (1991). Advances in design principle and fluid dynamics of flexible polymeric heart valve. *ASAIO Transactions*, 37(3):M451–3.
- Jesty, J. and Bluestein, D. (1999). Acetylated prothrombin as a substrate in the measurement of the procoagulant activity of platelets: elimination of the feedback activation of platelets by thrombin. *Analytical biochemistry*, 272(1):64–70.
- Jesty, J., Yin, W., Perrotta, P., and Bluestein, D. (2003). Platelet activation in a circulating flow loop: combined effects of shear stress and exposure time. *Platelets*, 14(3):143–149.
- Jiang, H., Campbell, G., Boughner, D., Wan, W. K., and Quantz, M. (2004). Design and manufacture of a polyvinyl alcohol (PVA) cryogel tri-leaflet heart valve prosthesis. *Medical Engineering and Physics*, 26(4):269–277.
- Jones, J. M., O’Kane, H., Gladstone, D. J., Sarsam, M. a., Campalani, G., MacGowan, S. W., Cleland, J., and Cran, G. W. (2001). Repeat heart valve surgery: risk factors for operative mortality. *The Journal of thoracic and cardiovascular surgery*, 122(5):913–918.
- Jono, S., McKee, M. D., Murry, C. E., Shioi, a., Nishizawa, Y., Mori, K., Morii, H., and Giachelli, C. M. (2000). Phosphate regulation of vascular smooth muscle cell calcification. *Circulation research*, 87(7):E10–E17.
- Kalath, S., Tsiouras, P., and Silver, F. H. (1986). Non-invasive assessment of aortic mechanical properties. *Annals of biomedical engineering*, 14(6):513–24.
- Kapalos, J., Mavrilas, D., Missirlis, Y., and Koutsoukos, P. G. (1997). Model experimental system for investigation of heart valve calcification in vitro. *Journal of biomedical materials research*, 38(3):183–90.
- Karatasos, K., Anastasiadis, S. H., Pakula, T., and Watanabe, H. (2000). On the loops-to-bridges ratio in ordered triblock copolymers: An investigation by dielectric relaxation spectroscopy and computer simulations. *Macromolecules*, 33(2):523–541.
- Keller, A., Pedemonte, E., and Willmouth, F. M. (1970). Macro lattice from segregated amorphous phases of a three block copolymer. *Nature*, 225(5232):538.
- Kelly, B. S., Heffelfinger, S. C., Whiting, J. F., Miller, M. A., Reaves, A., Armstrong, J.,

- Narayana, A., and Roy-Chaudhury, P. (2002). Aggressive venous neointimal hyperplasia in a pig model of arteriovenous graft stenosis. *Kidney International*, 62(6):2272–2280.
- Kester, R. C. (1984). The thrombogenicity of Dacron arterial grafts and its modification by platelet inhibitory drugs. *Annals of the Royal College of Surgeons of England*, 66(4):241–246.
- Kheradvar, A., Groves, E. M., Dasi, L. P., Alavi, H. S., Tranquillo, R. T., Grande-Allen, K. J., Simmons, C. A., Griffith, B., Falahatpisheh, A., Goergen, C. J., Mofrad, M. R. K., Baaijens, F. P., Little, S. H., and Canic, S. (2015). Emerging Trends in Heart Valve Engineering: Part I. Solutions for Future. *Annals of biomedical engineering*, 43(4):833–43.
- Kidane, A. G., Salacinski, H., Tiwari, A., Bruckdorfer, K. R., and Seifalian, A. M. (2004). Anticoagulant and antiplatelet agents: their clinical and device application(s) together with usages to engineer surfaces. *Biomacromolecules*, 5(3):798–813.
- Kim, I. Y., Kim, J. W., Jung, D. Y., Kim, C. S., and Min, B. G. (1991). Development of Polymer Prosthetic Heart Valve - Fabrication and In Vitro Test. *The Seoul Journal of Medicine*, 32(1):35–42.
- Kingston, J. and Muhr, A. (2012). Determination of effective flaw size for fatigue life prediction. In *Constitutive Models for Rubber*, volume VII, pages 337–342. CRC Press.
- Kini, V., Bachmann, C., Fontaine, A., Deutsch, S., and Tarbell, J. M. (2000). Flow visualization in mechanical heart valves: occluder rebound and cavitation potential. *Annals of biomedical engineering*, 28(4):431–41.
- Kiraly, R. J. and Hillegass, D. V. (1980). Polyolefin blood pump components. *Synthetic biomedical polymers concepts and applications*, pages 59–71.
- Kobayashi, J. (2011). Stentless aortic valve replacement: an update. *Vascular health and risk management*, 7:345–351.
- Kokubo, T. (1990). Surface chemistry of bioactive glass-ceramics. *Journal of Non-Crystalline Solids*, 120:138–151.
- Kolh, P., Kerzmann, A., Honore, C., Comte, L., and Limet, R. (2007). Aortic valve surgery in octogenarians: predictive factors for operative and long-term results. *European Journal of Cardio-thoracic Surgery*, 31(4):600–606.
- Krings, M., Kanellopoulou, D., Mavrilas, D., and Glasmacher, B. (2006). In vitro pH-

- controlled calcification of biological heart valve prostheses. *Materialwissenschaft und Werkstofftechnik*, 37(6):432–435.
- Kristensen, E. M. E., Larsson, R., Sánchez, J., Rensmo, H., Gelius, U., and Siegbahn, H. (2006). Heparin coating durability on artificial heart valves studied by XPS and antithrombin binding capacity. *Colloids and surfaces. B: Biointerfaces*, 49(1):1–7.
- Krucinski, S., Vesely, I., Dokainish, M. A., and Campbell, G. (1993). Numerical simulation of leaflet flexure in bioprosthetic valves mounted on rigid and expansile stents. *Journal of biomechanics*, 26(8):929–43.
- Kütting, M., Roggenkamp, J., Urban, U., Schmitz-Rode, T., and Steinseifer, U. (2011). Polyurethane heart valves: past, present and future. *Expert Reviews of Medical Devices*, 8(2):227–233.
- Kyrle, P. A., Eichler, H. G., Jäger, U., and Lechner, K. (1987). Inhibition of prostacyclin and thromboxane A₂ generation by low-dose aspirin at the site of plug formation in man in vivo. *Circulation*, 75(5):1025–1029.
- Labrosse, M. R., Beller, C. J., Robicsek, F., and Thubrikar, M. J. (2006). Geometric modeling of functional trileaflet aortic valves: Development and clinical applications. *Journal of Biomechanics*, 39(14):2665–2672.
- Lach, R., Schneider, K., Weidisch, R., Janke, a., and Knoll, K. (2005). Application of the essential work of fracture concept to nanostructured polymer materials. *European Polymer Journal*, 41(2):383–392.
- Lake, G. (1983). Aspects of fatigue and fracture of rubber. *Progress of Rubber Technology*, 45:89.
- Lake, G. J. and Thomas, A. G. (1967). The Strength of Highly Elastic Materials. *Proceedings of the Royal Society A: Mathematical, Physical and Engineering Sciences*, 300(1460):108–119.
- Lanzarone, E., Vismara, R., and Fiore, G. B. (2009). A new pulsatile volumetric device with biomorphic valves for the in vitro study of the cardiovascular system. *Artificial Organs*, 33(12):1048–1062.
- Larson, R. G. (1988). *Constitutive equations for polymer melts and solutions*. Butterworth Publishers, Stoneham, MA, USA.
- Le Gorju Jago, K. (2008). Fatigue life of rubber components: 3D damage evolution from X-ray computed microtomography. In *Constitutive Models for Rubber V*, page 173. Taylor & Francis/Balkema, London.

- Leat, M. E. and Fisher, J. (1994). A synthetic leaflet heart valve with improved opening characteristics. *Medical Engineering and Physics*, 16(6):470–476.
- Leat, M. E. and Fisher, J. (1995). The influence of manufacturing methods on the function and performance of synthetic leaflet heart valve. In *Proceedings of the Institution of Mechanical Engineers, Part H: Journal of Engineering in Medicine*, pages 65–70.
- Leefe, S. E. and Gentle, C. R. (1987). Theoretical evaluation of energy loss methods in the analysis of prosthetic heart valves. *Journal of biomedical engineering*, 9(2):121–7.
- LeFan, J. (2011). Liquid Silicone Rubber Injection Molding.
- Leibler, L. and Leibler, L. (1980). Theory of Microphase Separation in Block Copolymers. *Macromolecules*, 13(6):1602–1617.
- Leo, H. L. (2005). *An In Vitro Investigation of the Flow Fields Through Bileaflet and Polymeric Prosthetic Heart Valves*. Phd, Georgi Institute of Technology.
- Leo, H. L., Dasi, L. P., Carberry, J., Simon, H. a., and Yoganathan, A. P. (2006). Fluid dynamic assessment of three polymeric heart valves using particle image velocimetry. *Annals of biomedical engineering*, 34(6):936–52.
- Leo, H.-L., Simon, H., Carberry, J., Lee, S.-C., and Yoganathan, A. P. (2005). A Comparison of Flow Field Structures of Two Tri-Leaflet Polymeric Heart Valves. *Annals of Biomedical Engineering*, 33(4):429–443.
- Leopold, J. a. (2012). Cellular mechanisms of aortic valve calcification. *Circulation: Cardiovascular Interventions*, 5(4):605–614.
- Levy, R. J., Schoen, F. J., and Howard, S. L. (1983). Mechanism of calcification of porcine bioprosthetic aortic valve cusps: role of T-lymphocytes. *The American Journal of Cardiology*, 52(5):629–31.
- Li, J., Illeperuma, W. R. K., Suo, Z., and Vlassak, J. J. (2014). Hybrid hydrogels with extremely high stiffness and toughness. *ACS Macro Letters*, 3(6):520–523.
- Liedel, C., Pester, C. W., Ruppel, M., Urban, V. S., and Böker, A. (2012). Beyond Orientation: The Impact of Electric Fields on Block Copolymers. *Macromolecular Chemistry and Physics*, 213(3):259–269.
- Lindroos, M., Kupari, M., Heikkilä, J., and Tilvis, R. (1993). Prevalence of aortic valve abnormalities in the elderly: an echocardiographic study of a random population sample. *Journal of the American College of Cardiology*, 21(5):1220–1225.

- Liu, A. C., Joag, V. R., and Gotlieb, A. I. (2007a). The emerging role of valve interstitial cell phenotypes in regulating heart valve pathobiology. *The American journal of pathology*, 171(5):1407–18.
- Liu, Y., Kasyanov, V., and Schoephoerster, R. T. (2007b). Effect of fiber orientation on the stress distribution within a leaflet of a polymer composite heart valve in the closed position. *Journal of biomechanics*, 40(5):1099–106.
- Liu, Z.-X., Wang, X.-M., Wang, Q., Shen, X.-C., Liang, H., and Cui, F.-Z. (2012). Evolution of calcium phosphate crystallization on three functional group surfaces with the same surface density. *CrystEngComm*, 14(20):6695.
- Loerakker, S., Argento, G., Oomens, C. W. J., and Baaijens, F. P. T. (2013). Effects of valve geometry and tissue anisotropy on the radial stretch and coaptation area of tissue-engineered heart valves. *Journal of Biomechanics*, 46(11):1792–1800.
- Long, M. and Urry, D. (1981). On the molecular mechanism of elastic fiber calcification. *ASAIO Journal*, 27:690–696.
- Lu, G. and Xu, T. X. (2003). Inversion of a spherical shell. In *Energy Absorption of Structures and Materials*, chapter Cylindrica, pages 258–261. Elsevier.
- Luo, X. Y., Li, W. G., and Li, J. (2003). Geometrical stress-reducing factors in the anisotropic porcine heart valves. *Journal of biomechanical engineering*, 125(5):735–744.
- Ma, B., Wang, X., Wu, C., and Chang, J. (2014). Crosslinking strategies for preparation of extracellular matrix-derived cardiovascular scaffolds. *Regenerative Biomaterials*, 1(1):81–89.
- Mackay, T. G., Wheatley, D. J., Bernacca, G. M., Fisher, a. C., and Hindle, C. S. (1996). New polyurethane heart valve prosthesis: design, manufacture and evaluation. *Biomaterials*, 17(19):1857–63.
- Mackay, T. G. T. (1992). *Towards a Tri-Leaflet Polyurethane Heart Valve Prosthesis*. Phd, University of Strathclyde.
- Macosko, C. W. (1994). *Rheology Principles, Measurements and Applications*. Wiley-VCH, USA.
- Mai, Y. and Eisenberg, A. (2012). Self-assembly of block copolymers. *Chemical Society Reviews*, 41:5969–5985.

- Malhotra, A. (2012). The Changing Burden of Valvular Heart Disease. *British Cardiovascular Society*, June.
- Manji, R. a., Menkis, A. H., Ekser, B., and Cooper, D. K. C. (2012). Porcine bioprosthetic heart valves: The next generation. *American heart journal*, 164(2):177–85.
- Mark, J. E. (2007). *Physical properties of polymers handbook*. Springer Science+Business Media, LLC, 2007 edition.
- Marom, G., Peleg, M., Halevi, R., Rosenfeld, M., Raanani, E., Hamdan, A., and Haj-Ali, R. (2013). Fluid-structure interaction model of aortic valve with porcine-specific collagen fiber alignment in the cusps. *Journal of biomechanical engineering*, 135(10):101001–6.
- Mars, W. and Fatemi, A. (2002). A literature survey of fatigue analysis approaches for rubber. *International Journal of Fatigue*, 24:949–961.
- Mars, W. V. and Fatemi, A. (2003). Fatigue crack nucleation and growth in filled natural rubber. *Fatigue & Fracture of Engineering Materials & Structures*, 26(9):779–789.
- Martin, C. and Sun, W. (2015). Comparison of transcatheter aortic valve and surgical bioprosthetic valve durability: a fatigue simulation study. *Journal of Biomechanics*, page BMD1500350.
- Masoumi, N., Annabi, N., Assmann, A., Larson, B. L., Hjortnaes, J., Alemdar, N., Kharaziha, M., Manning, K. B., Mayer, J. E., and Khademhosseini, A. (2014). Tri-layered elastomeric scaffolds for engineering heart valve leaflets. *Biomaterials*, 35(27):7774–85.
- Mathison, M., Furuse, a., and Asano, K. (1988). Doppler analysis of flow velocity profile at the aortic root. *Journal of the American College of Cardiology*, 12(4):947–954.
- Mavridis, H. (1988). The Effect of Fountain Flow on Molecular Orientation in Injection Molding. *Journal of Rheology*, 32(6):639.
- Mavrilas, D. (2004). Screening biomaterials with a new in vitro method for potential calcification : Porcine aortic valves and bovine pericardium. *Journal of Materials Science: Materials in Medicine*, 15:699–704.
- Mavrilas, D., Apostolaki, A., Kapolos, J., Koutsoukos, P. G., Melachrinou, M., Zolota, V., and Dougenis, D. (1999). Development of bioprosthetic heart valve calcification in vitro and in animal models : morphology and composition. *Journal of crystal growth*, 205:554–562.

- Maxwell, A., Broughton, W., Dean, G., and Sims, G. (2005). Review of accelerated ageing methods and lifetime prediction techniques for polymeric materials. Technical report, Engineering and Process Control Divison, National Physical Laboratory, Middlesex, UK.
- MDDI Admin (1999). Silicone rubber for medical device applications.
- Medicore (2012). ECG Tutorial 1: Anatomy & Electrical System.
- Mendelson, K. and Schoen, F. J. (2006). Heart valve tissue engineering: Concepts, approaches, progress, and challenges. *Annals of Biomedical Engineering*, 34(12):1799–1819.
- Mercer, J., Benedicty, M., and Bahnson, H. (1973). The geometry and construction of the aortic leaflet. *Journal of Thoracic and Cardiovascular Surgery*, 65(4):511–8.
- Mohammadi, H., Boughner, D., Millon, L. E., and Wan, W. K. (2009). Design and simulation of a poly(vinyl alcohol)–bacterial cellulose nanocomposite mechanical aortic heart valve prosthesis. *Proceedings of the Institution of Mechanical Engineers, Part H: Journal of Engineering in Medicine*, 223(6):697–711.
- Mohammadi, H. and Mequanint, K. (2011). Prosthetic aortic heart valves: modeling and design. *Medical engineering and physics*, 33(2):131–47.
- Mohri, H., Hessel, E., Nelson, R., Anderson, H., Dillard, D., and Merendin, K. (1973). Design and durability test of silastic trileaflet aortic valve prostheses. *Journal of Thoracic and Cardiovascular Surgery*, 65(4):576–582.
- Morozov, A. N. and Fraaije, J. G. E. M. (2002). Orientations of the lamellar phase of block copolymer melts under oscillatory shear flow. *Physical Review E - Statistical, Nonlinear, and Soft Matter Physics*, 65(3):1–3.
- Morrison, F. A. (2001). *Understanding Rheology*. Oxford University Press, Michigan Tech University, 2001 edition.
- Mullen, M., Yap, J., Tzamtzis, S., Seifalian, A., and Burriesci, G. (2013). The TRISKELE Transcatheter Heart Valve. In *PCR London Valves*.
- Napier, R. (2012). *Hematology*. World Technologies.
- National Heart Lung and Blood Institute (2011). Heart valve disease. Technical report, US Department of Health and Human Services.
- Nawrat, Z. (2009). *Handbook of Polymer Applications in Medicine and Medical Devices*. Elsevier Inc.

- Neyt, M. and Van Brabandt, H. (2013). TAVI: reveal the truth, the whole truth, and nothing but the truth. *Journal of medical economics*, 16(5):581–5.
- Nistal, F., García-Martínez, V., Arbe, E., Fernández, D., Artiñano, E., Mazorra, F., and Gallo, I. (1990). In vivo experimental assessment of polytetrafluoroethylene trileaflet heart valve prosthesis. *Journal of Thoracic and Cardiovascular Surgery*, 99(6):1074–81.
- O'Brien, K. D. (2006). Pathogenesis of calcific aortic valve disease: a disease process comes of age (and a good deal more). *Arteriosclerosis, Thrombosis, and Vascular Biology*, 26(8):1721–8.
- Otto, C. M. (2012). *Practice of Clinical Echocardiography*. Elsevier Health Sciences, 4 edition.
- Papadopoulos, I. (2005). *Predicting the fatigue life of elastomer components*. PhD thesis, Queen Mary, University of London.
- Parfeev, V. M., Grushetskii, I. V., and Smurova, E. V. (1983). Mechanical properties of elastomers for artificial leaflet heart valves. *Mechanics of Composite Materials*, 19(1):92–99.
- Park, J.-C., Hwang, Y.-S., Han, D.-W., and Suh, H. (2000). A novel in vitro assessment of tissue valve calcification by a continuous flow type method. *Artificial organs*, 24(2):158–60.
- Park, J. M. and Park, S. J. (2011). Modeling and Simulation of Fiber Orientation in Injection Molding of Polymer Composites. *Mathematical Problems in Engineering*, 2011:1–14.
- Park, K. D., Lee, W. K., Yun, J. Y., Han, D. K., Kim, S. H., Kim, Y. H., Kim, H. M., and Kim, K. T. (1997). Novel anti-calcification treatment of biological tissues by grafting of sulphonated poly(ethylene oxide). *Biomaterials*, 18(1):47–51.
- Paul, A., Straub, A., Weber, N., Ziemer, G., and Wendel, H. P. (2009). CD41 Western blotting: a new method to detect platelet adhesion to artificial surfaces used in extra-corporeal circulation procedures. *Journal of materials science. Materials in medicine*, 20(1):373–8.
- Peacock, J. A. (1990). An in vitro study of the onset of turbulence in the sinus of Valsalva. *Circulation research*, 67(2):448–460.
- PECA Labs (2015). PECA Labs.
- Peskin, C. S. and McQueen, D. M. (1994). Mechanical equilibrium determines the fractal

- fiber architecture of aortic heart valve leaflets. *The American journal of physiology*, 266(1 Pt 2):H319–H328.
- Petrie, C. J. (2006). Extensional viscosity: A critical discussion. *Journal of Non-Newtonian Fluid Mechanics*, 137(1-3):15–23.
- Pettenazzo, E., Deiwick, M., Thiene, G., Molin, G., Glasmacher, B., Martignago, F., Bottio, T., Reul, H., and Valente, M. (2001). Dynamic in vitro calcification of bioprosthetic porcine valves: evidence of apatite crystallization. *The Journal of thoracic and cardiovascular surgery*, 121(3):500–9.
- Pezzella, T. A. (2005). Global Expansion of Cardiothoracic Surgery - The African Challenge. *African Annals of Thoracic and Cardiovascular Surgery*, 1:9–11.
- Phillip, W. a., O’neill, B., Rodwogin, M., Hillmyer, M. a., and Cussler, E. L. (2010). Self-assembled block copolymer thin films as water filtration membranes. *ACS Applied Materials and Interfaces*, 2(3):847–853.
- Pibarot, P. and Dumesnil, J. G. (2006). Prosthesis-patient mismatch: definition, clinical impact, and prevention. *Heart (British Cardiac Society)*, 92(8):1022–9.
- Pibarot, P. and Dumesnil, J. G. (2009). Prosthetic heart valves: selection of the optimal prosthesis and long-term management. *Circulation*, 119(7):1034–48.
- Pietsch, H., Kartheus, H., Holtzmann, H.-J., Sachau, G., and Reul, H. (1988). Heart valve prosthesis and process for its production.
- Pinchuk, L. (1994). A review of the biostability and carcinogenicity of polyurethanes in medicine and the new generation of ‘biostable’ polyurethanes. *Journal of Biomaterials Science, Polymer Edition*, 6(3):225–267.
- Pinchuk, L., Wilson, G. J., Barry, J. J., Schoephoerster, R. T., Parel, J.-M., and Kennedy, J. P. (2008). Medical applications of poly(styrene-block-isobutylene-block-styrene) (“SIBS”). *Biomaterials*, 29(4):448–60.
- Prawel, D. a., Dean, H., Forleo, M., Lewis, N., Gangwish, J., Popat, K. C., Dasi, L. P., and James, S. P. (2014). Hemocompatibility and Hemodynamics of Novel Hyaluronan-Polyethylene Materials for Flexible Heart Valve Leaflets. *Cardiovascular engineering and technology*, 5(1):70–81.
- Proto Labs Ltd. (2010). *Designing for mouldability*. Proto Labs, 2 edition.
- Puskas, J. E., Dos Santos, L. M., Fischer, F., Götz, C., El Fray, M., Altstädt, V., and Tomkins, M. (2009a). Fatigue testing of implantable specimens: Effect of sample size

- and branching on the dynamic fatigue properties of polyisobutylene-based biomaterials. *Polymer*, 50(2):591–597.
- Puskas, J. E., El Fray, M., Tomkins, M., Dos Santos, L. M., Fischer, F., and Altstädt, V. (2009b). Dynamic stress relaxation of thermoplastic elastomeric biomaterials. *Polymer*, 50(1):245–249.
- Radir, A. and Thomas, A. (1981). Tear behavior of rubbers over a wide range of rates. *Rubber Chemistry and Technology*, 54(1):15–23.
- Rahman, M. (2012). Degradation of Polyesters in Medical Applications. In Saleh, H., editor, *Polyester*, chapter 5. InTech.
- Rahmani, B., Tzamtzis, S., Ghanbari, H., Burriesci, G., and Seifalian, A. M. (2012). Manufacturing and hydrodynamic assessment of a novel aortic valve made of a new nanocomposite polymer. *Journal of biomechanics*, 45(7):1205–11.
- Rajamannan, N. M., Evans, F. J., Aikawa, E., Grande-Allen, K. J., Demer, L. L., Heistad, D. D., Simmons, C. a., Masters, K. S., Mathieu, P., O’Brien, K. D., Schoen, F. J., Towler, D. a., Yoganathan, A. P., and Otto, C. M. (2011). Calcific aortic valve disease: not simply a degenerative process: A review and agenda for research from the National Heart and Lung and Blood Institute Aortic Stenosis Working Group. Executive summary: Calcific aortic valve disease - 2011 update. *Circulation*, 124(16):1783–91.
- Ramstack, J. M., Zuckerman, L., and Mockros, L. F. (1979). Shear-induced activation of platelets. *Journal of biomechanics*, 12(2):113–125.
- Reade, L. (2009). Nanocages for flexible heart valves. *Materials World Magazine*.
- Remi, E., Khelil, N., Di Centa, I., Roques, C., Ba, M., Medjahed-Hamidi, F., Chaubet, F., Letourneur, D., Lansac, E., and Meddahi-Pelle, A. (2011). Pericardial Processing: Challenges, Outcomes and Future Prospects, Biomaterials Science and Engineering. In Pignatello, R., editor, *Biomaterials science and engineering*, chapter 22, pages 437–456. InTech.
- Rice, J. R. (1968). A Path Independent Integral and the Approximate Analysis of Strain Concentration by Notches and Cracks. *Journal of Applied Mechanics*, 35(2):379.
- Rivlin, R. and Thomas, A. (1953). Rupture of rubber. I. Characteristic energy for tearing. *Journal of Polymer Science*, 10(3):291–318.
- Rizzoli, G., Bottio, T., Thiene, G., Toscano, G., and Casarotto, D. (2003). Long-term durability of the Hancock II porcine bioprosthesis. *Journal of Thoracic and Cardiovascular Surgery*, 126(1):66–74.

- Robicsek, F. (1991). Leonardo da Vinci and the sinuses of Valsalva. *The Annals of Thoracic Surgery*, 52(2):328–335.
- Roche, N. and Perier, L. (2013). Influence of Elastomers Formulation on Fatigue Crack Growth Properties. *Procedia Engineering*, 66:705–712.
- Rock, C. A., Han, L., and Doehring, T. C. (2014). Complex collagen fiber and membrane morphologies of the whole porcine aortic valve. *PloS one*, 9(1):e86087.
- Rodés-Cabau, J. (2012). Transcatheter aortic valve implantation: current and future approaches. *Nature reviews. Cardiology*, 9(1):15–29.
- Roe, B. B. (1992). ‘Extinct’ Cardiac Valve Prosthesis. In Bodnar, E. and Frater, R., editors, *Replacement Cardiac Valves*, chapter 13, pages 307 – 332. McGraw-Hill, 1992 edition.
- Roe, B. B., Kelly, P. B. J., Myers, J. L., and Moore, D. W. (1966). Tricuspid Leaflet Aortic Valve Prosthesis. *Circulation*, 33(451):124–130.
- Rosamond, W., Flegal, K., Furie, K., Go, A., Greenlund, K., Haase, N., Hailpern, S. M., Ho, M., Howard, V., Kissela, B., Kissela, B., Kittner, S., Lloyd-Jones, D., McDermott, M., Meigs, J., Moy, C., Nichol, G., O’Donnell, C., Roger, V., Sorlie, P., Steinberger, J., Thom, T., Wilson, M., and Hong, Y. (2008). Heart disease and stroke statistics–2008 update: a report from the American Heart Association Statistics Committee and Stroke Statistics Subcommittee. *Circulation*, 117(4):e25–146.
- Rottenberg, D., Sondak, E., and Haimovich, D. (2000). Method for producing heart valves.
- Ruzette, A.-V. and Leibler, L. (2005). Block copolymers in tomorrow ’ s plastics. *Nature materials*, 4:19–31.
- Ruzicka, D. J., Hettich, I., Hutter, A., Bleiziffer, S., Badiu, C. C., Bauernschmitt, R., Lange, R., and Eichinger, W. B. (2009). The complete supraannular concept: in vivo hemodynamics of bovine and porcine aortic bioprotheses. *Circulation*, 120(11 Suppl):S139–45.
- Sacks, M., Smith, D., and Hiester, E. (1997). A small angle light scattering device for planar connective tissue microstructural analysis. *Annals of biomedical engineering*, 25(4):678–89.
- Sacristan, E., Corona, F., Suarez, B., Rodriguez, G., Duenas, B., Gorzelewski, a., and Calderon, M. (2003). Development of a universal second generation pneumatic ventricular assist device and drive unit. *Proceedings of the 25th Annual International*

- Conference of the IEEE Engineering in Medicine and Biology Society (IEEE Cat. No.03CH37439)*, 1:427–430.
- Sakurai, S. (2008). Progress in control of microdomain orientation in block copolymers - Efficiencies of various external fields. *Polymer*, 49:2781–2796.
- Sauren, A. A. H. J. (1981). *Mechanical behaviour of the aortic valve*. Phd, Eindhoven University of Technology.
- Schoen, F. J. and Levy, R. J. (1992). Bioprosthetic heart valve calcification: membrane-mediated events and alkaline phosphatase. *Bone and Mineral*, 17:129–133.
- Schoen, F. J. and Levy, R. J. (2005). Calcification of tissue heart valve substitutes: progress toward understanding and prevention. *The Annals of Thoracic Surgery*, 79(3):1072–80.
- Schoen, F. J. and Levy, R. J. (2009). SnapShot : Calcification of Bioprosthetic Heart Valves. *Biomaterials*, 30(26):4445–6.
- Schoen, F. J., Tsao, J. W., and Levy, R. J. (1986). Calcification of bovine pericardium used in cardiac valve bioprostheses. Implications for the mechanisms of bioprosthetic tissue mineralization. *The American journal of pathology*, 123:134–145.
- Sellaro, T. L. (2003). *Effects of collagen orientation on the medium-term fatigue response of heart valve biomaterials*. PhD thesis, University of Pittsburgh.
- Seyfert, U. T., Biehl, V., and Schenk, J. (2002). In vitro hemocompatibility testing of biomaterials according to the ISO 10993-4. *Biomolecular engineering*, 19(2-6):91–6.
- Shen, Z. L., Dodge, M. R., Kahn, H., Ballarini, R., and Eppell, S. J. (2008). Stress-strain experiments on individual collagen fibrils. *Biophysical journal*, 95(8):3956–3963.
- Sheriff, J., Bluestein, D., Girdhar, G., and Jesty, J. (2010). High-shear stress sensitizes platelets to subsequent low-shear conditions. *Annals of biomedical engineering*, 38(4):1442–50.
- Siddiqui, R. F., Abraham, J. R., and Butany, J. (2009). Bioprosthetic heart valves: modes of failure. *Histopathology*, 55(2):135–44.
- Sigler, M. and Jux, C. (2007). Biocompatibility of septal defect closure devices. *Heart (British Cardiac Society)*, 93(4):444–449.
- Sih, G. C., Paris, P. C., and Irwin, G. R. (1965). On cracks in rectilinearly anisotropic bodies. *International Journal of Fracture Mechanics*, 1(3):189–203.

- Sim, E. K. W., Muskawad, S., Lim, C.-S., Yeo, J. H., Lim, K. H., Grignani, R. T., Durrani, a., Lau, G., and Duran, C. (2003). Comparison of human and porcine aortic valves. *Clinical anatomy (New York, N.Y.)*, 16(3):193–6.
- Simmons, A., Hyvarinen, J., Odell, R. a., Martin, D. J., Gunatillake, P. a., Noble, K. R., and Poole-Warren, L. a. (2004). Long-term in vivo biostability of poly(dimethylsiloxane)/poly(hexamethylene oxide) mixed macrodiol-based polyurethane elastomers. *Biomaterials*, 25(20):4887–4900.
- Sinn, S., Scheuermann, T., Deichelbohrer, S., Ziemer, G., and Wendel, H. P. (2011). A novel in vitro model for preclinical testing of the hemocompatibility of intravascular stents according to ISO 10993-4. *Journal of materials science. Materials in medicine*, 22(6):1521–8.
- Society for Cardiothoracic Surgery in GB and Ireland (2011). National Adult Cardiac Surgery Audit. Technical report, UCL, London.
- Sperling, C., Schweiss, R. B., Streller, U., and Werner, C. (2005). In vitro hemocompatibility of self-assembled monolayers displaying various functional groups. *Biomaterials*, 26(33):6547–6557.
- Starcher, B. C. and Urry, D. W. (1973). Elastic coacervate as a matrix for calcification. *Biochemical and Biophysical Research Communications*, 53(1):210–216.
- Stasiak, J., Moggridge, G. D., Zaffora, A., Pandolfi, A., and Costantino, M. L. (2010). Engineering Orientation in Block Copolymers for Application To Prosthetic Heart Valves. *Functional Materials Letters*, 03(04):249–252.
- Stasiak, J., Nair, S., and Moggridge, G. D. (2014). Mechanical strength of sutured block copolymers films for load bearing medical applications. *Bio-Medical Materials and Engineering*, 24(1):563–569.
- Stasiak, J., Squires, A. M., Castelletto, V., Hamley, I. W., and Moggridge, G. D. (2009). Effect of Stretching on the Structure of Cylinder and Sphere Forming Styrene-Isoprene-Styrene Block Copolymers. *Macromolecules*, 42(14):5256–5265.
- Stasiak, J., Zaffora, A., Costantino, M. L., and Moggridge, G. D. (2011). A real time SAXS study of oriented block copolymers during fast cyclical deformation, with potential application for prosthetic heart valves. *Soft Matter*, 7:11475–11482.
- Staudinger, U., Satapathy, B. K., and Weidisch, R. (2008). Influence of block composition on crack toughness behaviour of styrene-b-(styrene-random-butadiene)-b-styrene triblock copolymers. *European Polymer Journal*, 44(6):1822–1833.

- Streller, U., Sperling, C., Hübner, J., Hanke, R., and Werner, C. (2003). Design and evaluation of novel blood incubation systems for in vitro hemocompatibility assessment of planar solid surfaces. *Journal of Biomedical Materials Research. Part B, Applied Biomaterials*, 66(1):379–90.
- Subhani, M., Kumar, R. K., and Balakrishnan, K. R. (2013). Normal aortic valves stay open much longer in systole than porcine substitutes. *Asian cardiovascular & thoracic annals*, 21(3):275–80.
- Sumpio, B. E., Timothy Riley, J., and Dardik, A. (2002). Cells in focus: Endothelial cell. *International Journal of Biochemistry and Cell Biology*, 34(12):1508–1512.
- Sun, W., Abad, A., and Sacks, M. S. (2005). Simulated bioprosthetic heart valve deformation under quasi-static loading. *Journal of biomechanical engineering*, 127(6):905–914.
- Swanson, W. and Clark, R. (1977). A simple cardiovascular system simulator: design and performance. *Journal of Bioengineering*, 1(2):135–45.
- Syedain, Z. H., Meier, L. A., Reimer, J., and Tranquillo, R. T. (2012). Tubular heart valves from decellularized engineered tissue. *Annals of biomedical engineering*, 41(12):2645–54.
- Talukder, N. and Reul, H. (1978). Fluid Mechanics of Natural Cardiac Valves. In Bauer, R. and Busse, R., editors, *The Arterial System*, pages 269–74. Springer Berlin Heidelberg.
- Tam, H., Zhang, W., Feaver, K. R., Parchment, N., Sacks, M. S., and Vyavahare, N. (2015). A novel crosslinking method for improved tear resistance and biocompatibility of tissue based biomaterials. *Biomaterials*, 66:83–91.
- Tanzi, M. C., Mantovani, D., Petrini, P., Guidoin, R., and Laroche, G. (1997). Chemical stability of polyether urethanes versus polycarbonate urethanes. *Journal of Biomedical Materials Research*, 36(4):550–559.
- Ten Berge, L. (1958). A flexible cardiac valve prosthesis; preliminary report on the development of an experimental valvular prosthesis. *Archivum Chirurgicum Neerlandicum*, 10(1):26–33.
- Teoh, S. (2000). Fatigue of biomaterials: a review. *International Journal of Fatigue*, 22(10):825–837.
- Thomas, A. (1994). The development of fracture mechanics for elastomers. *Rubber chemistry and technology*, 67(3):G50–G60.

- Thomas, V. and Jayabalan, M. (2009). A new generation of high flex life polyurethane urea for polymer heart valve—studies on in vivo biocompatibility and biodurability. *Journal of biomedical materials research. Part A*, 89(1):192–205.
- Thubrikar, M., Deck, J., Aouad, J., and Nolan, S. (1983). Role of mechanical stress in calcification of aortic bioprosthetic valves. *The Journal of Thoracic and Cardiovascular Surgery*, 86(1):115–25.
- Thubrikar, M. and Klemchuk, P. (1990). *The Aortic Valve*. CRC Press, Boca Raton, FL.
- Thubrikar, M., Piepgrass, W. C., Bosher, L. P., and Nolan, S. P. (1980). The elastic modulus of canine aortic valve leaflets in vivo and in vitro. *Circulation Research*, 47(5):792–800.
- Thyregod, H., Steinbrüchel, D., Ihlemann, N., Nissen, H., Kjeldsen, B., Petursson, P., Chang, Y., Franzen, O., Engstrøm, T., Clemmensen, P., Hansen, P., Andersen, L., Olsen, P., and Søndergaard, L. (2015). Transcatheter versus surgical aortic valve replacement in patients with severe aortic valve stenosis: 1-year results from the all-comers NOTION randomized clinical trial. *Journal of the American College of Cardiology*, 65(20):2184–94.
- Tien, W. H., Chen, H. Y., Berwick, Z. C., Krieger, J., Chambers, S., Dabiri, D., and Kassab, G. S. (2014). Role of sinus in prosthetic venous valve. *European Journal of Vascular and Endovascular Surgery*, 48(1):98–104.
- Tokita, N. and White, J. L. (1966). Milling Behavior of Gum Elastomers: Experiment and Theory. *Journal of Applied Polymer Science*, 10:1011–1026.
- Touma, H., Sahin, I., Gaamangwe, T., Gorbet, M. B., and Peterson, S. D. (2014). Numerical investigation of fluid flow in a chandler loop. *Journal of biomechanical engineering*, 136(7):1–8.
- Trantina-Yates, A. E., Human, P., Bracher, M., and Zilla, P. (2001). Mitigation of bioprosthetic heart valve degeneration through biocompatibility: In vitro versus spontaneous endothelialization. *Biomaterials*, 22(13):1837–1846.
- Trebbin, M., Steinhauser, D., Perlich, J., Buffet, A., Roth, S. V., Zimmermann, W., Thiele, J., and Förster, S. (2013). Anisotropic particles align perpendicular to the flow direction in narrow microchannels. *Proceedings of the National Academy of Sciences of the United States of America*, 110(17):6706–11.
- Vaesken, A., Heim, F., and Chakfe, N. (2014). Fiber heart valve prosthesis: Influence of

- the fabric construction parameters on the valve fatigue performances. *Journal of the mechanical behavior of biomedical materials*, 40C:69–74.
- Vahanian, A., Alfieri, O., Andreotti, F., Antunes, M. J., Barón-Esquivias, G., Baumgartner, H., Borger, M. A., Carrel, T. P., De Bonis, M., Evangelista, A., Falk, V., Iung, B., Lancellotti, P., Pierard, L., Price, S., Schäfers, H.-J., Schuler, G., Stepinska, J., Swedberg, K., Takkenberg, J., Von Oppell, U. O., Windecker, S., Zamorano, J. L., Zembala, M., Bax, J. J., Ceconi, C., Dean, V., Deaton, C., Fagard, R., Funck-Brentano, C., Hasdai, D., Hoes, A., Kirchhof, P., Knuuti, J., Kolh, P., McDonagh, T., Moulin, C., Popescu, B. a., Reiner, Z., Sechtem, U., Sirnes, P. A., Tendera, M., Torbicki, A., Von Segesser, L., Badano, L. P., Bunc, M., Claeys, M. J., Drinkovic, N., Filippatos, G., Habib, G., Kappetein, a. P., Kassab, R., Lip, G. Y. H., Moat, N., Nickenig, G., Otto, C. M., Pepper, J., Piazza, N., Pieper, P. G., Rosenhek, R., Shuka, N., Schwammenthal, E., Schwitter, J., Mas, P. T., Trindade, P. T., and Walther, T. (2012). Guidelines on the management of valvular heart disease (version 2012). *European heart journal*, 33(19):2451–96.
- van Bilsen, P. H. J., Krenning, G., Billy, D., Duval, J.-L., Huurdeman-Vincent, J., and van Luyn, M. J. a. (2008). Heparin coating of poly(ethylene terephthalate) decreases hydrophobicity, monocyte/leukocyte interaction and tissue interaction. *Colloids and surfaces. B, Biointerfaces*, 67(1):46–53.
- Van Steenhoven, A. A. and Van Dongen, M. E. H. (1979). Model studies of the closing behaviour of the aortic valve. *Journal of Fluid Mechanics*, 90(01):21.
- Varadarajan, P., Patel, R., Turk, R., Kamath, a. R., Sampath, U., Khandhar, S., and Pai, R. G. (2013). Etiology impacts survival in patients with severe aortic regurgitation: results from a cohort of 756 patients. *J Heart Valve Dis*, 22(1):42–49.
- Vesely, I. (1998). The role of elastin in aortic valve mechanics. *Journal of biomechanics*, 31(2):115–23.
- Vesely, I. (2003). The evolution of bioprosthetic heart valve design and its impact on durability. *Cardiovascular Pathology*, 12(5):277–286.
- Vesely, I., Boughner, D., and Song, T. (1998). Tissue buckling as a mechanism of bioprosthetic valve failure. *The Annals of Thoracic Surgery*.
- Vienken, J. (2008). Testing biomaterials for application in artificial organs: Impact of procedures, donor and patient properties. *Prilozi*, 37(2):25–37.
- Vlachopoulos, J. and Strutt, D. (2003). Polymer processing. *Materials Science and Technology*, 19(9):1161–1169.

- Vladkova, T. G. (2013). Surface Engineering of Blood Contacting Polymeric Biomaterials. In *Surface Engineering of Polymeric Biomaterials*, chapter 4, pages 231–294. Smithers Rapra.
- Vondracek, P. and Dolezel, B. (1984). Biostability of medical elastomers : a review. *Biomaterials*, 5:209–214.
- Vongapatanisin, W., Hillis, D., and Ange, R. (1996). Characteristics of prosthetic valves. *The New England Journal of Medicine*, August:407–416.
- Vyavahare, N. R., Chen, W., Joshi, R. R., Lee, C.-h., Hirsch, D., Levy, J., Schoen, F. J., and Levy, R. J. (1997a). Current Progress in Anticalcification for Bioprosthetic and Polymeric Heart Valves. *Cardiovascular Pathology*, 6(4):219–29.
- Vyavahare, N. R., Hirsch, D., Lerner, E., Baskin, J. Z., Schoen, F. J., Bianco, R., Kruth, H. S., Zand, R., and Levy, R. J. (1997b). Prevention of Bioprosthetic Heart Valve Calcification by Ethanol Preincubation. *Circulation*, 95:479–488.
- Wagner, I. M., Eichinger, W. B., Bleiziffer, S., Botzenhardt, F., Gebauer, I., Guenzinger, R., Bauernschmitt, R., and Lange, R. (2007). Influence of completely supra-annular placement of bioprostheses on exercise hemodynamics in patients with a small aortic annulus. *The Journal of thoracic and cardiovascular surgery*, 133(5):1234–41.
- Wang, Q., McGoron, A., and Bianco, R. (2010). In-vivo assessment of a novel polymer (SIBS) trileaflet heart valve. *Journal of Heart Valve Disease*, 19(4):499–505.
- Weber, N., Wendel, H. P., and Ziemer, G. (2002). Hemocompatibility of heparin-coated surfaces and the role of selective plasma protein adsorption. *Biomaterials*, 23(2):429–39.
- Weinberg, S. and King, M. (2004). Medical fibers and biotextiles. In Ratner, B. D., editor, *Biomaterials Science. An introduction to materials in medicine.*, chapter 2.4, pages 86–99. Academic Press.
- Weiss, A. S. (2010). The Science of Elastin. *Elastagen Media*, (February 2011):1–8.
- Weiss, R. M., Miller, J. D., and Heistad, D. D. (2013). Fibrocalcific aortic valve disease: Opportunity to understand disease mechanisms using mouse models. *Circulation Research*, 113(2):209–222.
- Wendel, H. P. and Ziemer, G. (1999). Coating-techniques to improve the hemocompatibility of artificial devices used for extracorporeal circulation. *European Journal of Cardio-Thoracic Surgery*, 16:342–350.

- Wheatley, D. J., Fisher, J., and Williams, D. (1998). Heart Valve Prosthesis.
- White, J. L. and Tokita, N. (1968). Instability and Failure Phenomena in Polymer Processing with Application to Elastomer Mill Behavior. *Journal of Applied Polymer Science*, 12:1589–1600.
- Williams, D. F. (2014). There is no such thing as a biocompatible material. *Biomaterials*, 35:10009–14.
- Williams, D. F. (2015). Regulatory biocompatibility requirements for biomaterials used in regenerative medicine. *Journal of Materials Science: Materials in Medicine*, 26(2):2014–2015.
- Winter, H. H. (1975). Calculation and measurement of the pressure distribution in radial flow of molten polymers between parallel discs. *Polymer Engineering & Science*, 15(6):460–69.
- World Heart Federation (2012). Rheumatic heart disease. Technical report, World Heart Federation.
- Wright, D. (1996). *Environmental stress cracking of plastics*. iSmithers Rapra Publishing.
- Wurzinger, L., Opitz, R., Blasberg, P., and Schmid-Schonbein, J. (1985). Platelet and coagulation parameters following millisecond exposure to laminar shear stress. *Thrombosis and Haemostasis*, 54(2):381–6.
- Yacoub, M. H. and Takkenberg, J. J. M. (2005). Will heart valve tissue engineering change the world? *Nature clinical practice. Cardiovascular medicine*, 2(2):60–1.
- Yang, M., Zhang, Z., Hahn, C., King, M., and Guidoin, R. (1999). Assessing the resistance to calcification of polyurethane membranes used in the manufacture of ventricles for a totally implantable artificial heart. *Journal of Biomedical Materials Research*, 48(5):648–59.
- Yap, C. H., Kim, H.-S., Balachandran, K., Weiler, M., Haj-Ali, R., and Yoganathan, A. P. (2010). Dynamic deformation characteristics of porcine aortic valve leaflet under normal and hypertensive conditions. *American journal of physiology. Heart and circulatory physiology*, 298(2):H395–405.
- Yeh, C. H., Hogg, K., and Weitz, J. I. (2015). Overview of the New Oral Anticoagulants: Opportunities and Challenges. *Arteriosclerosis, thrombosis, and vascular biology*, pages 1056–1065.

- Yoda, R. (1998). Elastomers for biomedical applications. *Journal of Biomaterials Science, Polymer Edition*, 9(6):561–626.
- Yoganathan, A. P., Chandran, K. B., and Sotiropoulos, F. (2005). Flow in prosthetic heart valves: state-of-the-art and future directions. *Annals of biomedical engineering*, 33(12):1689–94.
- Yoshida, M., Wearden, P. D., Dur, O., Pekkan, K., and Morell, V. O. (2011). Right Ventricular Outflow Tract Reconstruction With Contegra Bovine Valved Conduit. *The Annals of Thoracic Surgery*, 91(4):1235–8.
- Zaffora, A. (2011). *Computational method for the design of innovative materials for heart valve prosthesis*. PhD thesis, Politecnico di Milano.
- Zarrin-Ghalami, T. and Fatemi, A. (2012). Material Deformation and Fatigue Behavior Characterization for Elastomeric Component Life Predictions. *Polymer Engineering and Science*, pages 1795–1805.
- Zdrahala, R. J. and Zdrahala, I. J. (1999). Biomedical applications of polyurethanes: A review of past promises, present realities and a vibrant future. *Journal of Biomaterials Applications*, 14(1):67–90.
- Zegdi, R., Bruneval, P., Blanchard, D., and Fabiani, J.-N. (2011). Evidence of leaflet injury during percutaneous aortic valve deployment. *European Journal of Cardio-Thoracic Surgery*, 40(1):257–259.
- Zhang, M. and Wu, Q.-C. (2010). Intra-supra annular aortic valve and complete supra annular aortic valve: a literature review and hemodynamic comparison. *Scandinavian journal of surgery : SJS : official organ for the Finnish Surgical Society and the Scandinavian Surgical Society*, 99(1):28–31.
- Zilla, P., Brink, J., Human, P., and Bezuidenhout, D. (2008). Prosthetic heart valves: catering for the few. *Biomaterials*, 29(4):385–406.
- Zoghbi, W. A., Chambers, J. B., Dumesnil, J. G., Foster, E., Gottdiener, J. S., Grayburn, P. a., Khandheria, B. K., Levine, R. a., Marx, G. R., Miller, F. a., Nakatani, S., Quiñones, M. a., Rakowski, H., Rodriguez, L. L., Swaminathan, M., Waggoner, A. D., Weissman, N. J., and Zabalgoitia, M. (2009). Recommendations for Evaluation of Prosthetic Valves With Echocardiography and Doppler Ultrasound. A Report From the American Society of Echocardiography’s Guidelines and Standards Committee and the Task Force on Prosthetic Valves, Developed in Conjunction. *Journal of the American Society of Echocardiography*, 22(9):975–1014.